

**Development of novel allosteric
regulators of proteinase-activated
receptors**

Thesis presented by
Graeme McDermott Sloan

In fulfilment of the requirements for the degree of
Doctor of Philosophy
2019

Strathclyde Institute of Pharmacy and Biomedical Sciences

This thesis is the result of the author's original research. It has been composed by the author and has not been previously submitted for examination which has led to the award of a degree.

The copyright of this thesis belongs to the author under the terms of the United Kingdom Copyright Acts as qualified by University of Strathclyde Regulation 3.50. Due acknowledgement must always be made of the use of any material contained in, or derived from, this thesis.

Signed: 

Date: 17/10/19

Acknowledgements

Firstly, I would like to thank Dr Craig Jamieson and Prof. Robin Plevin. Thank you for being so accommodating in the final 15 months of my PhD, allowing me the opportunity to return to a chemistry lab and leave my PhD with complementary chemistry and pharmacology skillsets. Additionally, thanks to Dr Margaret Cunningham and Prof. Gail McConnell for allowing me to begin the journey towards my PhD.

To the past and present CJAM PhDs (Keith, Chris, Kirsty, Kirsty, Jen, Jen, Meghan, Gemma and Jenna) thanks for being so welcoming to a scientific turncoat and accepting my return to the chemical sciences. Thanks also to everyone else who has been through the lab in my short time back in the Thomas Graham building.

Thanks to everyone I know from SIPBS. Most importantly, thanks to Ross and John. We've all been there for each other and this experience wouldn't have been the same without you both. Additionally, huge thanks to Kerrie, Jeremy, Peter, Aimée and Mirna. To everyone else I've had the pleasure of meeting in SIPBS, thank you for the chats and drinks!

I would like to give a special thank you to Barry and Paul. In 2009, I left your classrooms and started my undergraduate degree in chemistry. 10 years on, I can truthfully say that were it not for the two of you, I would never have embarked on this journey into chemistry and eventually obtain my PhD.

Thanks to Dr Declan Bryans. You gave a lot of advice throughout the PhD that was truly invaluable. Remind me I owe you some number of drinks next time we are out!

Thanks to my family. Mum, Dad, Colin... without your unconditional love and support, getting to this stage would have been impossible. Being able to come home and know that I could talk about all the problems I have was a huge support, I just hope I didn't do it too much! I love you all!

Finally, thank you to Olga. I won't put too much here, I know you wouldn't want that. However, I will say that without you I would not have been able to get back on track and finish this PhD. I am eternally grateful for the love and support you gave me through the highs and the lows from 2016 to the end of my PhD.

Abstract

Proteinase-activated receptors (PARs), members of the G-protein coupled receptor (GPCR) superfamily of proteins, represent highly attractive targets for therapy across a wide range of diseases. Of specific interest are PAR1 and PAR2, the major signalling members of the PAR family which are associated with cardiovascular disease, cancer and inflammatory disease. However, despite significant efforts, there is only one marketed drug for the PARs available in Vorapaxar, which is used to inhibit PAR1 in the treatment of thrombosis.¹ Thus, exploring different chemical approaches to developing better lead molecules is important to explore novel methods for modulating the PARs.

Pepducins, peptidic compounds containing a palmitoyl chain, have represented a novel approach to allosteric modulation of PARs, with PZ-128 targeting PAR1 and PZ-235 targeting PAR2 as promising lead compounds.^{2,3} However, deviation from the general pepducin structure has not been explored and represent possible areas of improvement. Herein, 10 novel PZ-128 analogues are described as potential improvements to PZ-128 highlighting the impact of linker modification as well as cyclisation of the peptide sequence. Additionally, off-target activity of PZ-128 is also explored, highlighting some intrinsic problems with the pepducin approach. These problems were alleviated to an extent with the novel PZ-128 analogues but identifying overall improvements to the pharmacological character of the series proved challenging.

Recently, two potential lead molecules were published targeting PAR2 with AZ8838 and AZ3451.⁴ These compounds have provided new insight into how we can target PAR2, allowing access to novel chemicals with improved properties. Through a series of modifications to the published chemical structures, we have accessed novel compounds that display similar biological properties to AZ8838. Herein, 15 novel analogues of AZ8838 have been synthesised and their propensity for PAR2 inhibition tested in *in vitro* assays, identifying one compound of comparable potency whilst exploring the SAR surrounding the AZ8838 binding pocket. Additionally, an expanded library of AZ8838 analogues has been computationally docked to assess binding within PAR2 *in silico*.

Publications

Cunningham, M.; McIntosh, K.; Bushell, T.; **Sloan, G.**; Plevin, R. Proteinase-Activated Receptors (PARs) as Targets for Antiplatelet Therapy. *Biochem. Soc. Trans.* **2016**, *44* (2), 606–612

Conference Communications

Graeme M. Sloan, Helmus Van de Langemheen, Gail McConnell, Robin Plevin, Robert Liskamp, Margaret Cunningham (2016) Potential off-target activity of proteinase-activated receptor (PAR) pepducins. Poster presentation at XIX SIF Seminar on Pharmacology and Similar Sciences, Rimini, Italy

Graeme M. Sloan, Helmus Van de Langemheen, Gail McConnell, Robin Plevin, Robert Liskamp, Margaret Cunningham (2017) Potential off-target activity of proteinase-activated receptor (PAR) pepducins. Poster presentation at Scottish Cardiovascular Forum, Glasgow, UK

List of Abbreviations

AC	Adenylate cyclase	GTP	Guanosine triphosphate
ADP	Adenosine diphosphate	GEF	Guanine nucleotide exchange factor
AMP	Adenosine monophosphate	HEK	Human embryonic kidney
APC	Activated protein C	HMBC	Heteronuclear multiple bond correlation
ATP	Adenosine triphosphate	HPLC	High pressure liquid chromatography
Bn	Benzyl	HSQC	Heteronuclear single quantum coherence
Boc	<i>tert</i> -Butyloxycarbonyl	HRMS	High resolution mass spectrometry
BTK	Bruton's tyrosine kinase	ESI	Electrospray ionisation
cAMP	Cyclic AMP	ICL	Intracellular loop
CaS	Calcium sensing receptor	IP3	Inositol triphosphate
CDC	Cell division control protein	IR	Infrared spectroscopy
CuAAC	Copper-catalysed azide-alkyne cycloaddition	KLK	Kallikrein
CXCR	CXC chemokine receptor	LAH	Lithium aluminium hydride
DAG	Diacylglycerol	LCMS	Liquid chromatography mass spectrometry
DMF	Dimethylformamide	LE	Ligand efficiency
DMSO	Dimethylsulfoxide	LUMO	Lowest unoccupied molecular orbital
ECL	Extracellular loop	MAPK	Mitogen-activated protein kinase
ER	Endoplasmic reticulum	MASP	Mannan-binding lectin serine protease
ERK	Extracellular signal regulated kinases	MMP	Matrix metalloprotease
EWG	Electron withdrawing group	MTT	3-(4,5-Dimethylthiazol-2-yl)-2,5-diphenyltetrazolium bromide for
Fmoc	Fluorenylmethyloxycarbonyl	MWt	Molecular weight
FVIIa	Recombinant factor VIIa	N/D	Not described
FXa	Blood coagulation factor Xa		
GABA	γ -aminobutyric acid		
GAIN	GPCR autoproteolysis inducing (domain)		
GDP	Guanosine diphosphate		
GPCR	G-protein coupled receptor		
GRK	GPCR kinase		

NAM	Negative allosteric modulator	RFU	Relative fluorescence units
NFκB	Nuclear factor kappa-light-chain-enhancer of activated B cells	RGS RhoA	Regulator of G-protein signalling Ras homolog gene family, member A
NMR	Nuclear magnetic resonance	ROS	Reactive oxygen species
s	Singlet	RT	Room temperature
d	Doublet	SAR	Structure-activity relationship
t	Triplet	SEM	2-Trimethylsilylethoxymethyl
q	Quartet	(Chemistry)	
m	Multiplet	SEM	Standard error of the mean
dd	Doublet of doublets	(Statistical)	
dt	Doublet of triplets	Smo	Smoothened receptor
td	Triplet of doublets	SPPS	Solid phase peptide synthesis
PAF	Platelet-activating factor	SRC	
PAM	Positive allosteric modulator	TBAF	Tetrabutylammonium fluoride
PAR	Proteinase-activated receptor	TBTA	Tris(benzyltriazolylmethyl)amine
PDC	Pyridinium dichromate	TFA	Trifluoroacetic acid
pERK	Phosphorylated ERK	THF	Tetrahydrofuran
PI3K	Phosphoinositide 3-kinase	TLC	Thin layer chromatography
PIP2	Phosphatidylinositol 4,5-bisphosphate	TMP	Tetramethylpiperidine
PIP3	Phosphatidylinositol (3,4,5)-trisphosphate	TotERK	Total ERK
PKC	Protein kinase C	Ts	Tosyl
PLC	Phospholipase C		
PS	Phosphatidylserine		

Table of Contents

Acknowledgements	ii
Abstract.....	iii
Publications.....	iv
Conference Communications	iv
List of Abbreviations	v
Table of Contents.....	vii
List of Figures, Tables and Schemes.....	x
Chapter 1 Introduction	1
1.1 G-Protein Coupled Receptors	1
1.1.1 General Structure of GPCRs	1
1.1.2 Mechanism of Action for GPCRs	4
1.1.3 Relevance to Drug Discovery	12
1.2 Proteinase-Activated Receptors	17
1.2.1 Structure of PARs	17
1.2.2 Mechanism of Action for PARs	18
1.2.3 PARs in Disease	24
1.3 Modulation of PAR Function.....	31
1.3.1 Background	31
1.3.2 Pepducin-mediated Modulation of PAR1	35
1.3.3 PAR2 Inhibitors	39
1.4 Aims	44
1.4.1 Allosteric Modulation of PAR1.....	44
1.4.2 Small Molecule Allosteric Inhibitors of PAR2.....	44
Chapter 2 Allosteric Modulation of PAR1.....	45
2.1 Introduction	45
2.2 Aims and Objectives.....	46
2.3 Synthesis and Validation of PZ-128.....	48
2.3.1 Synthesis of 2.1 and 2.2	48
2.3.2 Pharmacology of PAR1 antagonists PZ-128 and SCH79797.....	51
2.4 Aberrant Activity of PZ-128.....	59
2.4.1 Off-target activity of PZ-128	59
2.4.2 Kinetics of PZ-128-mediated activity	65
2.4.3 PAR1-Independence of PZ-128-mediated activity.....	74

2.4.4	Inhibiting the off-target effects of PZ-128	80
2.4.5	Effect of pepducins on cell viability	84
2.5	Improving upon PZ-128	90
2.5.1	PAR1 cyclic pepducins.....	90
2.5.2	Elongated linker	97
2.5.3	Summary	103
2.6	Fluorescent-tagged pepducins.....	104
2.7	Summary	108
Chapter 3	Small Molecule Allosteric Inhibitors of PAR2.....	109
3.1	Introduction	109
3.2	Aims and Objectives.....	111
3.3	<i>In Silico</i> Docking Studies.....	113
3.3.1	Validation of Computational Studies – AutoDock Vina	113
3.3.2	Validation of GOLD.....	115
3.3.3	Docking of AZ8838 analogues.....	119
3.3.4	Summary of Docking	137
3.4	Synthesis of (±)-AZ8838	141
3.5	Synthesis of AZ8838 analogues	148
3.5.1	Synthesis of Imidazole Analogues.....	148
3.5.2	Synthesis of Linker Analogues.....	167
3.5.3	Synthesis of Propyl Analogues	169
3.5.4	Alkenyl analogues	179
3.5.5	Summary of Synthesis.....	184
3.6	Biological Data	186
3.6.1	Confirmation of 3.1 Function.....	187
3.6.2	Initial Screening of AZ8838 Library	189
3.6.3	Further Analysis	197
3.6.4	Summary of Biological Experiments	198
Chapter 4	Conclusions	201
4.1	Allosteric Modulation of PAR1.....	201
4.2	Allosteric Modulation of PAR2.....	203
Chapter 5	Future Work	205
5.1	PAR1 Pepducins	205
5.1.1	Completing the study of PZ-128	205

5.1.2	Advancing the PAR1-derived pepducin strategy	205
5.2	PAR2 small molecule modulators	206
5.2.1	<i>In silico</i> studies	206
5.2.2	Synthetic chemistry	206
5.2.3	Enantiopure synthesis.....	207
Chapter 6	Materials and Methods.....	209
6.1	Allosteric Modulation of PAR1 – Chemical Synthesis	209
6.1.1	General Techniques	209
6.1.2	General Procedures	210
6.1.3	Characterisation Data	211
6.2	Allosteric Modulation of PAR1 – Biological Methods.....	214
6.2.1	Reagents	214
6.2.2	Equipment.....	217
6.2.3	Biological Methods	218
6.3	Small Molecule Allosteric Inhibitors of PAR2.....	227
6.3.1	General Techniques	227
6.3.2	Computational Studies.....	229
6.3.3	General Procedures	229
6.3.4	Characterisation Data	232
6.3.5	Biological Methods	279
Chapter 7	References.....	280
Appendix I	– 2D NMR Spectra for 3.50	296
Appendix II	– 2D NMR Spectra for 3.51	300
Appendix III	– Variable Temperature Studies with 3.24	304

List of Figures, Tables and Schemes

Figure 1.1: Representative structure of a GPCR showing general structural features	2
Figure 1.2: General mechanism of activation for GPCRs	5
Figure 1.3: Self-regulation of GPCR activated states	6
Figure 1.4: Structure of heterotrimeric G-protein with G_α shown in blue, G_β shown in red and G_γ shown in green	7
Figure 1.5: Tertiary structure of G_α in complex with GDP with α -helices in red and β -sheets in blue	8
Figure 1.6: G_s and $G_{i/o}$ signalling cascades as a result of GPCR activation	9
Figure 1.7: $G_{q/11}$ and $G_{12/13}$ signalling cascades as a result of GPCR activation	10
Figure 1.8: Tertiary structure of G_β (A) and G_γ (B) subunits with α -helices in red and β -sheets in blue	11
Figure 1.9: $G_{\beta\gamma}$ signalling cascades as a result of GPCR activation.....	12
Figure 1.10: Homology of the PAR subfamily of GPCRs.....	18
Figure 1.11: A simplified mechanism for activation of PARs by a serine protease	19
Figure 1.12: Serine proteases predominately responsible for activation of PARs and the associated G proteins for each PAR.....	20
Figure 1.13: Heterodimerisation of PAR1 and PAR4 allowing activation of a second PAR within a single binding event for the serine protease.....	22
Figure 1.14: Simplified mechanism for inactivation of PARs by protease enzyme	23
Figure 1.15: Biased signalling as a result of activation of PAR1 by a range of proteases.....	24
Figure 1.16: Steps involved in haemostasis.....	25
Figure 1.17: Simplified schematic for immune response.....	28
Figure 1.18: Known binding sites utilised for PAR modulation	32
Figure 1.19: Vorapaxar bound within the transmembrane domain of PAR1.....	34
Figure 1.20: Molecular structure of PAR1 pepducin PZ-128	35
Figure 1.21: Proposed mechanism of action for transfer of pepducins across the cell membrane ..	37
Figure 1.22: Chemical structures of PAR2 antagonists ENMD-1068 and GB88.....	40
Figure 1.23: Overlaid crystal structure of PAR2 in complex with AZ3451 and AZ8838	41
Figure 1.24: Chemical structure of PZ-235	42
Figure 2.1: General structure for A typical pepducins, B cyclic pepducins and C linear analogue of cyclic pepducins.....	46
Figure 2.2: Chemical structure of control pepducins 2.1 and 2.2	48
Figure 2.3: Activation of PAR1 in HEK-293 cells stained with Fluor-4 Direct™	53
Figure 2.4: Chemical structure of competitive antagonist SCH79797 (2.3) and control cyclic peptide 2.4	54
Figure 2.5: Inhibition of PAR1 in HEK-293 cells using PAR1 antagonists 2.1 and 2.3 , and negative controls 2.2 and 2.4 , at concentrations of 1-100 μ M	55
Figure 2.6: Schild analysis of 2.1 and 2.3	57
Figure 2.7 Schild analysis of 2.1 inhibiting thrombin-mediated calcium release in Fluo-4 stained HEK-293 cells.....	58
Figure 2.8: Activation of Ca^{2+} Signalling in HEK-293 cells.....	60
Figure 2.9: Activation of calcium signalling in HEK-293 cells loaded with Fluo-4 Direct Dye in a buffer with $[Ca^{2+}] = 0$ mM.....	61
Figure 2.10: Activation of ERK1/2 in response to thrombin and TFLLR-NH ₂	62
Figure 2.11 Activation of ERK1/2 in response to thrombin	63

Figure 2.12 Activation of ERK1/2 in response to 2.1 and 2.2	64
Figure 2.13 Chronic activation of ERK1/2 in response to 2.1 and 2.2	65
Figure 2.14 Representative extended time courses for the activation of calcium signalling in HEK-293 cells with thrombin, TFLLR-NH ₂ , 2.1 and 2.2	67
Figure 2.15: Activation of calcium signalling in HEK-293 cells loaded with Fura-2 AM.....	69
Figure 2.16: Experimental setup for perfusion of drugs over HEK-293 cells whilst monitoring with Dual-LED microscope.....	70
Figure 2.17 Activation of calcium signalling in HEK-293 cells loaded with Fura-2 AM.....	71
Figure 2.18: Average time courses for the activation of calcium signalling in HEK-293 cells loaded with Fluo-4 Direct or Fura-2 dye.....	73
Figure 2.19: Desensitisation studies of 2.1 acting on HEK-293 cells.....	74
Figure 2.20 Activation of calcium signalling in HEK-293 cells loaded with Fura-2 AM.....	76
Figure 2.21: Activation of calcium signalling pathways in mouse platelets.....	78
Figure 2.22: Activation of platelet aggregation in isolated mouse platelets.....	79
Figure 2.23: Cells pretreated with 2.3 for 60 mins were then treated with 2.1 at a concentration of 50 μ M.....	80
Figure 2.24: Inhibition of thrombin and PZ-128-mediated calcium signalling in HEK-293 cells loaded with Fluo-4 Direct Dye using phospholipase C inhibitor U73122 with a concentration range of 0.03-30 μ M.....	81
Figure 2.25: Inhibition of thrombin and PZ-128-mediated calcium signalling in HEK-293 cells loaded with Fluo-4 Direct Dye using G _{aq} inhibitor YM-254890 with a concentration range of 0.3-30 μ M.....	82
Figure 2.26: G _q signalling cascade following PAR1 activation in human platelets including known inhibitors of PAR1, G _q and IP3.....	84
Figure 2.27: MTT Assay showing the effect of 2.1 , 2.2 , thrombin and 2.3 on cell viability.....	86
Figure 2.28: Flow cytometric analyses of HEK-293 cells stained with Annexin V dye.....	88
Figure 2.29: Chemical structure of three cyclic pepducins 2.5 , 2.6 and 2.7	90
Figure 2.30: Energy minimised structures of peptide backbone using 2.5 (A) and the free peptide sequence CKKSRLC with no linker bound.....	92
Figure 2.31: Chemical structure of linear pepducin analogues 2.15 , 2.16 and 2.17	93
Figure 2.32: Characterisation of PAR1-derived pepducin library.....	95
Figure 2.33: Characterisation of PAR1-derived pepducin library.....	96
Figure 2.34: Chemical structure of A cyclic pepducins containing a triazole linker and B a linear pepducin with a triazole linker.....	98
Figure 2.35: Proposed effect of elongated linkers on intracellular pepducin localisation.....	101
Figure 2.36: Characterisation of PAR1-derived pepducin library containing a triazole within the linker moiety.....	102
Figure 2.37: Chemical structure of fluorescent tag, BODIPY TMR.....	104
Figure 2.38: Emission spectra for a solution of 2.29 (50 μ M) at two excitation wavelengths of 494 nm and 545 nm.....	106
Figure 2.39: Activation of ERK1/2 in response to thrombin, 2.1 and 2.29	107
Figure 3.1: Observed hydrogen bonding between AZ8838 and PAR2.....	111
Figure 3.2: Initial docking of (S)- 3.1 within the PAR2 crystal structure with AutoDock Vina....	113
Figure 3.3: Further docking of (S)- 3.1 within the PAR2 crystal structure with AutoDock Vina..	114
Figure 3.4: Hydrogen bond interaction between AZ8838 and a water molecule in the PAR2 binding site.....	115

Figure 3.5: Equations for the derivation of ChemPLP (A) and, correspondingly, PLP (B) scoring functions	117
Figure 3.6: Overlaid docking modes of (S)- 3.1 with published binding mode of AZ8838	118
Figure 3.7: Comparison of docking in PAR2 with (S)- 3.1 and (R)- 3.1	119
Figure 3.8: Proposed sites within AZ8838 for diversification	120
Figure 3.9: Effect of removal of hydrogen bonding functionalities in the imidazole region on binding within PAR2	122
Figure 3.10: Effect of modification of hydrogen bonding vectors within the imidazole on binding within PAR2	124
Figure 3.11: Effect of increases in steric volume within the imidazole on binding within PAR2	126
Figure 3.12: Effect of modification to the linker region on docking within PAR2	128
Figure 3.13: AZ8838 within the PAR2 binding pocket and associated disulfide bridge	129
Figure 3.14: Effect of non-aromatic modifications to the propyl region on docking within PAR2.	131
Figure 3.15: Effect of aromatic modifications to the propyl region on docking within PAR2.....	133
Figure 3.16: Effect of substituted aromatic modifications to the propyl region on docking within PAR2.....	135
Figure 3.17: Binding mode of aryl analogues of AZ8838 displayed within the AZ8838-PAR2 complex.....	139
Figure 3.18: Confirmation of deprotonation at the 2-position of 3.33	146
Figure 3.19: Highlighted interactions in 3.50 and 3.51 identified through HMBC NMR experiments	157
Figure 3.20: Proposed linker analogues exploring modifications to the hydroxyl group	167
Figure 3.21: Initial targets for propyl analogue synthesis of 3.1	172
Figure 3.22: Rotameric nature of 3.24	176
Figure 3.23: Variable temperature NMR experiments for 3.24	178
Figure 3.24: Variable temperature NMR experiments of 3.24	179
Figure 3.25: Allyl and vinyl analogues of AZ8838, 3.18 and 3.19	180
Figure 3.26: Synthesised analogues of AZ8838 (3.1) covering SAR of three main regions of the molecule.....	185
Figure 3.27: Canonical signalling occurring as a result of PAR2 activation.	187
Figure 3.28: Initial screening of AZ8838 and 3.1 within NFκB luciferase reporter assay	188
Figure 3.29: Concentration-response curve for inhibition of trypsin-mediated PAR2 activation in NFκB luciferase reporter assays using PAR2 antagonists AZ8838 and 3.1 . Data represents N = 2 for AZ8838 and N=3 for 3.1 , with mean ± SEM.	189
Figure 3.30: Initial screening of imidazolyl analogues 3.4 , 3.5 , 3.6 , 3.9 and 3.10 within NFκB luciferase reporter assay.....	191
Figure 3.31: Initial screening of intermediates 3.56 , 3.57 , 3.58 and 3.59 within NFκB luciferase reporter assay	192
Figure 3.32: Initial screening of linker analogue 3.13 within NFκB luciferase reporter assay.....	193
Figure 3.33: Initial screening of propyl analogues 3.15 , 3.16 , 3.17 and 3.21 within NFκB luciferase reporter assay	195
Figure 3.34: Initial screening of propyl analogues 3.24 , 3.25 , 3.26 , 3.27 and 3.28 within NFκB luciferase reporter assay.....	196
Figure 3.35: Concentration-response curve for inhibition of trypsin-mediated PAR2 activation in NFκB luciferase reporter assays using AZ8838 analogues 3.5 and 3.10	197

Figure 3.36: Concentration-response curve for inhibition of trypsin-mediated PAR2 activation in NFκB luciferase reporter assays using AZ8838 analogue **3.17** 198

Table 1.1: Further information on activation of PAR1-4 including additional agonist proteases as well as agonist peptide sequences.....	21
Table 1.2: List of disarming proteases for each of the PARs.....	23
Table 1.3: Information on antagonists of PARs. Compounds in bold represent species used within this study.....	33
Table 2.1: Chemical structure and pharmacological properties of PZ-128 (2.1).....	45
Table 2.2: EC ₅₀ values for activation of PAR1 in HEK-293 cells.....	53
Table 2.3: IC ₅₀ values obtained for the inhibition of TFLLR-NH ₂ mediated calcium signalling. ...	55
Table 2.4: Schild Data obtained for PZ-128 and SCH79797 in HEK-293 cells treated with TFLLR-NH ₂	57
Table 2.5: EC ₅₀ values generated from Schild study of 2.1 inhibition of thrombin.....	58
Table 2.6: EC ₅₀ values obtained for the activation of calcium signalling in HEK-293 cells by 2.1 and 2.2	60
Table 2.7: EC ₅₀ data for activation of calcium signalling in the presence of 0 mM extracellular calcium.....	61
Table 2.8: EC ₅₀ values for thrombin, 2.1 and 2.2 addition to HEK-293 cells loaded with either Fluo-4 Direct or Fura-2 AM calcium dyes. Data for Fluo-4 relates to the N = 4 carried out alongside the N=4 for Fura-2, excluding other N's generated in previous experiments.....	69
Table 2.9: EC ₅₀ values for the addition of thrombin and 2.1 to HEK-293 cells pre-treated with thrombin (3 U/mL).....	75
Table 2.10: EC ₅₀ values obtained for the activation of calcium signalling in mouse platelets.	78
Table 2.11: EC ₅₀ values for the activation of mouse platelet aggregation using thrombin, PZ-128 and PZ-Scram.	79
Table 2.12: Inhibition data for U73122 on the action of thrombin and PZ-128.	81
Table 2.13: Inhibition data for YM-254890 on the action of thrombin and PZ-128 in HEK-293 cells.....	83
Table 2.14: EC ₅₀ and IC ₅₀ values for PAR1-derived pepducins. ^a EC ₅₀ values obtained by treating HEK-293 cells loaded with the calcium dye Fluo-4 and recording the change in fluorescent output. ^b IC ₅₀ values obtained by pre-treating HEK-293 cells loaded with Fluo-4 with pepducins and further treating with PAR1 agonist (TFLLR-NH ₂).....	97
Table 2.15: EC ₅₀ and IC ₅₀ values for PAR1-derived pepducins containing a triazole within the linker. ^a EC ₅₀ values obtained by treating HEK-293 cells loaded with the calcium dye Fluo-4 Direct and recording the change in fluorescent output (Figure 2.36). ^b IC ₅₀ values obtained by pre-treating HEK-293 cells loaded with Fluo-4 with pepducins and further treating with PAR1 agonist (TFLLR-NH ₂).....	102
Table 3.1: Published PAR2 antagonists AZ8838 (3.1) and AZ3451 (3.2).....	109
Table 3.2: Optimisation of Suzuki-Miyaura Cross-Coupling towards 3.31	143
Table 3.3: Optimisation of manganese dioxide oxidation towards ketone 3.57	162
Table 3.4: Suzuki-Miyaura Cross-Couplings towards diverse benzaldehyde intermediates 3.80-90	173
Table 3.5: ⁿ BuLi-mediated couplings towards propyl analogues of AZ8838.....	175
Table 6.1: Reagents used for experiments.....	215
Table 6.2: Western Blot Antibodies.....	217

Scheme 2.1: General procedure for automated solid phase peptide synthesis (SPPS).....	50
Scheme 2.2: Synthesis of 2.1 and 2.2 by solid-phase peptide synthesis	51
Scheme 2.3: Reaction of Fluo-4 with Ca ²⁺ leading to a fluorescently active species	52
Scheme 2.4: Formation of Ca ²⁺ -Fura-2 complex, with reverse reaction prevented in presence of 2.1	73
Scheme 2.5: Reduction of MTT to formazan by mitochondrial reductase enzymes.....	85
Scheme 2.6: Synthesis of cyclic pepducins.....	91
Scheme 2.7: Synthesis of linear pepducin analogues 2.15-17	94
Scheme 2.8: Synthesis of elongated cyclic pepducins 2.19-21 via alkylation and Click reaction ...	99
Scheme 2.9: Synthesis of linear analogue of extended pepducins, 2.22	100
Scheme 2.10: Synthesis of BODIPY-tagged pepducin 2.29 via the CuAAC reaction of an alkynylated analogue 2.27 with BODIPY-TMR-azide 2.28	105
Scheme 3.1: Reported synthetic route towards AZ8838 (3.1) as used by Cheng et al.....	141
Scheme 3.2: Initial attempt at Suzuki-Miyaura Cross-Coupling towards 3.31	142
Scheme 3.3: Synthesis of benzaldehyde intermediate 3.31	144
Scheme 3.4: Synthesis of SEM-protected imidazole 3.33	144
Scheme 3.5: Initial attempt at the synthesis of 3.34	145
Scheme 3.6: Lithiation of 3.33 towards 3.34	146
Scheme 3.7: Deprotection of intermediate 3.34 to yield (±)-AZ8838, 3.1	147
Scheme 3.8: General synthesis of AZ8838 analogues, diversifying at the imidazole functionality	148
Scheme 3.9: Grignard reaction towards phenyl analogue 3.5	149
Scheme 3.10: Synthesis of 3.4 via bromine/magnesium exchange of 3.36	149
Scheme 3.11: 3-step synthesis of benzimidazolyl analogue 3.10	150
Scheme 3.12: Attempted synthesis of pyrrolyl analogue 3.41	151
Scheme 3.13: Tosyl protection of bromopyrazoles 3.42 and 3.43	152
Scheme 3.14: Attempted synthesis of 3.7 and 3.8 via Grignard reaction between tosyl-protected bromopyrazoles 3.44-45 and 3.31	153
Scheme 3.15: Proposed mechanism for deprotection of N-tosylated heterocycles resulting in the desired product (A) or methylated side-product (B).....	154
Scheme 3.16: SEM-protection of 4-bromopyrazole 3.43	155
Scheme 3.17: ⁿ BuLi-mediated coupling of bromopyrazole 3.49 with 3.31 to yield protected pyrazoles 3.50 and 3.51	155
Scheme 3.18: Stabilisation of organolithium species via the oxygen atom of the SEM protecting group	156
Scheme 3.19: Failed deprotection reactions towards pyrazole analogues 3.8 and 3.7	158
Scheme 3.20: Tosyl-protection of 4-bromoimidazole 3.52 towards 3.53	158
Scheme 3.21: Failed Grignard reaction of 3.53 towards intermediate 3.54	159
Scheme 3.22: Planned synthetic route towards heterocyclic analogues of AZ8838.	160
Scheme 3.23: Initial attempt at the synthesis of triazole 3.9 via [3+2] dipolar cycloadditions.....	160
Scheme 3.24: Attempted oxidation of 3.56 using PDC.....	161
Scheme 3.25: Oxidation of 3.56 towards ketone 3.57	162
Scheme 3.26: Synthesis of triazole analogue 3.9	163
Scheme 3.27: Sample reactions of trimethylsilyl diazomethane including metal catalysed cyclopropanation of alkenes (A), methyl esterification of carboxylic acids (B) and 1,3-dipolar cycloaddition towards substituted pyrazolines (C) and pyrazoles (D)	164

Scheme 3.28: Synthesis of pyrazole analogue 3.8	164
Scheme 3.29: Generation of reactive azomethine ylide from N-benzyl-1-methoxy-N- ((trimethylsilyl)methyl)methanamine	165
Scheme 3.30: [3+2] dipolar cycloadditions leading to bis-pyrrolidine 3.61	165
Scheme 3.31: Synthesis of pyrroline 3.60 using reduced equivalents of azomethine precursor	166
Scheme 3.32: Failed reductions towards pyrrolidine 3.11 and bis-pyrrolidine 3.12	167
Scheme 3.33: Synthesis of carbonyl analogue 3.13 from common AZ8838 intermediate 3.34	168
Scheme 3.34: Synthesis of racemic Ellman imine (\pm)- 3.49	168
Scheme 3.35: General scheme for the synthesis of AZ8838 analogues via a reversed synthetic route	169
Scheme 3.36: Attempted coupling of imidazole 3.33 and bromobenzaldehyde 3.30 to yield 3.65 and side-product 3.66	170
Scheme 3.37: Failed Suzuki-Miyaura cross-coupling reaction of 3.65 towards 3.67	170
Scheme 3.38: Failed protection of 3.65 with SEM-chloride	171
Scheme 3.39: Deprotection of 3.65 to provide bromo-analogue 3.16	171
Scheme 3.40: Synthesis of o-tolyl analogue 3.24	177
Scheme 3.41: Attempted Suzuki-Miyaura Cross-Coupling towards 3.94 resulting in the formation of 3.95	180
Scheme 3.42: Proposed mechanism of Roush-like Allylation towards allyl alcohol 3.95	181
Scheme 3.43: Revised reaction conditions for Suzuki-Miyaura reaction resulting in the formation of 3.96	181
Scheme 3.44: Suzuki-Miyaura cross-coupling and organolithium coupling towards vinyl intermediate 3.99	182
Scheme 3.45: Side-product 3.100 and preceding intermediate 3.101 formed during the Suzuki reaction towards 3.97	182
Scheme 3.46: Proposed mechanism for palladium-mediated cross-coupling of alkenyl boronic acids and functionalised alkenes. ⁹⁷	183
Scheme 3.47: Revised Suzuki reaction resulting in 3.92 and 3.95	184

Chapter 1 Introduction

1.1 G-Protein Coupled Receptors

G-protein coupled receptors (GPCRs) are cell surface receptors which play key roles in a wide range of biological processes. They facilitate the passage of information from extracellular sources through the cell membrane and into the cytosol by both extra- and intracellular binding.⁵

With approximately 800 different GPCRs expressed in humans, they represent the largest class of potential drug targets for the treatment of human diseases.⁶ This prevalence is reflected in drug development, with roughly 35% of all approved drugs targeting GPCRs across a vast array of diseases including cardiovascular disease, a range of inflammatory diseases and neurological diseases such as schizophrenia and Alzheimer disease, among many others.⁷

1.1.1 General Structure of GPCRs

All GPCRs share a common structural archetype, as shown in **Figure 1.1**. Specifically, they are characterised by their seven transmembrane helices, connected by a series of intra- and extracellular loops (ICL and ECL).⁸ The extracellular domain consists of the N-terminal region as well as the three extracellular loops.⁸ The transmembrane domain contains the seven α -helices which wind through the cell membrane. Finally, the intracellular domain contains the C-terminal region and the three intracellular loops. Additionally, GPCRs are typically associated with a heterotrimeric G-protein which propagates the signal from the GPCR into the cell interior, although this relationship is not exclusive. Recent studies have shown regions of the GPCR engaging in non G-protein coupled signalling, acting through other cytoplasmic proteins as well as directly interacting with effectors of intracellular signalling.⁹

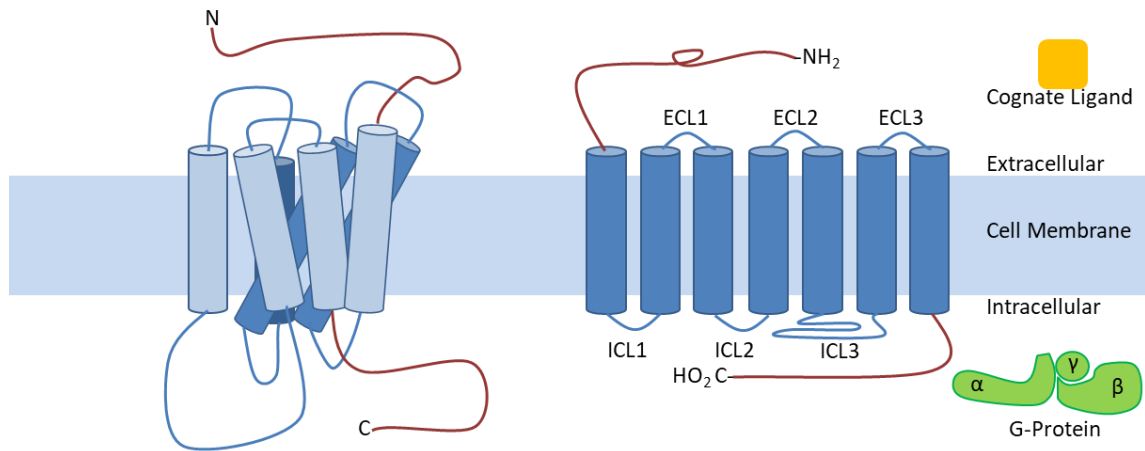


Figure 1.1: Representative structure of a GPCR showing general structural features. (Left) Folded structure of a GPCR (Right) Simplified view of a GPCR.

1.1.1.1 Subfamilies

Whilst all GPCRs share the common structural archetype detailed above (*vide supra* **Figure 1.1**), the broad range of GPCR structures share very little sequence identity. Traditionally, GPCRs were described as one of six different subclasses:¹⁰

- Class A – rhodopsin-like
- Class B – secretin receptor family
- Class C – metabotropic glutamate
- Class D – fungal mating pheromone receptors
- Class E – cyclic AMP receptors
- Class F – frizzled/smoothened receptors

However, of these subclasses, class D and class E are not represented within vertebrates. As such, an alternative “GRAFS” system is used to divide vertebrate GPCRs into five classes based on structure and agonist homology:¹¹

- Glutamate family
- Rhodopsin family
- Adhesion family
- Frizzled family
- Secretin family

The glutamate family of GPCRs consists of 22 GPCRs, of which 8 are orphan receptors and 3 are sensory receptors for taste.⁷ The remaining 11 receptors are activated by either amino acids, with 8 metabotropic glutamate receptors (mGluR₁₋₈) and 2 γ -aminobutyric acid (GABA) receptors (GABA_{B1-2}), or ions, with a single calcium-sensing receptor (CaS receptor).¹² These receptors typically display a longer extracellular domain which is hydrophilic in nature for agonist binding, replete with many conserved cysteine residues facilitating the formation of disulfide bridges.¹²

The rhodopsin family of GPCRs represent the largest subclass containing a total of 285 individual GPCRs.¹³ Of these, 81 are orphan receptors whilst 7 are sensory receptors for sight. The leftover 197 rhodopsin family proteins are activated by a range of agonists, with peptide, aminergic and lipid receptors making up most of the family containing 76, 36 and 36 receptors, respectively.¹³ There are also smaller groups which are activated by proteins, nucleotides, carboxylic acids, steroids and melatonin. Despite the broad range of agonist types for the rhodopsin family, sequence homology is relatively conserved, especially within the transmembrane helical bundle, displaying a sequence similarity of $\geq 25\%$.¹⁴

The adhesion family consists of 33 GPCRs which are suspected to contribute to intercellular communication.¹³ Adhesion receptors are split into 9 groups, each with extended N-terminal domains of >4000 amino acids.¹⁵ While each adhesion GPCR maintains a GPCR autoproteolysis-inducing (GAIN) domain, responsible for self-cleavage of the N-terminal region, other protein domains within the N-termini belong to specific adhesion family subtypes over others.

The frizzled family contain 11 amino acids which are activated by Wnt proteins, a series of lipid-modified signalling proteins associated with developmental pathways in cell growth including cell differentiation, cell proliferation and cell migration.^{8,16} The frizzled proteins maintain a cysteine-rich N-terminus to enable binding of the Wnt proteins.

Finally, the secretin family consists of 15 peptide receptors.^{8,17} The secretin receptors possess cysteine-rich residues to allow binding of peptides varying in length between 20 and 50 amino acids.

1.1.2 Mechanism of Action for GPCRs

1.1.2.1 Activation of GPCRs

The extracellular domain of a GPCR is typically responsible for ligand binding whereas the intracellular domain controls interactions with related signalling proteins within the cell.¹⁸ The transmembrane domain is mostly responsible for providing structure to the protein, although movement of the individual helices is also crucial for allowing the transduction of information to the inside of the cell.¹⁸ The intracellular region of GPCRs is responsible for interacting with associated G-proteins, heterotrimeric proteins consisting of G_α , G_β and G_γ units responsible for signalling cascades occurring as a result of GPCR activation.¹⁹

The mechanism of action for GPCRs remains consistent across the receptor family, although the binding site of the stimulus can differ.¹⁴ Small organic molecules and peptides will typically bind within an extracellular hollow formed between the seven transmembrane helices. On the other hand, proteins will typically bind on the N-terminus and activate the GPCR away from the cell membrane.

Binding of the cognate ligand within the extracellular surface leads to a conformational change in the GPCR (**Figure 1.2a**), facilitated by the transmembrane helices, which then allows recruitment of the G-protein within the intracellular loops and C-terminus (**Figure 1.2b**).²⁰ The heterotrimeric G-protein is broken into two subunits (G_α and $G_{\beta\lambda}$) which go on to interact with other receptors, kinases and arrestin molecules within the cell as part of cell signalling cascades.¹⁸ (**Figure 1.2c**). The resulting signalling cascades lead to physiological changes in cells in response to external stimuli which can manifest in a myriad of ways.

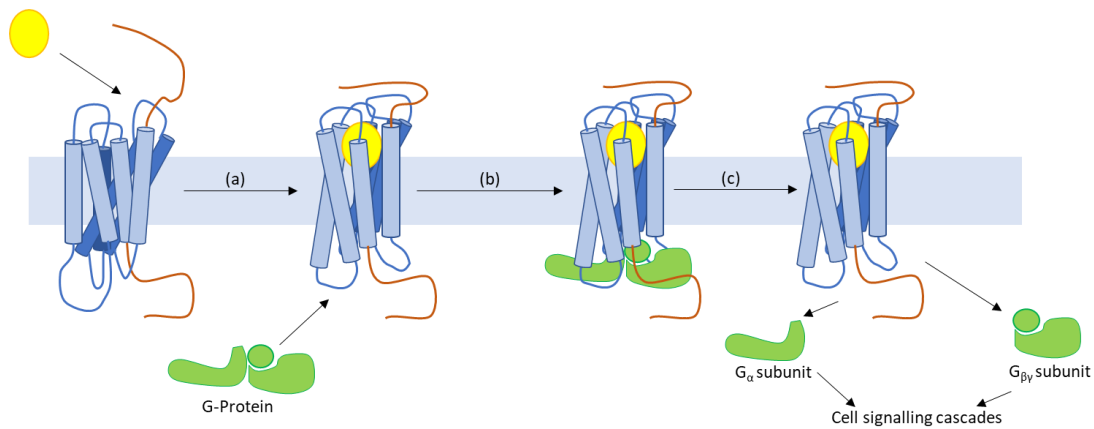


Figure 1.2: General mechanism of activation for GPCRs. (a) Recruitment of agonist by extracellular region of the GPCR resulting in modification of the transmembrane structure. (b) Recruitment of G-protein by the intracellular domain. (c) Cleavage of G-protein into G_α and G_{βγ} subunits, leading to further cell signalling events.

1.1.2.2 Self-regulation of GPCRs

GPCRs also elucidate a self-regulation mechanism (**Figure 1.3**).²¹ Upon activation by their cognate ligands (**Figure 1.3a**), GPCRs begin to undergo phosphorylation on their intracellular loops and C-terminus (**Figure 1.3b**). The phosphorylated residues label the receptor for β-arrestin binding. Once bound, β-arrestin leads to the internalisation of the GPCR into a vesicle (**Figure 1.3d-e**) where β-arrestin is removed and the GPCR is dephosphorylated (**Figure 1.3f**). It is then returned to the cell surface in an inactivated state (**Figure 1.3g**). By this method, GPCR expression at the cell membrane can be self-regulated, ensuring there is not an excess of activated GPCRs.

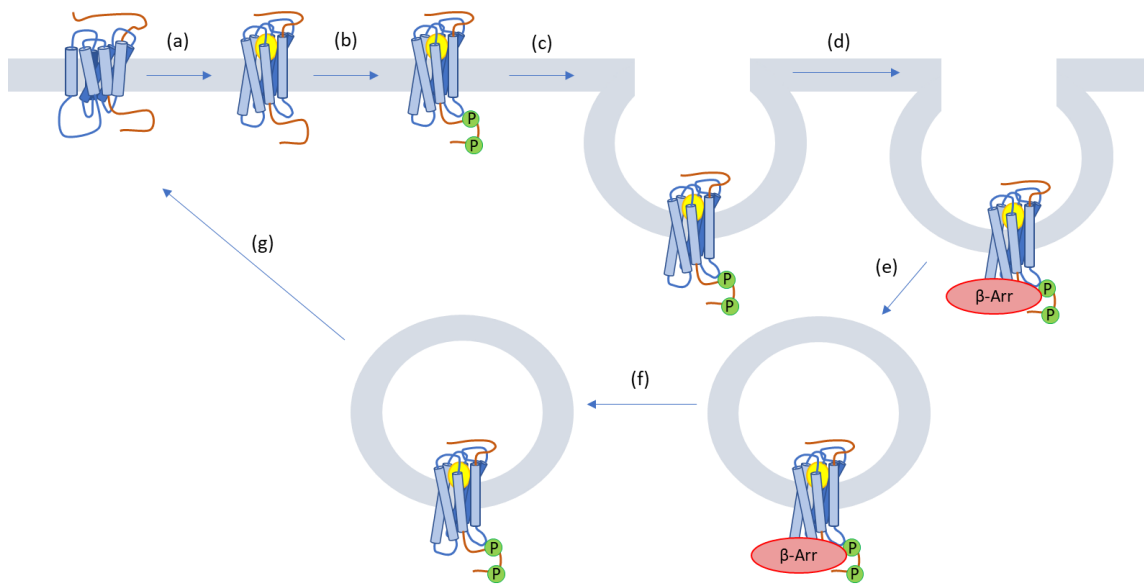


Figure 1.3: Self-regulation of GPCR activated states. (a) GPCR becomes activated by its cognate ligand. (b) The activated GPCR begins to undergo phosphorylation on its intracellular loops and C-terminus. (c) Vesicle begins to form containing the GPCR. (d) Phosphorylated sites signal for the recruitment of β -Arrestins. (e) Presence of β -arrestin signals for internalisation of the GPCR where β -arrestin becomes unbound (f) and the GPCR is dephosphorylated before returning to the cell membrane (g). Adapted from.²¹

1.1.2.3 Associated G-Proteins

As described previously, GPCRs elicit their signalling through the binding and cleavage of heterotrimeric G-proteins, made up of G_{α} , G_{β} and G_{γ} subunits (**Figure 1.4**).²² Each of these G-protein subunits possess multiple subfamilies, each with their own subtypes divided broadly by structural similarity.

The activation of a G-protein is driven by the exchange of GDP within the G_{α} subunit for a GTP molecule following binding to the activated GPCR, causing the heterotrimer to split into the G_{α} subunit replete with GTP and the dimeric $G_{\beta\gamma}$ subunit.²² These separate subunits then go on to elicit their individual signalling cascades. Following activation of the GPCR, G-proteins will continue to be activated until such time as phosphorylation of the GPCR has led to its deactivation.²¹

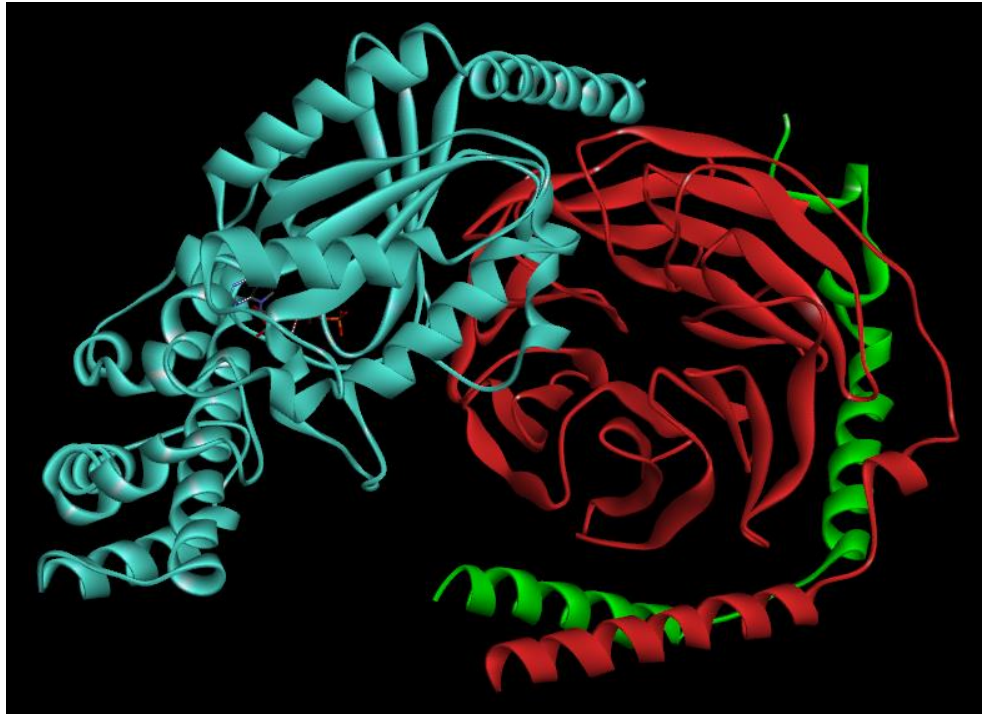


Figure 1.4: Structure of heterotrimeric G-protein with G_{α} shown in blue, G_{β} shown in red and G_{γ} shown in green. G_{α} shown in complex with GDP.²³

G_{α} Subunit

The G_{α} subunit contains two key structural regions: a GTPase domain which participates in the binding and hydrolysis of GTP, and a helical domain which locks the GDP/GTP molecule within the centre of the protein (**Figure 1.5**).²⁴ The GTPase domain will eventually cause hydrolysis of the bound GTP molecule, producing GDP and inactivating the subunit.

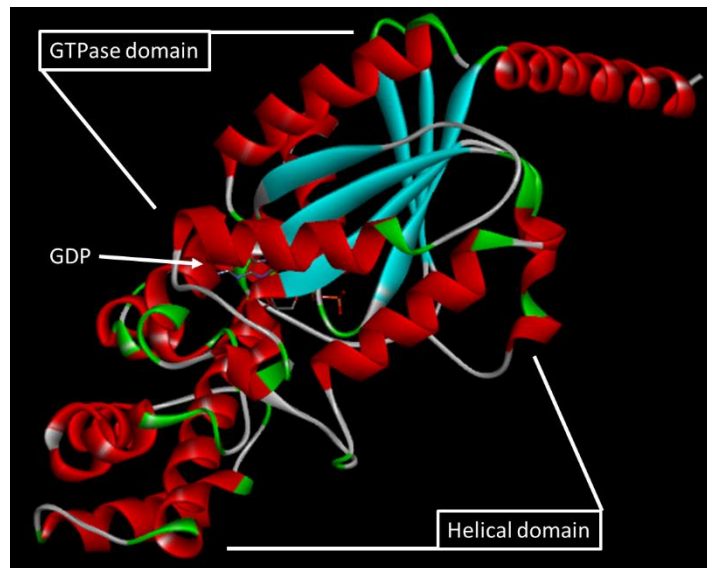


Figure 1.5: Tertiary structure of G_{α} in complex with GDP with α -helices in red and β -sheets in blue.²³

There are 4 families of G_{α} subunits, G_s , $G_{i/o}$, $G_{q/11}$ and $G_{12/13}$, and each of these families cause unique signalling events (**Figure 1.6**). The G_s family are primarily responsible for the activation of adenylate cyclase (AC), which is an enzyme responsible for the hydrolysis of adenosine triphosphate (ATP) to provide cyclic adenosine monophosphate (cAMP).²⁵ The hydrolysis of cAMP leads to the production of adenosine monophosphate (AMP), which fulfils multiple roles within cells as a nucleotide used in RNA synthesis, activation of a small range of kinases and also as a means of energy transfer by conversion into adenosine di/triphosphate (ADP/ATP). Additionally, G_s subunits also activate proto-oncogene tyrosine-protein kinase Src (SRC), which has a physiological role in cell growth and has implications in cancer.²⁶

The $G_{i/o}$ family typically act in opposition to the G_s family, inhibiting the functions of AC.²⁵ However, the G_i family are very slow to hydrolyse their docked GTP molecule into GDP. To prevent overactivation, the G_i family also interact with the regulator of G-protein signalling (RGS) proteins. Once activated, RGS proteins inhibit the function of GTP-bound G_i , preventing over-inhibition of AC.^{27,28}

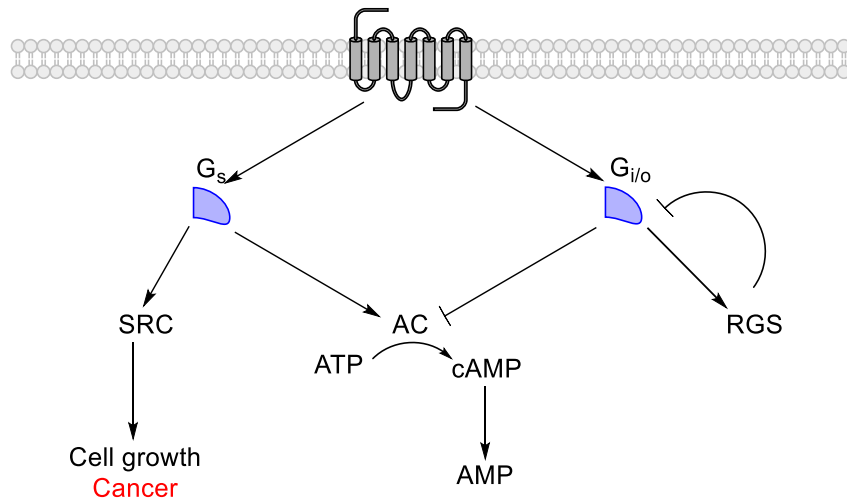


Figure 1.6: G_s and G_{i/o} signalling cascades as a result of GPCR activation. **SRC** = proto-oncogene tyrosine-protein kinase Src, **AC** = adenylate cyclase, **AMP** = adenosine monophosphate, **cAMP** = cyclic adenosine monophosphate, **ATP** = adenosine triphosphate, **RGS** = Regulator of G-protein signalling (RGS) protein. Adapted from reactome.org. 25-30

The G_{q/11} family are mainly responsible for the action of phospholipase C beta (PLC β) (**Figure 1.7**).³¹ PLC β leads to the production of inositol 1,4,5-trisphosphate (IP₃) and diacylglycerol (DAG) from phosphatidylinositol 4,5-bisphosphate, which then go on to activate calcium efflux from the endoplasmic reticulum (ER) and protein kinase C (PKC), respectively (**Figure 1.7**).³¹ These signals then lead on to a range of other pathways including, but not limited to, activation of calcium-regulated kinases and phosphatases as well as MAPK signalling, and many other key pathways in disease-relevant locales such as platelets (*vide infra*, **Section 1.2.2.1**).³²

In addition to activation of PLC β , G_{q/11} proteins have also been shown to inhibit phosphoinositide 3-kinase (PI3K), a key protein in cell cycle processes including cell growth and proliferation as well as motility and intracellular trafficking (**Figure 1.7**).³³ Further, G_{q/11} activates G protein-coupled receptor kinases (GRK) as well as Bruton's tyrosine kinase (BTK) and shows interactions with RGS proteins (**Figure 1.7**).^{27,28,34,35} GRKs are responsible for protein phosphorylation and help to regulate activated GPCRs,

labelling them for internalisation and recycling (*vide supra*, **Figure 1.3**).³⁵ On the other hand, BTKs are responsible for the differentiation of lymphocytes.³⁴

Finally, $G_{12/13}$ represent the least researched family of G_{α} subunits. It is known that $G_{12/13}$ interact with BTKs in a similar manner to $G_{q/11}$, impacting lymphocyte development.³⁶ However, they also activate Rho guanine nucleotide exchange factors (RhoGEF), which lead to the activation of Ras homolog gene family, member A (RhoA) which plays a role in the maintenance of the cellular actin cytoskeleton.³⁷

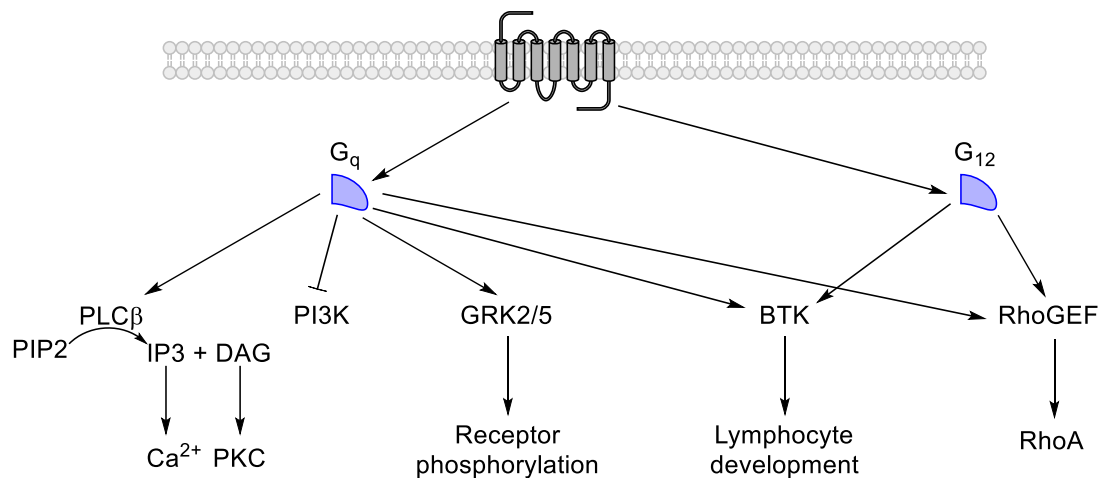


Figure 1.7: $G_{q/11}$ and $G_{12/13}$ signalling cascades as a result of GPCR activation. **PLC** = phospholipase C, **PIP₂** = phosphatidylinositol 4,5-bisphosphate, **IP₃** = inositol 1,4,5-trisphosphate, **DAG** = diacylglycerol, **PKC** = protein kinase C, **PI3K** = phosphoinositide 3-kinase, **GRK** = G protein-coupled receptor kinase, **BTK** = tyrosine-protein kinase BTK, **RhoGEF** = Rho guanine nucleotide exchange factor, **RhoA** = Ras homolog gene family, member A. Adapted from reactome.org.^{27,28,30,31,33–38}

$G_{\beta\gamma}$ Subunit

For a long period of time, the $G_{\beta\gamma}$ subunits (**Figure 1.8**) were thought to not display any signalling, instead acting as an inhibitor of G_{α} -mediated signalling by restoring the G-protein heterotrimer.³⁹ However, they have since been shown to participate in a diverse range of signalling cascades, particularly involving the recruitment of other proteins and small molecules to the cell membrane.³⁹

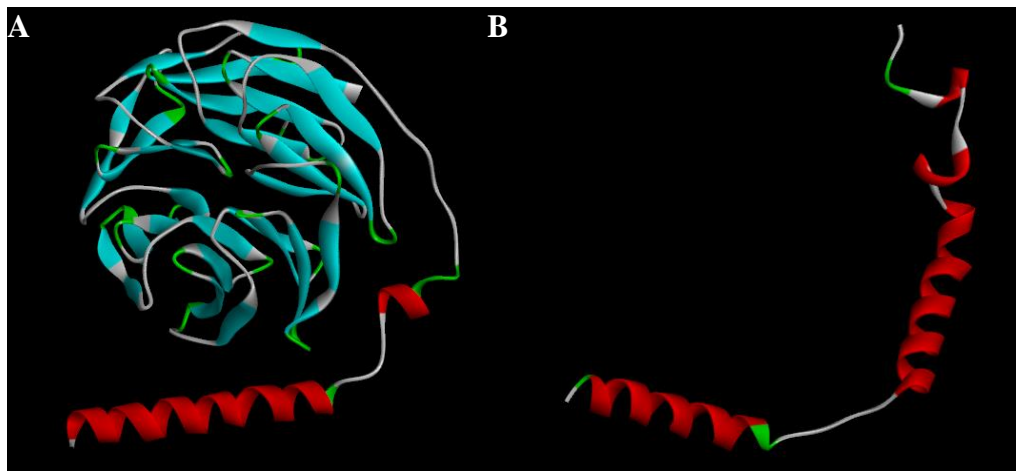


Figure 1.8: Tertiary structure of G_{β} (A) and G_{γ} (B) subunits with α -helices in red and β -sheets in blue.²³

They have a proven role in the activation of RhoA, whereby $G_{\beta\gamma}$ activates phosphoinositide 3-kinase gamma ($PI3K_{\gamma}$) enabling the conversion of PIP2 to PIP3, a RhoA agonist (**Figure 1.9**).⁴⁰ Additionally, $G_{\beta\gamma}$ facilitates the activation of cell division through firstly coupling with serine/threonine-protein kinase PAK1 and, following translocation to the cell membrane, subsequent activation of CDC42, which propagates cell division (**Figure 1.9**).⁴¹ CDC42 also further activates PAK1, building a positive feedback loop for the cell division process. Finally, the $G_{\beta\gamma}$ subunits are also known to activate BTK as well as $PLC\beta$ (**Figure 1.9**).^{42,43}

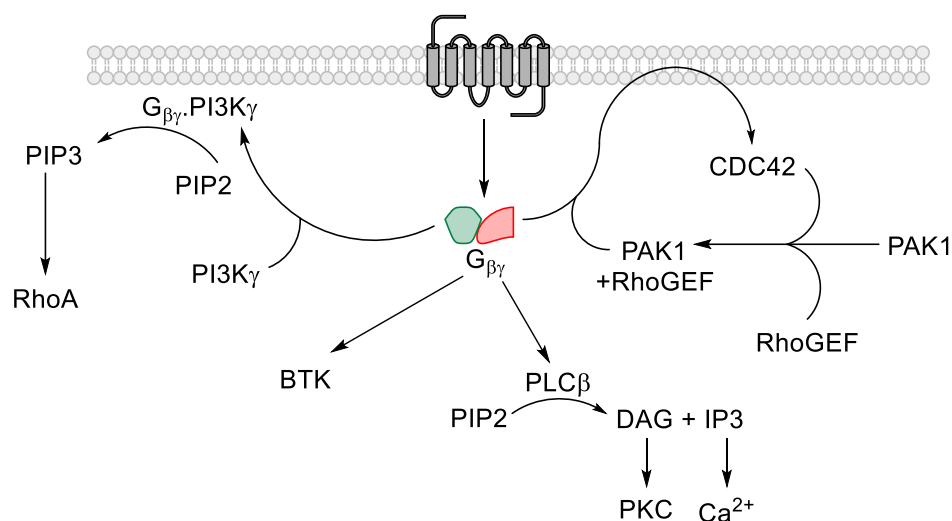


Figure 1.9: $G_{\beta\gamma}$ signalling cascades as a result of GPCR activation. **PI3K γ** = phosphoinositide 3-kinase gamma, **PIP2** = phosphatidylinositol 4,5-bisphosphate, **PIP3** = phosphatidylinositol (3,4,5)-trisphosphate, **RhoA** = Ras homolog gene family, member A, **RhoGEF** = Rho guanine nucleotide exchange factor, **CDC42** = Cell division control protein 42, **PLC** = phospholipase C, **IP3** = inositol 1,4,5-trisphosphate, **DAG** = diacylglycerol, **PKC** = protein kinase C, **PI3K** = phosphoinositide 3-kinase, **GRK** = G protein-coupled receptor kinase, **BTK** = tyrosine-protein kinase BTK. Adapted from reactome.org.^{30,39-43}

1.1.3 Relevance to Drug Discovery

1.1.3.1 Trends in GPCR drug discovery

GPCRs represent the single largest class of proteins targeted by modern therapeutics. In total, 475 approved drugs target the GPCR family, representing ~35% of all marketed drugs and ~27% of the global market share of therapeutics.⁷ An additional 323 drugs are in clinical trials for therapeutic effects targeting GPCRs.⁷ Despite this, only 44% of GPCRs are established targets for drugs approved for clinical use or currently in clinical trials, leaving 224 GPCRs with no approved drugs.⁷ This highlights a relatively large area of research for potential new therapies.

The mechanism of action for drugs targeting GPCRs shows somewhat limited variability (**Table 1.1**). Most predominately, approved drugs will act as either competitive agonists or antagonists, whereby binding within the orthosteric site of a GPCR replaces the cognate ligand or inhibits its function, respectively.^{7,44} Antagonists represent the most abundant

mode of function, with 260 approved drugs, representing 53% of all approved drugs.^{7,13} Competitive agonists represent 42%, with 206 agonist drugs approved for therapeutic use.^{7,13} The remaining 5% of approved drugs are made up of partial agonists, inverse agonists, positive allosteric modulators and negative allosteric modulators.^{7,13}

The observed trends between the modes of action remain largely the same when considering clinical trial candidates. However, a slightly lower percentage of antagonists is offset by increased numbers of agonists as well as positive and negative allosteric modulators. This could suggest a change in drug discovery strategies, with allosteric modulation providing an exciting alternative to competitive drug binding.⁴⁵

Table 1.1: Observed trends in drug mode of action for approved and clinical trial drugs targeting GPCRs. Information presented from gpcrdb.org.¹³

Drug Mode of Action	Approved Drugs		In clinical trial drugs	
	Number	Percentage	Number	Percentage
Antagonist	260	53.3%	157	47.2%
Agonist	206	42.2%	148	44.6%
Partial agonist	12	2.5%	4	1.2%
Inverse agonist	1	0.2%	3	0.9%
Positive allosteric modulator	2	0.4%	4	1.2%
Negative allosteric modulator	1	0.2%	6	1.8%
Unknown/Not available	6	1.2%	10	3%

GPCRs not only represent the largest targeted family of proteins by drugs but also present therapeutic targets for a vast array of diseases. The most targeted diseases by approved drugs include allergy, hypertension, analgesia, schizophrenia, cancer and cardiovascular disease, amongst many others.^{7,13} Further to this, current clinical trial candidates have also highlighted diabetes, Parkinson disease and asthma as further popular disease targets for drugs.^{7,13}

1.1.3.2 Mechanisms for GPCR modulation

The mechanisms by which drugs modulate GPCR function are varied in both their binding modes and pharmacological effects.⁴⁴ Broadly speaking, drugs tend to have one of two pharmacological outcomes upon binding to a target: agonism, where functions of the protein are activated, or antagonism, where the protein function is prevented.⁴⁴ However, this is an oversimplification. A short study of approved drugs targeting mostly rhodopsin family GPCRs, the most heavily targeted GPCR family for drugs, highlights the breadth of pharmacological effects displayed by therapeutics (**Figure 1.10**).¹³ The exception is cinacalcet, which targets a calcium sensing receptor, a member of the glutamate family of GPCRs.

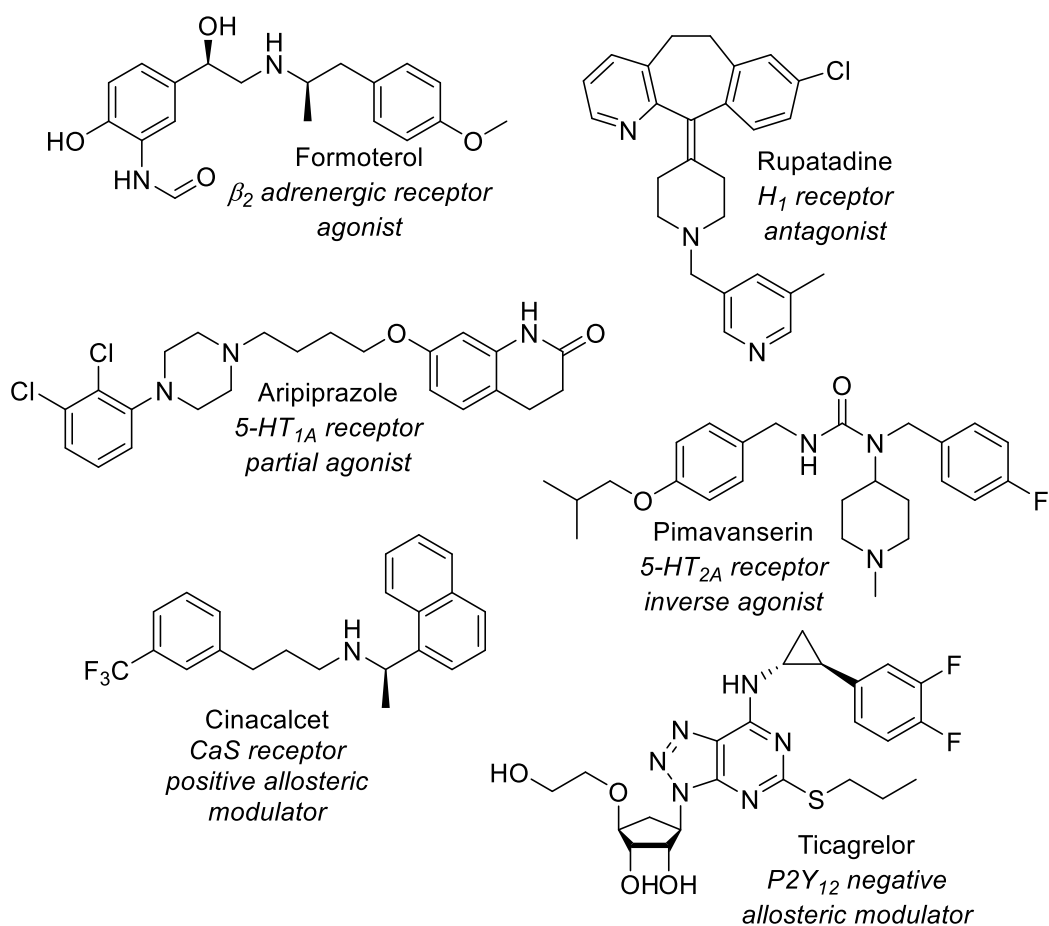


Figure 1.10: Examples of approved drugs targeting mostly rhodopsin family GPCRs.

Formoterol is a β_2 -adrenergic receptor agonist which occupies the active site of the GPCR within the transmembrane domain, acting as a traditional agonist would be expected.⁴⁶ The core of the molecule resembles adrenaline, the natural agonist of β_2 -adrenergic receptor (**Figure 1.11**), allowing it to bind within the same active site as the cognate agonist and elicit an agonist effect (**Figure 1.12A**).⁴⁴ The use of formoterol has been approved for treatment as an anti-asthmatic/bronchodilating agent as well as in the treatment of chronic obstructive pulmonary disease.^{47,48}

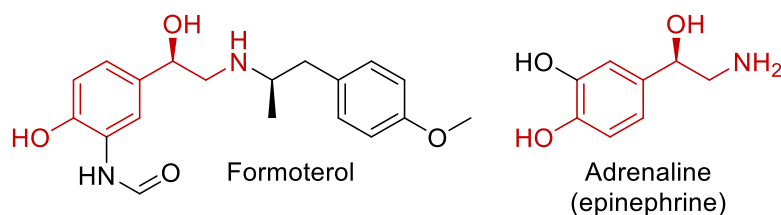


Figure 1.11: Comparison of the chemical structure of formoterol with adrenaline.

Rupatadine represents an antagonistic drug molecule, inhibiting the function of H_1 receptor.⁴⁹ The mechanism of action for rupatadine is competitive, meaning it occupies the same binding site as the natural agonist for H_1 receptor, histamine, where it limits the response of the GPCR to the agonist.^{44,49} Rupatadine was initially discovered in 1997 as a dual inhibitor of H_1 and platelet-activating factor (PAF) and has been approved as a fumarate salt for use as an antiallergic treatment.⁴⁹

Aripiprazole is a partial agonist of $5-HT_{1A}$ receptor, a receptor for serotonin, which has been approved for use as an antipsychotic and in the treatment of schizophrenia.^{50,51} A partial agonist will act much like a normal agonist but provide a reduced effect in comparison to the natural ligand (**Figure 1.12B**).⁴⁴

On the other hand, pimavanserin acts as an inverse agonist of $5-HT_{2A}$ receptor, providing a therapeutic effect for the treatment of Parkinson's disease.⁵² An inverse agonist will display the opposite response to a normal agonist.⁴⁴ Receptors will be capable of acting in

the absence of a ligand, which will be referred to as basal activity.⁴⁴ While an agonist will increase the response above basal levels, an inverse agonist will cause a loss of response.⁴⁴

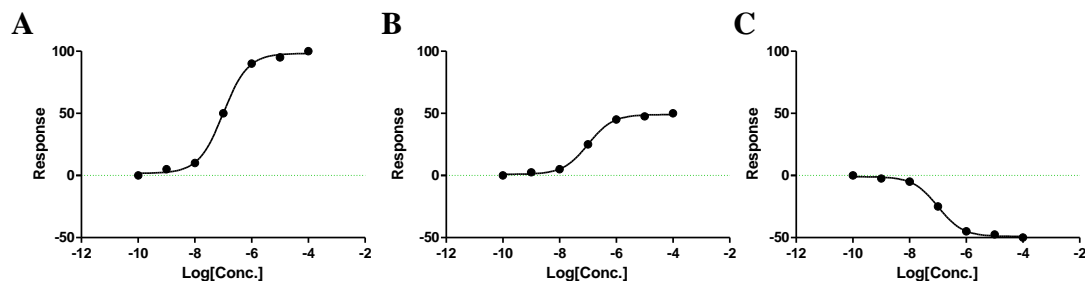


Figure 1.12: Example responses observed following treatment of a GPCR with **A** a full agonist, **B** a partial agonist and **C** an inverse agonist.⁴⁴

Cinacalcet and ticagrelor represent examples of a growing trend in modern drug discovery as allosteric modulators.⁴⁵ Allosteric modulators of GPCRs do not bind within the active site of the protein.⁴⁴ Instead, their presence in a distinct binding site elicits a biological effect on cognate ligand binding.⁴⁴ Cinacalcet is a positive allosteric modulator (PAM), whereby it binds to calcium sensing receptors and increases their sensitivity, elevating the response from the GPCR.^{44,53} Cinacalcet is used as a calcimimetic and to treat hyperparathyroidism.⁵⁴

Meanwhile, ticagrelor is the opposite, acting as a negative allosteric modulator (NAM) of P2Y₁₂. Like a PAM, a NAM will bind into a distinct binding site from the active site.⁴⁴ However, instead of amplifying the response to an endogenous ligand, a NAM will suppress the GPCR response.⁴⁴ In this case, ticagrelor suppresses the action of ADP on P2Y₁₂, allowing it to be used as an antithrombotic agent, for which it gained approval in 2010.⁵⁵

1.2 Proteinase-Activated Receptors

Within the rhodopsin family of GPCRs, one subfamily displays unique characteristics compared to all other GPCRs: the proteinase-activated receptors (PARs). Whereas most GPCRs are activated by the recruitment of an independent biological or chemical entity, the PARs are activated by proteolytic cleavage of their N-terminal domain to liberate a tethered ligand. There are currently four PARs which have been successfully cloned and characterised: PAR1, PAR2, PAR3 and PAR4.⁵⁶⁻⁵⁹

1.2.1 Structure of PARs

The PARs display typical GPCR structural and mechanistic traits. They conserve the seven transmembrane helices associated with GPCRs and are activated by recruitment of a ligand into the extracellular domain of the protein.⁶⁰ Additionally, they maintain an association with G-proteins. However, they display some key differences making them unique within both the rhodopsin subfamily and the GPCR superfamily as a whole.⁶⁰

While the PARs do display the typical GPCR structural archetype, their activation does not derive from the binding of an extracellular entity. Instead, the cognate ligand for PAR activation lies in a small peptide sequence within the N-terminus.^{56,60} Binding of this tethered ligand leads to activation of the protein (**Figure 1.13**).^{56,60} This tethered ligand requires proteolytic cleavage of the N-terminus to allow binding to ECL2 of the PAR (*vide infra*, **Section 1.2.2**).

Another key structural feature of the PARs is the hirudin-like domain (**Figure 1.13**).⁶¹ Only present within PAR1 and PAR3, these sequences of amino acids share similarities with a key binding domain within hirudin, a natural thrombin antagonist.⁶¹ This domain acts as a beacon for thrombin binding, providing a signal for the thrombin to seek and bind to before cleaving the N-terminus. As such, thrombin binds with higher affinity to PAR1 and PAR3 than to PAR4,⁶² although PAR1 and PAR3 can act as cofactors to PAR4 *via* hetero-dimerisation to overcome this low-affinity activation.^{63,64}

Finally, both PAR1 and PAR2 contain plentiful serine residues within the C-terminus.⁶⁰ These serine residues are phosphorylated following activation, signalling for recycling of

the GPCR and leading to termination of the associated cell signalling pathways (*vide supra*, **Section 1.1.2**). However, PAR3 and PAR4 contain significantly fewer serine residues leading to longer response times following activation.

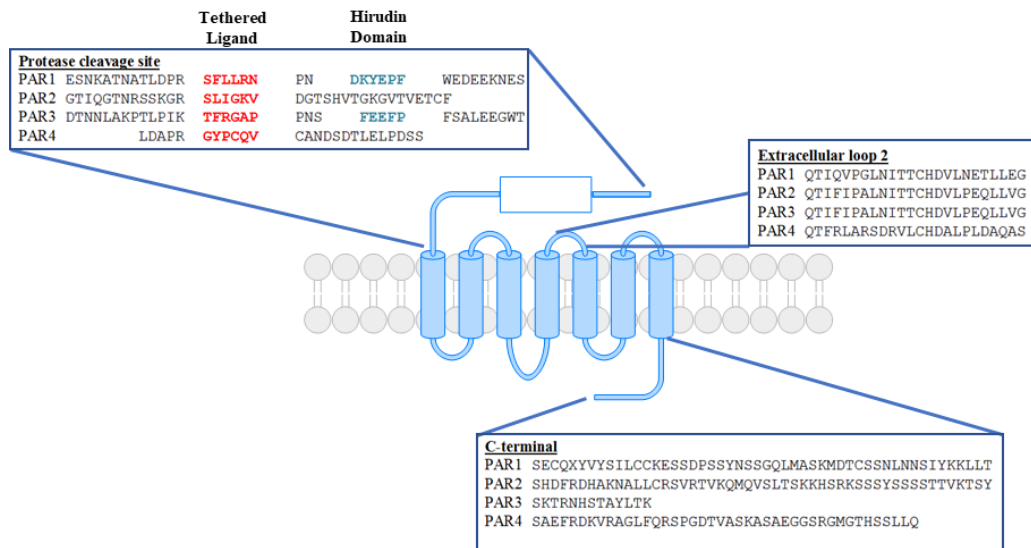


Figure 1.13: Homology of the PAR subfamily of GPCRs. The tethered ligand domains are shown in red and represent the amino acid sequences defined as the ligand. These domains bind to extracellular loop 2, which is a domain that is highly conserved across the PARs.⁶⁵

1.2.2 Mechanism of Action for PARs

As stated above, activation of a PAR arises from the cleavage of the N-terminal region by a serine protease. This cleavage leads to the exposure of the tethered ligand, liberating it for binding to ECL2 of the protein (**Figure 1.14**).⁶² It is this cleavage-dependent mechanism of action that sets the PARs apart from all other GPCRs. Once the tethered ligand has bound, a conformational change in the GPCR allows recruitment of G-protein to interact with the intracellular surface before being split into the G_{α} monomeric subunit and the $G_{\beta\gamma}$ heterodimeric subunit (**Figure 1.14**).⁶⁶ The G_{α} and $G_{\beta\gamma}$ subunits can then go on to induce their respective signalling cascades (**Figure 1.14**).

Once activated, the C-terminus of the PAR becomes available for phosphorylation by G-protein coupled receptor kinases (GRKs) (**Figure 1.14**).^{35,67} This has only been shown to occur on PAR1 and PAR2, and signals these PARs for binding with β -arrestins (**Figure 1.14**).^{67,68} The β -arrestins then signal for the endocytosis of the PAR, causing internalisation into a vesicle and recycling of the PAR.⁶⁹ While other GPCRs return to the cell membrane to act again post-recycling, this is not possible for the PARs given their cleavage-dependent mode of activation. PARs can become terminally downregulated post-activation with a proteolytic enzyme.⁶⁹

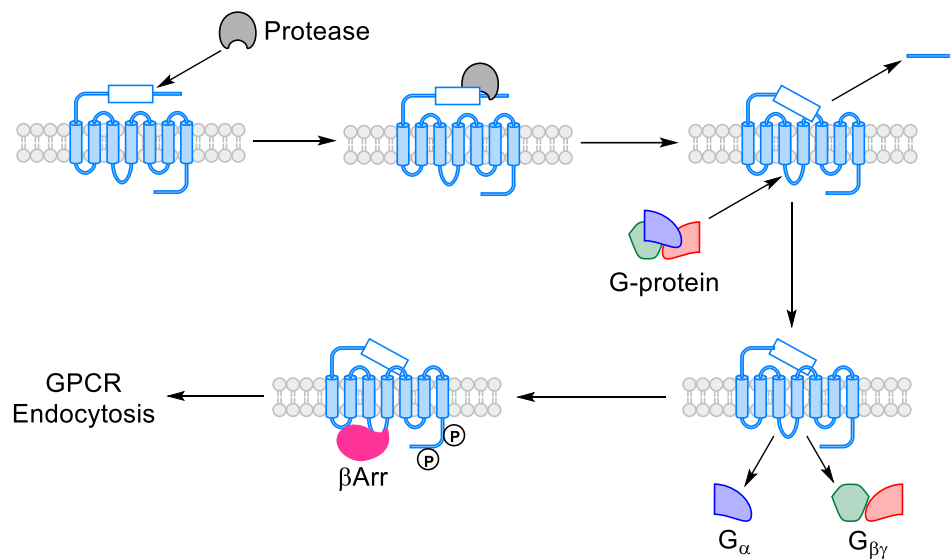


Figure 1.14: A simplified mechanism for activation of PARs by a serine protease. The serine protease cleaves the N-terminal chain, exposing the tethered ligand that can then go on to bind to ECL2, activating the protein and releasing the G_{α} subunit into the cell.⁷⁰ Phosphorylation by GRKs signals the GPCR for binding with β -Arrestins, which subsequently signals for the internalisation and recycling of the PAR.⁶⁹

Activation of the PARs *in vivo* occurs due to the action of a serine protease (*vide supra*, **Section 1.2.1**).⁷¹ However, not all are activated by the same proteases. While PAR1, PAR3 and PAR4 are most commonly associated with activation by thrombin, PAR2 is

activated by trypsin (**Figure 1.15**) and each PAR is also susceptible to activation by a wider range of proteases (**Table 1.2**).⁷¹

The activation of PARs leads to activation of multiple families of G proteins. Namely, PAR1 and PAR2 activate $G_{i/o}$, $G_{q/11}$ and $G_{12/13}$ signalling, whilst PAR4 only activates $G_{q/11}$ and $G_{12/13}$ signalling.⁷²⁻⁷⁴ Notably, PAR3 does not function in a signalling capacity, instead acting to regulate thrombin-mediated signalling *via* dimerization with PAR1.⁷⁵

Additionally, PARs can be activated by the recruitment of small peptides into their extracellular domain which contain analogous amino acid sequences to their own tethered ligand sequences, with a variety being reported for PAR1, PAR2 and PAR4 (**Table 1.2**).⁷⁶ However, there are no such peptides reported for PAR3.⁷⁶

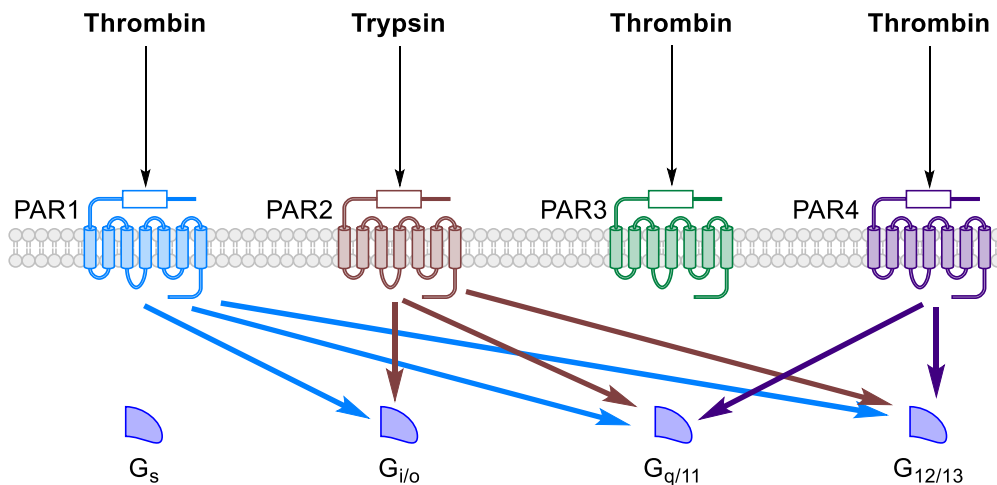


Figure 1.15: Serine proteases predominately responsible for activation of PARs and the associated G proteins for each PAR.

Table 1.2: Further information on the activation of PAR1-4 including additional agonist proteases as well as agonist peptide sequences. Compounds in bold represent compounds of interest to the current study.

	PAR1	PAR2	PAR3	PAR4
Associated G_{α} signalling	$G_{i/o}$ $G_{q/11}$ $G_{12/13}$	$G_{i/o}$ $G_{q/11}$ $G_{12/13}$	Non-signalling	$G_{q/11}$ $G_{12/13}$
Agonist proteases	Thrombin Factor Xa Plasmin APC MMP1/MMP13 Elastase Proteinase 3 Granzyme K KLK4	Trypsin Tryptase FVIIa/FXa KLK2/4/14 Neutrophil elastase Cathepsin S Gingipain Testisin Matriptase	Thrombin APC FXa	Thrombin Trypsin Plasmin Cathepsin G MASP1 KLK14
Agonist peptides	TFLLR-NH₂ SFLLR-NH ₂	SLIGKV-NH ₂ SLIGRL-NH ₂ SLAAAA-NH ₂	N/D	AYPGKF-NH₂ GYPGKF-NH ₂ AYPGKV-NH ₂ AYPGQV-NH ₂

However, as mentioned above (**Figure 1.13**) PAR1 and PAR3 contain a hirudin domain which acts as a beacon for thrombin binding.^{56,77} Conversely, PAR4, which is also activated by thrombin, does not contain a hirudin binding domain.⁶⁰ Despite this inherent lack of signalling for thrombin binding, PAR4 can still be activated with high potency attributed to the heterodimerisation inherent in GPCRs (**Figure 1.16**). Through the dimerization of PAR4 with PAR1 or PAR3, thrombin can bind and cleave PAR1/3 as would normally be expected (**Figure 1.16**).^{63,78} Following the initial cleavage, the N-terminus of PAR4 can fold into the active site of thrombin whilst it remains bound to PAR1/3, allowing PAR4 to be cleaved and continue its own signalling cascades (**Figure 1.16**).⁶³ Dimerisation of this manner also occurs between the PARs and other GPCRs, allowing activation of one partner to lead to modulation of the other.⁷⁹

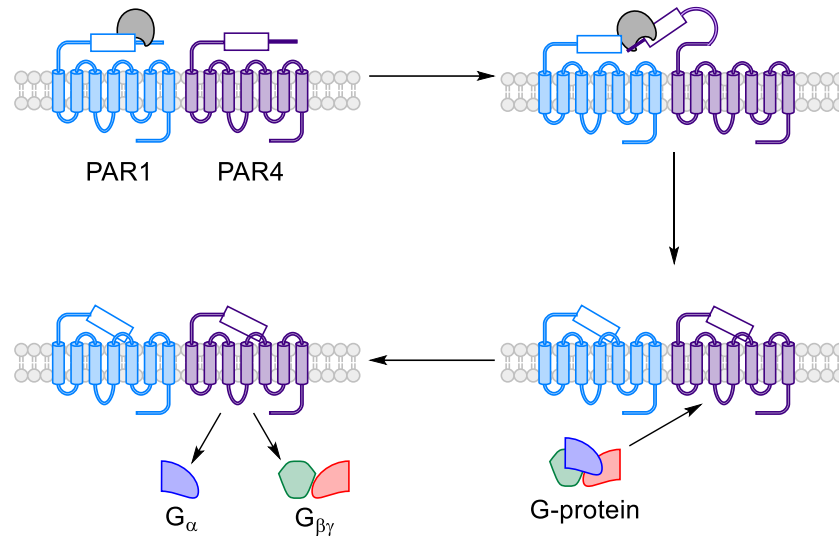


Figure 1.16: Heterodimerisation of PAR1 and PAR4 allowing activation of a second PAR within a single binding event for the serine protease.^{63,79}

In addition to the expected activation of PARs from interaction with a serine protease, the PARs can also be inactivated by protease function (**Figure 1.17**). The plethora of protease enzymes will bind at different points on the N-terminus of a PAR before cleaving the N-terminal domain (**Table 1.3**).⁸⁰ In this way, the tethered ligand can be partially or completely cleaved from the protein, preventing the PAR from functioning normally and, ultimately, preventing further cell signalling cascades.

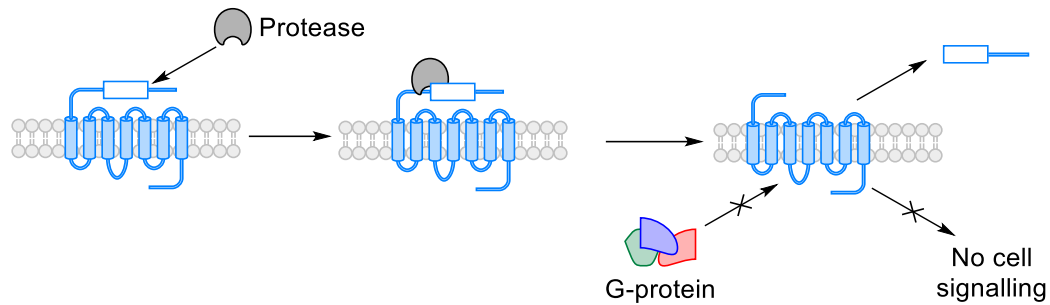


Figure 1.17: Simplified mechanism for inactivation of PARs by protease enzyme. The protease cleaves the N-terminal chain in a different region, leading to partial or complete cleavage of the tethered ligand from the rest of the PAR.⁶⁰

Table 1.3: List of disarming proteases for each of the PARs.⁷⁶

	PAR1	PAR2	PAR3	PAR4
Disarming proteases	Trypsin Cathepsin G Chymotrypsin Kallikreins ISP2	Neutrophil elastase Cathepsin G Proteinase 3 EPa ISP2	Neutrophil elastase Cathepsin G	ISP2

Finally, the protease enzymes can elicit biased signalling of the PARs, whereby cleavage at different points on the N-terminus leads to the release of different tethered ligands capable of activating specific downstream effects *via* PAR activation (**Figure 1.18**).⁸⁰ For example, while thrombin is known to activate each of the associated G-proteins with PAR1 as well as initiate phosphorylation and internalisation of PAR1 *via* beta-arrestins, other proteases can selectively activate a single G-protein signalling pathway.⁸⁰

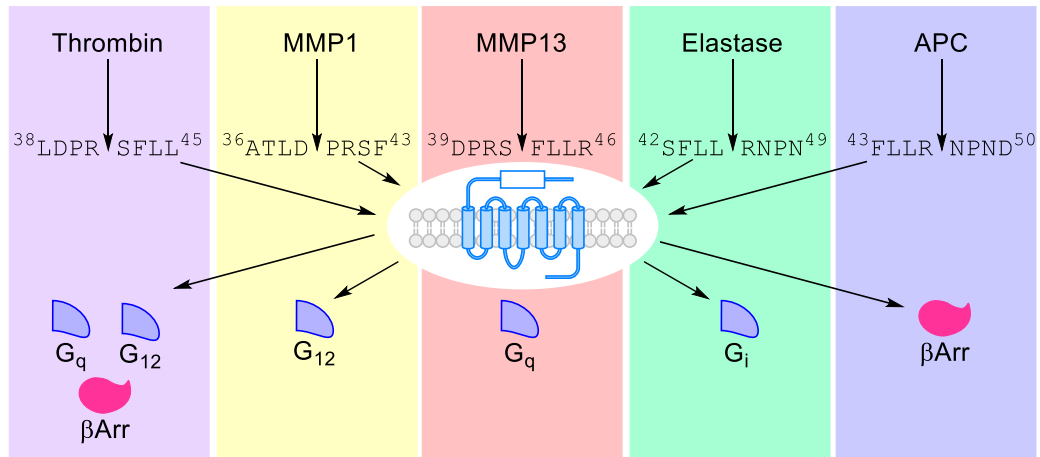


Figure 1.18: Biased signalling as a result of activation of PAR1 by a range of proteases.⁸⁰

1.2.3 PARs in Disease

The function of the individual PARs depends on the localisation of the protein and on the subsequent G-protein activation. The following section provides a brief overview of disease states associated with the PARs.

1.2.3.1 PARs in Cardiovascular Disease

Whilst the PARs have extensive disease implications, PAR1 and, to a lesser extent, PAR4 have been of particular interest in the research of cardiovascular disease.⁸¹ Cardiovascular disease takes many forms but the two most prominent are heart disease and stroke which, when combined, accounted for 85% of deaths out of 17.9 million associated with cardiovascular diseases in 2016.⁸²

The involvement of PAR1 and PAR4 in cardiovascular disease is associated with their role in human platelets and haemostasis (**Figure 1.19**). When a blood vessel becomes damaged, von Willebrand's factors and collagen fibres are released, allowing platelets in the bloodstream to become bound around the wound (**Figure 1.19a**).⁸³ At this point, platelets are activated *via* their GPCRs by agonists present in the bloodstream (**Figure 1.19b**). For PAR1 and PAR4, this activation is carried out primarily by thrombin.⁸¹

Following activation, signalling cascades from PAR1/4 and other GPCRs lead to shape change of the platelets and the secretion of platelet granules (**Figure 1.19c-d**).⁸⁴ These

granules contain agonists for further activation of platelets, such as thrombin as well as ADP and thromboxane A₂.⁸⁵ This cascade of platelet activation enables the platelets to bind together around the wound, limiting blood loss (**Figure 1.19e-f**). This platelet plug can then be bound together by polymeric fibrin, forming a blood clot (**Figure 1.19g**).⁸⁶

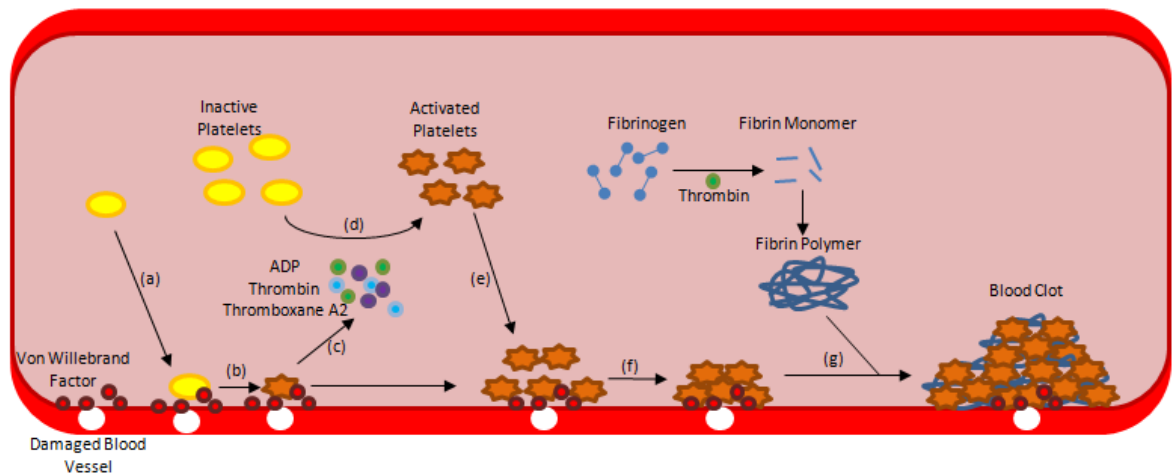


Figure 1.19: Steps involved in haemostasis. (a) Platelet binding to the vessel wall. (b) Activation of platelets. (c) The release of granules containing activation factors. (d) Activation of platelets. (e) Recruitment of activated platelets to the vessel wall. (f) Platelet aggregation. (g) Blood clot formation. Thrombin is also responsible for the release of fibrin monomers from fibrinogen, which then form fibrin polymers capable of binding with the platelet plug to form a blood clot.^{87,88}

Within human platelets, the activation of PAR1 and PAR4 occurs as a result of thrombin-mediated cleavage, as described previously (*vide supra* **Section 1.2.2**). PAR1 and PAR4 can be seen to be involved in the G_q pathways leading to shape change of the platelet via the release of inositol triphosphate (IP₃) and subsequent activation of calcium signalling (**Figure 1.20**). This pathway, as well as the diacylglycerol (DAG) pathway, can also be seen to lead to the activation of integrins, causing platelets to aggregate together.⁸⁹ Another major aspect of platelet signalling is granule secretion, the process by which agonists are released into the blood stream to facilitate further platelet activation. PAR1 can also be seen to be involved in this pathway, signalling via G_q through Src Family Kinase (SFK) and its subsequent signalling cascade.⁹⁰ PAR1 is also known to signal via G₁₃, which can be seen to be involved in the activation and aggregation of platelets, and

PAR4 is also known to signal via G_q .^{91,92} With this in mind, PAR1 and PAR4 combined seem to contribute to most, if not all, of the aspects of platelet activation and aggregation, making the modulation of these receptors desirable for anti-thrombotic therapies.^{70,93}

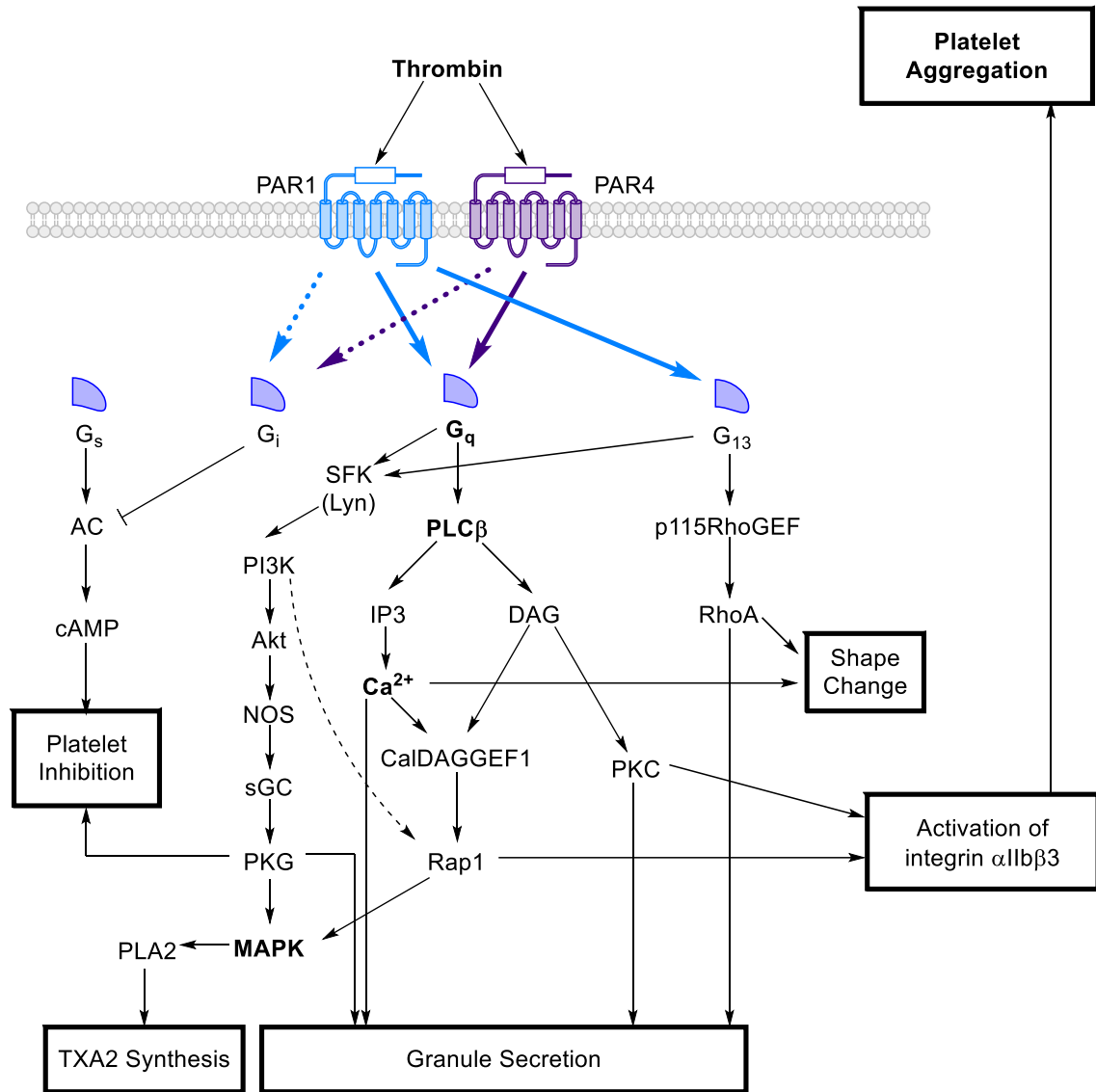


Figure 1.20: Thrombin-mediated signalling cascades responsible for the activation and aggregation of platelets during primary haemostasis. G_q subunits G_s , G_i , G_q and G_{13} are shown. Upon activation, the PARs cause the release of the G_q subunits from G-proteins. Depending on the G_q subunit released, an array of signalling pathways can be activated, with the cascades resulting in changes to the platelet. From the activation of the platelet via shape change to aggregation via the activation of integrins, the thrombin-mediated signalling pathways through the PARs are involved in all aspects of platelet activity. Labels in bold represent signals utilised in experiments carried out herein.^{89,94}

While the processes detailed above are required by the human body for survival upon injury, aberrant activation of platelets, whether *via* PAR1/4 or other GPCRs, can lead to the haemostatic processes occurring when they are not needed or, indeed, an overactivation when they are required.⁹⁵ This overactivation could lead to thrombosis, where the blood clot builds up to a sufficient level where it is blocking blood flow. This restricted blood flow is a major factor in cardiovascular disease and stroke, where low blood flow limits the levels of oxygen being delivered throughout the body. Due to the involvement of PAR1/PAR4 in this process, the PARs have been well researched as targets for anti-thrombotic drugs.⁷⁶

1.2.3.2 PARs in Inflammatory Disease

As with the cardiovascular response to blood vessel damage, the immune response is also a necessary process for recovery following injury or disease. The immune response takes place after tissue damage or in reaction to invasion from an external agent (**Figure 1.21**).⁹⁶ An occurrence of a stressor, whether in the form of an injury or the invasion of an extracellular pathogen, provokes the release of various signalling molecules from the epithelial cells which begin to propagate an immune response (**Figure 1.21(i- ii)**).⁹⁶ Most importantly, the release of histamine occurs from mast cells, with histamine being one of the key effectors of the inflammatory response (**Figure 1.21(iii)**).⁹⁷ By transferring to the blood vessel wall, histamine can cause vasodilation of the blood vessel *via* binding with histamine receptors, reducing blood pressure (**Figure 1.21(iv)**).^{96,98} The expansion increases the permeability of the blood vessel wall, allowing the passage of white blood cells and other small molecules, typically pro-platelet chemicals, and proteins out of the bloodstream and into the interstitial fluid, where they work to combat the invading pathogens (**Figure 1.21(v-vi)**).⁹⁹ Consequences of the inflammatory response include swelling of the wounded site in addition to redness of the skin and a sharp rise in temperature and pain (**Figure 1.21(vii)**).

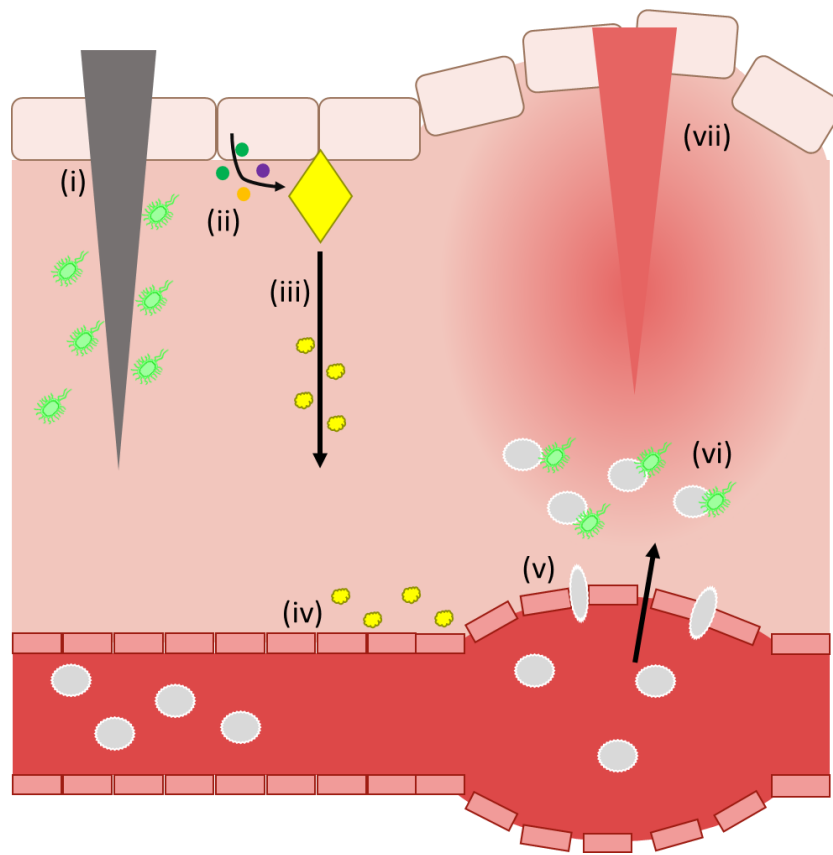


Figure 1.21: Simplified schematic for immune response. Following damage or invasion under the epithelial layer of cells (i), chemical factors released from epithelial cells (ii) initiate the release of histamine from mast cells (iii). Histamine, transferring through the interstitial fluid to the blood vessel wall where it promotes vasodilation (iv) allowing passage of white blood cells, among other chemical entities, into the interstitial fluid (v). White blood cells combat invading pathogens (vi) resulting in swelling and redness of the wound accompanied by warmth and pain (vii).

However, activation of the immune response in the absence of external stimuli can occur as a symptom of various disease states including arthritis, obesity and cancer.^{100,101} The PARs, with their roles as signal transducers from the extracellular environment into the cells, have been shown to be involved in immune responses throughout the body. Specifically, PAR2 has been extensively researched for its role within inflammatory disease and disease-dependent inflammatory responses.¹⁰²

Tissue factor (TF), or platelet tissue factor/factor III, is a protein structurally similar to the cytokine receptors which is induced by inflammatory mediators that, among other

signalling properties, is responsible for the release of thrombin into the bloodstream.¹⁰³ The structure of TF consists of an extracellular domain, which contains two hydrophobic sequences presenting a joint hydrophobic binding pocket, and a short intracellular domain, which regulates downstream signalling, joint by a transmembrane domain.¹⁰⁴ Through its extracellular domain, TF forms complexes with other coagulation factors – VIIa and Xa.¹⁰⁵ The TF.VIIa and TF.VIIa.Xa complexes each cause the cleavage of the PAR2 N-terminus, causing activation of associated signalling cascades which, amongst other roles, promote pro-inflammatory processes.¹⁰⁵

The critical role played by the TF.VIIa.PAR2 signalling cascade in inflammation has been highlighted in multiple inflammatory diseases.^{106–108} Within arthritis, both PAR2 deficiency and TF mutation, specifically to the cytoplasmic tail, positively impact the severity of arthritic symptoms.^{106,107} Additionally, PAR2 deficiency attenuates inflammation models of autoimmune encephalitis and multiple sclerosis, highlighting therapeutic effects upon PAR2 inhibition or knockout.¹⁰⁸

Within neuronal cells, the function of PAR2 remains the same as a pro-inflammatory pathway.¹⁰⁹ However, due to the absence of TF in the vicinity of neuronal cells, PAR2 activation is carried out by tryptases released from mast cells.¹⁰⁹ Activation leads to a decrease in the threshold for TRP ion channels within the periphery nerve endings.^{110–112} This lowering of the threshold translates to hypersensitivity to pain and irritation, thought to be a predominant factor in disease-mediated pain.¹¹⁰ Inflammation around the neuronal cells is also directly driven by PAR2 activation *via* the release of Substance P and calcitonin gene-related peptides (CGRP).¹¹³ Substance P initiates the expression of pro-inflammatory cytokines while CGRP receptors are also responsible for the downstream signalling leading to inflammation and control of pain.¹¹³

Inflammatory role of PAR2 in cancer

Finally, the inflammatory role of PAR activation is exploited by cancer cells. Tumours typically initiate a pro-thrombotic state through the expression of TF.¹¹⁴ The increase in TF expression subsequently allows prothrombotic function through the release of thrombin, as described above. However, while PAR2 is not activated by thrombin it can

be cross activated *via* dimerization with PAR1.¹¹⁵ This cross-activation has been shown to lead to an increase in the metastatic potential of melanoma cells.¹¹⁵

Additionally, the expression of TF, VIIa and PAR2 has been heavily described within invasive breast cancer.¹¹⁶⁻¹¹⁸ The downstream signalling events of this complex have been associated with hypermobility in breast cancer cells. Promisingly, PAR2 deficiency has been shown to delay tumour progression and inhibition of PAR2 is also shown to inhibit tumour growth.

With the wide-ranging function of PAR1 and PAR2 within disease, they present promising targets for ongoing therapeutic study.

1.3 Modulation of PAR Function

With the varied disease implications discovered for the PARs, they have been the topic of research as targets for new drugs for many years. However, there has been relatively little success in obtaining a validated drug for PAR inhibition, with only one compound successfully completing clinical trials and reaching FDA approval.¹

1.3.1 Background

The modulation of PAR activity has previously been carried out by three main mechanisms (**Figure 1.22**). Firstly, by blocking the docking site of the tethered ligand within the extracellular domain of the PAR with a competitive antagonist, interactions between the ligand and ECL2 can be disrupted.¹¹⁹ Secondly, antibodies targeting amino acid sequences around the tethered ligand can prevent the docking of the serine proteases and thus the liberation of the tethered ligand itself.⁷⁰ Finally, allosteric antagonists have been used to interrupt the interactions between the intracellular domain and the G-proteins, with allosteric sites found within the transmembrane domain and the intracellular domain (**Figure 1.22**).²

Within the PARs, PAR1 and PAR2 are shown to be the most targeted for inhibition due to their well understood physiological profile and detailed understanding of their signalling cascades (**Table 1.4**).⁷⁰ Conversely, PAR3 has no known inhibitors due most likely to its non-signalling nature, which makes quantification of inhibition extremely difficult (**Table 1.4**).⁷⁰ There is also a paucity of data known for PAR4 inhibition, which could represent a promising target for novel therapeutics especially in cases where the slow release and suppression of PAR4 signalling could allow softer inhibition (**Table 1.4**).¹²⁰

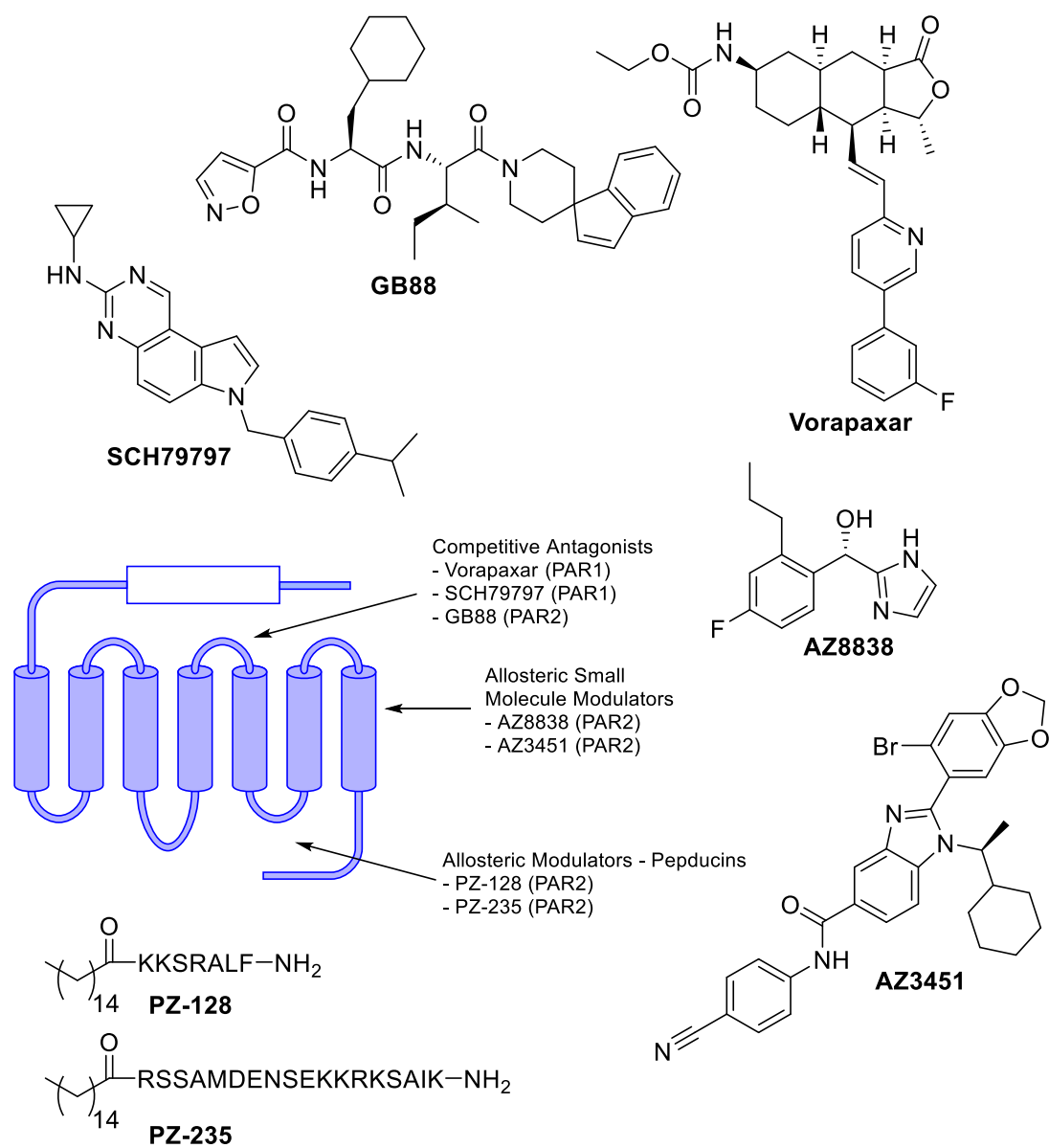


Figure 1.22: Known binding sites utilised for PAR modulation. (a) N-terminal domain surrounding the tethered ligand (b) Extracellular Loop 2, the site at which the tethered ligand would bind once exposed (c) intracellular sites linked to G-protein coupling.⁷⁰

Table 1.4: Information on antagonists of PARs. Compounds in bold represent compounds of interest to the current study.

	PAR1	PAR2	PAR3	PAR4
Selective antagonists	Vorapaxar			
	PZ-128	GB83		
	SCH79797	GB88		
	Atopaxar	ENMD-1068		tc-YGPKF
	RWJ-56110	K14585	N/D	YD-3
	ER-129614-06	AZ8838		
Clinically used antagonists	BMS-200261	AZ3451		
	Parmodulin2			
	Q94.HCl			
	Vorapaxar	N/D	N/D	N/D
Antagonists in clinical trials	Atopaxar	PZ-235	N/D	N/D
	PZ-128			

Blocking the docking site within the extracellular domain prevents the tethered ligand from initiating the cell signalling cascade. This is the typical method of binding for small molecule, competitive antagonists such as vorapaxar or SCH79797, both of which are PAR1 antagonists.^{1,121} These antagonists tend to have a section of the drug residing within the hydrophobic transmembrane domain, which can lead to some near-irreversible antagonism events such as in the case of vorapaxar (**Figure 1.23**).¹¹⁹

An analogue of the naturally occurring alkaloid himbacine, vorapaxar was first discovered as an exceptionally potent inhibitor of PAR1.¹ However, due to its long half-life and high potency, vorapaxar has been shown to increase the risk of severe bleeding events, causing intracranial haemorrhage in some patients.¹²² This led to a premature end for one clinical trial, although it has since been approved for use as an antiplatelet agent for those without a history of stroke.¹²² With this in mind, alternative therapies for PAR1 need to be considered. As well as searching for novel competitive antagonists, consideration should also be given to the other binding sites within PAR1.

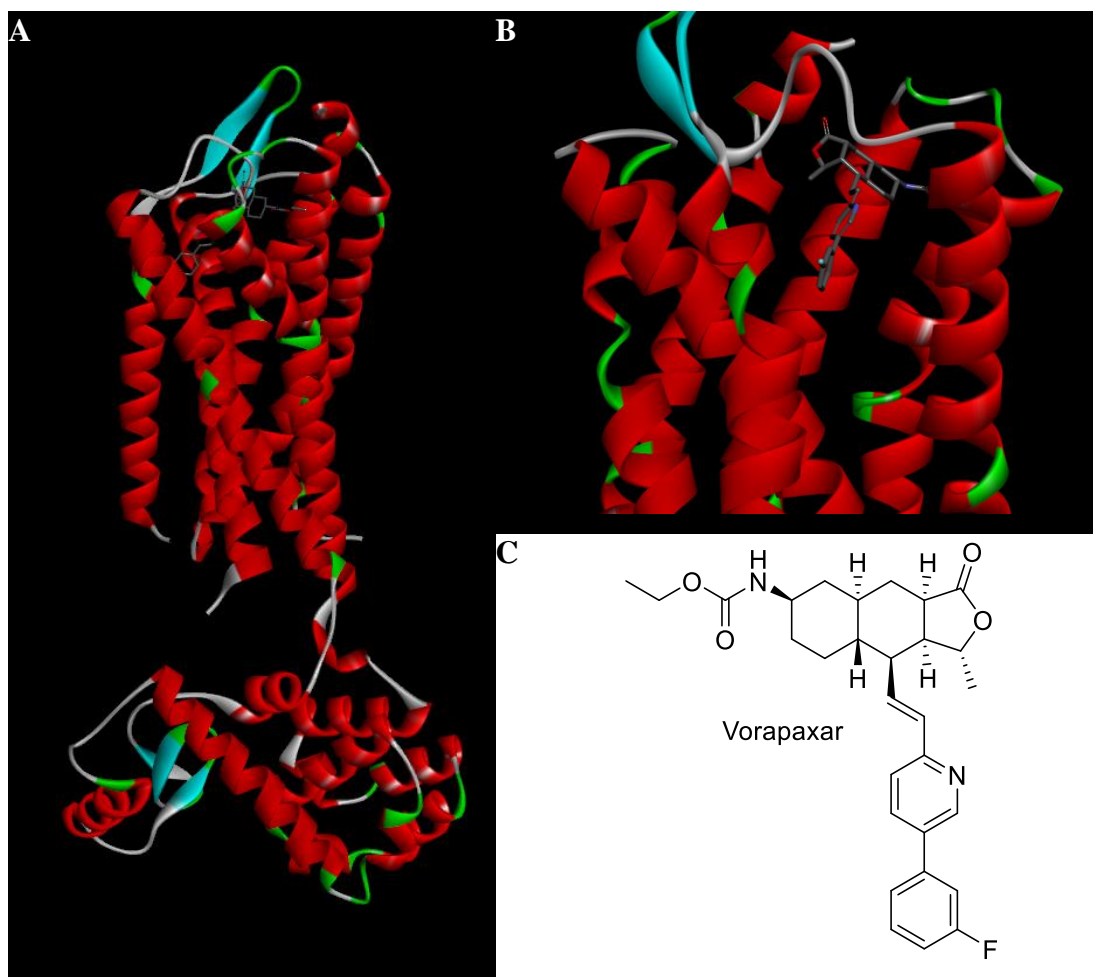


Figure 1.23: Vorapaxar bound within the transmembrane domain of PAR1 (Protein Database code: 3VW7). **A** Full PAR1 crystal structure co-crystallised with Vorapaxar. **B** Extracellular pocket of PAR1 co-crystallised with Vorapaxar, the aromatic moiety extends down into the transmembrane domain while the more polar tricyclic system points out away from the transmembrane domain. **C** Chemical structure of PAR1 inhibitor vorapaxar.¹¹⁹

It has been shown that the use of antibodies can prevent the cleavage of the N-terminal region, reducing the exposure of the tethered ligand in the N-terminal tail of the PARs. ATAP2 and WEDE15 are two examples of such antibodies, with both inhibiting thrombin-mediated cleavage of PAR1.¹²³ This, in effect, prevents the thrombin-induced pathways from functioning and has been particularly useful in studying the mechanism of PARs in greater detail. However, no progress appears to have been made in getting an antibody into clinical trials as a PAR1 inhibitor.

Steps have also been taken towards identifying a series of peptide mimetic drugs which are capable of binding to PARs on the inside of the cell membrane.¹²⁴ These cell-penetrating peptide mimetics have been named pepducins and are typically based on intracellular loop sequences of GPCRs.

1.3.2 Pepducin-mediated Modulation of PAR1

1.3.2.1 Background

Pepducins are cell-penetrating, peptide mimetic compounds that are typically derived from amino acid sequences within their target protein.² There have been examples of pepducin agonists and antagonists for a variety of GPCR proteins, including Smoothed (SMO), CXC chemokine receptors (CXCRs) as well as the PARs.^{125–128} The pepducin approach takes a biologically relevant section of a GPCR sequence and couples it with a hydrophobic chain to facilitate binding within the cell membrane. The peptide sequence can then bind allosterically to the GPCR of interest, eliciting its modulatory effect.

A pepducin consists of three main components: a polypeptide sequence, most often derived from an intracellular loop of a GPCR, a hydrophobic tail such as a palmitoyl chain and an amide linker holding these two ends together (**Figure 1.24**). One example of the pepducins is PZ-128, the first pepducin to see clinical success, completing Phase I clinical trials.¹²⁹

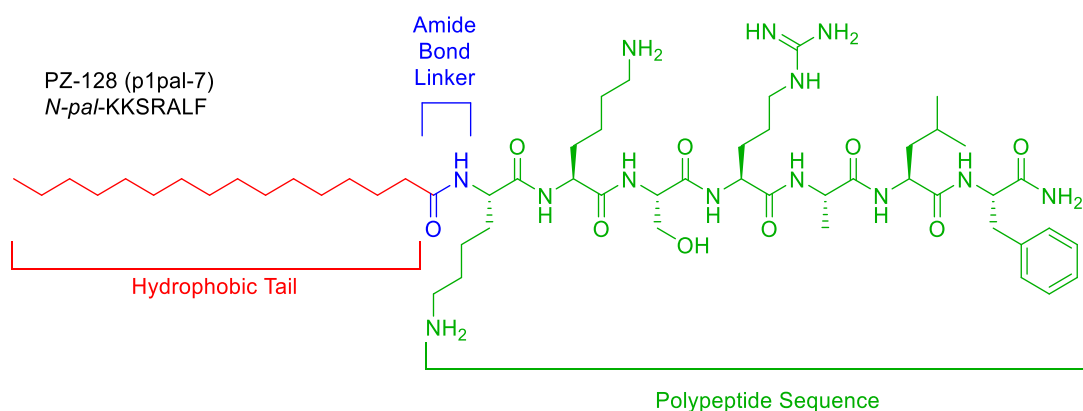


Figure 1.24: Molecular structure of PAR1 pepducin PZ-128.²

The polypeptide chains have typically consisted of no more than 20 amino acids and have classically been based on the amino acid sequences of intracellular loops within the GPCRs.¹³⁰ The tail of the molecule needs to be capable of lodging within the cell membrane. As such, a highly hydrophobic lipid moiety is most often used (e.g. palmitoyl, myristoyl or lithocholic acid).¹³⁰ The hydrophobic nature of these groups also helps facilitate binding to the cell membrane. Finally, the linker is required to hold the hydrophobic tail and the peptide sequence together in transit to and within the cell. Amide bonds are the most commonly reported moieties in this capacity.¹³⁰

Work has shown that the length of the hydrophobic chain and the peptide sequence both have an impact on the properties of the pepducin, and with this in mind the molecules have become an area of interest within this study.

1.3.2.2 Mechanism

The hydrophobic functionality plays a key role in both steps of the pepducins mechanism of action.² Firstly, it allows binding to the extracellular surface of the cell membrane by lodging itself within the hydrophobic domain of the phospholipid bilayer (**Figure 1.25**). The molecule is then proposed to invert and transfer through the cell membrane to the intracellular surface.¹³¹ The peptide head of the pepducin is then tethered to the cell membrane near the GPCR and can bind at the appropriate binding site. The binding of pepducin antagonists is thought to interrupt the interactions between the GPCR and associated G-proteins.²

More recently, the PAR1 pepducin agonist P1pal-19 was shown to bind to a region known as helix 8 (H8), a highly conserved region within the C-terminus of GPCRs, to allosterically activate PAR1.¹³² The H8 region of the GPCR has been shown to be involved in signal transduction from PAR1 into the G-protein and has been suggested as the binding site for pepducins across a range of GPCRs.¹³³

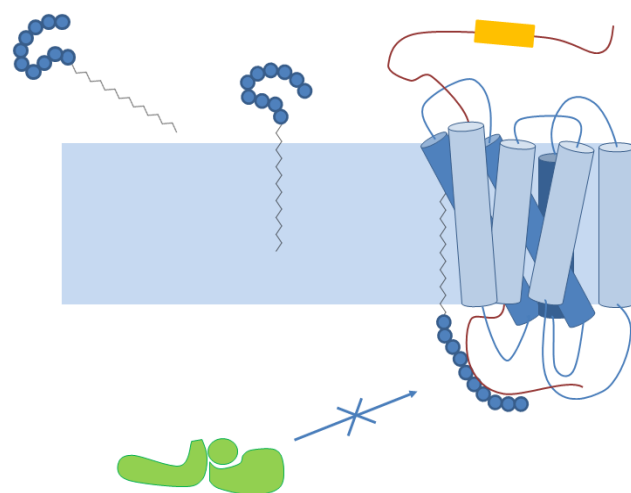


Figure 1.25: Proposed mechanism of action for transfer of pepducins across the cell membrane.¹³¹

1.3.2.3 Case Study - PZ-128

The use of pepducins in the modulation of PARs has become well documented in recent years, with agonist and antagonist pepducins being reported.^{129,132} One particular example, PZ-128, is a pepducin derived from PAR1 which has passed phase 1 clinical trials as an anti-thrombotic agent targeting PAR1.¹³⁴ While there are many examples of pepducins for PAR1, PAR2 and PAR4, only two molecules have made progress towards clinical trials: PZ-128, which has completed Phase I (NCT01806077 and NCT02561000) is awaiting Phase II trials (pending funding) as an inhibitor of PAR1 for the treatment of thrombosis, and PZ-235, which is currently waiting to start Phase I trials as an inhibitor of PAR2.³

As shown in **Figure 1.24**, PZ-128 is a palmitoylated, peptide mimetic drug based on the intracellular loop 3 (ICL3) region of PAR1 with the structure N-pal-KKSRALF-NH₂.^{2,129} Initially named P1pal-7, the molecule was developed as part of an investigation into the allosteric binding of GPCRs. Two classes of molecule were described in this study, each containing peptide sequences of varying length derived from the ICL3 region of PAR1. One class contained purely the peptide sequence and the other combined the peptide sequence with a palmitoyl group bound on the N-terminus.² The palmitoylated peptides were dubbed "pepducins." Of these pepducins, some were discovered to activate calcium signalling and platelet activation pathways in human platelets (P1pal-19 and P1pal-13).

Of those that did not activate these pathways, P1pal-7 and P1pal-12, only one was described as a PAR1 antagonist - P1pal-12. This palmitoylated pepducin displayed inhibition of SFLLRN-NH₂ mediated platelet aggregation with an IC₅₀ of 1 μM. No such pharmacological data were reported for P1pal-7 at this time.

In 2005, the role of PAR1 as a matrix metalloprotease-1 receptor was described.¹³⁵ In this fashion, PAR1 was found to promote the invasion and tumorigenesis of breast cancer cells. P1pal-7 was described within the supplementary figures for this paper as a "full antagonist" of PAR1, displaying inhibition of thrombin mediated [³H]-inositol phosphate (InsP) formation (and hence, PLC-β activity) with an IC₅₀ of 1-2 μM. In addition to this, P1pal-7 was also shown to inhibit the growth of breast cancer xenografts and prevent the migration of MDA-MB-231 cells. In 2009, P1pal-7 was shown to inhibit the migration of cancer cells in ovarian cancers as well.¹³⁶

In 2011, a report on PAR1 pepducins as antagonists in the treatment of lung cancer was published.¹³⁷ In this report, P1pal-7 was shown to inhibit thrombin mediated expression of pERK in A549 cells as well as inhibit the migration of lung cancer in a wide range of cell lines and in primary lung tumours.

Further investigation of P1pal-7 as a PAR1 antagonist was detailed in 2012, at which point the pepducin was renamed as PZ-128 and repurposed an antithrombotic agent.¹²⁹ PZ-128 was shown to inhibit PAR1 with high specificity, inhibiting SFLLRN-NH₂-mediated platelet aggregation in human platelets with an IC₅₀ of 0.5 μM but having no effect on ADP- or AYPGKF-mediated responses, which are P₂Y and PAR4 specific agonists, respectively. As well as this, the action of PZ-128 as an antithrombotic was described in multiple *in vivo* thrombosis models in guinea pigs and in baboons.¹²⁹

Since 2013, PZ-128 has been registered for two clinical trials (NCT01806077 and NCT02561000).^{129,138} Firstly, from April 2013 to November 2014 studies on the safety and tolerability of PZ-128 in individuals with risk factors for coronary artery disease were carried out (NCT01806077). The results of this study were recently published, highlighting once again the high specificity for PZ-128 to inhibit PAR-1 while not

inhibiting responses to AYPGKF, ADP or collagen.¹³⁴ Plasma concentrations of PZ-128 were shown to peak between 1 and 2 hours, with the half-life being described as 1.3-1.8 hours. As well as this, there were no significant effects caused by PZ-128 on the bleeding time, coagulation, clinical chemistry or ECG profile within those administered by the drug. On the other hand, some mild allergic reactions were documented, although these were considered not life-threatening and were rapidly reversed by stopping the infusion of the drug or by applying antihistamines. While this could suggest aberrant activity from PZ-128, PAR1 is known to be expressed in human endothelial cells where it contributes to pro- and anti-inflammatory pathways through cleavage by different proteases.¹³⁹

Another study on PZ-128 was disclosed in September 2015.¹³⁸ As of June 2019, recruitment for this study has been halted pending funding. This study was initially started to investigate the safety of PZ-128 in individuals undergoing non-emergent percutaneous coronary intervention.

Given the success demonstrated by PZ-128 in reaching clinical trials, and in PZ-235, the pepducin strategy shows great promise for the development of future antiplatelet therapies. The use of biologically relevant peptide sequences suggests an extremely large scope for design of novel pepducins.

1.3.3 PAR2 Inhibitors

PAR2 has also become a desirable target within novel drug discovery as a means of inhibiting its role in various inflammatory, respiratory, cardiovascular and neurological diseases, amongst others.

1.3.3.1 GB-88

Until the last few years, two antagonists were widely used as molecular tools for the investigation of PAR2.¹⁴⁰ Firstly, ENMD-1068 was utilised in the treatment of *in vivo* joint inflammation but ultimately displayed low efficacy and did not proceed into clinical trials (**Figure 1.26**).¹⁴¹ However, in 2012 a more potent PAR2 inhibitor was discovered in GB88, which was shown to prevent PAR2-mediated calcium release and also displayed a therapeutic effect in inflammatory disease (**Figure 1.26**).¹⁴² Interestingly, while GB88

was shown to inhibit the G_q-mediated signalling originating from PAR2 activation, it was also activating other pathways, with cAMP, ERK and Rho signalling all being activated following treatment with GB88.¹⁴³ This quirk of GB88 activity highlighted the potential for inhibitors of GPCRs to function as biased antagonists.

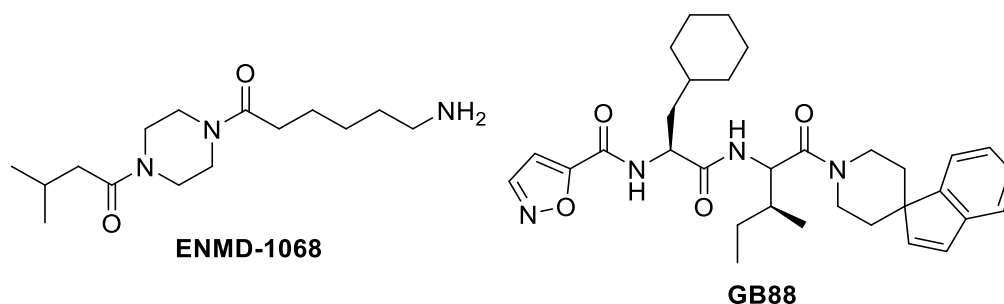


Figure 1.26: Chemical structures of PAR2 antagonists ENMD-1068 and GB88.

More recently, a study on the structure-activity relationship (SAR) of GB88 was carried out which highlighted key roles for each region of the molecule.¹⁴⁴ In particular, the isoxazole, isoleucine and C-terminal spiro-indene moiety each displayed the propensity for switching between antagonism and agonism following derivatisation, suggested to be caused by variable space within the PAR2 transmembrane binding pocket.¹⁴⁴

1.3.3.2 AZ8838/AZ3451

In 2017, two new inhibitors of PAR2 were reported, including the first reported crystal structures for PAR2, with AZ8838 and AZ3451 (**Figure 1.27**).⁴ These inhibitors highlighted the presence of multiple allosteric binding sites within the PAR2 transmembrane domain. Each inhibitor displayed potent inhibition of PAR2, with AZ8838 displaying IC₅₀ = 1.5-2.3 μM and AZ3451 providing IC₅₀ = 5.4-23 nM for the inhibition of SLIGRL-NH₂-mediated PAR2 function. While AZ8838 binds in a shallow binding pocket within the transmembrane helical bundle, AZ3451 displays binding on the periphery of PAR2 in a deeper binding pocket between the transmembrane helices and the cell membrane. However, as these new chemical tools were not tested in physiologically

relevant assays, their impact on PAR2 function within disease models has yet to be considered.

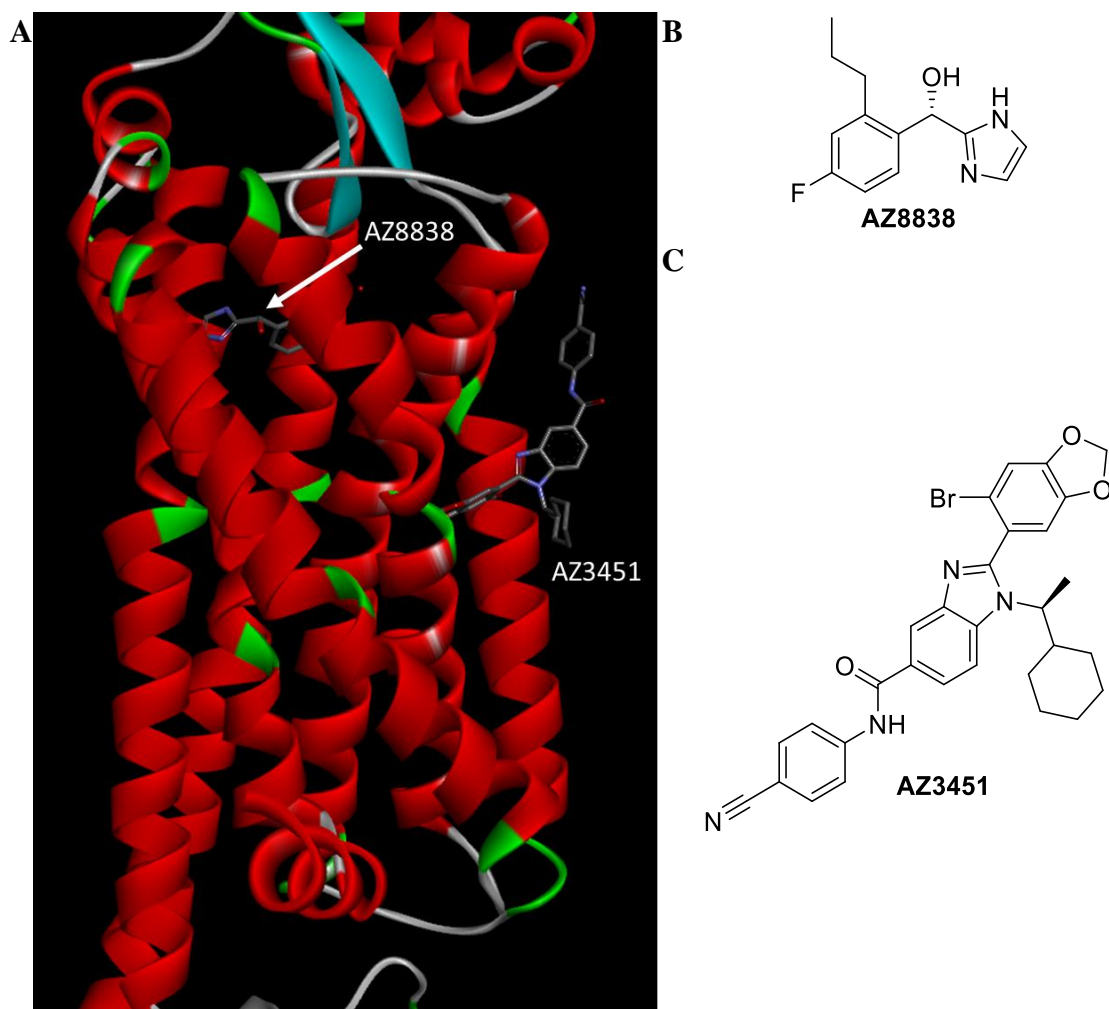


Figure 1.27: A Overlaid crystal structure of PAR2 in complex with AZ3451 and AZ8838. B Chemical structure of AZ8838. C Chemical structure of AZ3451.⁴

1.3.3.3 PZ-235

The pepducin approach to PAR inhibition has also shown a small amount of success within PAR2 modulation, with a single pepducin described as a promising treatment for inflammatory disease: PZ-235.³ PZ-235 is a significantly larger pepducin than PZ-128, with a peptide sequence containing 18 amino acids (**Figure 1.28**). The PZ-235 peptide

sequence is derived from an extended ICL3 sequence, with ICL3 comprising of Ala273, Met274 and Asp275.³ The rest of the peptide sequence is based on the residues immediately before and after the ICL3 sequence found within TM5 and TM6.

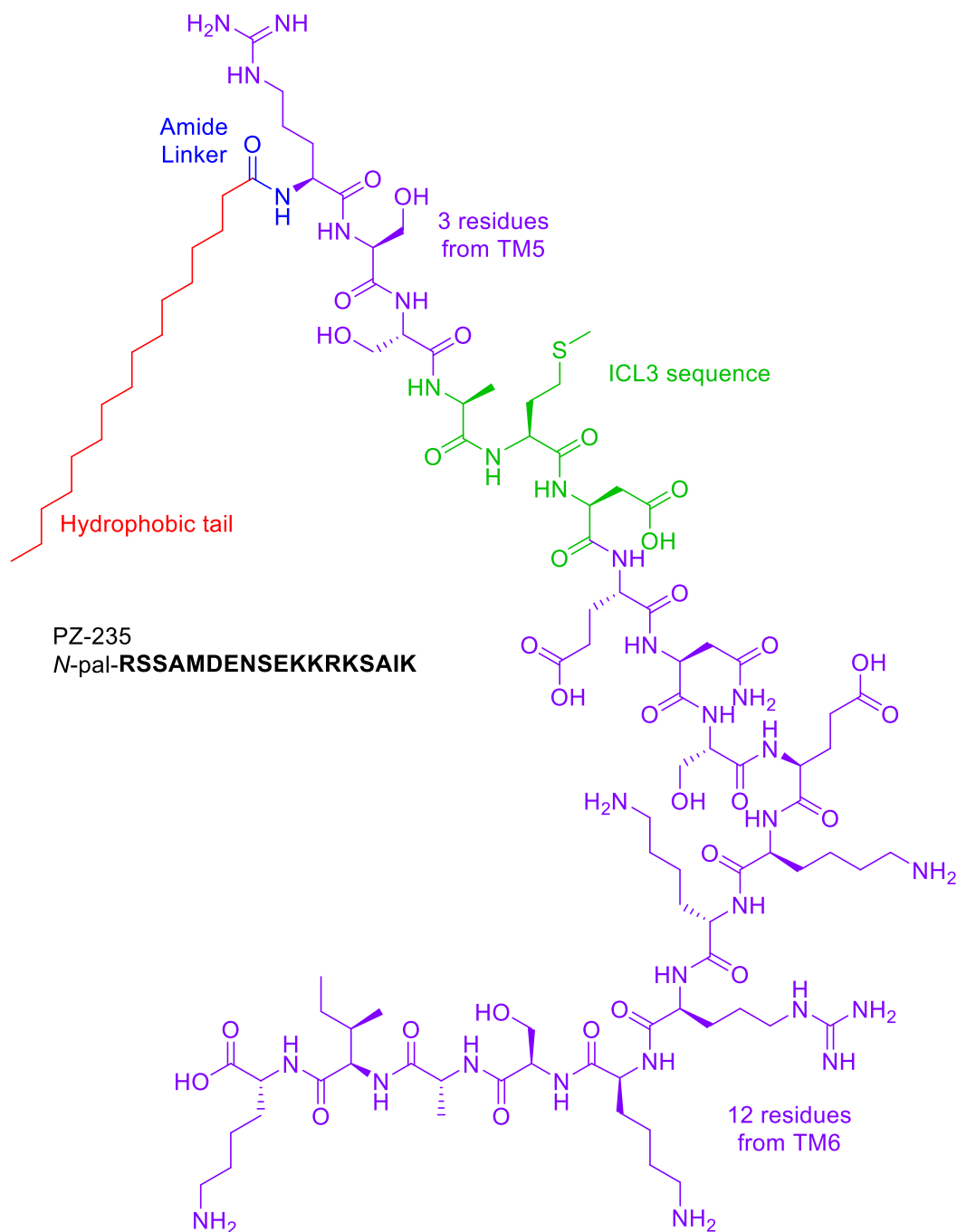


Figure 1.28: Chemical structure of PZ-235

PZ-235 was described as a full antagonist of PAR2, inhibiting SLIGRL-NH₂-mediated calcium signalling with an IC₅₀ of 2.4 µM in adenocarcinoma cells, as well as inhibiting the calcium response in HUH7 hepatocytes.³ PZ-235 also displayed suppression of liver fibrosis and inflammatory cytokines and protected against PAR2-mediated reactive oxygen species (ROS) production.³ Localisation studies with PZ-235 highlighted the low biodistribution of the pepducin within the body, collecting in the liver and kidneys primarily, followed by the lungs with very low quantities of the pepducin making it into the brain, heart, spleen, pancreas, small intestine and colon.³ While this data presents a strong case for the use of PZ-235 in treatment of liver fibrosis, the low bioavailability of the pepducin could prevent it from being more widely used as a PAR2 inhibitor.

1.4 Aims

The aims of this thesis are, firstly, the interrogation and development of SAR for novel chemical entities towards allosteric PAR inhibition and, secondly, the identification of novel analogues of known PAR inhibitors with improved inhibitive properties. The thesis will explore a range of allosteric strategies for PAR inhibition, utilising novel pepducin structures for the inhibition of PAR1 (**Chapter 2**) as well as novel small molecules derived from known allosteric regulators for inhibition of PAR2 (**Chapter 3**).

1.4.1 Allosteric Modulation of PAR1

It is hypothesised that the introduction of the PZ-128 peptide sequence into novel, cyclic pepducin structures would allow improved pharmacological properties to be obtained. The novel pepducins will be assayed utilising *in vitro* calcium ion signalling events to quantify their potency in comparison to PZ-128. Additionally, off-target effects of the pepducin strategy which arise during the study will also be researched through further *in vitro* signalling assays.

1.4.2 Small Molecule Allosteric Inhibitors of PAR2

Investigation into the structure-activity relationships of AZ8838 with PAR2 will also be carried out, looking to modify key functionalities within the chemical structure of the drug molecule to identify novel inhibitors of PAR2 function. The synthesis of AZ8838 analogues will initially be performed with divergent steps at the end of the syntheses, to allow expedient synthesis of analogues, before expanding to less efficient syntheses where necessary.

Analysis of the AZ8838 analogues will be carried out by two methods. Firstly, *in silico* assessment of the analogues will be performed using docking studies with published PAR2 crystallographic data. Secondly, *in vitro* assessment of the analogues will be performed using NFκB reporter cells, with NFκB representing a known downstream signal of PAR2 activation.

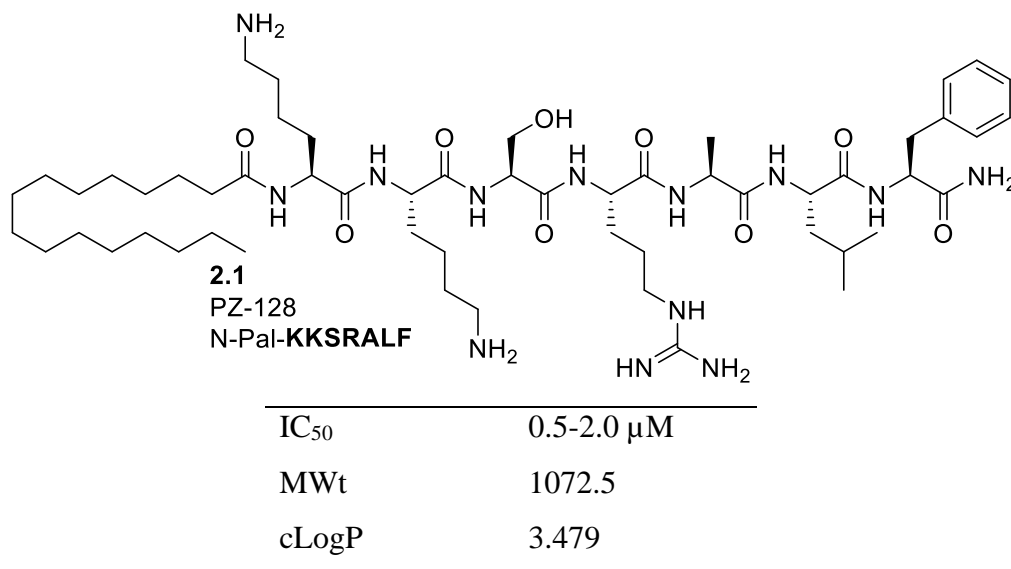
Chapter 2 Allosteric Modulation of PAR1

2.1 Introduction

With the introduction of pepducins in 2002 by Covic *et al.*, a novel method for modest inhibition of GPCRs had been discovered.¹²⁷ The pepducin approach to GPCR modulation has been shown to provide inhibitors of modest potency. PZ-128 (**2.1**) has been described multiple times as a PAR1 antagonist and has passed Phase I clinical trials as a cardiovascular therapy, although Phase II studies have been suspended pending further funding.^{134,138} Additionally, PZ-128 has also shown potential as a cancer therapeutic, with inhibition of invasion and metastasis of ovarian cancer tumours in nude mice.¹³⁶

Whilst compound **2.1** provided an interesting approach to PAR modulation, the pepducin class of molecules does not lend itself well to a traditional drug discovery approach. Given the size of the molecule, its molecular weight lies out with the normal considerations of a “lead-like”, or indeed drug-like, molecule.¹⁴⁵

Table 2.1: Chemical structure and pharmacological properties of PZ-128 (**2.1**)



Whilst initial studies on pepducins as potential therapeutics focused on the length of the peptide sequence, very little work has been carried out to challenge this paradigm.² This

leaves open chemical space to explore linking moieties between the peptide and palmitoyl chain, as well as applying restraints to the peptide sequence instead of leaving it as a flexible, single chain.

2.2 Aims and Objectives

The aim of this project is to design, synthesise and test a library of novel pepducins derived from known PAR1 inhibitor PZ-128. We reasoned that maintaining the peptide sequence whilst introducing a linker between the peptide and the palmitoyl chain would provide deeper insight into the structure-activity relationship (SAR) between PZ-128 and PAR1. Additionally, the applications of PZ-128 as a probe molecule will also be explored, utilising fluorescent tags and a variety of assaying techniques.

The design of PZ-128 analogues will be focused on the introduction of a linker moiety between the peptide sequence and the palmitoyl chain, deviating from traditional pepducin design (**Figure 2.1A**). The nature of the linker will allow the peptide to be stapled, forming a cyclic pepducin (**Figure 2.1B**). In addition to this, a series of linear variants utilising analogous linking moieties bound to the N-terminal amino acid will also be tested (**Figure 2.1C**).

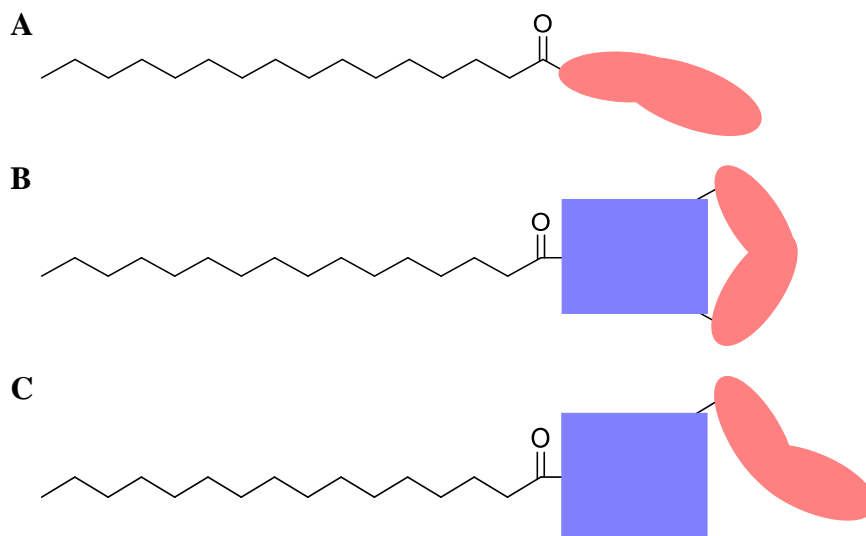


Figure 2.1: General structure for **A** typical pepducins, **B** cyclic pepducins and **C** linear analogue of cyclic pepducins. Linker moiety is shown in blue and peptide sequence shown in red (not to scale).

Initially, a pharmacological profile will be established for PZ-128 as well as a negative control to ascertain the robustness of the assays for the library of PZ-128 analogues. This will primarily be carried out in *in vitro* calcium signalling assays.

Following confirmation of PZ-128 and relevant controls, further assays will be used to assess the inhibitory properties of the PZ-128 analogues in order to identify pepducins with potentially improved IC₅₀ for PAR1 inhibition.

Finally, PZ-128 will be modified with a fluorescent tag. It is hoped this tag would provide a platform on which microscopic imaging of pepducin activity could be carried out in a cellular context.

2.3 Synthesis and Validation of PZ-128

Prior to analysing the novel pepducins, it was necessary to synthesise **2.1** to gain access to a relevant control compound for assaying. Additionally, assays would need to be performed to validate the use of **2.1** within this study and ensure comparisons between PZ-128 and the generated pepducin library used subsequently were suitable.

2.3.1 Synthesis of **2.1** and **2.2**

Two pepducins were synthesised: **2.1** and scrambled pepducin **2.2** (**Figure 2.2**). **2.1**, being a clinical trial candidate for PAR1 inhibition, would provide access to the current gold-standard for PAR1-inhibiting pepducins.² Meanwhile, **2.2** contained a peptide sequence with the same amino acids as **2.1** but in a randomised order. It was reasoned that **2.2** would be a suitable negative control which would submit cells to similar stresses as those treated with **2.1** but would ultimately lack any inhibitory functions.

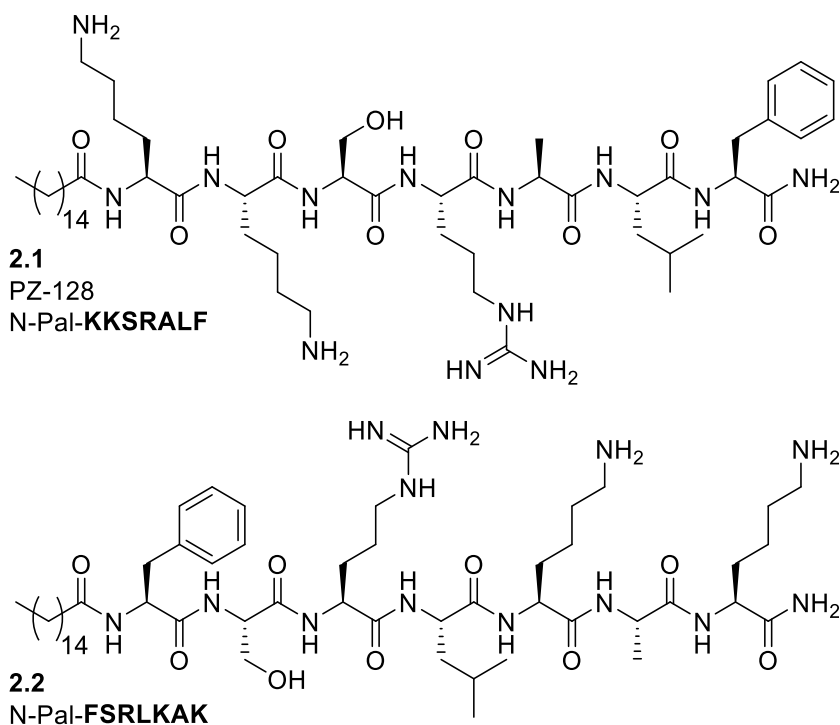
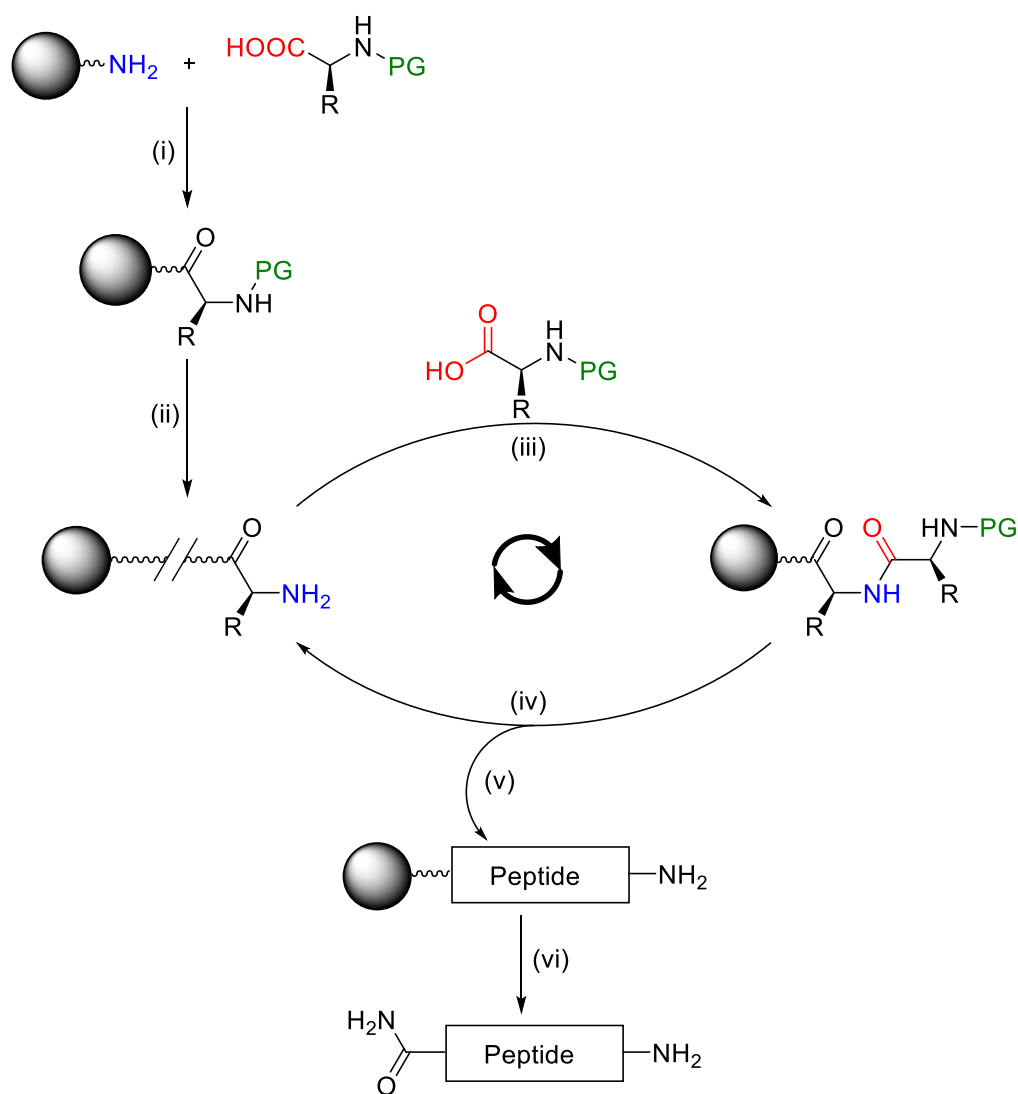


Figure 2.2: Chemical structure of control pepducins **2.1** and **2.2**

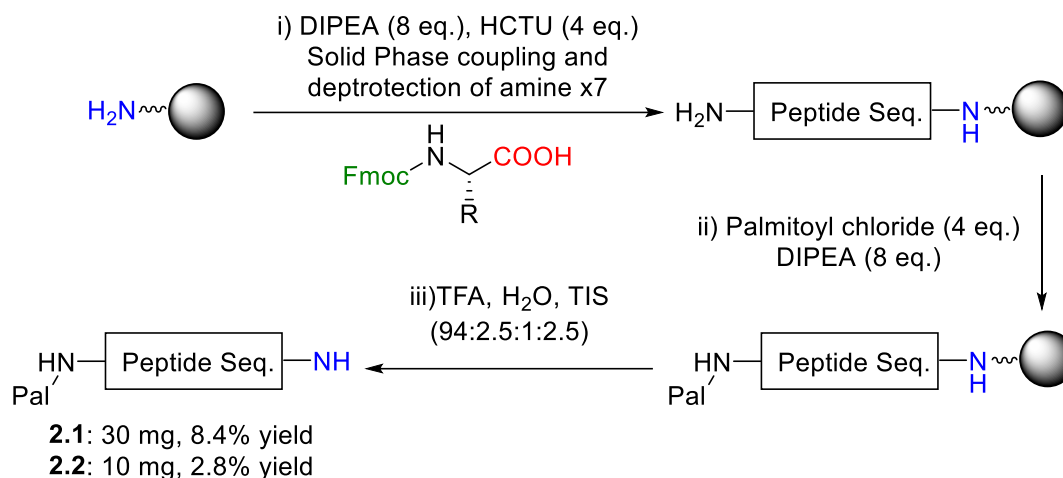
Peptide analogues **2.1** and **2.2** were synthesised using solid-phase peptide synthesis (SPPS). SPPS is a technique which allows a peptide sequence to be built upon a solid resin and lends itself well to automated preparation.¹⁴⁶ The technique involves firstly loading a protected amino acid onto the solid resin through an amide bond between the carboxylic acid of the amino acid and a free amine on the resin (**Scheme 2.1(i)**). Deprotection of the amino acid amine group provides a new amine functionality for the next coupling (**Scheme 2.1(ii)**). Typically, the protecting groups utilised for SPPS will be either *tert*-butoxycarbonyl (Boc) or fluoren-9-ylmethoxycarbonyl (Fmoc). Following deprotection, the resin-bound amino acid undergoes repeated amide couplings and deprotections with further protected amino acids to extend the peptide chain, resulting in a new free amine following each coupling and deprotection cycle (**Scheme 2.1(iii)-(iv)**). Once the peptide has been completely furnished (**Scheme 2.1(v)**), the resin can be cleaved to provide the free peptide (**Scheme 2.1(vi)**).



Scheme 2.1: General procedure for automated solid-phase peptide synthesis (SPPS). **(i)** Initial loading of C-terminal amino acid to resin. **(ii)** Deprotection of the amine on the C-terminal amino acid. **(iii)-(iv)** Amide coupling of next amino acid onto resin-bound amine terminus (iii) followed by deprotection of the new terminal amino acid (iv), repeated until desired peptide is fully furnished. **(v)-(vi)** Once fully furnished peptide has been achieved (v), the resin can be cleaved from the C-terminus, yielding the free peptide.¹⁴⁶

Peptide analogues **2.1** and **2.2** were synthesised using a modified SPPS procedure, with SPPS furnishing the respective peptide sequences as described previously (**Scheme 2.2(i)**) followed by coupling to palmitoyl chloride at the N-terminus providing the full, resin-bound pepducin (**Scheme 2.2(ii)**). Cleavage from the resin followed by purification of the

crude products by preparative HPLC provided **2.1** in 8.4% yield and **2.2** in 5.6% yield (**Scheme 2.2(iii)**).



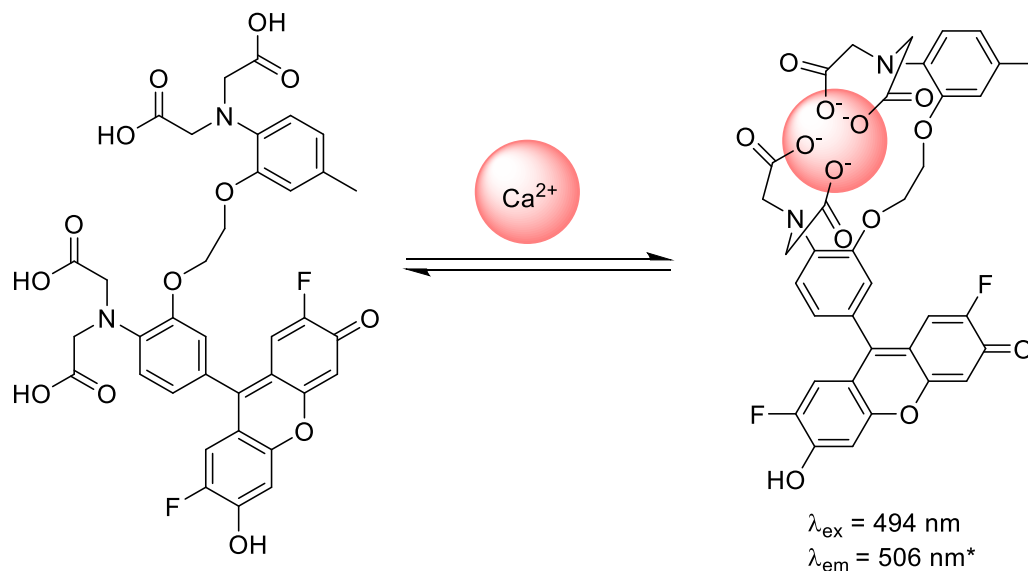
Scheme 2.2: Synthesis of **2.1** and **2.2** by solid-phase peptide synthesis

2.3.2 Pharmacology of PAR1 antagonists PZ-128 and SCH79797

The PAR1 pepducin library would primarily be tested using calcium signalling assays in HEK-293 cells, a cell line which endogenously expresses PAR1.¹⁴⁷ The release of Ca²⁺ ions from intracellular stores is a known downstream effect of PAR activation (*vide supra* **Section 1.2.3, Figure 1.20**). Prior to screening the novel PAR1 pepducins, validation of the use of **2.1** as a comparison needed to be performed. However, before testing the control pepducins, it was required to develop dose-response curves for the activation of PAR1 in HEK-293 cells for two control agonists. A short peptide sequence, TFLLR-NH₂, which is analogous to the tethered ligand itself in PAR1, was tested alongside thrombin, a serine protease that naturally cleaves the N-terminus of PAR1 to release the tethered ligand.^{93,148} Both agonists show specificity for PAR1-mediated signalling in HEK-293 cells, which lack PAR4 as a secondary thrombin target.

A Fluo-4 DirectTM calcium signalling assay kit was used for the assay, staining HEK-293 cells with Fluo-4. The Fluo-4 dye would provide a fluorescent response in the presence of increased concentrations of Ca²⁺ ions, which itself would be indicative of PAR1 signalling

cascades being activated (**Scheme 2.3**). The Fluo-4 Direct™ assay kit also allowed a robust and straightforward protocol whereby the excess dye was not required to be removed, allowing less stress for the cells prior to treatments being performed.



Scheme 2.3: Reaction of Fluo-4 with Ca^{2+} leading to a fluorescently active species. * Structure shown is Fluo-4, Fluo-4 Direct™ structure is not publicly disclosed and has $\lambda_{\text{em}} = 516 \text{ nm}$.

Both agonists at a range of concentrations were shown to induce transient increases in calcium levels within HEK-293 cells (**Figure 2.3A-B**). By plotting the maximal increase in fluorescence with concentration of the agonists, each control can be shown to induce concentration-dependent increases in calcium signalling (**Figure 2.3C-D**).

Thrombin was shown to activate calcium signalling *via* PAR1 with an EC_{50} of 1.1 U/mL (9.1 nM) whereas TFLLR-NH₂ displayed calcium signalling with an EC_{50} of 1.7 μM (**Table 2.2**). Moving forward, these values would provide the working range for agonist treatments in the inhibition assays.

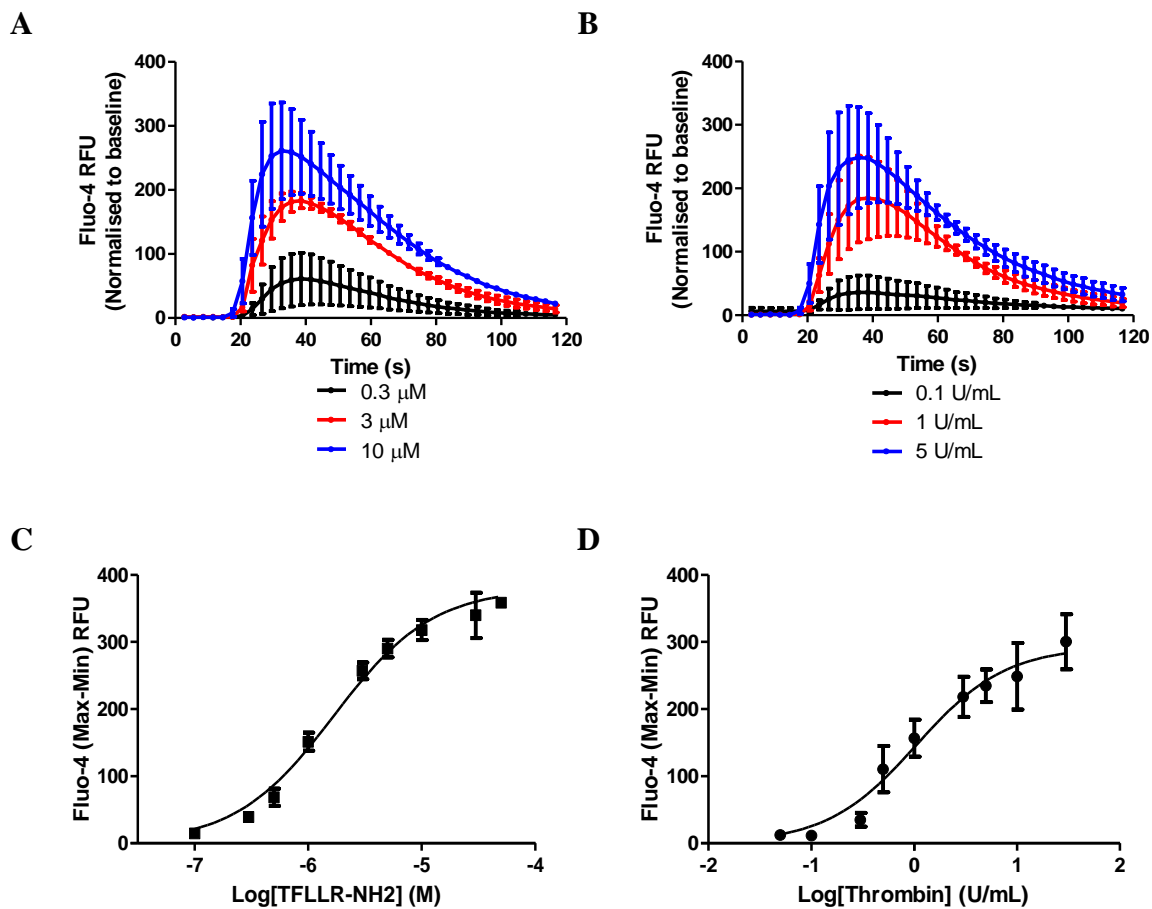


Figure 2.3: Activation of calcium signalling in HEK-293 cells stained with Fluo-4 DirectTM. **A** Change in fluorescence following activation of PAR1 with TFLLR-NH₂ (t = 17 s). **B** Change in fluorescence following treatment with thrombin (t = 17 s). **C** Concentration-response curve for activation with TFLLR-NH₂ (0.1-50 μM). **D** Concentration-response curve for activation with thrombin (0.05-30 U/mL). Data represents N=15 with mean ± SEM normalised to the basal levels of fluorescence.

Table 2.2: EC₅₀ values for activation of PAR1 in HEK-293 cells

Agonist	Log[EC ₅₀]	EC ₅₀	
TFLLR-NH ₂	-5.77 ± 0.05	1.7 μM	N = 15
Thrombin	0.02 ± 0.13	1.1 U/mL	N = 15

Following the generation of control dose-response curves for the agonists, investigations into antagonist pharmacology could be carried out. Firstly, experiments were carried out to confirm literature findings on the inhibitory function of pepducin **2.1** and the

competitive PAR1 antagonist SCH79797 (**2.3**, **Figure 2.4**).¹⁴⁹ The tricyclic compound **2.3** was chosen for inclusion in this study to provide a further comparison for the novel pepducins which inhibits PAR1 at a different site. In addition to these compounds, **2.2** was also included in the study as well as **2.4**, which was provided as a non-PAR1 targeting cyclic peptide (**Figure 2.4**).

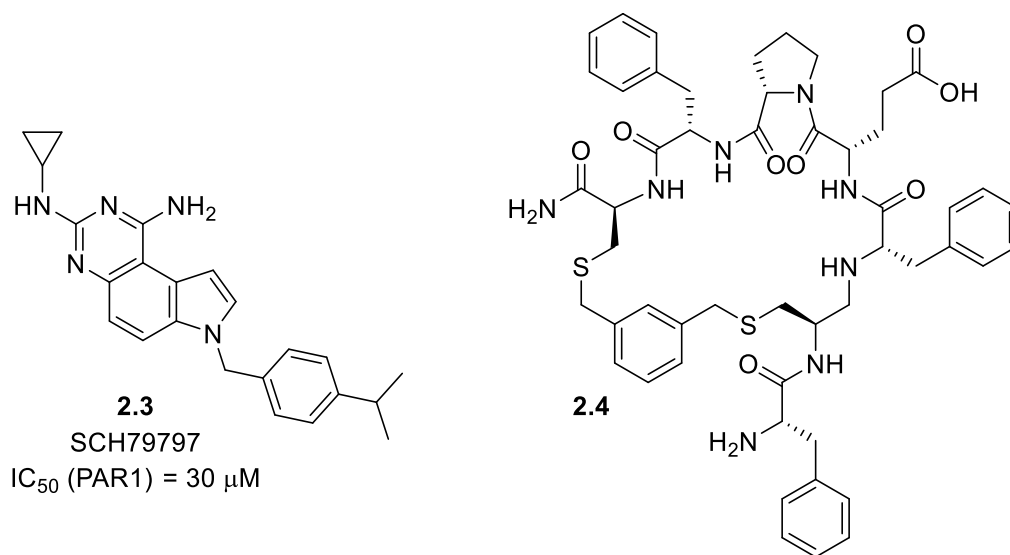


Figure 2.4: Chemical structure of competitive antagonist SCH79797 (**2.3**) and control cyclic peptide **2.4**.¹²¹

Cells were pre-treated with the compounds (1-100 μ M) prior to treatment with the PAR1 selective agonist peptide TFLLR-NH₂ (3 μ M). This concentration of agonist was chosen based on the effective range described previously (*vide supra* **Figure 2.3C**). Using the inhibition assay, both **2.1** and **2.3** were confirmed as PAR1 inhibitors, displaying concentration-dependent inhibition of TFLLR-NH₂ with IC_{50} values of 26 μ M and 5 μ M, respectively (**Figure 2.5**). This is consistent with previously reported data for the compounds.^{121,135} Additionally, **2.2** and **2.4** were proven to be ineffective inhibitors within the concentration range tested, enabling their use as negative controls throughout further assays. Moving forward, randomised pepducin **2.2** was the preferred negative control as its isomeric relationship to **2.1** would in principle allow it to function typically as a

pepducin, exposing the cells to similar stresses when under treatment with **2.1** and other pepducins.

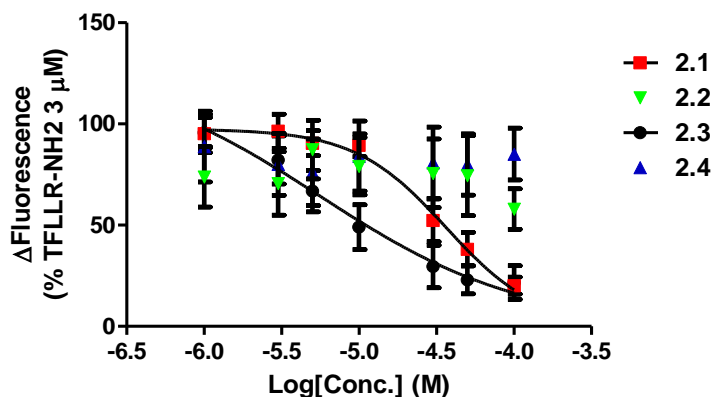


Figure 2.5: Inhibition of PAR1-mediated Ca^{2+} signalling in Fluo-4 stained HEK-293 cells using PAR1 antagonists **2.1** and **2.3**, and negative controls **2.2** and **2.4**, at concentrations of 1-100 μM . Data represents $N=10$ for **2.1** and **2.3** and $N=5$ for **2.2** and **2.4**, with mean \pm SEM of maximal calcium responses normalised to the uninhibited maximal response to 3 μM TFLLR-NH₂.

Table 2.3: IC_{50} values obtained for the inhibition of TFLLR-NH₂ mediated calcium signalling.

Compound	Log[IC_{50}]	IC_{50}	
2.1	-4.58 ± 0.10	26 μM	$N = 10$
2.2	N/D	N/D	$N = 5$
2.3	-5.30 ± 1.31	5.0 μM	$N = 10$
2.4	N/D	N/D	$N = 5$

Following the generation of inhibition curves for **2.1** and **2.3**, it was thought that producing Schild plots for their inhibition would provide insight into their interactions with PAR1 and its agonists.¹⁵⁰ By investigating the rightward-shift of a concentration-response curve of PAR1 agonist (TFLLR-NH₂) in increasing concentrations of the antagonist, it can be noted that inhibition is being achieved with **2.1** and **2.3** (**Figure 2.6A** and **C**). The EC_{50} at each concentration of inhibitor can then be used to produce a Schild plot of the data

(**Figure 2.6B** and **D**), which can then be used to inform of the relationship between the inhibitor and the agonist.

For **2.1**, the Schild plot (**Figure 2.6B**) initially follows a slope of unity, which is a Schild plot with a slope of 1.0 and typically represents competitive antagonism. However, the Schild plot of **2.1** begins to deviate from this, despite a calculated Schild slope of 0.93 ± 0.25 . This behaviour differs from competitive antagonism models and is similar in profile to other known allosteric antagonists.¹⁵¹

To further investigate the allosteric nature of **2.1**, an allosteric shift model was applied to the inhibition with **2.1** to provide a cooperativity factor, $\text{Log}(\alpha)$.¹⁵² The cooperativity factor, α , describes the relationship between two effectors of protein function which bind at different sites, with the relationship between the respective antagonists, **2.1** and **2.3**, with TFLLR-NH₂ being described in this study. With values of $\alpha > 1$ ($\text{Log}(\alpha) > 10$), a positive allosteric interaction is observed whereby the presence of an allosteric ligand within a substrate is increasing the affinity of an orthosteric ligand. Conversely, when $\alpha < 1$ ($0 < \text{Log}(\alpha) < 10$) a negative allosteric interaction is observed, with the allosteric ligand lowering the affinity of the orthosteric ligand.

With a very large and negative value for $\text{Log}(\alpha)$ (**Table 2.4**), α for **2.1** can be estimated as being close to 0. This is indicative of a negative allosteric interaction with TFLLR-NH₂, providing confirmation of the pepducin decreasing the agonistic properties of TFLLR-NH₂ in the orthosteric binding site.

Conversely, with **2.3** (**Figure 2.6C** and **D**) the Schild plot produced matches the expectations of a competitive antagonist. A straight line with Schild slope of 1.0 would be expected from a competitive antagonist and **2.3** provided a gradient of 1.1 ± 0.19 with each data point closely conforming to this line, confirming the literature findings of its competitive antagonism.¹²¹

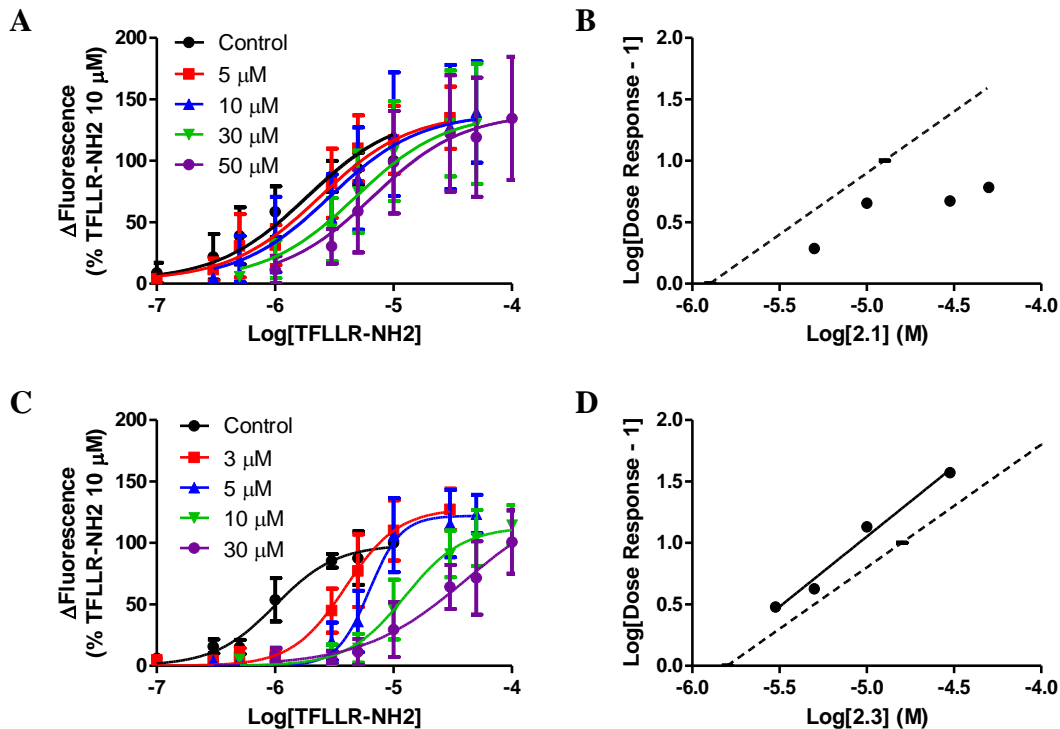


Figure 2.6: Schild analysis of **2.1** and **2.3**. **A/C** Series of concentration-response curves for TFLLR-NH₂-mediated activation of calcium signalling in the presence of increasing concentrations of **2.1** (**A**) and **2.3** (**C**), normalised to the maximal response obtained with 10 μ M TFLLR-NH₂. **B/D** Schild plots for the inhibition of TFLLR-NH₂-mediated calcium signalling using **2.1** (**B**) and **2.3** (**D**), comparing the generated plots alongside a line of unity with slope = 1.00. Data represents N=5 for SCH79797 and N=10 for PZ-128, with mean \pm SEM.

Table 2.4: Schild Data obtained for PZ-128 and SCH79797 in HEK-293 cells treated with TFLLR-NH₂

Antagonist	pA ₂	Schild Slope	Cooperativity (Log(α))	
2.1	4.8 \pm 0.2	0.93 \pm 0.25	-2.1 \times 10 ⁸	N = 10
2.3	5.9 \pm 0.2	1.1 \pm 0.2	N/D	N = 5

In addition to inhibiting TFLLR-NH₂, attempts were made to produce a Schild plot for inhibition of thrombin using **2.1**. While the EC₅₀ under increasing doses of **2.1** shifted to

the right, the values were not significantly different from each other, including the uninhibited EC_{50} . The difficulty with inhibition of thrombin-mediated activation of PAR1 was likely due to the increase in the effective concentration of the liberated tethered ligand on PARs. The localisation of the ligand while bound on the extracellular surface of the protein allows much easier access to the orthosteric binding site than with the analogous ligand sequence, TFLLR-NH₂, in solution within the assay. The barrier for inhibition was therefore much harder to overcome, resulting in less efficient inhibition of protein activation. As such, future inhibition experiments would be carried out using TFLLR-NH₂ as the agonist.

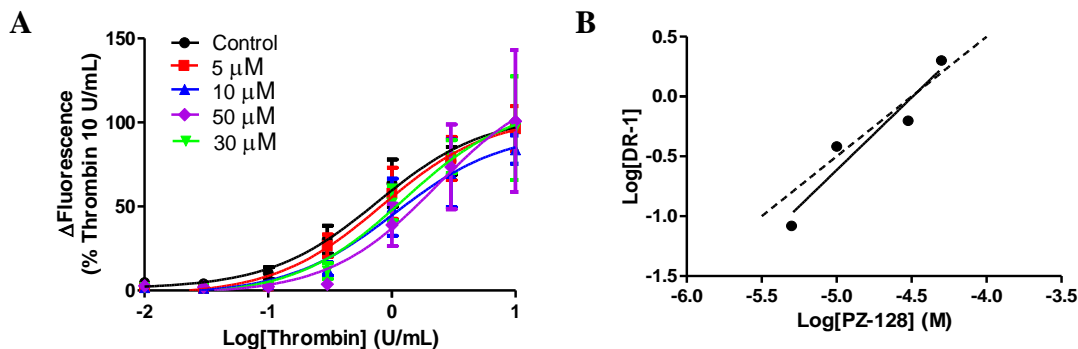


Figure 2.7 Schild analysis of **2.1** inhibiting thrombin-mediated calcium release in Fluo-4 stained HEK-293 cells. **A** Series of concentration-response curves for thrombin-mediated activation of calcium signalling in the presence of increasing concentrations of **2.1**, normalised to the maximal response obtained with 10 U/mL thrombin. **B** Schild plot for inhibition of thrombin with **2.1**, comparing the generated plots alongside a line of unity with slope = 1.00. Data represents an N=3 with mean \pm SEM.

Table 2.5: EC_{50} values generated from Schild study of **2.1** inhibition of thrombin.

[2.1]	Log[EC_{50}] \pm SEM	Thrombin EC_{50}
No Inhibition	-0.12 ± 0.14	0.76 U/mL
5 μ M	-0.08 ± 0.18	0.83 U/mL
10 μ M	0.02 ± 0.23	1.1 U/mL
30 μ M	0.10 ± 0.24	1.2 U/mL
50 μ M	0.36 ± 0.37	2.3 U/mL

2.4 Aberrant Activity of PZ-128

With initial validation experiments performed, the use of **2.2** was confirmed to be suitable for a negative control in the inhibition assays to screen novel PAR1 pepducins. However, anomalous data was obtained from the use of **2.1** during the validation studies, requiring the pharmacology of the pepducin to be further interrogated.

2.4.1 Off-target activity of PZ-128

While its activity as an inhibitor of PAR1 activation was confirmed, pepducin **2.1** was also shown to activate Ca²⁺ signalling in HEK-293 cells (**Figure 2.8**). By monitoring the fluorescence of Fluo-4 stained cells during the pre-treatment for the previous inhibition assays, it was noted that **2.1** was causing concentration-dependent calcium signals in the cells with an EC₅₀ of 27 µM (**Figure 2.8A**, **Table 2.6**). By contrast, randomised pepducin **2.2** showed no such activation of PAR1 allowing the assumption to be made that pepducin-mediated activation of the signalling cascade was sequence-dependent (**Figure 2.8A**).

It was also observed that the activation profile for the calcium signalling event with **2.1** (**Figure 2.8B**) significantly deviated from the transient responses observed following treatment with TFLLR-NH₂ (**Figure 2.8B**) or thrombin (*vide supra* **Figure 2.3C**). The difference in activation profile could indicate activation *via* a different pathway following treatment with **2.1**.

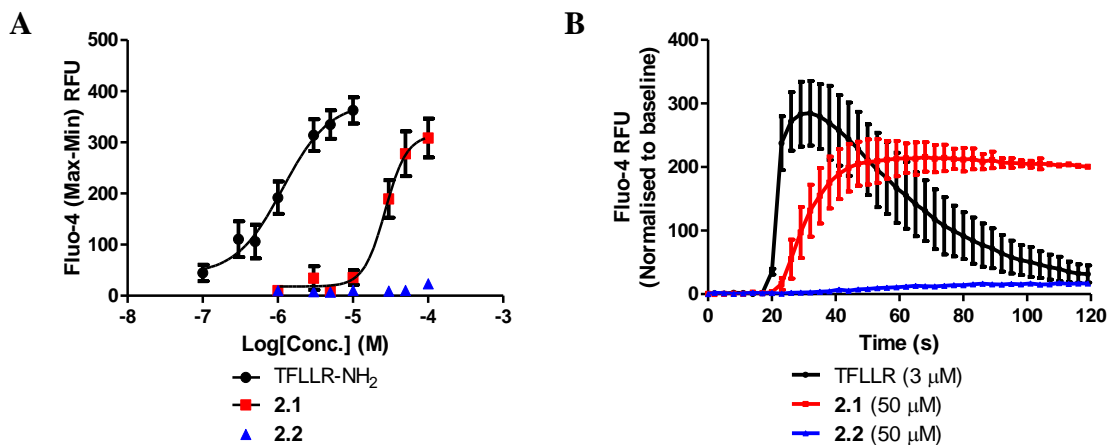


Figure 2.8: Identification of aberrant Ca²⁺ signalling in HEK-293 cells following treatment with **2.1**. **A** Concentration-response curve for activation of Ca²⁺ signalling using TFLLR-NH₂ (0.1-10 μM), **2.1** (1-100 μM) and **2.2** (1-100 μM). **B** Average time courses for activation of Ca²⁺ signalling comparing the activation profile of **2.1** to TFLLR-NH₂ and **2.2**. Addition of compounds carried out at t = 17 s. Data represents an N=9 with mean ± SEM.

Table 2.6: EC₅₀ values obtained for the activation of calcium signalling in HEK-293 cells by **2.1** and **2.2**.

Compound	Log[EC ₅₀]	EC ₅₀	
TFLLR-NH ₂	-5.9 ± 0.1	1.2 μM	N = 9
2.1	-4.6 ± 0.1	27 μM	N = 9
2.2	N/A	N/A	N = 9

Initially, the difference in fluorescent responses to **2.1** in comparison to the PAR1 agonists was thought to arise from a difference in the calcium source, with **2.1** potentially causing an influx of calcium from the Fluo-4 buffer rather than efflux from intracellular stores. To test this hypothesis, assays were run using a modified buffer which contained no calcium ions through the removal of calcium chloride (**Figure 2.9A-B**). However, each agonist continued to display concentration-dependent increases in calcium signalling, with thrombin, TFLLR-NH₂ and **2.1** yielding EC₅₀ values of 0.39 U/mL, 7.2 μM and 32 μM, respectively (**Table 2.7**). These results indicate the source of the calcium must be the intracellular calcium stores.

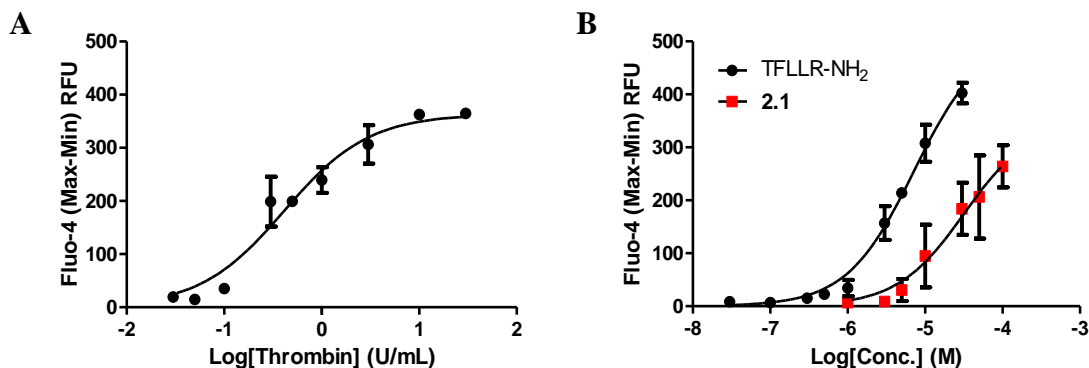


Figure 2.9: Activation of calcium signalling in HEK-293 cells loaded with Fluo-4 Direct Dye in a buffer with $[Ca^{2+}] = 0$ mM. Cells were quiesced as normal and the assay carried out in an environment with no extracellular calcium ions. **A** Concentration-response curve for thrombin addition (0.03-30 U/mL). **B** Concentration-response curve for TFLLR-NH₂ addition (0.05-50 μ M) and **2.1** addition (1-100 μ M). Data represents an N=3 with mean \pm SEM of the maximal fluorescent signals minus the minimal signal.

Table 2.7: EC₅₀ data for activation of calcium signalling in the presence of 0 mM extracellular calcium.

Compound	Log[EC ₅₀]	[EC ₅₀]	
Thrombin	-0.41 \pm 0.11	0.39 U/mL	N = 3
TFLLR-NH ₂	-5.1 \pm 0.1	7.2 μ M	N = 3
2.1	-4.5 \pm 0.3	32 μ M	N = 3

After confirming the source of the calcium released following treatment with **2.1**, other aspects of the PAR1 signalling cascade were considered. Primarily, the mitogen-activated protein kinase (MAPK) pathway was targeted (*vide supra* **Figure 1.20**). A common marker used in the study of cancer, MAPK, originally called extracellular signal-regulated kinases (ERK), contributes to the regulation of cell adhesion, migration and survival as well as cell cycle progression, differentiation, metabolism, proliferation and transcription.¹⁵³ Activation of PAR1 is known to induce ERK activation *via* phosphorylation and, as such, changes in levels of ERK1 and ERK2 can be monitored by utilising Western Blotting (*vide supra* **Figure 1.20**).⁹⁴ However, before probing ERK

signalling with pepducin **2.1**, control experiments were carried out using thrombin and TFLLR-NH₂ (**Figure 2.10**).

HEK-293 cells were treated with the agonists at increasing concentrations over a period of 5 mins. The cells were then lysed, and their contents processed by gel electrophoresis, allowing quantification of ERK1 and ERK2 in comparison to a control (untreated cells). Using Western Blotting, it can be noted that thrombin and TFLLR-NH₂ induce concentration-dependent increases in activated, or phosphorylated, ERK1 and ERK2 (pERK) (**Figure 2.10**). These levels can then be normalised to the total ERK levels, containing both activated and unactivated ERK (TotERK).

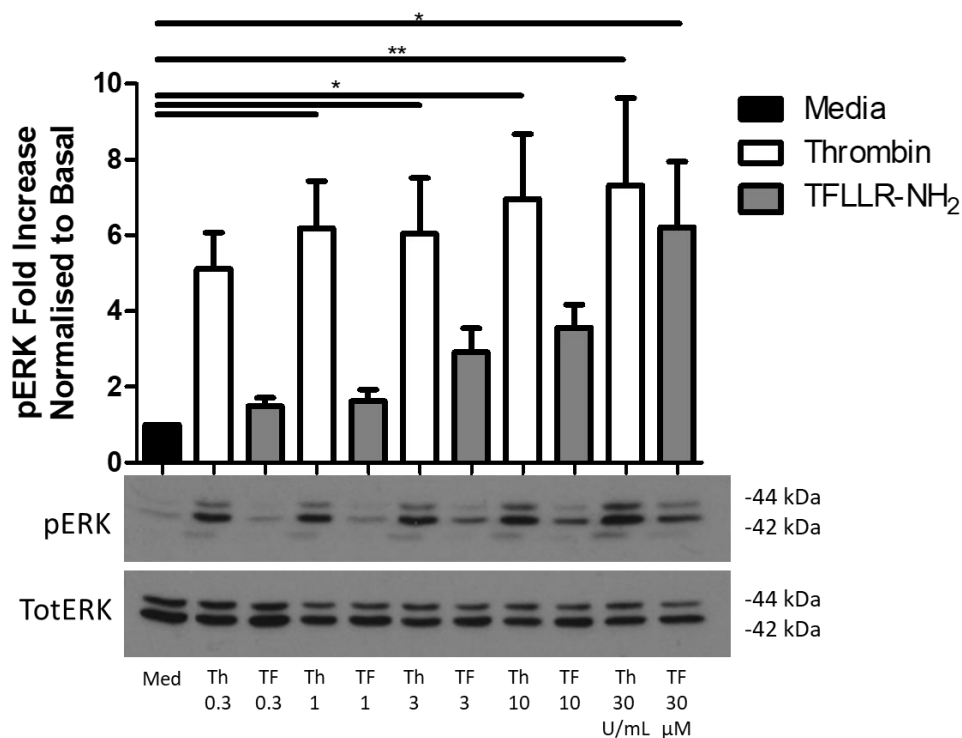


Figure 2.10: Activation of ERK1/2 in response to thrombin and TFLLR-NH₂. Thrombin was used at concentrations of 0.3, 1, 3, 10 and 30 U/mL and TFLLR-NH₂ was applied at concentrations of 0.3, 1, 3, 10 and 30 μM. Treatments were carried out for 5 minutes. Data represents an N=4 with mean ± SEM, with individual timepoints being expressed as fold increase over the basal levels of pERK (media treated sample).

Following initial validation using a time-independent treatment, cells were then exposed to thrombin over a range of time points at the same concentration (**Figure 2.11**). This was carried out primarily to identify incubation times which would result in strong pERK signals, as well as ascertaining the behaviour associated with activation of PAR1 signalling cascades under thrombin or TFLLR-NH₂, prior to treatment with **2.1**. Treatment with thrombin and TFLLR-NH₂ both demonstrated a maximum in the pERK levels 2 minutes after exposure to agonist, before falling to near basal levels after 15-30 minutes.

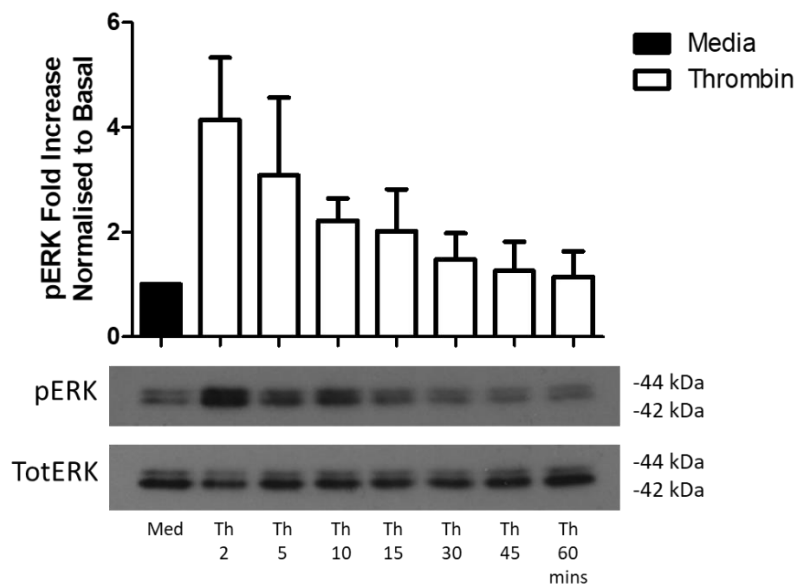


Figure 2.11 Activation of ERK1/2 in response to thrombin. Thrombin at a concentration of 3 U/mL was applied for a range of time points (2-60 minutes), including an untreated sample as a negative control. Data represents an N=3 with mean \pm SEM, with individual timepoints being expressed as fold increase over the basal levels of pERK (media treated sample).

After performing control experiments with PAR1 agonists, HEK-293 cells were then treated using **2.1** and **2.2**. Initially, these experiments were performed using 30 μ M concentrations with a range of time points from 5 mins to 1 hour (**Figure 2.12**). Here, the opposite trend to PAR1-agonist function (**Figure 2.10**, **Figure 2.11**) can be observed, with ERK activation occurring slowly following exposure to agonist, rising to a peak with the 60-minute treatment.

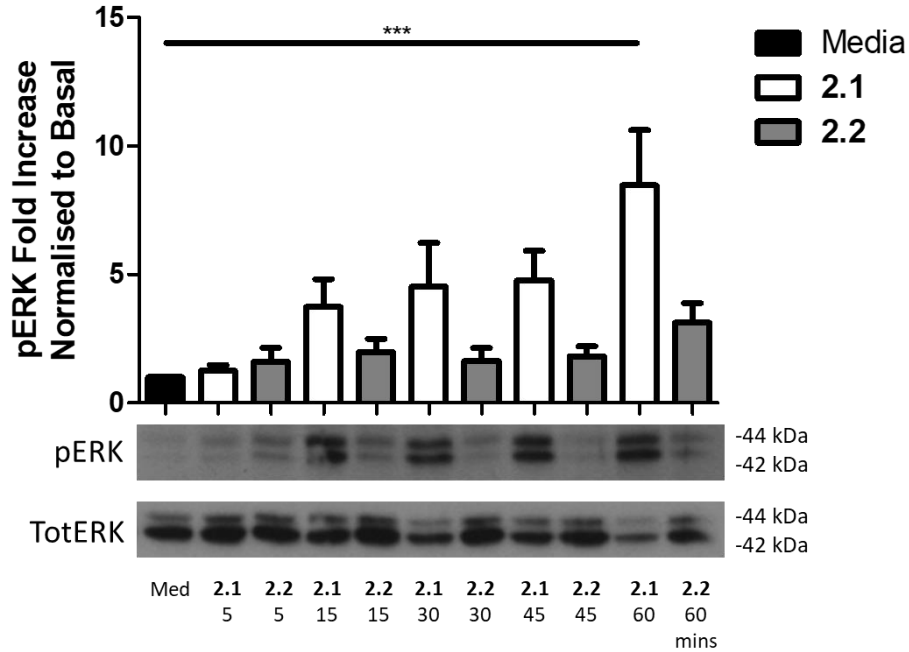


Figure 2.12 Activation of ERK1/2 in response to pepducins **2.1** and **2.2**. Pepducins were applied at 30 μ M and the cells incubated for the noted times prior to lysis. Data represents an N=3 with mean \pm SEM, with individual timepoints being expressed as fold increase over the basal levels of pERK (media treated sample).

The incubation periods were then extended to 24 hours, in order to determine if the peak for ERK activation following treatment with **2.1** occurs after the 60-minute time point (**Figure 2.13**). In this case, the levels of pERK are shown to peak after 5 hours of treatment, before decreasing towards basal levels after 24 hours. Like the calcium signalling kinetics (*vide supra* **Figure 2.8**), the pERK levels with time highlight another differentiation in the function of **2.1** from thrombin and TFLLR-NH₂. Additionally, randomised pepducin **2.2** failed to significantly activate ERK signalling with prolonged exposure over 5 hours. With this result, **2.2** would continue to be utilised as a negative control.

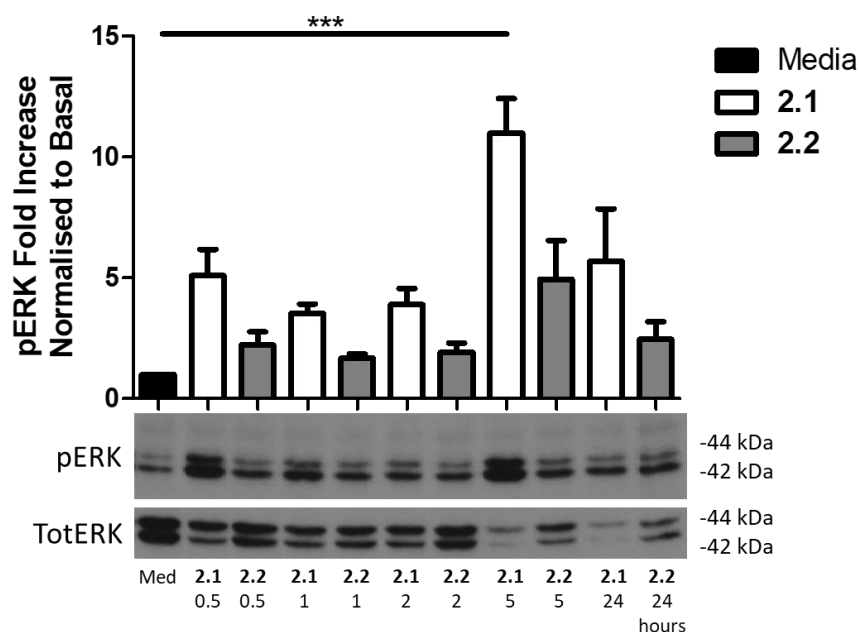


Figure 2.13 Chronic activation of ERK1/2 in response to pepducins **2.1** and **2.2**. Pepducins were applied at 30 μ M and the cells incubated for the noted times prior to lysis. Data represents an N=5 with mean \pm SEM, with individual timepoints being expressed as fold increase over the basal levels of pERK (media treated sample).

With the treatment of HEK-293 cells with **2.1** leading to activation of calcium signalling and ERK activation, concerns were made with regards to the validity of **2.1** as an inhibitor on which to base further analogues. Before testing the novel pepducins in the PAR1 assays, it was decided to further elucidate the means by which **2.1** was facilitating these undesired physiological consequences and the consequences of **2.1**-mediated activation.

2.4.2 Kinetics of PZ-128-mediated activity

Differences in the activation profile between **2.1** and other PAR1 agonists have been demonstrated, with a **2.1**-mediated calcium signal remaining elevated after the two minutes of scanning was finished (*vide supra*, **Figure 2.8B**). Further, **2.1** also caused a more prolonged ERK1/2 response than thrombin (*vide supra*, **Figure 2.12**, **Figure 2.13**).

With these differences being shown, extended time courses were taken for the activation of calcium signalling in HEK-293 cells with thrombin, TFLLR, **2.1** and **2.2** in order to further investigate the differences in the kinetics of the calcium events (**Figure 2.14**).

With readings taken over 30 minutes, thrombin and TFLLR-NH₂ once again are shown to cause relatively fast, transient responses with fluorescent levels falling back to baseline within two minutes (**Figure 2.14A-B**). However, maximal concentrations of thrombin did result in a second wave of calcium release. This effect could have been caused by the recruitment of PAR1 from within the cell to the extracellular surface following the initial activation event.

On the other hand, **2.1** causes a much more prolonged increase in the Fluo-4 signal in comparison to thrombin/TFLLR-NH₂. Following an initial, slower increase in fluorescence, the response falls off very slowly over the 30 minute period, with the signal finally falling to baseline after 20 mins (**Figure 2.14C**). Curiously, the signal remains elevated for longer during extended treatment with **2.1** at 30 µM in comparison to the treatment with 100 µM. This could indicate that the function of **2.1** is solely dependent on concentration of **2.1** and does not rely on expression of GPCRs at the extracellular surface.

Finally, **2.2** continues to display low activation of calcium signalling events, once again confirming the sequence-dependent nature of the pepducin-mediated calcium signalling events (**Figure 2.14D**).

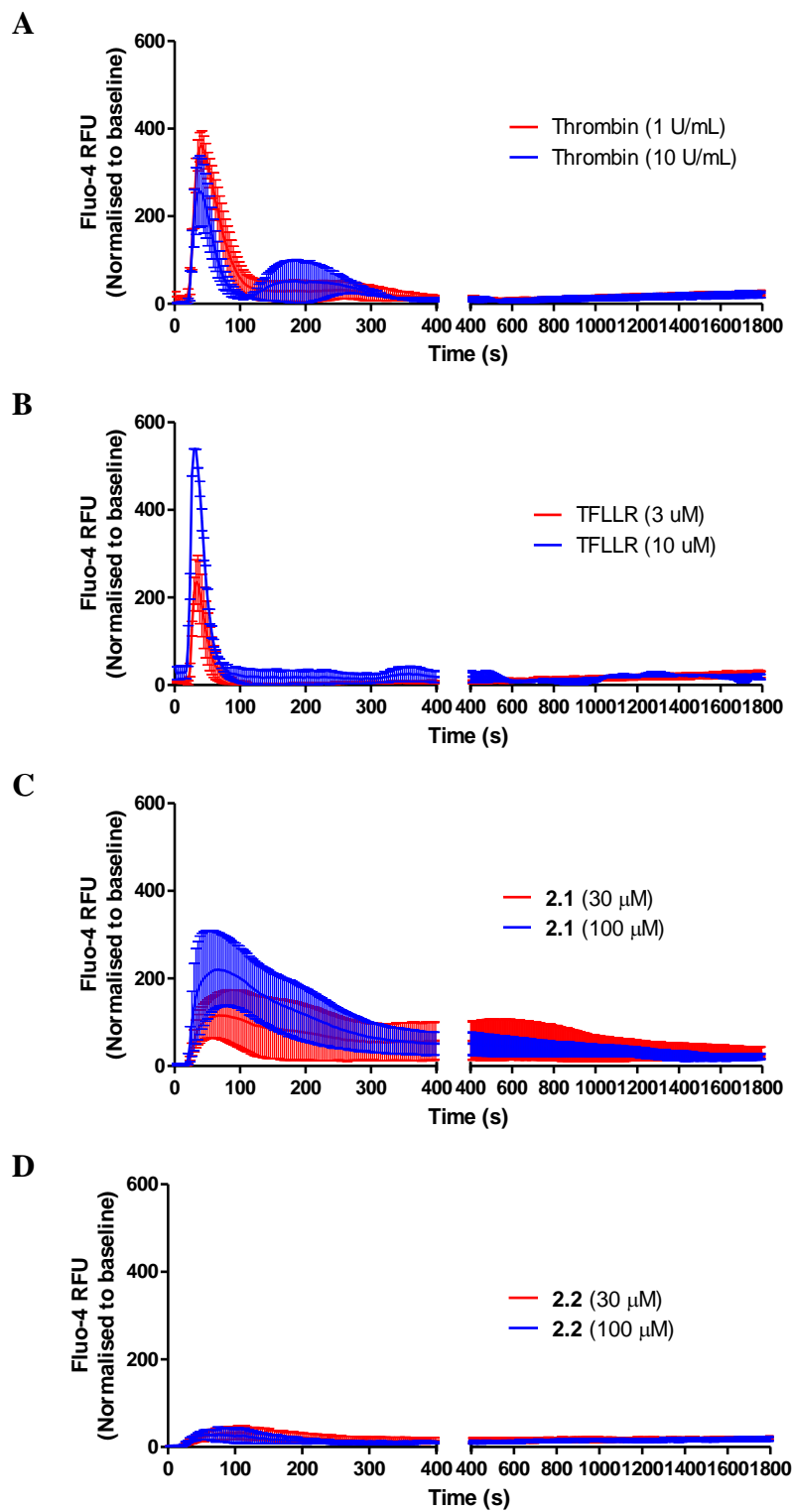


Figure 2.14 Representative extended time courses for the activation of calcium signalling in HEK-293 cells with thrombin, TFLLR-NH₂, 2.1 and 2.2. Readings were taken every 3 seconds over a period of 1800 seconds with addition of the compounds occurs at t = 17s.

Calcium signalling experiments carried out thus far were performed in static systems, where the individual test samples were added into a plate and remained there for the duration of each assay. This could have been the cause for aberrant activity from thrombin witnessed during the prolonged exposure studies. As such, a mobile system was required to ensure the activation was occurring at the point of impact and cells were allowed to recover in the absence of stimuli. To compare the effects of **2.1** within a mobile system, an experimental dual-LED microscope system was proposed to be used to undergo ratiometric analysis of Fura-2 AM, another fluorescent Ca^{2+} dye, in HEK-293 cells whilst perfusing on and off the pepducin analogues.¹⁵⁴ Unlike Fluo-4, where only the Ca^{2+} -bound dye is fluorescent, Fura-2 displays a fluorescent signal in its bound ($\lambda_{\text{em}} = 340 \text{ nm}$) and unbound ($\lambda_{\text{em}} = 380 \text{ nm}$) state, with the final signal often reported as the ratio of the bound to unbound signals.

As a means of validating the assay, cells stained with Fura-2 were firstly treated within 96-well plates and monitored using a fluorimeter (**Figure 2.15**). For this purpose, cells seeded into half of the 96-well plate were stained with Fura-2 AM and the other half of the plate with Fluo-4 as an internal comparison. Then, in duplicate, cells with each dye were treated with thrombin, **2.1** and **2.2** to gain direct, within-plate comparisons between the two dyes. By comparing the data generated from each dye, it can be noted that the calcium responses in Fura-2 AM stained cells (**Figure 2.15A-B**) were similar to those generated in the Fluo-4 Direct stained cells (**Figure 2.15C-D**).

Additionally, the EC_{50} value for thrombin with Fura-2 AM staining remained relatively consistent (**Figure 2.15A, Table 2.8**), falling slightly from the value generated previously of 1.1 U/mL (*vide supra*, **Section 2.3.2, Figure 2.3**) to 0.65 U/mL. However, the calcium response to thrombin in Fluo-4 stained cells provided a much lower EC_{50} of 0.12 U/mL, suggesting the cells used in the assay were particularly sensitive to thrombin-mediated signalling (**Figure 2.15C, Table 2.8**). Similarly, the EC_{50} values for **2.1** were comparable between the two systems, with 67 μM in Fluo-4-stained cells and 46 μM with Fura-2 (**Table 2.8**). While these values differ from the observed EC_{50} in previous experiments (*vide supra* **Table 2.6**), the lack of complete concentration-response curves suggests some

caution needs to be applied in interpreting the data especially considering the elevated responses to **2.1** at 100 μ M exceed the maximal response to thrombin (**Figure 2.15B** and **D**).

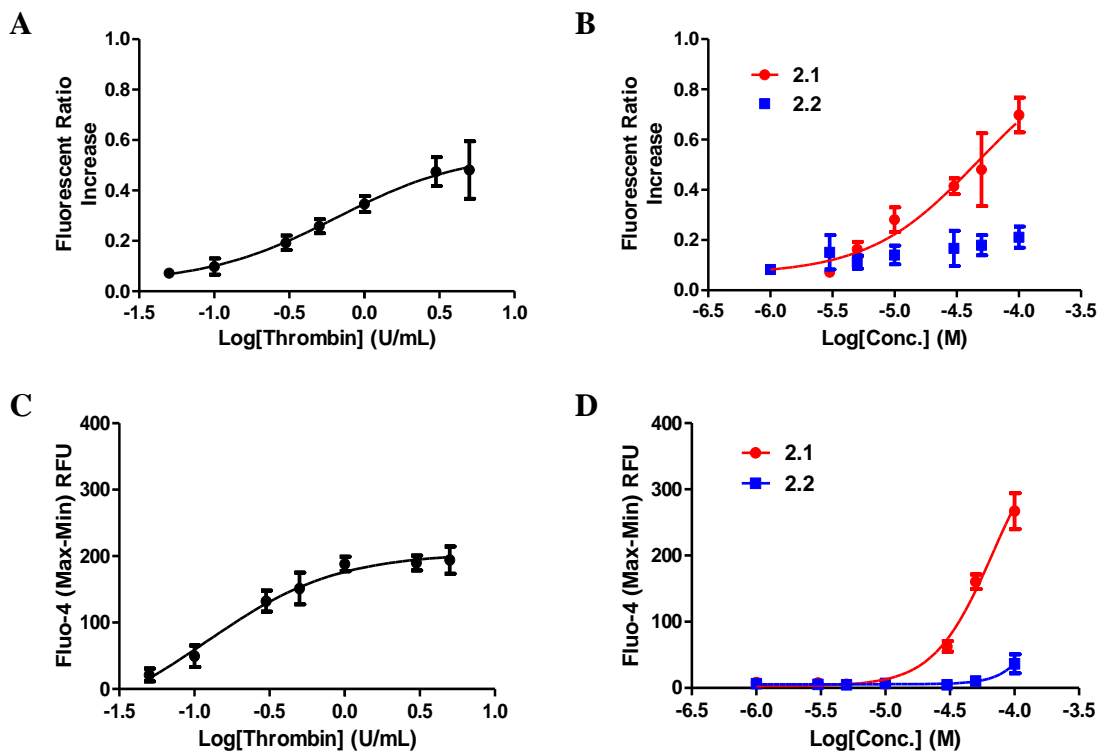


Figure 2.15: Activation of calcium signalling in HEK-293 cells loaded with Fura-2 AM. Cells were treated with concentration gradients of thrombin, **2.1** and **2.2** and fluorescence readings taken at $\lambda_{ex} = 240$ and 380 nm and $\lambda_{em} = 510$ nm. Data represents an N=4 with mean \pm SEM of the maximal fluorescent signal following treatment ($t = 17$ s).

Table 2.8: EC₅₀ values for thrombin, **2.1** and **2.2** addition to HEK-293 cells loaded with either Fluo-4 Direct or Fura-2 AM calcium dyes. Data for Fluo-4 relates to the N = 4 carried out alongside the N=4 for Fura-2, excluding other N's generated in previous experiments.

Agonist	Fluo-4		Fura-2	
	Log[EC ₅₀]	EC ₅₀	Log[EC ₅₀]	EC ₅₀
Thrombin	-0.92 \pm 0.22	0.12 U/mL	-0.19 \pm 0.24	0.65 U/mL
2.1	-4.2 \pm 0.02	67 μ M	-4.3 \pm 0.3	46 μ M
2.2	N/A	N/A	N/A	N/A

With the validation of the use of Fura-2 obtained, the cells could then be set up under a dual-LED microscope for imaging. The setup of the system would allow a coverslip containing HEK-293 cells to be placed in buffer solution under a dipping microscope whilst solutions consisting of only buffer as well as containing thrombin/**2.1**/**2.2** are slowly perfused over the specimen (**Figure 2.16**).

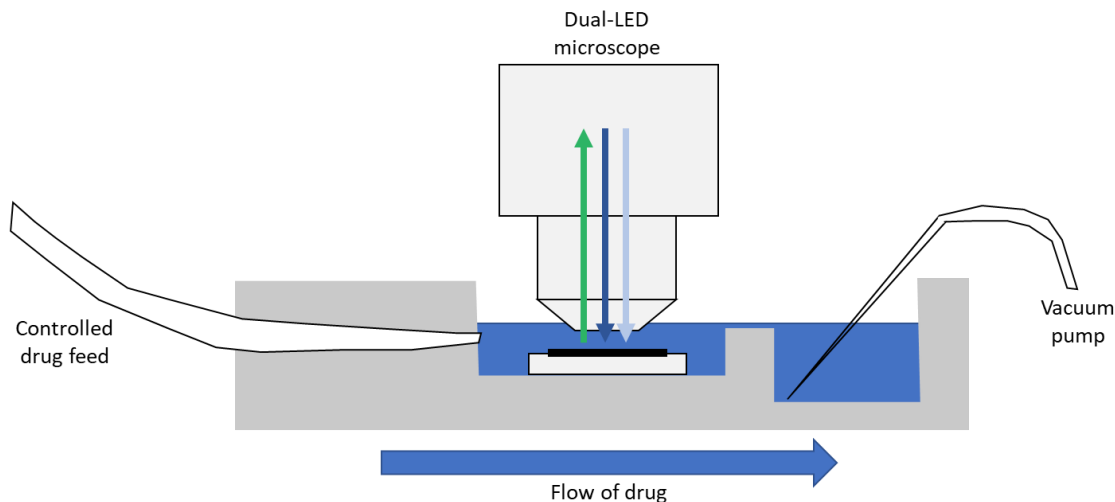


Figure 2.16: Experimental setup for perfusion of drugs over HEK-293 cells whilst monitoring with Dual-LED microscope.¹⁵⁴

Thrombin was first used to confirm PAR1-mediated calcium responses could be visualised using the mobile system, prior to carrying out treatments with **2.1** or **2.2**. Using this method, **2.1** displayed a 7.5-fold increase in fluorescent ratio (0.160 M increase in $[Ca^{2+}]$) and **2.2** caused a 0.44-fold increase (78.9 nM) (**Figure 2.17A-B**). Thrombin caused a ~2.1-fold increase, relating to an increase in $[Ca^{2+}]$ of 281 nM. The representative time courses highlight the difference in kinetics between thrombin and **2.1** once again, with thrombin causing transient responses as in the static, 96-well plate system and **2.1** causing a prolonged response despite perfusing the drug over the cells (**Figure 2.17C-D**).

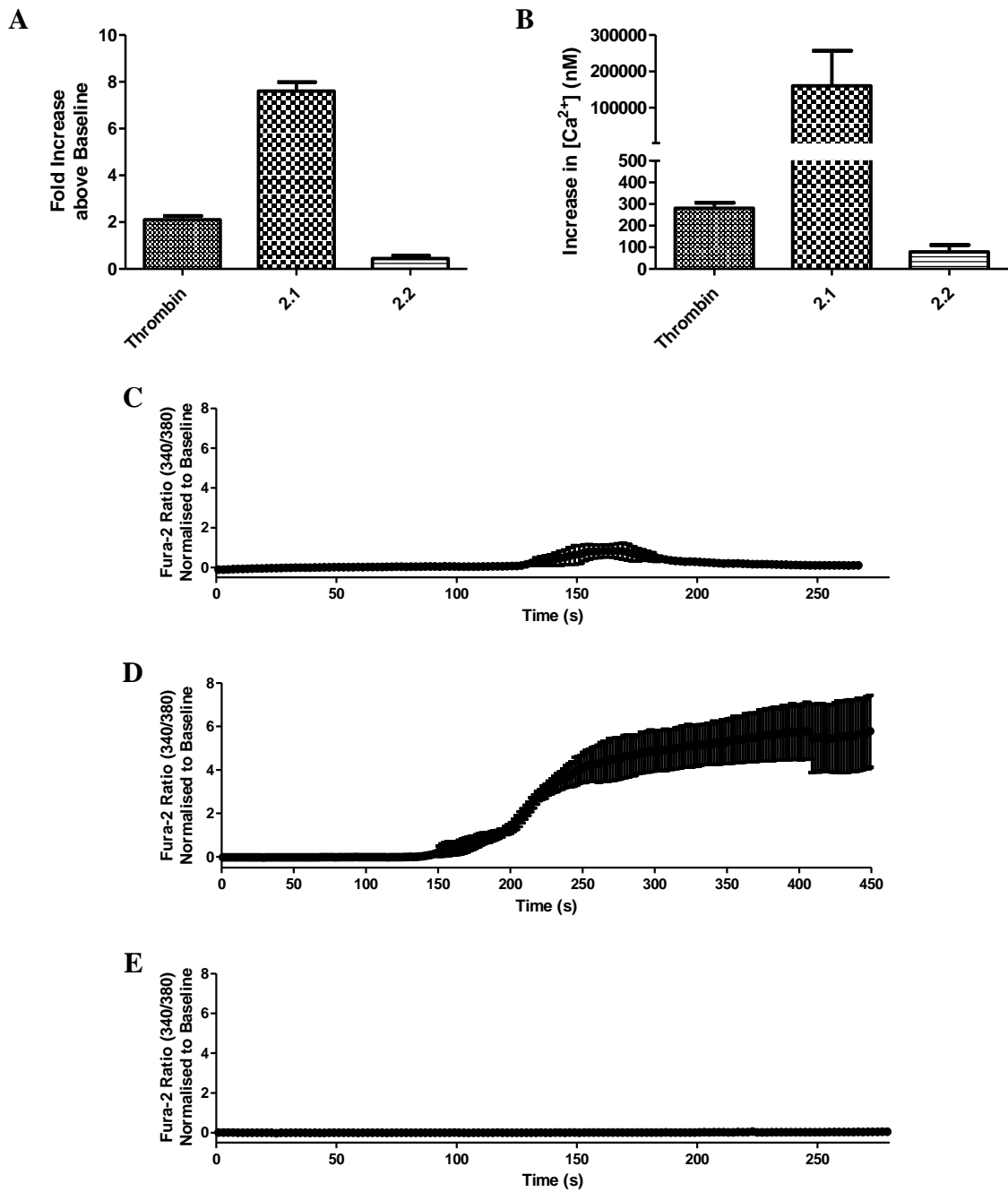
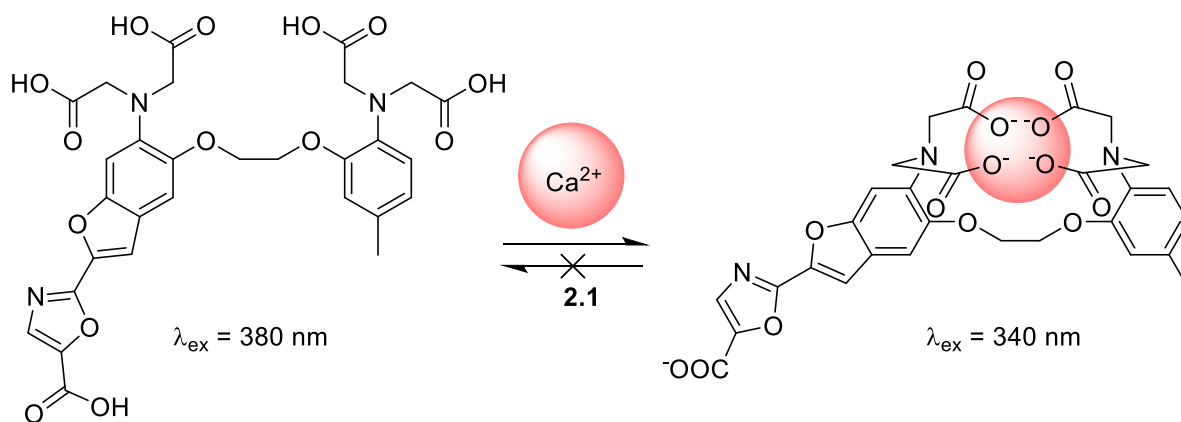


Figure 2.17 Activation of calcium signalling in HEK-293 cells loaded with Fura-2 AM. Agonists added *via* perfusion at 3-3.5 mL/min and fluorescent responses tracked at 340 nm (Ca^{2+} bound) excitation and 380 nm (Ca^{2+} unbound) excitation. **A** The maximum response for each agonist expressed as the fold increase over the basal signal (mean \pm SEM). **B** Increase in calcium concentration within cells upon perfusion of agonists (mean \pm SEM). **C-E** Average traces showing the ratio of Ca^{2+} bound dye (340 nm) to Ca^{2+} unbound (380 nm) emissions of Fura-2 with time following addition of thrombin (**C**, 1 U/mL), **2.1** (**D**, 30 μ M) and **2.2** (**E**, 30 μ M). Data represents a total of 143 regions for thrombin, 193 regions for **2.1** and 200 regions for **2.2** over three individual experiments (N = 3).

While the calcium responses to **2.1** within the mobile system closely resembled the profiles observed under treatment in the previously used static system, one aspect of the activity shown by **2.1** within the Fura-2 AM system was particularly interesting (**Figure 2.18**). By comparing the traces for fluorescent signals, similarities for both thrombin and **2.2** are highlighted. Thrombin in Fluo-4 cells causes an initial rise in fluorescence before rapidly returning to basal levels. Meanwhile, in Fura-2 AM cells, thrombin treatment provides an increase in the calcium bound Fura-2 form and a decrease in the non-calcium bound form, resulting in a transient increase in the ratio of $[Ca^{2+} \text{ bound}]$ to $[non-Ca^{2+} \text{ bound}]$ Fura-2. Further to this, **2.2** leads to no changes in either cells fluorescent outputs. However, **2.1** causes an anomaly in the Fura-2 AM response. While the signal for the calcium bound Fura-2 form rises and slowly falls, matching the Fluo-4 response, the signal for the non-calcium bound form initially falls but does not recover. Given the method by which the ratio is calculated ($Ratio = [Ca^{2+} \text{ bound}]/[Ca^{2+} \text{ unbound}]$), this would translate to an abnormally high ratio as $[Ca^{2+} \text{ unbound}]$ tends towards 0. This is observed in the extremely high increases the ratio over the basal levels (**Figure 2.17A**) and in the calculated $[Ca^{2+}]$ levels (**Figure 2.17B**).¹⁵⁴

This could be indicating the presence of **2.1** within the cells was preventing the return of Fura-2 to the non-calcium bound form (**Scheme 2.4**). However, while treatment with **2.1** was leading to aberrant responses in the fluorescent signal, treatment with **2.2** did not show the same effect. This suggests the impact on the 380 nm signal from Fura-2 is a result of **2.1**-mediated signalling and not binding with the pepducin, as **2.2** was prepared in the same way as **2.1** and shares an isomeric structure and peptide sequence. It should be noted that this quirk of Fura-2 responses has not been documented previously, thus explanations can only be hypothesised.



Scheme 2.4: Formation of Ca^{2+} -Fura-2 complex, with reverse reaction prevented following treatment with **2.1**.

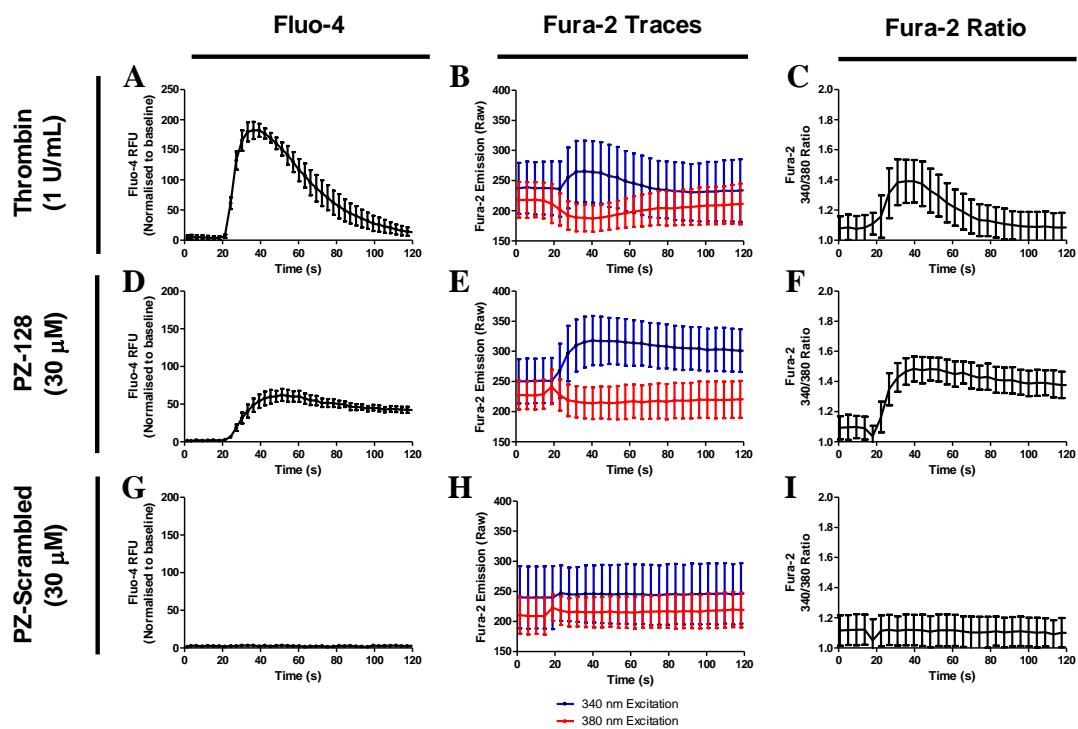


Figure 2.18: Average time courses for the activation of calcium signalling in HEK-293 cells loaded with Fluo-4 Direct or Fura-2 dye. **A-C** Treatment of cells loaded with Fluo-4 (**A**) or Fura-2 (**B-C**) were treated with thrombin (1 U/mL) and the resulting fluorescent change over time obtained. **D-F** Treatment with **2.1** (30 μM). **G-I** Treatment with **2.2** (30 μM). Graphs **B**, **E** and **H** show the change in fluorescence of Fura-2 at two wavelengths: 340 nm and 380 nm. Graphs **C**, **F** and **I** show the change in the ratio of fluorescence signals from Fura-2 (340 nm/380 nm) over time. Data represents $N = 4$ with mean \pm SEM.

2.4.3 PAR1-Independence of PZ-128-mediated activity

With the difference in kinetics of the **2.1**-mediated activity demonstrated, it was thought **2.1** may be acting in a PAR1-independent manner. In order to test the activity of **2.1** in a system containing no PAR1, HEK-293 cells were treated with thrombin (3 U/mL) prior to the addition of **2.1** (**Figure 2.19**). This pre-addition of thrombin would desensitise the PAR1 present in the cell membranes, causing all the PAR1 to be internalised. The lack of a calcium signal after the second dose of thrombin confirms full removal of PAR1 from the cell membrane (**Figure 2.19A-B**). However, the addition of **2.1** to the pre-treated HEK-293 cells maintained a Ca^{2+} response with an elevated EC_{50} of 440 μM (**Figure 2.19A, C**).

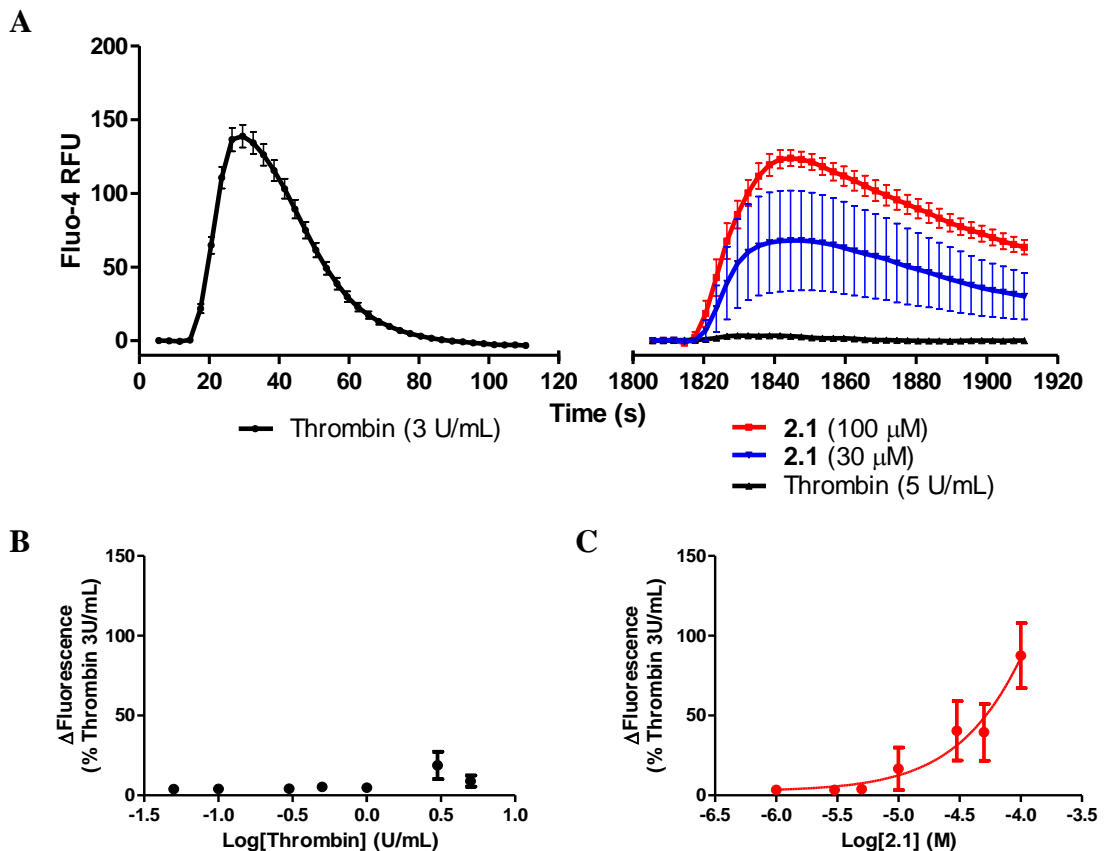


Figure 2.19: Desensitisation studies of **2.1** acting on HEK-293 cells. **A** Time course showing the change in fluorescence with time after the application of thrombin at $T = 17$ s and the addition of a variety of agonists/concentrations at $T = 1817$ s. **B** Concentration-response data for addition of thrombin (0.05-5 U/mL) following pretreatment with thrombin (3 U/mL). **C** Concentration-response curve for the addition of **2.1** (1-100 μM) following pretreatment with thrombin (3 U/mL). Data represents an $N=5$ with mean \pm SEM.

Table 2.9: EC₅₀ values for the addition of thrombin and **2.1** to HEK-293 cells pre-treated with thrombin (3 U/mL).

Agonist	Log[EC₅₀]	EC₅₀	
Thrombin	N/A	N/A	N = 5
2.1	-3.4 ± 1.5	440 μM	N = 5

The PAR1 independence of **2.1**-mediated activity was also demonstrated within the dual-LED, perfusion experiments (**Figure 2.20**). Here, initial thrombin activation leads to two waves of PAR1 activation before falling to basal fluorescence readings. Following the initial activation, **2.1** leads to a large calcium event which, as shown in **Section 2.4.2**, never returned to basal levels due to the interaction with Fura-2 within the cells (**Figure 2.20A-C**).

However, unlike previous treatments in the perfusion system with **2.2**, pre-activation of PAR1 with thrombin followed by treatment with **2.2** caused a calcium response of lower intensity but similar profile to **2.1** to be observed, with the fluorescence rising and not returning to baseline within the timescale observed (**Figure 2.20A-B, D**). These results could indicate the presentation of a different biological target for **2.2** as a result of thrombin activation or that the impact of the pepducin mechanism of action is detrimental to cells following thrombin activation. However, this was not researched in more detail meaning the extent of **2.2**-mediated activity could not be further assessed.

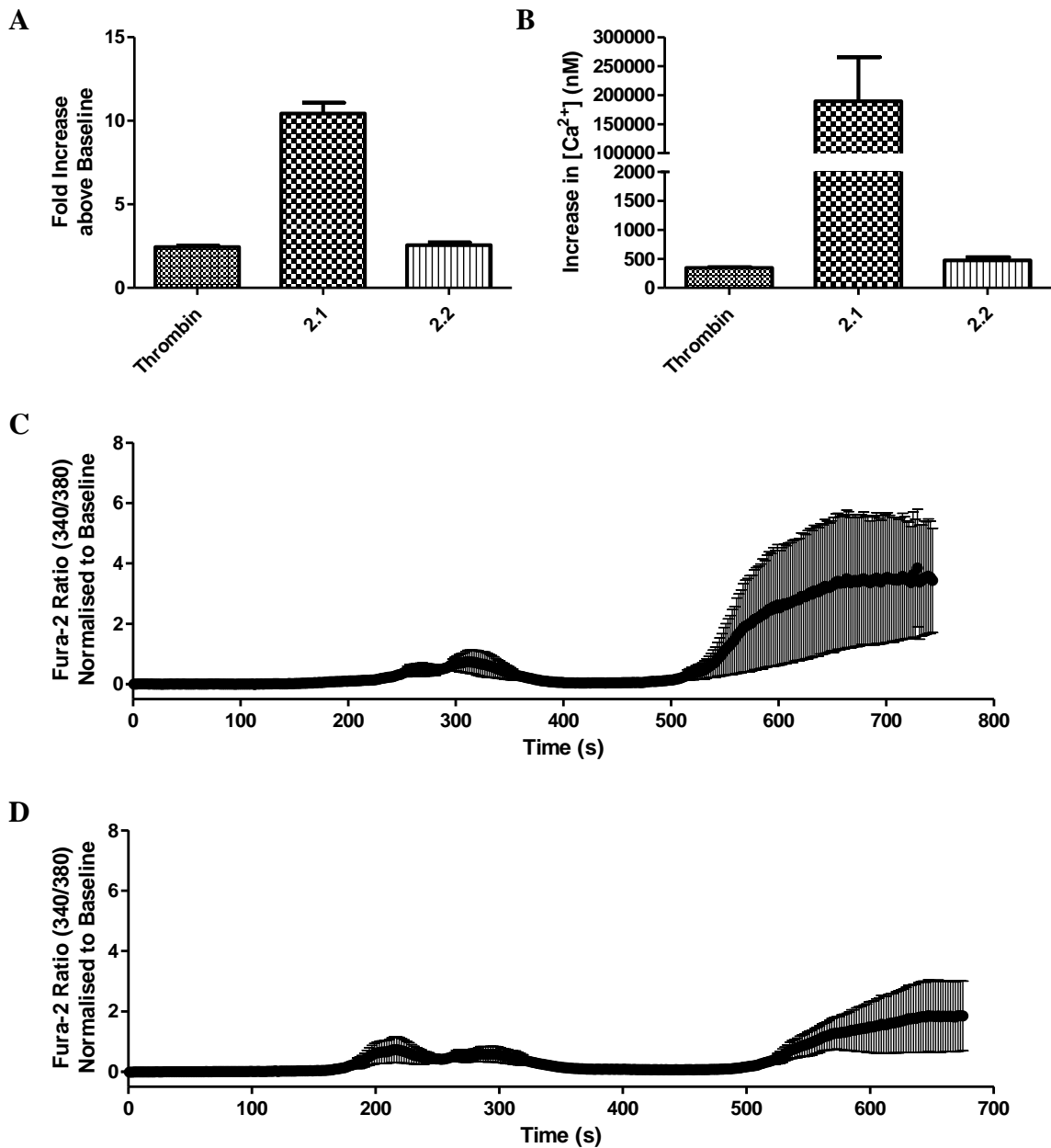


Figure 2.20 Activation of calcium signalling in HEK-293 cells loaded with Fura-2 AM. Agonists added *via* perfusion at 3-3.5 mL/min and fluorescent responses tracked at 340 nm excitation and 380 nm excitation. **A** The maximum response for each agonist expressed as the fold increase over the basal signal (mean ± SEM). **B** Increase in calcium concentration within cells upon perfusion of agonists (mean ± SEM). Cells were primarily washed with thrombin (1 U/mL) followed by **2.1/2.2** at 30 μM. **C-E** Average traces showing the ratio of 340 nm to 380 nm emissions of Fura-2 with time for addition of thrombin (1 U/mL) followed by **2.1** (**C**, 30 μM) and **2.2** (**D**, 30 μM). Data represents 150 regions of interest for **2.1** and **2.2** over N=3. Thrombin data represents a collated 300 regions of interest over N=3.

In addition to this, the calcium signalling assay was performed in mouse platelets, which do not express PAR1 but do express PAR3 and PAR4, using a Cal-6 (Calcium 6) staining protocol utilised within our laboratories. Attempts to utilise Fluo-4 within mouse platelets had been unsuccessful, with low consistency in experimental outputs within our research group. Cal-6 is another example of a calcium dye which allows simplification of the assay procedure, with reduced fluorescent background provided in the extracellular buffer, which showed more consistent results within the assay.¹⁵⁵

Addition of thrombin, **2.1** and the PAR4 activating peptide AYPGKF-NH₂ caused concentration-dependent increases in fluorescence with EC₅₀ values of 1.95 U/mL, 46 μM and 45 μM respectively (**Figure 2.21A and B, Table 2.10**). TFLLR-NH₂ was included as a negative control, showing no increase in fluorescence within the platelets to confirm the lack of PAR1 in the system (**Figure 2.21B, Table 2.10**). The differences in the activation profile can be noticed between **2.1** and the PAR4 agonists, with **2.1** continuing to cause a more sustained response which is still increasing at the end of the time period of the experiment. Cyclic peptide control **2.4** was used here as the randomised pepducin was synthesised at a later period of time (**Figure 2.21B, Table 2.10**).

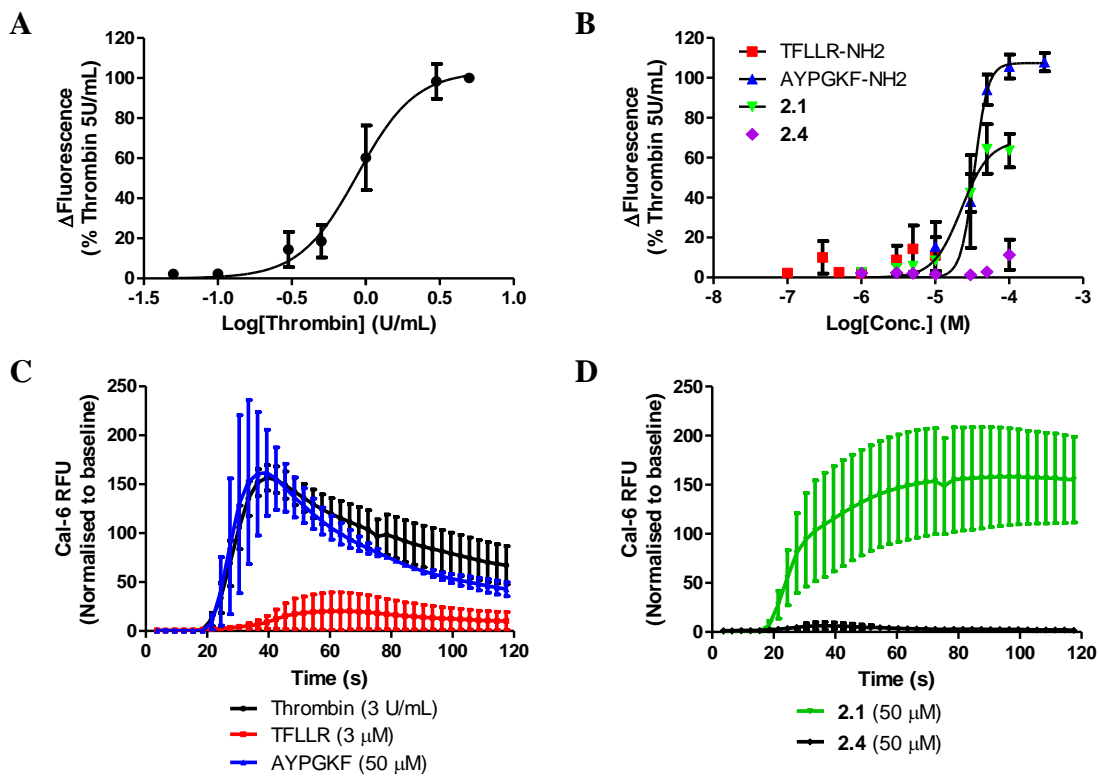


Figure 2.21: Activation of calcium signalling pathways in mouse platelets stained with Cal-6. **A** Activation of calcium signalling using Thrombin. **B** Activation of calcium signalling using PAR1 activating peptide (TFLLR-NH₂) and PAR4 activating peptide (AYPGKF-NH₂), **2.1** and **2.4**. Data obtained was normalised against the reading obtained upon addition of thrombin at 5 U/mL. Dose-response curves were fitted using GraphPad Prism. **C** Representative time courses for activation of calcium signalling using thrombin, TFLLR-NH₂, AYPGKF-NH₂, **2.1** and **2.4** normalised to the baseline signal. Data represents N=6 for **2.1**, N=4 for thrombin and **2.4**, and N=3 for TFLLR-NH₂ and AYPGKF-NH₂ with mean \pm SEM.

Table 2.10: EC₅₀ values obtained for the activation of calcium signalling in mouse platelets.

Agonist	Log[EC ₅₀]	EC ₅₀	
Thrombin	0.29 \pm 0.15	2.0 U/mL	N = 4
TFLLR-NH ₂	N/A	N/A	N = 3
AYPGKF-NH ₂	-4.3 \pm 0.16	45 μ M	N = 3
2.1	-4.4 \pm 0.21	46 μ M	N = 4
2.4	N/A	N/A	N = 4

Finally, a platelet aggregation assay was carried out in mouse platelets using thrombin, **2.1** and **2.2** (**Figure 2.22A-B**). Measuring platelet aggregation within mouse platelets would provide physiologically relevant data for **2.1** and **2.2** within cardiovascular disease, where PZ-128 was initially targeted. Each compound yielded a concentration-dependent response in the mouse platelets, with EC₅₀ values calculated to be 0.49 U/mL for thrombin, 115 μM for PZ-128 and 116 μM for PZ-Scram (**Figure 2.22, Table 2.11**). These results are particularly discouraging for the use of **2.1** within the study, as the aggregation of platelets starkly contrasts with the initially reported details of PZ-128 function where it was shown not to impact platelet aggregation in human platelets.² Additionally, this directly contrasts the intended therapeutic application of PZ-128 within clinical trials, where it is being tested as an antiplatelet therapy for the treatment of cardiovascular disease.

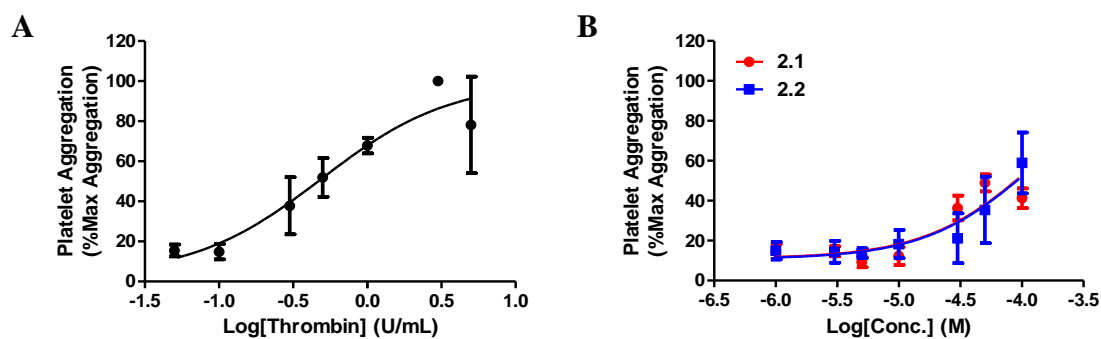


Figure 2.22: Activation of platelet aggregation in isolated mouse platelets. **A** Concentration-response curve for platelet aggregation caused by thrombin (0.5-5 U/mL). **B** Concentration-response curve for platelet aggregation caused by **2.1** and **2.2** (1-100 μM). Responses for each experiment normalised to the maximum aggregation. Data represents an N=4 with mean ± SEM.

Table 2.11: EC₅₀ values for the activation of mouse platelet aggregation using thrombin, PZ-128 and PZ-Scram.

Compound	Log[EC ₅₀]	[EC ₅₀]	
Thrombin	-0.39 ± 0.18	0.49 U/mL	N = 4
2.1	-3.9 ± 0.1	115 μM	N = 4
2.2	-3.9 ± 0.2	116 μM	N = 4

2.4.4 Inhibiting the off-target effects of PZ-128

To identify the effectors of the calcium signalling events induced in response to **2.1**, attempts were made to inhibit **2.1**-mediated activity using multiple antagonists which have the annotated pharmacological activity. Firstly, inhibition with **2.3** was attempted to investigate the effect of PAR1 inhibition of **2.1**-mediated calcium signalling (**Figure 2.23**) and to further exclude the unlikelihood that **2.1** was acting dependently of PAR1, helping to confirm the studies carried out in **Section 2.4.3**. As anticipated, this resulted in no quantifiable inhibition of **2.1**-mediated activity.

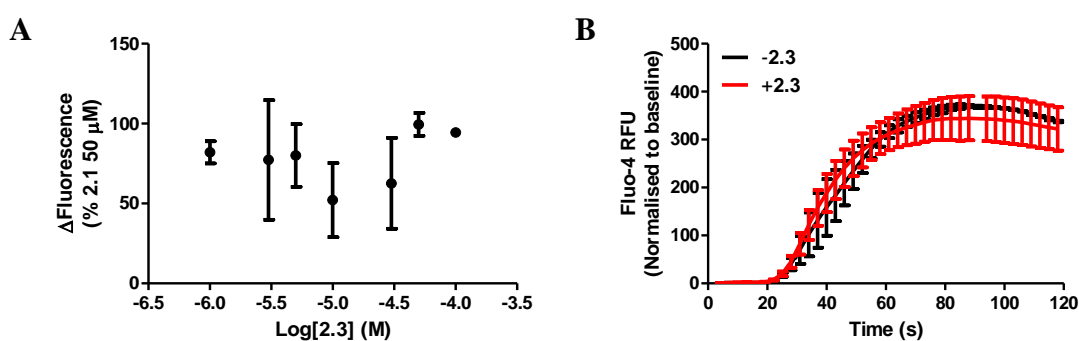


Figure 2.23: Attempted inhibition of **2.1**-mediated Ca²⁺ signalling with **2.3** (SCH79797) in HEK-293 cells stained with Fluo-4. **A** Concentration-response data for inhibition of **2.1**-mediated Ca²⁺ signalling with competitive PAR1 antagonist **2.3**. Data were normalised against the uninhibited **2.1** response at 50 μM. **B** Change in fluorescence with time following activation of PAR1 with **2.1** (t = 17 s) in the presence and absence of **2.3**, normalised to the basal fluorescent signal. Data represents N=3 with mean ± SEM.

Secondly, inhibition was attempted using U73122, a phospholipase C inhibitor (**Figure 2.24**).¹⁵⁶ As the first protein to interact with G_q following activation of the GPCR, this would confirm if the pathway through which calcium signalling is occurring is the same as that in the G_q-mediated activity (*vide supra* **Figure 1.20**).¹⁵⁷ This assay showed successful inhibition, with an IC₅₀ of 6.9 μM being shown for the inhibition of PZ-128-mediated activation of calcium signalling (**Figure 2.24, Table 2.12**) suggesting that the Ca²⁺ signalling observed was mediated through the G_q pathway. Furthermore, U73122 also inhibited thrombin-mediated activity with an IC₅₀ of 2.5 μM.

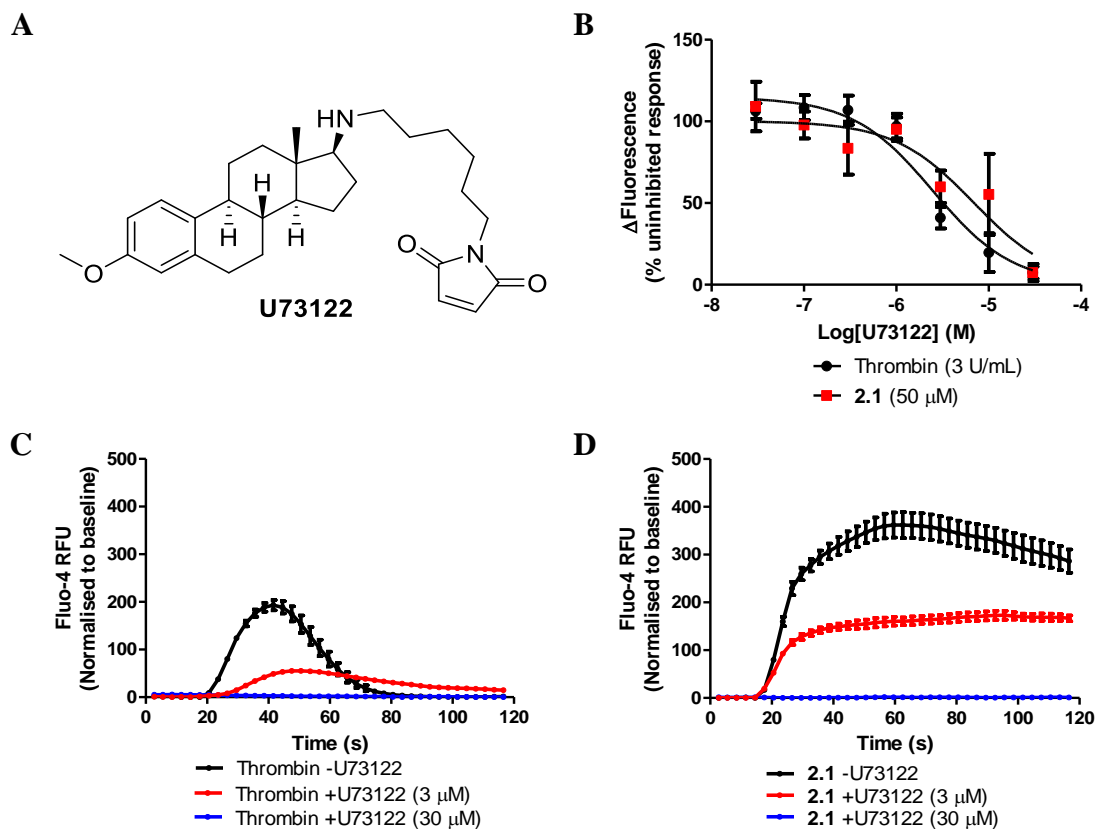


Figure 2.24: Inhibition of **2.1**-mediated Ca^{2+} signalling with PLC inhibitor U73122 in HEK-293 cells stained with Fluo-4. **A** Chemical structure of U73122. **B** Concentration-response data for inhibition of thrombin (black) and **2.1**-mediated (red) Ca^{2+} signalling with PLC antagonist U73122. Data were normalised against the uninhibited thrombin response (3 U/mL) or **2.1** response (50 μM) respectively. **C** Change in fluorescence with time following activation of PAR1 with thrombin ($t = 17$ s) in the presence and absence of U73122, normalised to the basal fluorescent signal. **D** Change in fluorescence with time following activation of PAR1 with **2.1** ($t = 17$ s) in the presence and absence of U73122, normalised to the basal fluorescent signal. Data represents $N=5$ with mean \pm SEM.

Table 2.12: Inhibition data for U73122 on the action of thrombin and PZ-128.

Agonist	Log[IC ₅₀]	IC ₅₀	
Thrombin (3 U/mL)	-5.6 ± 0.1	2.5 μM	N = 5
PZ-128 (50 μM)	-5.2 ± 0.2	6.9 μM	N = 5

Finally, an inhibitor of the G_{α} -protein subunit G_q , YM-254890, was utilised in this case (**Figure 2.25A**).¹⁵⁸ The calcium signalling response to PAR1 activation is known to occur

as a part of the G_q pathway and, as such, YM-254890 would provide insight into the consequences of G_q inhibition on PZ-128 function (*vide supra* **Figure 1.20**).⁷³ Pre-treatment of HEK-293 cells with YM254890 was shown to result in concentration-dependent inhibition of TFLLR-NH₂-mediated Ca²⁺ signalling with an EC₅₀ of 20 μ M, confirming the inhibitory nature of YM254890 (**Figure 2.25B-C**). However, the presence of YM-254890 did not result in inhibition of **2.1**-mediated Ca²⁺ signalling, suggesting **2.1** is not activating signalling cascades through a G_q dependent pathway.

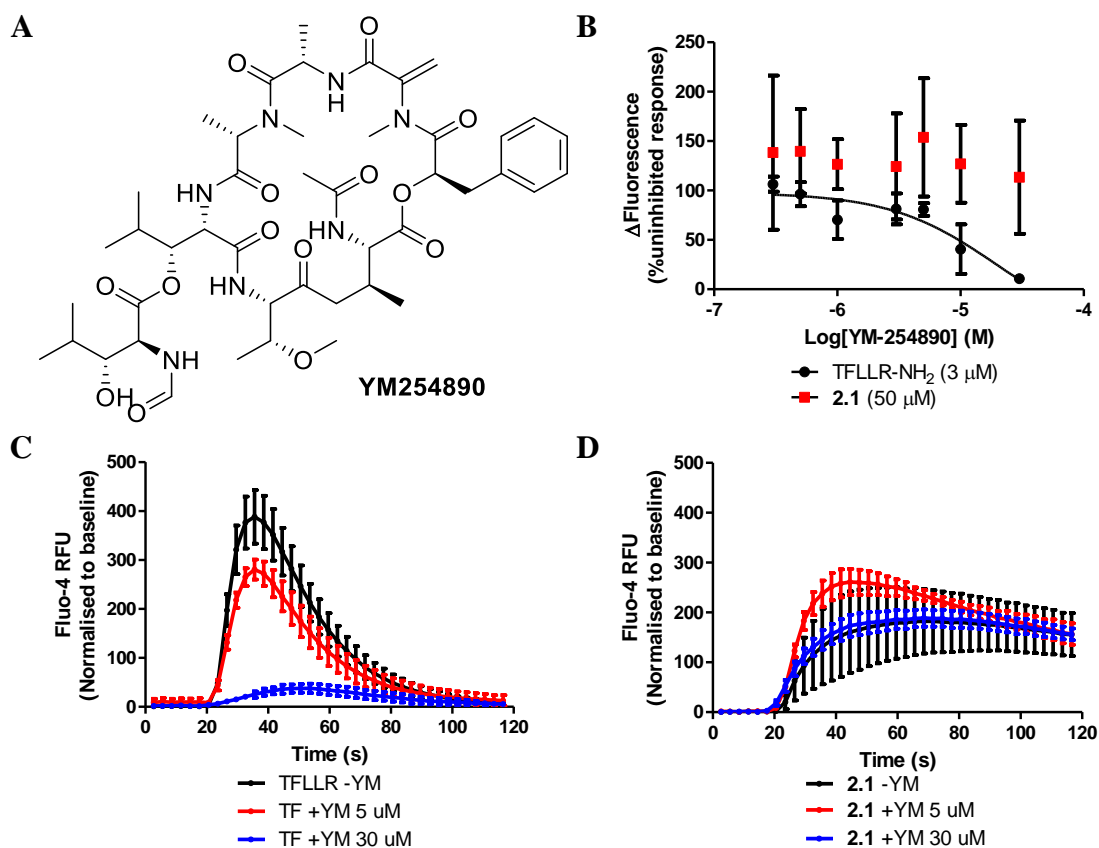


Figure 2.25: Inhibition of **2.1**-mediated Ca²⁺ signalling with PLC inhibitor YM254890 in HEK-293 cells stained with Fluo-4. **A** Chemical structure of YM254890. **B** Concentration-response data for inhibition of thrombin (black) and **2.1**-mediated (red) Ca²⁺ signalling with G_q antagonist YM254890. Data were normalised against the uninhibited thrombin response (3 U/mL) or **2.1** response (50 μ M) respectively. **C** Change in fluorescence with time following activation of PAR1 with thrombin (t = 17 s) in the presence and absence of YM254890, normalised to the basal fluorescent signal. **D** Change in fluorescence with time following activation of PAR1 with **2.1** (t = 17 s) in the presence and absence of YM254890, normalised to the basal fluorescent signal. Data represents N=5 with mean \pm SEM.

Table 2.13: Inhibition data for YM-254890 on the action of thrombin and PZ-128 in HEK-293 cells.

Agonist	Log[IC₅₀]	IC₅₀	
TFLLR-NH ₂ (3 μM)	-4.7 ± 0.5	20 μM	N = 5
PZ-128 (50 μM)	N/A	N/A	N = 5

These results indicate a potential binding site for **2.1** in PLCβ (**Figure 2.26**). Inhibition of PLCβ using U73122 led to a concentration-dependent decrease in **2.1**-mediated signalling (**Figure 2.26**). Additionally, inhibition at G_q using YM-254890 did not lead to a decrease in **2.1**-mediated signalling (**Figure 2.26**). Further to this, treatment of PAR1 with a competitive inhibitor, **2.3**, did not lead to a decrease in **2.1**-mediated signalling, complementing data obtained earlier in the study with regards to the PAR1-independent mechanism of action for **2.1** (**Figure 2.26**, *vide supra* **Section 2.4.3**).

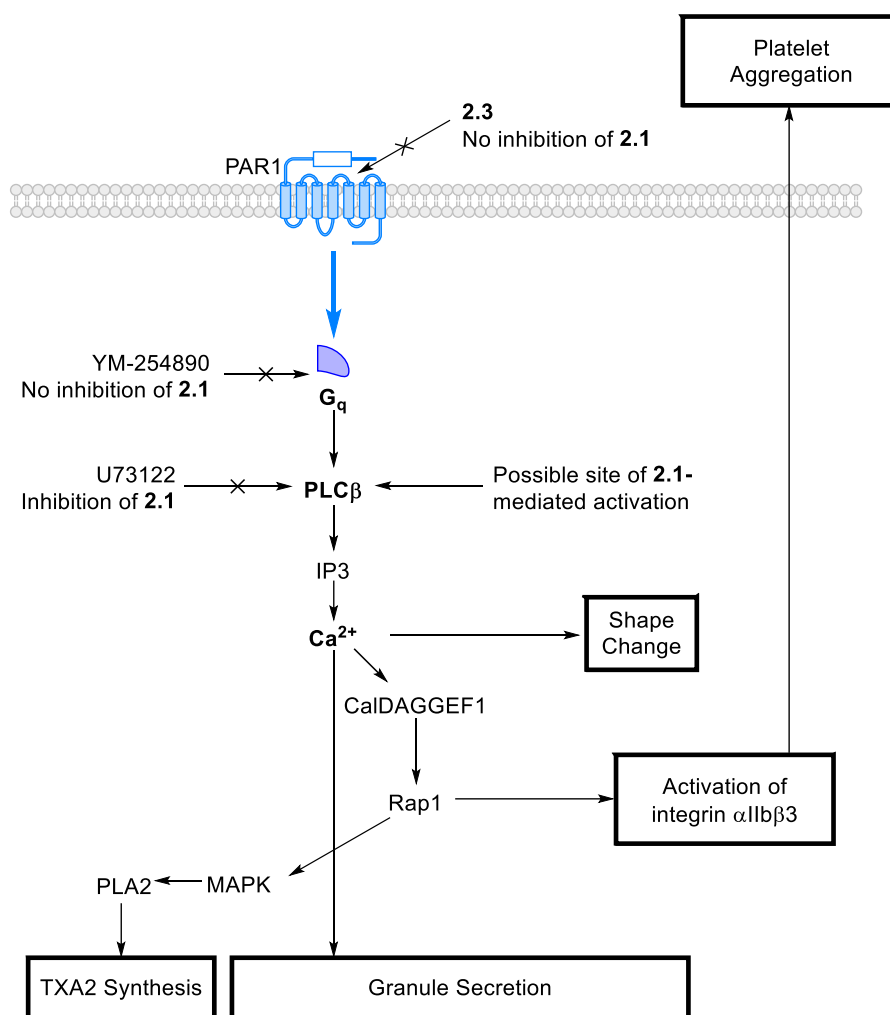
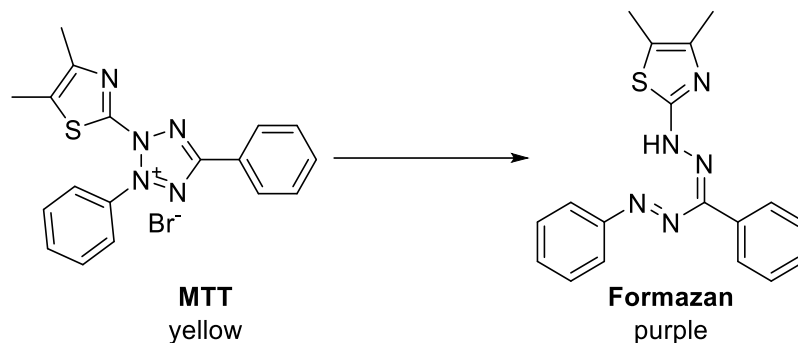


Figure 2.26: G_q signalling cascade following PAR1 activation in human platelets including known inhibitors of PAR1, G_q and IP3. Possible site of 2.1-mediated activation of the signalling cascade also highlighted.

2.4.5 Effect of pepducins on cell viability

With the vast differences in the kinetics and the PAR1 independence of 2.1-mediated activity in comparison to natural agonists, a further consideration was if the cells were compromised under the influence of the pepducins. To investigate this, an MTT cell viability assay was performed researching the effect of varying concentrations and times for 2.1 treatment on the cells. MTT, or 3-(4,5-dimethylthiazol-2-yl)-2,5-diphenyltetrazolium bromide, is reduced to formazan in living cells by reductase enzymes located in the mitochondria (**Scheme 2.5**).¹⁵⁹ Once reduced, formazan levels can be

measured using absorbance ($\lambda = 570 \text{ nm}$) and the resulting readings would be directly proportional to live cells.



Scheme 2.5: Reduction of MTT to formazan by mitochondrial reductase enzymes

By firstly treating HEK-293 cells with **2.1** at $1 \mu\text{M}$, no significant change was demonstrated in the number of viable cells in comparison to the media-treated and DMSO-treated controls (**Figure 2.27A**). By increasing to $10 \mu\text{M}$, initially, the trend is much the same, with no significant change in viable cell numbers (**Figure 2.27A**). However, when the cells are exposed to **2.1** for 24 hours, cell viability has been lost. This loss of cell viability continues increasing the concentration to $30 \mu\text{M}$ (**Figure 2.27A**), slightly higher than the EC_{50} described previously (*vide supra* **Section 2.3.2**). At $30 \mu\text{M}$, even a 2-hour treatment causes loss of cell viability, with 24-hour treatment leading to a significant loss in live cell numbers.

Surprisingly, the above trend continues with treatment of HEK-293 cells with **2.2** (**Figure 2.27B**). Outside of platelet aggregation, treatments with **2.2** typically did not yield physiological responses. However, many of the previous treatments, except for Western Blotting (*vide supra* **Figure 2.13**), were not performed for longer than a few minutes. This could suggest that prolonged exposure to pepducins in general, and not **2.1** and **2.2** specifically, could be causing stress to the cells, eventually culminating in cell death.

Finally, cell viability following treatments with thrombin and **2.3** were measured using concentrations slightly higher than EC₅₀ and IC₅₀ respectively (**Figure 2.27C**). In each case, cell death was not occurring even after 24-hour treatments. In each of these experiments, water and hydrogen peroxide were used as positive controls, causing significant levels of cell death following 2-hour treatments (**Figure 2.27A-C**).

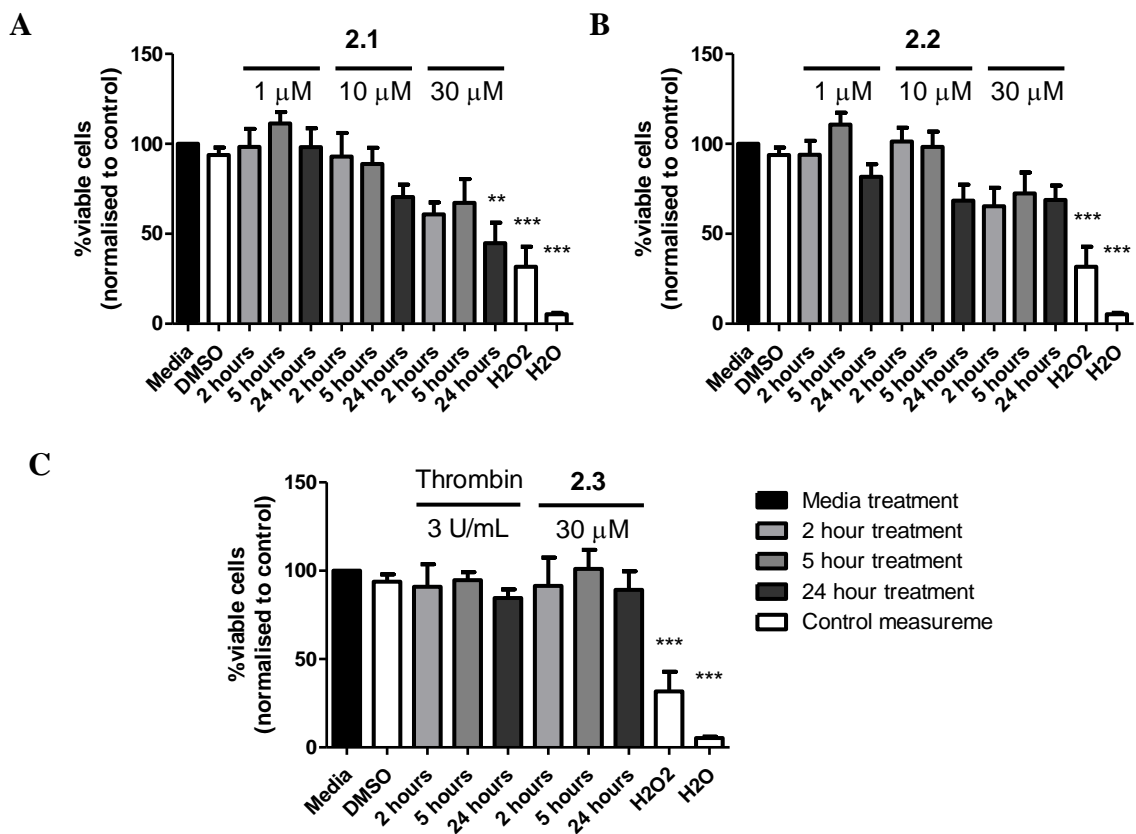


Figure 2.27: MTT Assay showing the effect of **2.1** (A), **2.2** (B) and thrombin and **2.3** (C) on cell viability. Data represents an N=5 for **2.1**, **2.2** and controls and N=4 for thrombin and **2.3** with mean \pm SEM. Data normalised to viable cells in media treated wells.

As another output for measuring cell death, Annexin V was used to bind to and quantify levels of exposed phosphatidylserine (PS) on the extracellular surface of cells following treatments with **2.1**, **2.2** and thrombin.¹⁶⁰ PS exposure displays a variety of functions, especially within platelets where it helps facilitate coagulation processes.¹⁶¹ However,

within other cell types the exposure of PS on the extracellular surface is also a marker for cell destruction, arising during the apoptotic pathway of cell death.¹⁶²

Following treatment of cells, Annexin V was used to stain the cells allowing flow cytometric analyses to be performed. The Annexin V is conjugated with allophycocyanin (APC), a fluorescent tag, which allows the cells to be identified within the APC channel of the flow cytometer. Within this study, elevated levels of PS would theoretically be indicative of cells entering apoptosis.

As expected, flow cytometric analysis of cells which were not stained with Annexin V resulted in extremely low numbers of cells being counted within the gated population (**Figure 2.28A, G**). This gated population, denoted as “PS +ve” (positive), contains the cells which have Annexin V bound to their extracellular domain as detected within the flow cytometer (**Figure 2.28A-F**). Media and DMSO treatments prior to staining represent control readings, where the number of cells stained with Annexin V would represent the basal levels of extracellular phosphatidylserine (**Figure 2.28B-C, G**).

However, treatment with pepducins **2.1** and **2.2** reduced the levels of Annexin V bound on the extracellular surface (**Figure 2.28D-E, G**). This would suggest that the presence of the pepducins is preventing phosphatidylserine from migrating to the extracellular surface of the cell membrane. Meanwhile, thrombin treatment once again displayed no impact on cell viability in comparison to the media and DMSO controls (**Figure 2.28F-G**).

The lack of Annexin V binding, coupled with the results obtained from the MTT assay (*vide supra*, **Figure 2.27**), could suggest that cell death is occurring *via* a non-apoptotic pathway. However, time constraints prevented this particular topic from being explored further.

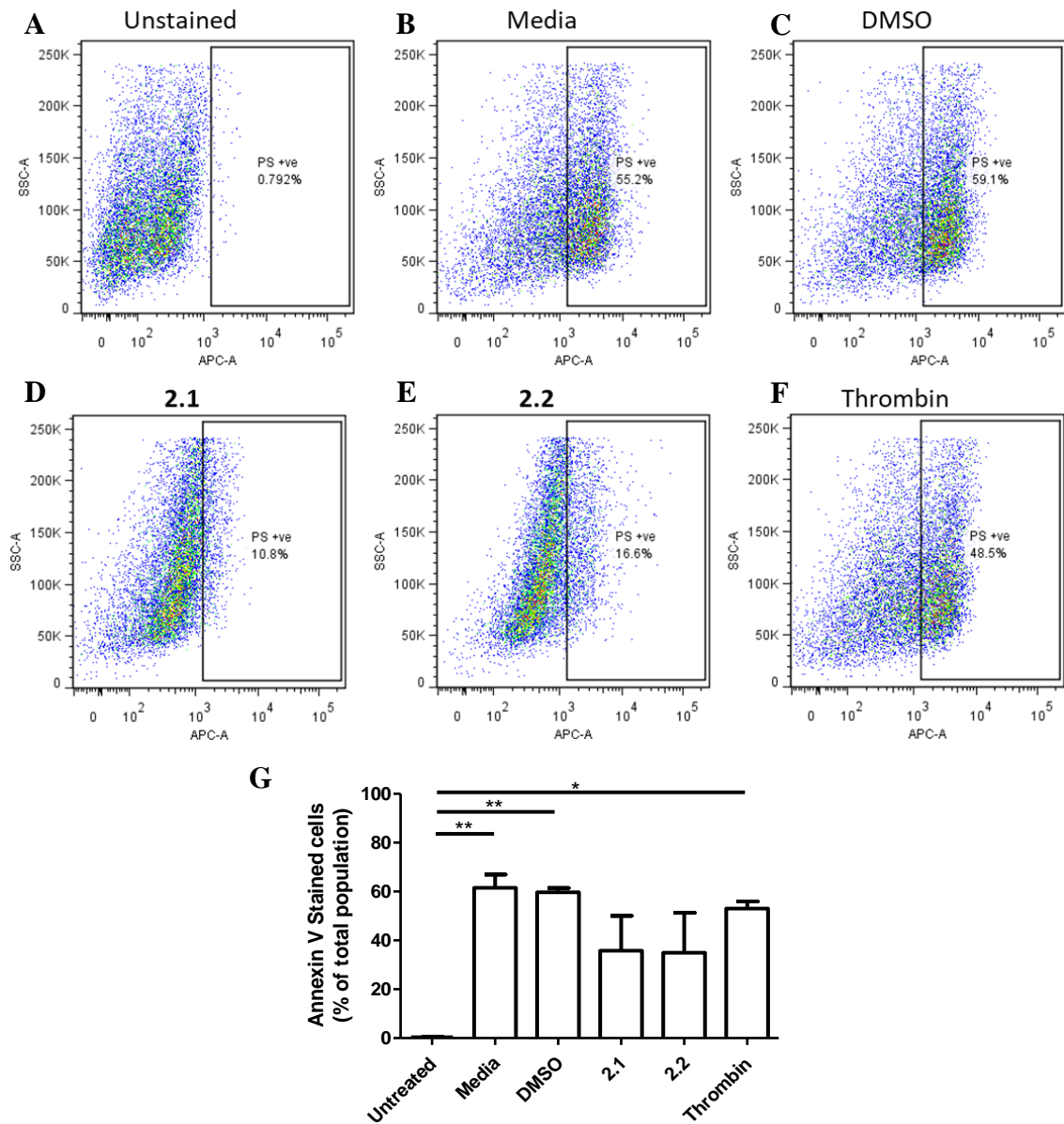


Figure 2.28: Flow cytometric analyses of HEK-293 cells stained with Annexin V dye. Cells were analysed using flow cytometry following 1-hour stimulations with a variety of stimuli (**2.1**, **2.2** and thrombin) as well as several controls (DMSO, media-treated and unstained cells). **A-F** Representative dot plots showing the populations that resulted from treatments. Gated region denoted “PS +ve” contains all cells for which Annexin V was detected. **G** Processed data showing the percentage of cells contained within the “PS +ve” gated domain. Data represents an N=3 with mean \pm SEM.

The work carried out on **2.1** has highlighted inconsistencies with its reported pharmacological profile and intended therapeutic purpose.^{127,134} Previous work has shown **2.1** to be an effective inhibitor of PAR1 function whilst showing little off-target pharmacology. However, this study showed a propensity for the activation of Ca²⁺ signalling with **2.1**. This activation was shown to be kinetically different from activation with traditional PAR1 agonists (*vide supra*, **Section 2.4.2**) and subsequently shown to be occurring in a PAR1-independent manner (*vide supra*, **Section 2.4.3**). Additionally, attempts to inhibit **2.1**-mediated activation led to successful inhibition at IP3 using U73122 (*vide supra*, **Figure 2.24**) whilst inhibition at G_q and PAR1 did not inhibit **2.1**-mediated activity. This could suggest PAR1 is binding at PLC β , which lies between G_q and IP3 on the G_q signalling cascade, or at IP3, where inhibition was shown to reduced **2.1** mediated signalling. However, **2.1** was also shown to be reducing cell viability within HEK-293 cells (*vide supra*, **Section 2.4.5**). This could help explain why the calcium signalling is PAR1 independent, where it is occurring through a different signalling pathway related to cell death.

2.5 Improving upon PZ-128

2.5.1 PAR1 cyclic pepducins

As stated previously, another objective of the current study was the design and synthesis of pepducins analogous to PZ-128. Based on this, a library of PAR1-derived pepducins was assembled containing pepducins with a modified linker between the palmitoyl chain and the peptide sequence. The linkers used would be bonded twice to the peptide sequence, thus forming a cyclic pepducin. The cyclic pepducins utilised a peptide derived from **2.1** with a sequence of KKSRAL. The peptides were then joined to a linker through carbon-sulfur bonds to cysteine residues residing at the termini of the peptide sequence, providing a final sequence of CKKSRALC. Initially, three different linking moieties were introduced covering a range of polarities: a phenyl group (**2.5**), a triazine group (**2.6**) and a triazinane group (**2.7**) (**Figure 2.29**).¹⁶³

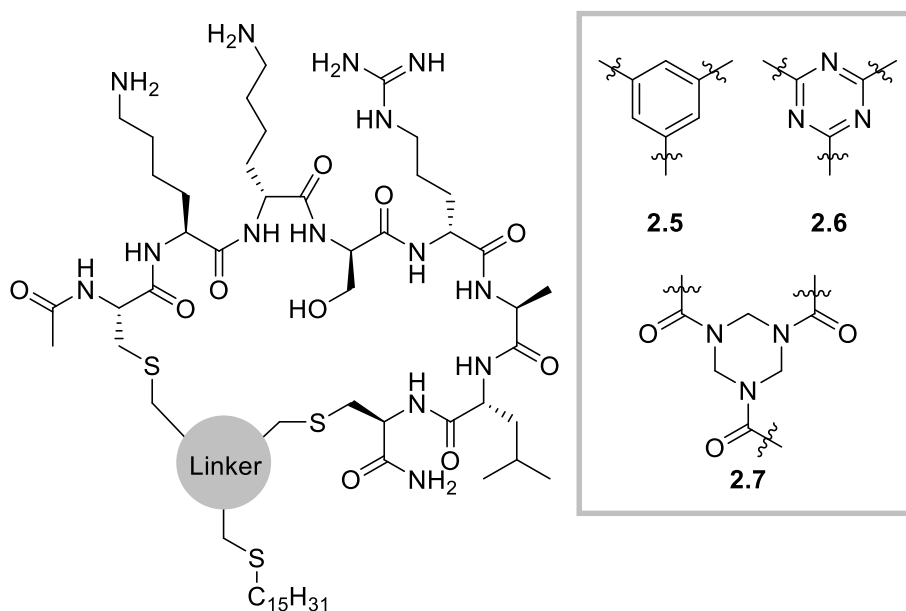
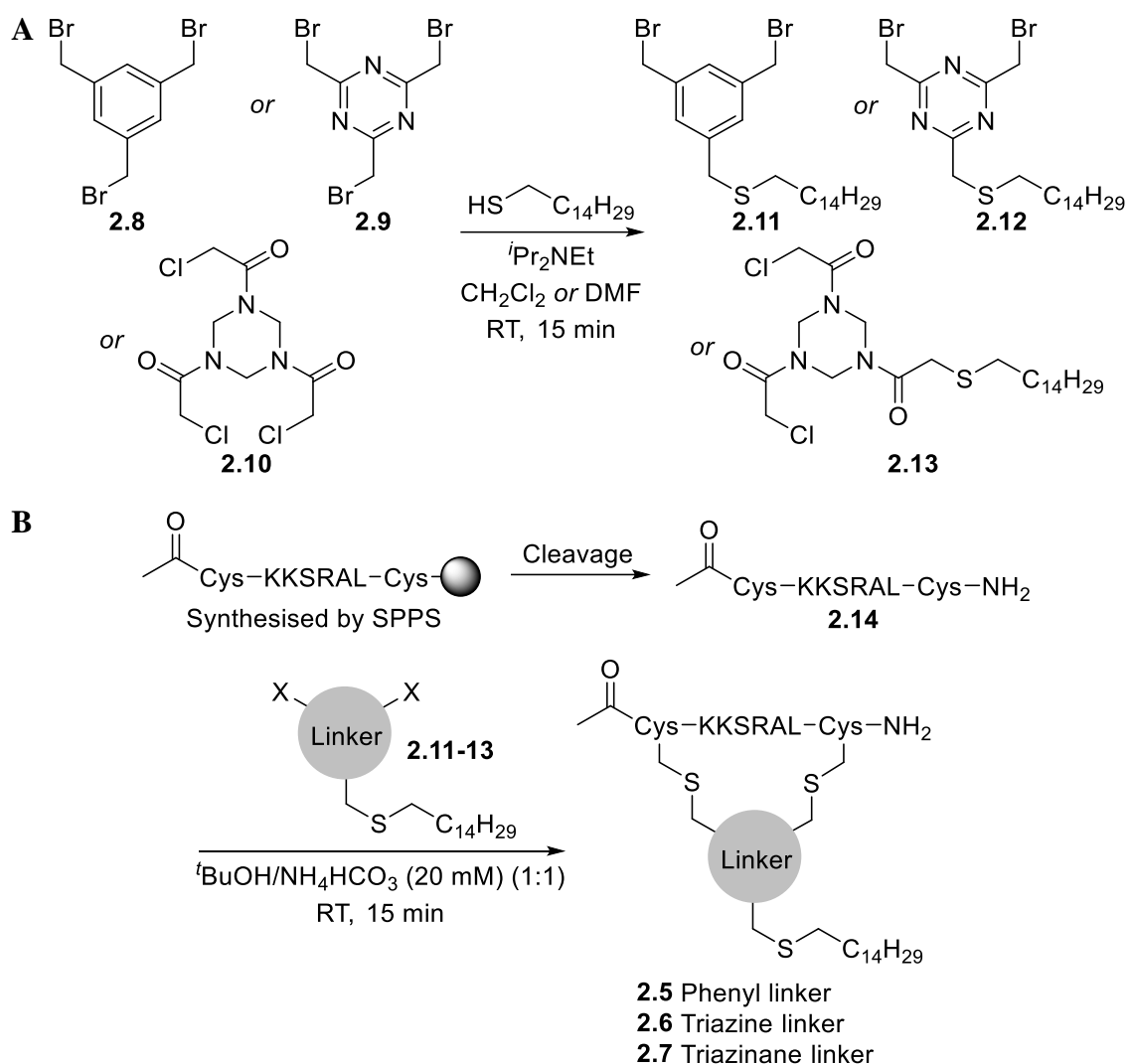


Figure 2.29: Chemical structure of three cyclic pepducins **2.5**, **2.6** and **2.7**.

The cyclic pepducins were synthesised externally within the laboratory of Prof. Robert Liskamp (University of Glasgow).¹⁶⁴ To access the pepducins, firstly a series of tris-

halogenated compounds **2.8-10** were reacted with pentadecane-1-thiol to yield monoalkylated linkers **2.11-13** (**Scheme 2.6A**).¹⁶⁴ Following the alkylation reaction, peptide sequence **2.14**, synthesised using SPPS, was then coupled with the remaining halides on linkers **2.11-13**, reacting at the cysteine residues to furnish the cyclic pepducins **2.5-7** through the formation of new S-C bonds (**Scheme 2.6B**).¹⁶⁴ The furnished cyclic pepducins were provided as trifluoroacetic acid salts following their synthesis.



Scheme 2.6: Synthesis of cyclic pepducins. **A** Synthesis of monoalkylated linkers **2.11-13**. **B** Coupling of peptide **2.14** with linkers towards cyclic pepducins **2.5-7**.

It was proposed that the design of the cyclic pepducins would allow the peptide chain to fold into a typical protein structure, imitating the conformation of a GPCR loop. This protein-like folding of the peptide sequence was proposed to provide more favourable interactions with the target protein, PAR1.¹⁶⁵ As can be noted following energy minimisation with Chem3D, the cyclic peptide bound to a linker (**2.5**) is tightly arranged in a hook-like structure (**Figure 2.30A**) while a flexible single-chain peptide maintains a relatively straight peptide backbone (**Figure 2.30B**).

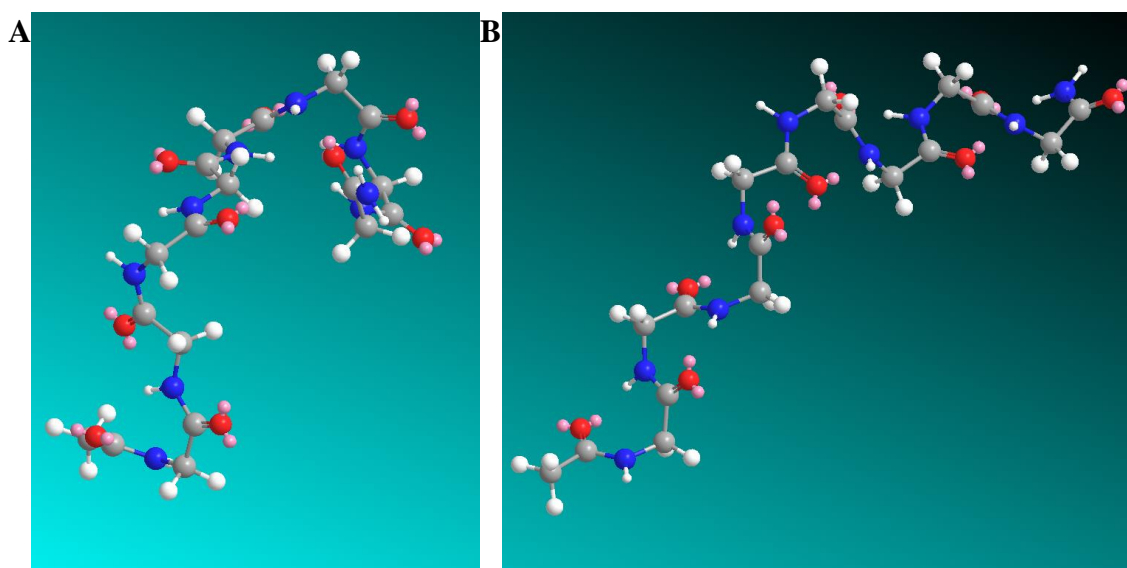


Figure 2.30: Energy minimised structures of peptide backbone using **2.5** (**A**) and the free peptide sequence CKKSRALC with no linker bound (**B**). Amino acid side chains, linking moiety and palmitoyl chain were included for energy minimisation and hidden afterwards using Discovery Studio.

In addition to the cyclic pepducins, analogous linear pepducins **2.15-17** were also included in the study to provide a comparison for their cyclic counterparts (**Figure 2.31**). These analogues maintained a similar peptide structure, excepting the C-terminal cysteine which was replaced with an alanine residue to simulate a non-functional residue for protein binding. Further, they were each bound to linkers *via* the cysteine at the N-terminus of the

sequence. Finally, a methyl thioether was introduced to the linker groups to replace the C-terminal cysteine bridge.

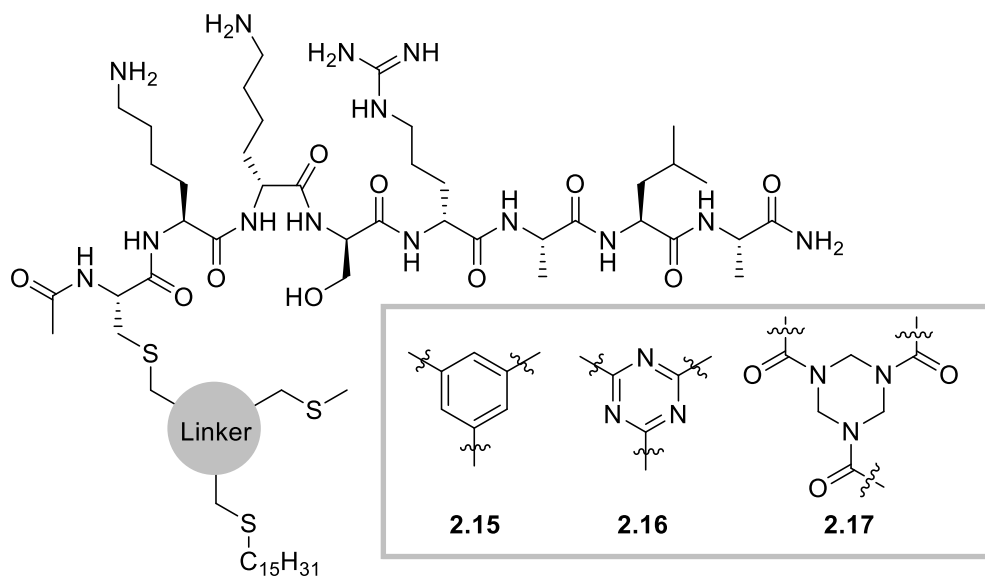
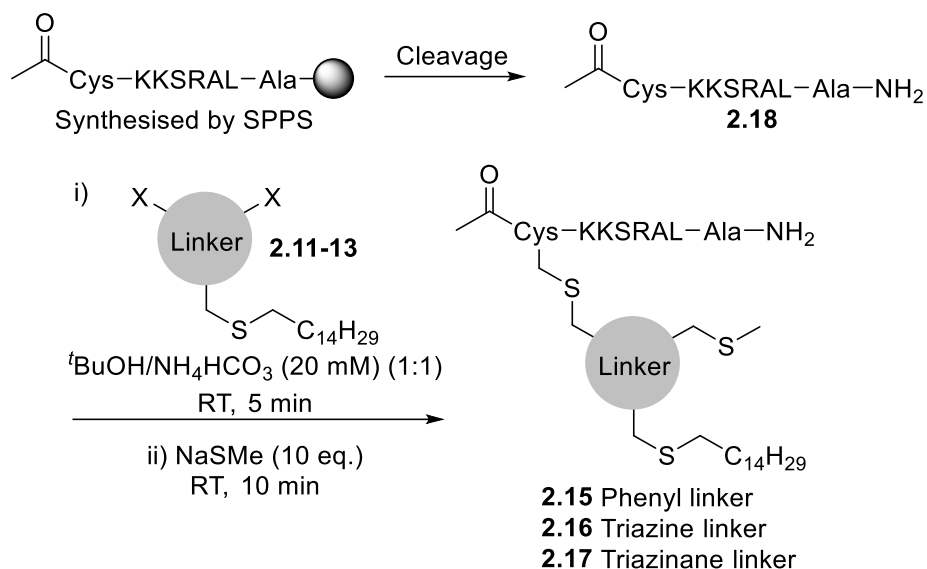


Figure 2.31: Chemical structure of linear pepducin analogues **2.15**, **2.16** and **2.17**.

The linear analogues were synthesised using an analogous procedure to the cyclic pepducins whereby peptide **2.18**, synthesised using SPPS, was coupled with linkers **2.11-13**. Following the initial coupling, the remaining halide on the linker was capped using sodium thiomethoxide to provide the linear pepducin analogues **2.15-17** which were provided as TFA salts.



Scheme 2.7: Synthesis of linear pepducin analogues **2.15-17**

Given the aberrant behaviour displayed by **2.1** previously (*vide supra* **Section 2.4**), it was decided that, prior to screening the inhibitive properties of the pepducins, the agonist properties of **2.5-10** would first be tested (**Figure 2.32**).

In this study, HEK-293 cells which were stained with Fluo-4 DirectTM were treated with each pepducin whilst fluorescent readings were being taken. For cyclic pepducins **2.5-7**, it can be seen that maximal concentrations of each pepducin results in the release of calcium within the cells (**Figure 2.32A**). However, while the differences do not show statistical significance, phenyl analogue **2.5** provides a much lower fluorescent signal than triazine **2.6** and triazinane **2.7**, which each provide concentration-dependent responses.

Conversely, the phenyl linear pepducin **2.15** provides elevated, concentration-dependent fluorescent responses, suggesting the cyclisation of the peptide sequence can provide improvements in the pharmacological properties of pepducins (**Figure 2.32B**). Similarly to **2.15**, triazine **2.16** and triazinane **2.17** also provided concentration-dependent release of calcium in the cells (**Figure 2.32B**).

These results indicate the sequence specificity under which **2.1** was functioning (*vide supra* **Section 2.4.3**) could have translated into the novel analogues which utilise part of

the same sequence. However, the decrease in the intensity of the response with **2.5** suggests that improvements to the agonist activity of **2.1** could be made through modification of the pepducin structure.

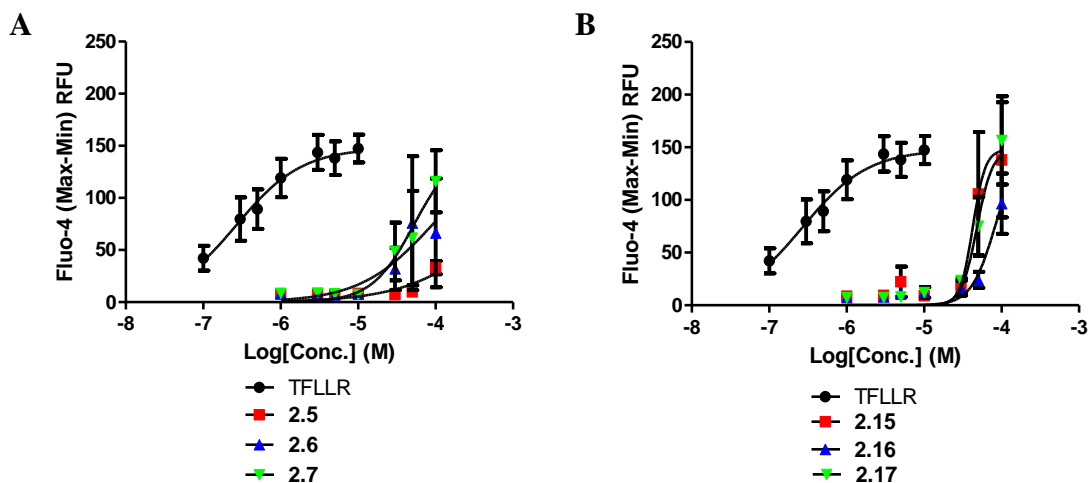


Figure 2.32: Characterisation of PAR1-derived pepducin library. HEK-293 cells loaded with Fluo-4 Direct were treated with PAR1 cyclic (**A**) and linear (**B**) pepducins and the resulting fluorescence change monitored. Dose-response curves were then plotted for each pepducin. Data represent an N=4 with mean \pm SEM.

Despite the agonist properties of the pepducins highlighted above (**Figure 2.32**), attempts were made to generate inhibition data for each pepducin (**Figure 2.33**). As was performed with **2.1** previously (*vide supra* **Section 2.3.2**), cells were pre-treated with the pepducins (1-100 μ M) prior to treatment with PAR1 agonist TFLLR-NH₂.

With the initial cyclic PZ-128 analogues, it can be seen that the heterocyclic **2.6** and **2.7** both provide concentration-dependent decreases in the response to TFLLR-NH₂ (**Figure 2.33A**). However, phenyl pepducin **2.5** fails to inhibit TFLLR-NH₂-mediated activation of PAR1 (**Figure 2.33A**). Meanwhile, the linear analogues **2.15-17** each provided concentration-dependent inhibition of TFLLR-NH₂-mediated activation of calcium signalling (**Figure 2.33B**).

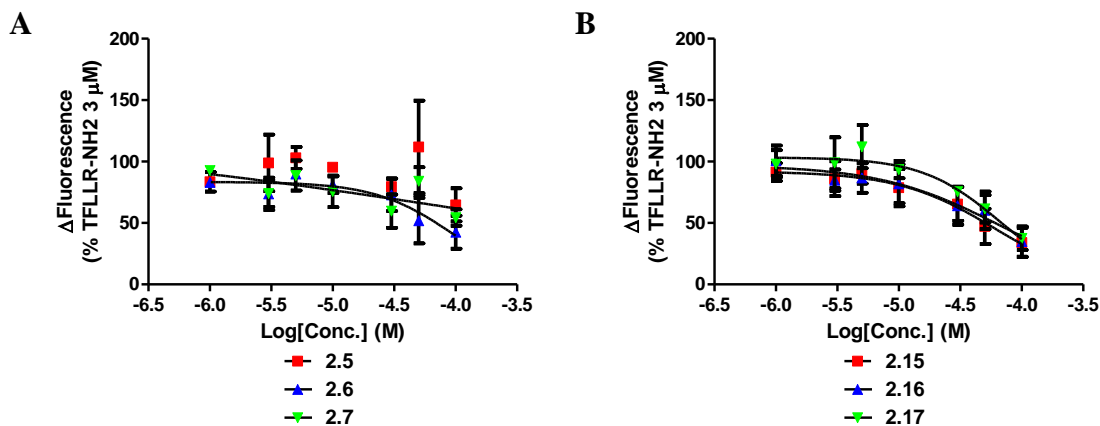


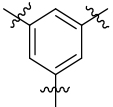
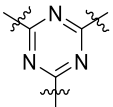
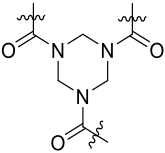
Figure 2.33: Characterisation of PAR1-derived pepducin library. HEK-293 cells loaded with Fluo-4 Direct were pre-treated with cyclic (**A**) and linear (**B**) PAR1 pepducins and then further treated with PAR1 peptide, TFLLR-NH₂ (3 μM). Dose-response curves were then plotted for each pepducin. Data represents an N=4 with mean ± SEM normalised to uninhibited responses to TFLLR-NH₂ (3 μM) carried out within each experiment.

Whilst the above experiments did not provide complete concentration-response curves, assumptions could be made with the data to extrapolate EC₅₀ and IC₅₀ values for each pepducin. For the agonistic events, it could be asserted that a maximal response from pepducin-mediated activation would be equal to the maximum response following activation with TFLLR-NH₂. Conversely, the concentration-response curves for inhibition were presumed to have a bottom value equal to 0% of the TFLLR-NH₂ mediated response, indicative of full inhibition of PAR1. GraphPad Prism could then be used to fit a curve which would fit these constraints.

With these conditions in place, EC₅₀ values estimated for each pepducin highlight cyclic phenyl pepducin **2.5** as the only analogue to yield significantly reduced levels of calcium signalling activation in comparison to **2.1**. The reduced agonist activity with **2.5** is demonstrated with an improved EC₅₀ of 672 μM (**Table 2.14**) in comparison to 24 μM for **2.1** (**Figure 2.8, Table 2.6**). Each other pepducin displayed only slight improvements in EC₅₀ over **2.1**, with the cyclic pepducins displaying marginally improved EC₅₀ values over the linear analogues. In each case, EC₅₀ values were mostly comparable to **2.1**.

However, in comparison to **2.1**, each pepducin failed to yield improved inhibition of PAR1 with **2.6-7** and **2.15-17** all providing slightly poorer IC₅₀ values. Furthermore, **2.5** failed to yield a measurable IC₅₀ despite its decreased propensity for activation of calcium signalling.

Table 2.14: EC₅₀ and IC₅₀ values for PAR1-derived pepducins. ^aEC₅₀ values obtained by treating HEK-293 cells loaded with the calcium dye Fluo-4 and recording the change in fluorescent output. ^bIC₅₀ values obtained by pre-treating HEK-293 cells loaded with Fluo-4 with pepducins and further treating with PAR1 agonist (TFLLR-NH₂).

Linker	Pepducin Type	EC ₅₀ ^a	IC ₅₀ ^b
	Cyclic (2.5)	672 μM	-
	Linear (2.15)	42 μM	59 μM
	Cyclic (2.6)	90 μM	93 μM
	Linear (2.16)	82 μM	65 μM
	Cyclic (2.7)	52 μM	113 μM
	Linear (2.17)	48 μM	65 μM

2.5.2 Elongated linker

Following initial testing of the modified pepducins, a further four pepducins containing an additional spacer were included in the study. As with the previous series, cyclic pepducins containing phenyl (**2.19**), triazine (**2.20**) and triazinane (**2.21**) cores were included, with a triazole acting as a spacer between the linking group and the palmitoyl chain, connecting to the alkyl chain with an amide bond (**Figure 2.34A**). Additionally, given the improvements to agonist properties displayed by phenyl analogue **2.5**, an additional analogue was included with **2.22**, where the amide spacer has been removed (**Figure 2.34B**).

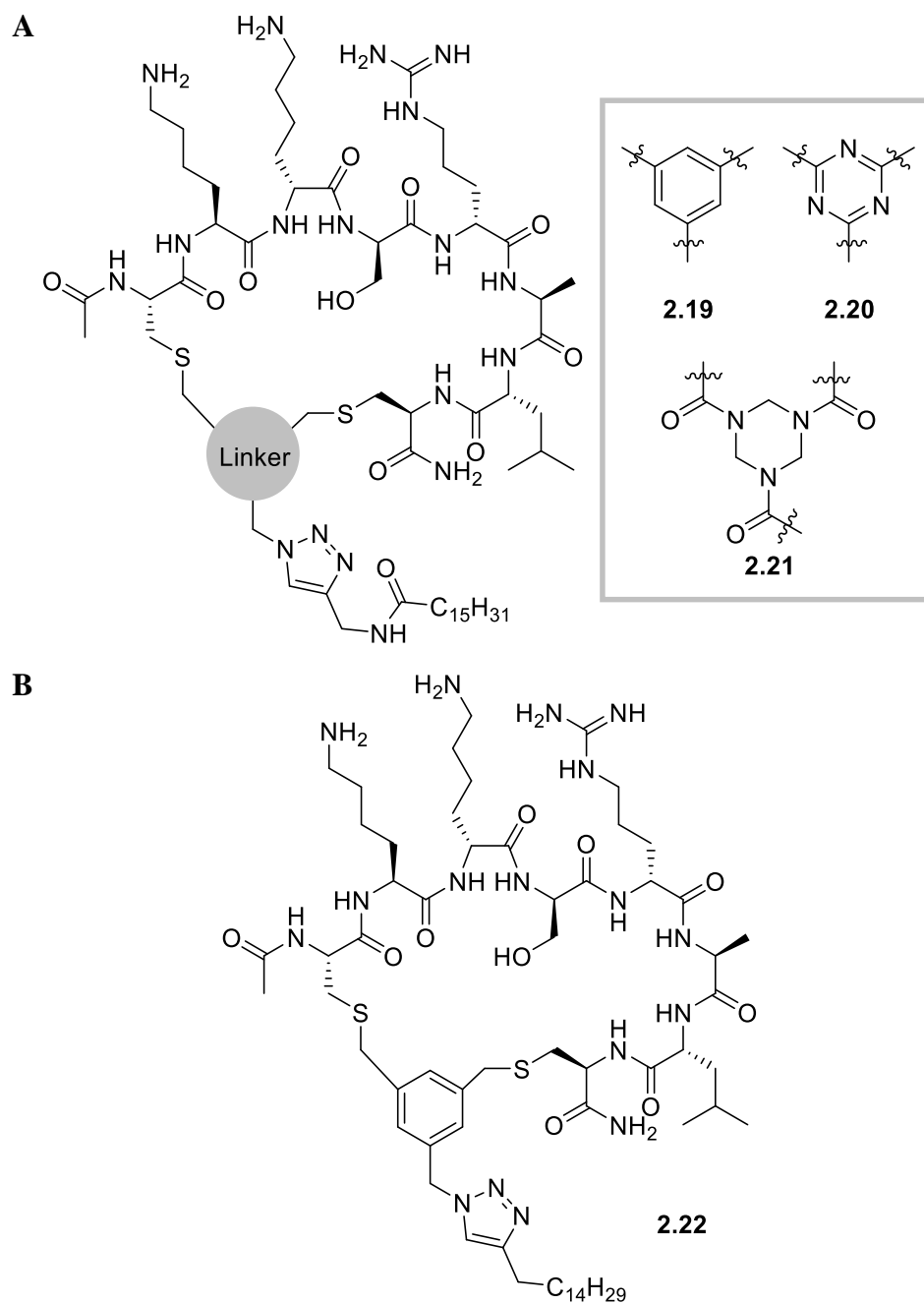
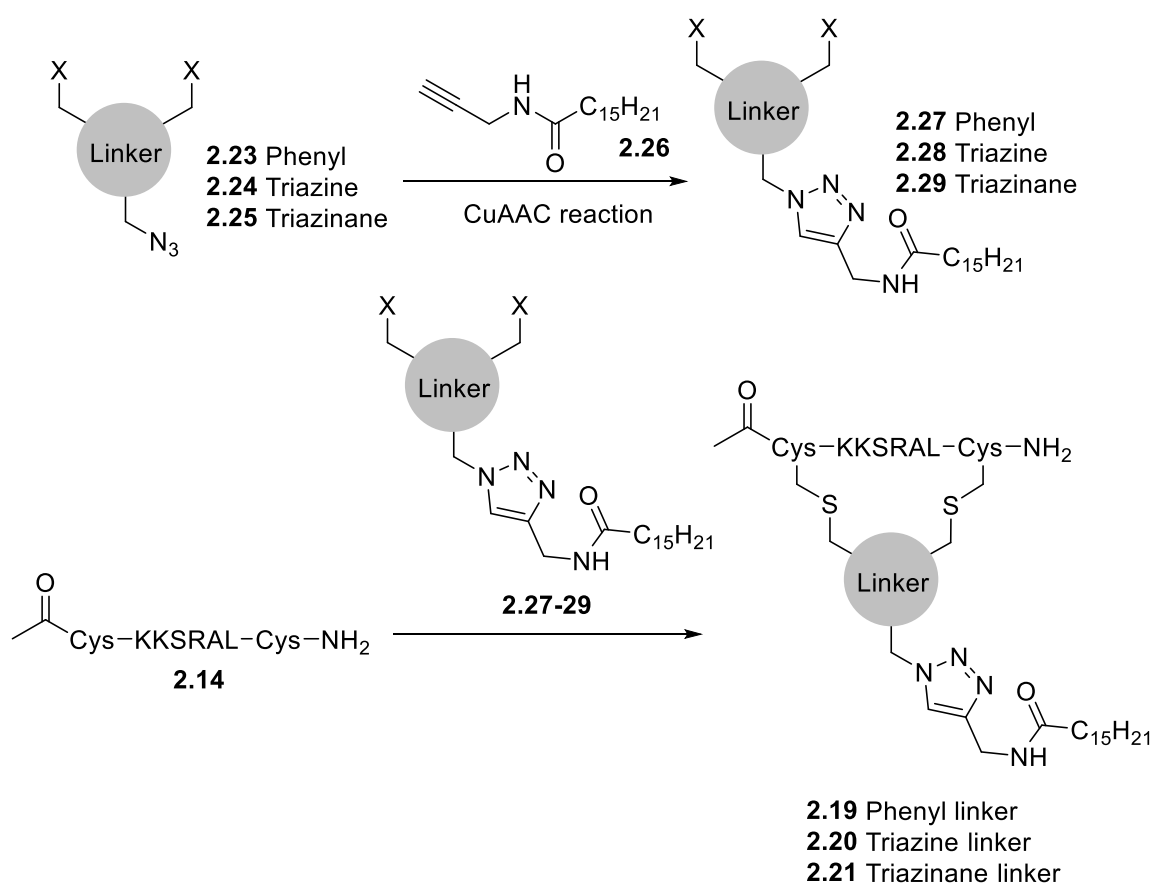


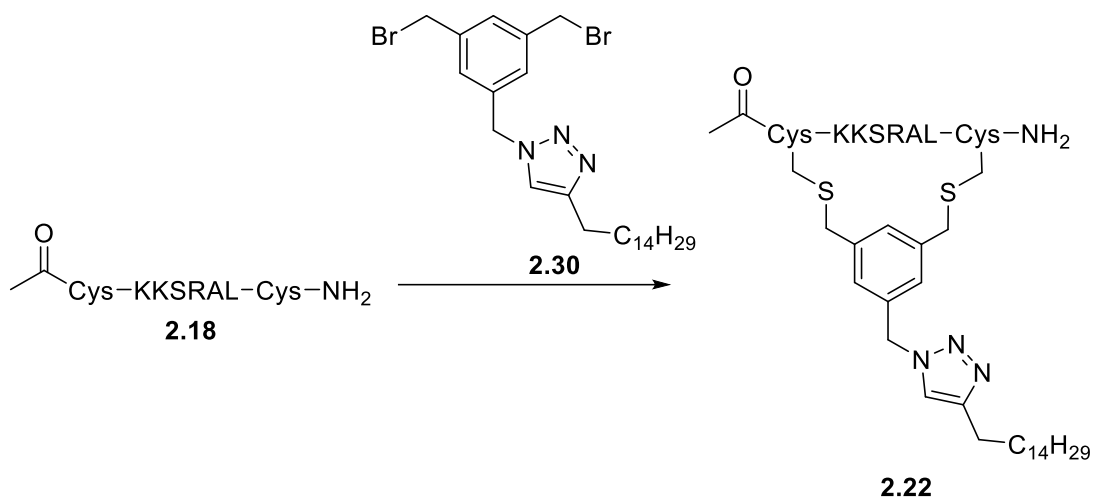
Figure 2.34: Chemical structure of cyclic peptidocyclins containing a triazole linker with amide spacer (**A**) and without an amide spacer (**B**).

The extended linker was introduced to the cyclic pepducins by using an analogous procedure to that used for **2.5-8** (*vide supra* **Scheme 2.6**), firstly reacting peptide **2.14** with azide-modified linkers **2.22-24** (**Scheme 2.7**).¹⁶⁴ Following the initial alkylation, a copper(I)-catalysed alkyne-azide cycloaddition (CuAAC) reaction was performed between the azide and alkyne **2.25** to yield the desired triazole-modified pepducins **2.19-21** (**Scheme 2.7**).¹⁶³ The CuAAC reaction is one of many Click reactions which are high yielding and possess a wide substrate scope, with demonstrated uses in polymeric reactions and within biochemistry.¹⁶⁶ Click reactions can be conducted in a wide array of solvents, including water, and create easily removed byproducts, with nitrogen gas being the only by-product in the CuAAC reaction.¹⁶⁶



Scheme 2.8: Synthesis of elongated cyclic pepducins **2.19-21** via alkylation and Click reaction.¹⁶⁴

Similarly, the triazole was introduced without the amide linker into analogue **2.22** by reacting peptide **2.18** with phenyl linker **2.30** (Scheme 2.9).¹⁶⁴



Scheme 2.9: Synthesis of linear analogue of extended pepducins, **2.22**.¹⁶⁴

It was reasoned that elongating the linker with a triazole moiety would allow the peptide chain to localise further from the cell membrane once inside the cell (**Figure 2.35**). The change in localisation of the peptide sequence, as the pharmacologically active moiety within the pepducins, would allow modification of the binding observed with PAR1.

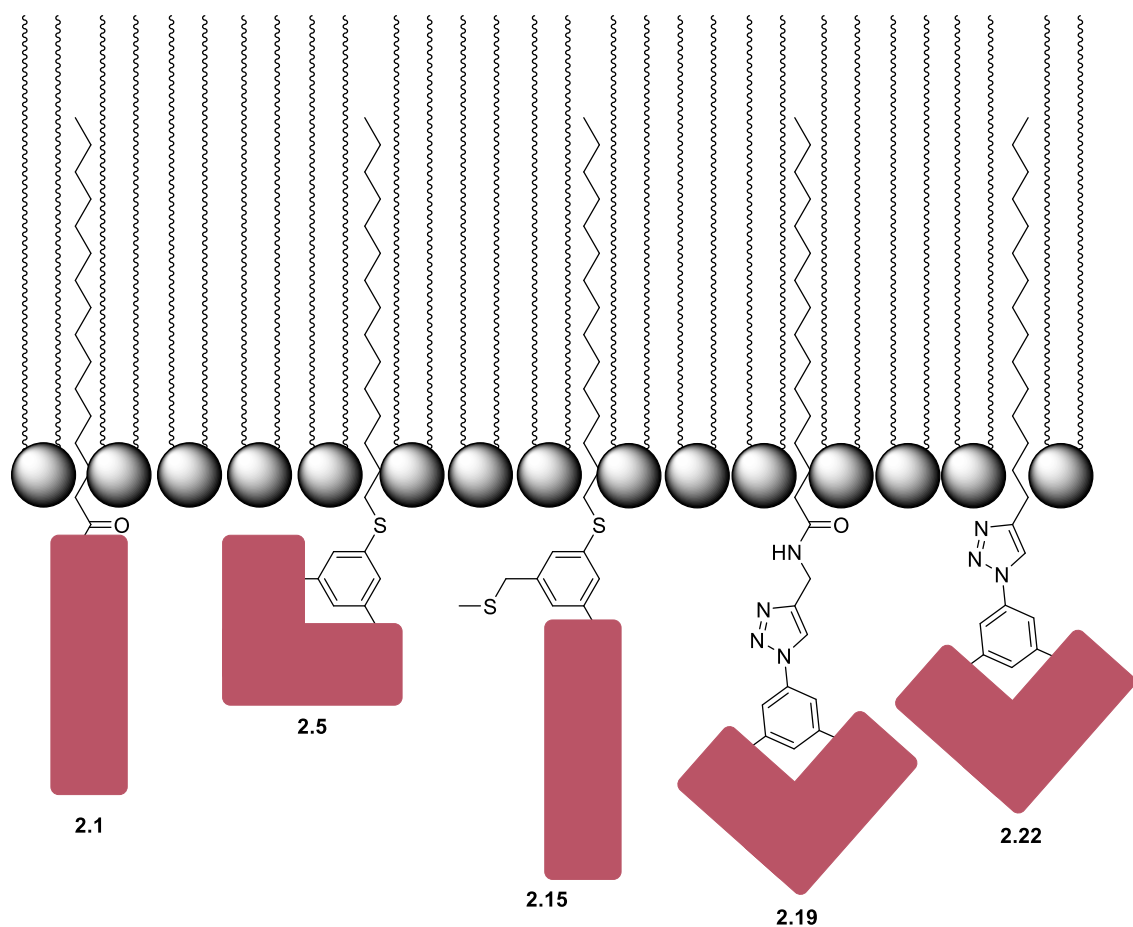


Figure 2.35: Proposed effect of elongated linkers on intracellular pepducin localisation. General peptide sequence is shown in red and not to scale.

Treatment of HEK-293 cells with the extended pepducins resulted in strong concentration-dependent calcium efflux for triazine **2.20** and triazinane **2.21** with EC_{50} values of $39 \mu\text{M}$ and $38 \mu\text{M}$, respectively, providing comparable EC_{50} values to **2.1** (**Figure 2.36A**, **Table 2.15**). However, the phenyl linker again provided a large improvement in reducing the agonist activity of the series, with amide linker phenyl pepducin **2.19** yielding an EC_{50} of $160 \mu\text{M}$ and non-amide linker pepducin **2.22** not yielding a calculable EC_{50} (**Figure 2.36A**, **Table 2.15**).

Inhibition assays for the extended pepducins demonstrated inhibitive properties for triazine **2.20** and triazinane **2.21**. While triazine **2.20** displayed a reduced IC_{50} with 54 μ M, triazinane **2.21** yielded a slightly improved IC_{50} in comparison to **2.1** with 22 μ M.

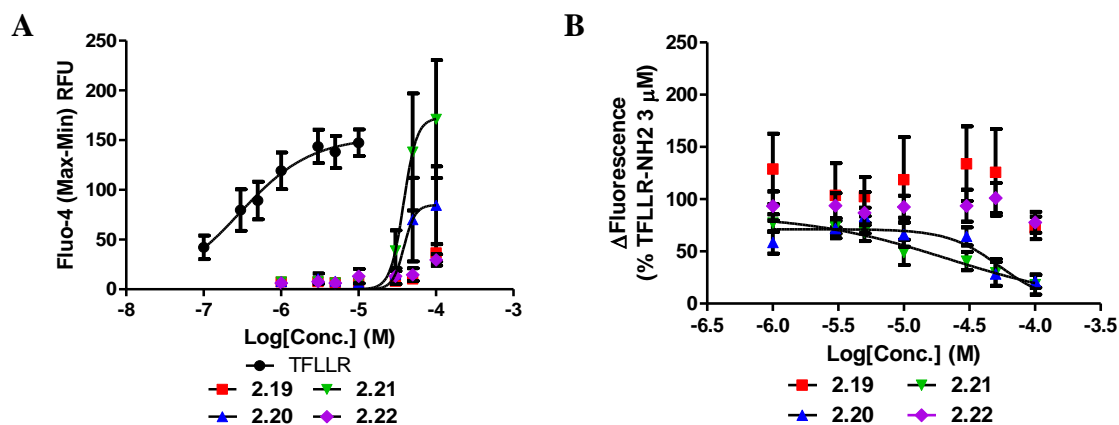
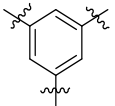
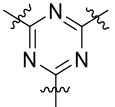
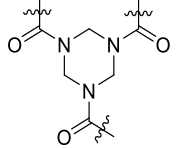


Figure 2.36: Characterisation of PAR1-derived pepducin library containing a triazole within the linker moiety. **A** HEK-293 cells loaded with Fluo-4 Direct were treated with PAR1 pepducins and the resulting fluorescence change monitored. Dose-response curves for activation of calcium signalling were then plotted for each pepducin. **B** Following pre-treatment of HEK-293 cells with the pepducins, cells were treated with TFLLR-NH₂ at 3 μ M. Dose response curves for inhibition of TFLLR-NH₂ were then plotted for each pepducin. Data represent an N=4 with mean \pm SEM.

Table 2.15: EC_{50} and IC_{50} values for PAR1-derived pepducins containing a triazole within the linker. ^a EC_{50} values obtained by treating HEK-293 cells loaded with the calcium dye Fluo-4 Direct and recording the change in fluorescent output (**Figure 2.36**). ^b IC_{50} values obtained by pre-treating HEK-293 cells loaded with Fluo-4 with pepducins and further treating with PAR1 agonist (TFLLR-NH₂).

Linker	Pepducin Type - Name	EC_{50}^a	IC_{50}^b
	Amide – 2.19	160 μ M	N/A
	Alkyl – 2.22	N/A	N/A
	Amide – 2.20	39 μ M	54 μ M
	Amide – 2.21	38 μ M	22 μ M

2.5.3 Summary

Given the off-target activity shown for PZ-128, the parameters for an improved PAR1-derived pepducin are straightforward: firstly, the pepducin would need to show a lower level of off-target activation in various assays (higher EC_{50}); secondly, the pepducin would need to have an equivalent or improved inhibitory property in the form of lower IC_{50} values. Drugs which fulfil both criteria would be considered significant advancement on PZ-128.

It can be clearly seen that the pepducins which contain the phenyl linker (**2.5**, **2.15**, **2.19** and **2.22**) were all unsuccessful as candidates. While **2.5**, **2.19** and **2.22** caused very little response in calcium signal compared to the rest of the library they also displayed the worst levels of inhibition. Extended analogues **2.19** and **2.22** caused no inhibition at all of TFLLR-NH₂ mediated calcium signalling. Conversely, **2.15** inhibited TFLLR-NH₂ mediated signalling with $IC_{50} = 59 \mu\text{M}$ but also caused activation of calcium signalling with $EC_{50} = 41 \mu\text{M}$, failing to provide an improvement over PZ-128.

The pepducins with triazine linkers proved slightly better with inhibition, with linear analogue **2.16** and extended analogue **2.20** providing IC_{50} values of $65 \mu\text{M}$ and $54 \mu\text{M}$ respectively. However, each triazine pepducin also caused an increase in calcium signal upon treatment.

Triazinane analogues **2.7**, **2.17** and **2.21** displayed a similar profile, with all displaying modest inhibition of PAR1 alongside comparable agonistic properties to **2.1**. Most notably, treatment with extended triazine **2.20** and triazinane **2.21** provided the lowest EC_{50} values within the triazole class of pepducin, both displaying slightly under $40 \mu\text{M}$.

Overall, the most promising new candidate would be **2.21**. The IC_{50} value of $22 \mu\text{M}$ is comparable to those of PZ-128 and SCH79797, $26 \mu\text{M}$ and $5 \mu\text{M}$, respectively (**Figure 2.5**). Despite the low EC_{50} value of $38 \mu\text{M}$ for **2.21**, an improvement was still made over **2.1** with an EC_{50} of $27 \mu\text{M}$.

2.6 Fluorescent-tagged pepducins

As a means of monitoring pepducin localisation during cell-based application, a modified pepducin was proposed incorporating a fluorescent tag into the chemical structure to allow experiments using microscopy to be performed. The fluorescent tag chosen for this application was BODIPY-TMR, due to its peak emission (λ_{ex}) occurring at 570 nm, far removed from the 516 nm used for readings within the 96-well plate assays (**Figure 2.37**).

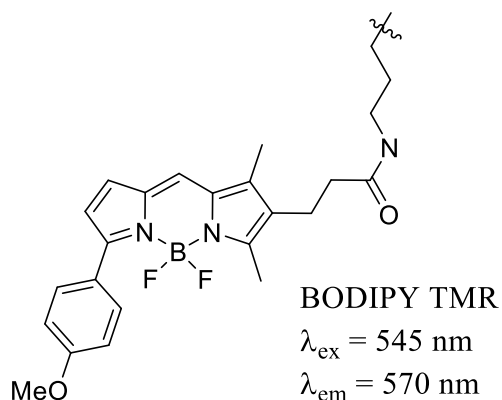
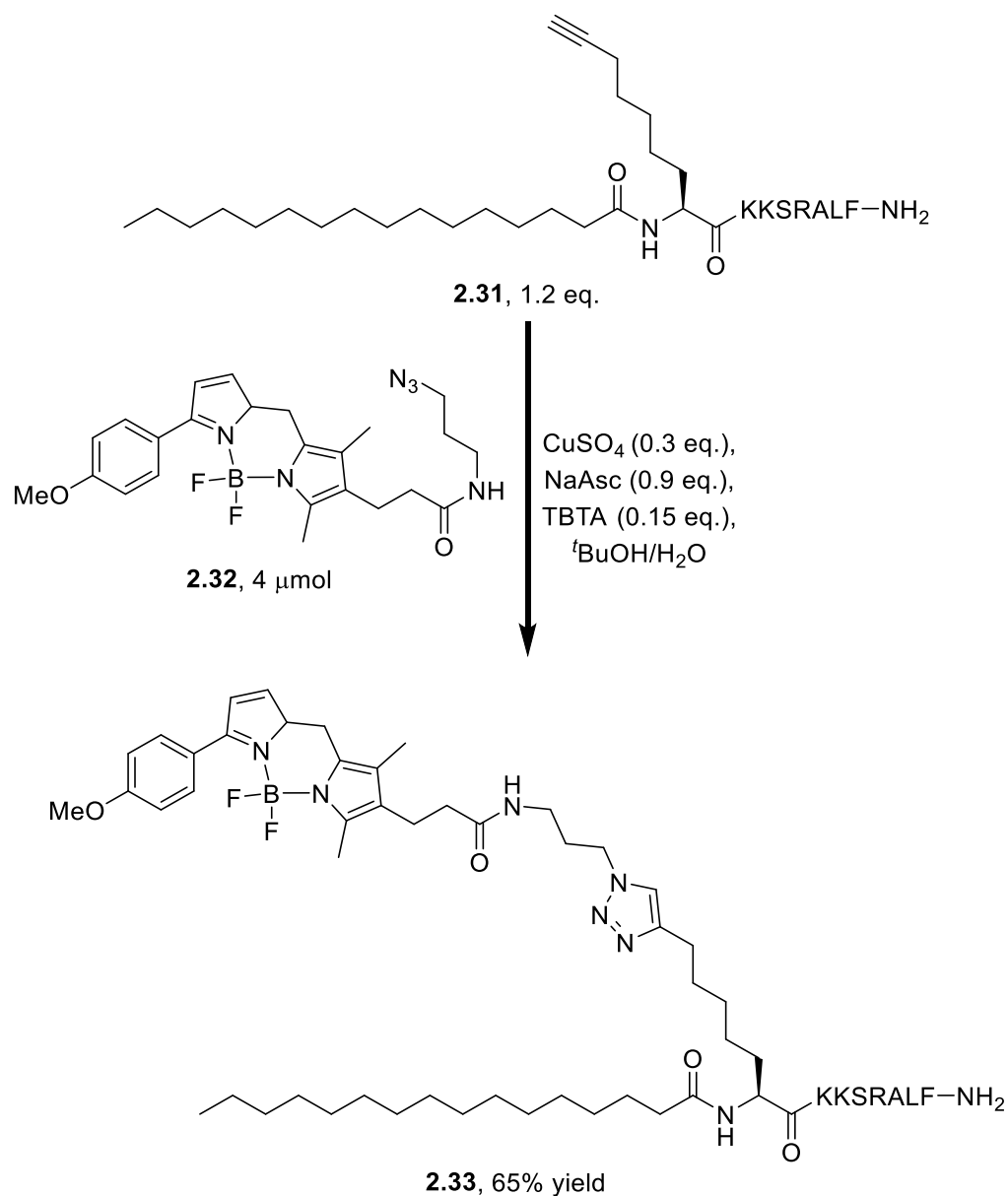


Figure 2.37: Chemical structure of fluorescent tag, BODIPY TMR.

With regards to the incorporation into the pepducin, **2.1** was used as the initial scaffold. By elongating the peptide sequence to 8 amino acids, the BODIPY tag could be introduced at the N-terminal amino acid residue followed by the **2.1** peptide sequence: KKSRALF. This localisation hypothetically would prevent the BODIPY tag from interfering with the function of the 7-amino acid chain inherent in **2.1**. Additionally, the peptide sequence was chosen as the location for the tag as the alternative, binding within the palmitoyl chain, would likely lead to deterioration in the pepducins capability of travelling across the cell membrane.

To introduce the BODIPY tag into the pepducin, a CuAAC reaction was performed using an alkynylated analogue of **2.1**, **2.31**, and BODIPY TMR Azide **2.32**. The CuAAC reaction provided BODIPY-tagged pepducin **2.33** in 65% yield.



Scheme 2.10: Synthesis of BODIPY-tagged pepducin **2.33** via the CuAAC reaction of an alkynylated analogue **2.31** with BODIPY-TMR-azide **2.32**.

Having gained access to BODIPY-tagged pepducin **2.29**, the pepducin was tested for its fluorescent emission under the same excitation wavelength used within the Fluo-4 assays ($\lambda_{\text{ex}} = 494 \text{ nm}$). Regrettably, by obtaining emission spectra for this excitation wavelength, it can be seen that **2.33** was providing a fluorescent response within the plate. Based on

this, it would be difficult to measure the impact of the BODIPY-TMR tag within **2.33** on its function in the calcium signalling assays.

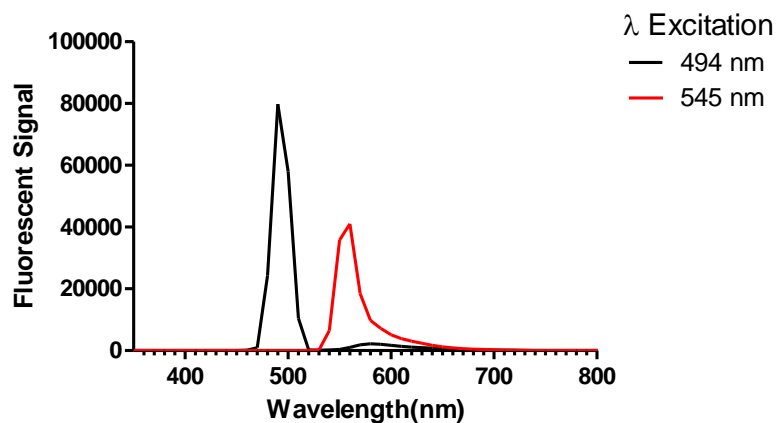


Figure 2.38: Emission spectra for a solution of **2.33** (50 μ M) at two excitation wavelengths of 494 nm and 545 nm. Data represents a single experiment.

Despite the conflicting emission spectra obtained above, it was necessary to ascertain if the inclusion of a fluorescent tag in pepducin **2.33** would have a significant impact on the biological function of the compound in comparison to **2.1**. Western Blot experiments were used to quantify the effect of each compound on ERK1/2 activation within HEK-293 cells (**Figure 2.39**). Here, it can be seen that **2.29** treatment does still activate ERK1/2, but to lower levels than with the same concentration of **2.1**.

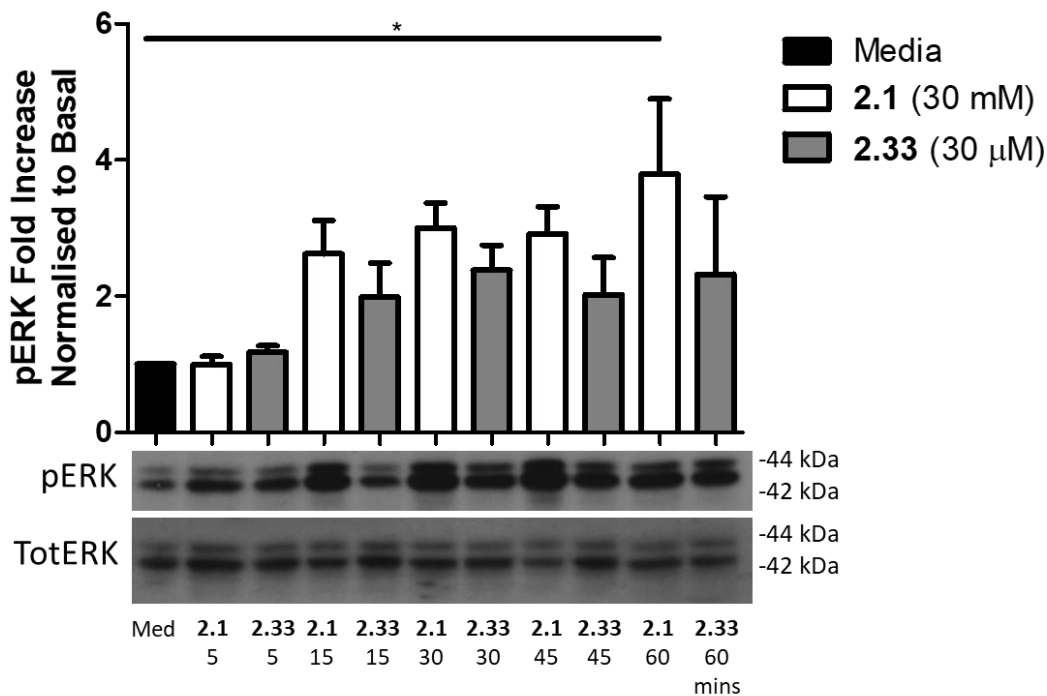


Figure 2.39: Activation of ERK1/2 in response to thrombin, **2.1** and **2.33**. Thrombin was applied at 3 U/mL while PZ-128 and BODIPY-PZ-128 were applied at 30 μM for a range of time points. Data represents an N=3 with mean ± SEM, with individual timepoints being normalised to the levels of pERK caused by thrombin.

Given the outcome of the initial experiments with **2.33** not providing clear insight into its impact on PZ-128-mediated signalling, as well as time constraints, it was decided to stop pursuing the fluorescent platform for pepducin monitoring.

2.7 Summary

By using robust signalling assays, an in-depth pharmacological profile was developed for PZ-128 (**2.1**). This study verified the allosteric nature for the inhibition of PAR1 as described in the literature using Schild plots and allosteric shift models. However, the pharmacological profile also highlighted the capability for PZ-128 to activate pathways associated strongly with platelet function. Following the initial inhibition and activation experiments, the pathway through which the signalling was mediated was investigated. Experiments showed the source of calcium ions to be intracellular and also suggested a different mechanism of action in comparison to the natural PAR1 agonists. This led to an investigation into PAR1 independence for PZ-128-mediated activity, which was confirmed using various assays in systems either temporarily lacking PAR1 (desensitised HEK-293 cells) or completely devoid of PAR1 (mouse platelets) where PZ-128 continued to mediate activation of signalling pathways.

The structure dependence of **2.1**-associated activity demonstrated herein would suggest the peptide sequence is interacting in such a way as to propagate signalling within cells. With regards to the design of pepducins, the implementation of key GPCR sequences involved in downstream signalling seems flawed. By utilising a GPCR ICL for the structure, interactions demonstrated by these regions of the protein could be inherited. This is evident with the modification of the sequence, whereby many pharmacological events recorded with **2.1** were reversed with the scrambled peptide sequence in **2.2**.

Potential improvements to the pharmacology of PZ-128 were examined, with a small library of novel pepducins derived from PAR1 being investigated. Ultimately, only one pepducin showed a capability to inhibit at a comparable level to PZ-128 in elongated triazinane pepducin **2.21** which displayed an IC_{50} of 22 μ M. Unfortunately, those molecules which did successfully inhibit PAR1-mediated signalling also activated signalling on their own. Moving forward, **2.21** would be the only pepducin of interest given its much-improved IC_{50} over the rest of the library.

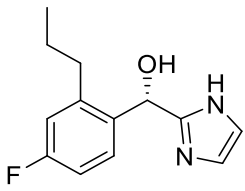
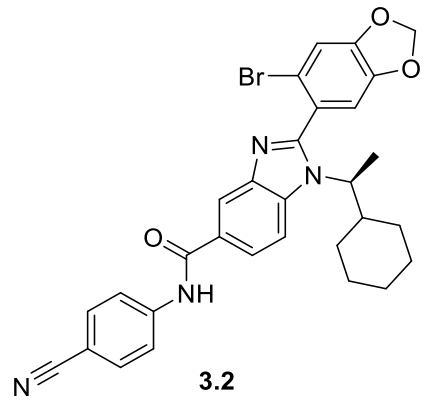
Chapter 3 Small Molecule Allosteric Inhibitors of PAR2

3.1 Introduction

Recent work published by Cheng *et al.* described the synthesis and biological activity of two novel allosteric inhibitors of PAR2: AZ8838 (**3.1**) and AZ3451 (**3.2**) (**Table 3.1**).⁴

Of the two published compounds, AZ8838 was highlighted as a good starting point for a Fast-Follower approach for lead identification. By calculating the ligand efficiency (LE), a drug efficiency metric used prominently in fragment based drug discovery, for each species using the formula $LE = (1.4 \times -\log IC_{50})/\#HA$, where #HA is the number of heavy atoms (non-hydrogen atoms), a comparison between the two reported molecules was drawn (**Table 3.1**).^{167,168} Despite modest potency compared to AZ3451, its lower mass provides AZ8838 with an improved LE, ideal for lead-like drug compounds.^{145,169} Therefore, the lead-like properties of AZ8838 mean there is a larger space to explore in modifications to the chemical structure in order to secure improved binding with PAR2, and thus improved IC_{50} , assuming LE could be maintained while exploring the structure-activity relationship (SAR) between PAR2 and AZ8838.

Table 3.1: Published PAR2 antagonists AZ8838 (**3.1**) and AZ3451 (**3.2**). LE calculated for **3.1** and **3.2** using the formula: $E = (1.4 \times -\log IC_{50})/\#HA$, where #HA is the number of heavy atoms (non-hydrogen atoms).

		
3.1	3.2	
IC_{50}	1500 nM	5 nM
MWt	234.27	571.48
LE	0.480	0.306
CLog P	1.9	8.0

In addition to the presented biological data, Cheng *et al.* also reported a crystal structure of both AZ8838 and AZ3451 bound within PAR2.⁴ This provided information about the interactions within the binding pocket, highlighting important functionalities within the lead structure and key residues within the protein (**Figure 3.1A-B**). Of note in the binding site were the hydrogen bonds observed between AZ8838 and PAR2. The imidazole group was shown to interact with Tyr82, located in the first transmembrane helix, and Asp228, located in the second ECL. Additionally, hydrogen bonding between the linking hydroxyl group and His135, residing in the second transmembrane helix, was also highlighted. However, despite the available X-ray data, there was a paucity of SAR information known for the AZ8838 template.

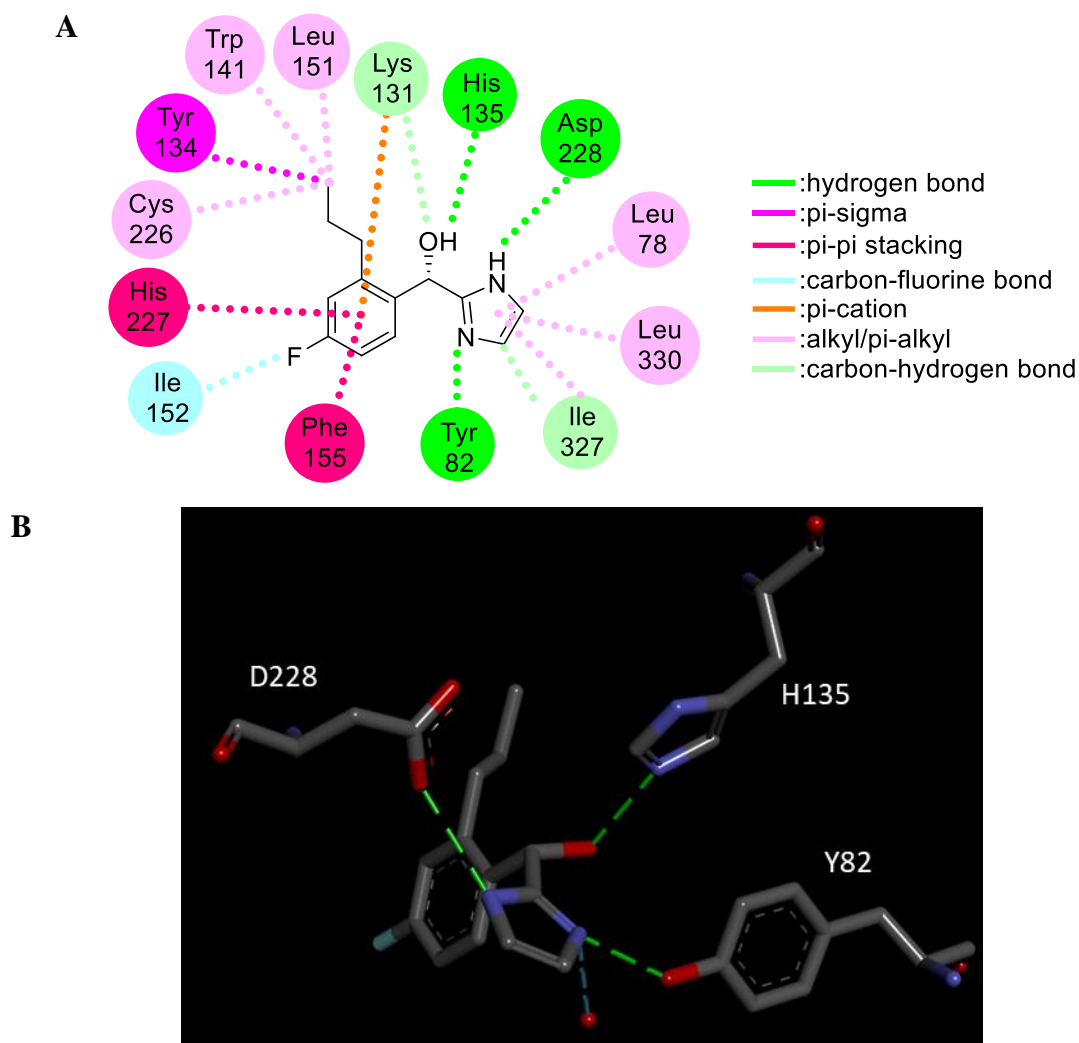


Figure 3.1: Observed hydrogen bonding between AZ8838 and PAR2. **A** Chemical structure of AZ8838 denoted with amino acid interactions with PAR2 binding pocket. **B** AZ8838 within the PAR2 binding site, hydrogen bonding denoted in green.⁴

3.2 Aims and Objectives

The aim of this project is to design, synthesise and evaluate the effectiveness of novel analogues of known the PAR2 inhibitor AZ8838 (**3.1**). We reasoned that by making discrete modifications to the structure of AZ8838, it would be possible to elucidate a more detailed SAR between AZ8838 and PAR2. Additionally, modification of the chemical structure could lead to improved potency for inhibition of PAR2 function.

The design of AZ8838 analogues will be focused on three distinct regions of the molecule: the imidazole ring, the hydroxyl linker and the propyl substitution on the phenyl ring. Binding of the designed analogues will be simulated using computational docking techniques. These techniques will utilise the crystallographic data published by Cheng *et al.* with AZ8838 bound within PAR2 to accommodate the novel structures generated herein and report on calculated binding potencies.⁴ Analogues will be synthesised using procedures adapted from the synthetic route towards AZ8838 utilised by Cheng *et al.*.⁴ Modification from the route will be made where necessary to provide structurally diverse analogues.

Following synthesis, biological assessment of the AZ8838 analogues will be carried out using a luciferase assay in Nf- κ B reporter cells, activation of which PAR2 is a known effector.¹⁷⁰

3.3 *In Silico* Docking Studies

As part of the study published by Cheng *et al.*, AZ8838 was successfully co-crystallised with PAR2 and X-ray crystallographic data obtained.⁴ The resulting protein database (.pdb) file was used herein to analyse the docking of AZ8838 analogues *in silico*. However, prior to docking the analogues, validation of the software would need to be carried out.

3.3.1 Validation of Computational Studies – AutoDock Vina

AutoDock Vina was initially chosen for the *in silico* study as it is open access software requiring little specialised knowledge to run basic experiments.¹⁷¹ Before docking the compound library into the PAR2 crystal structure, a validation experiment was carried out whereby AZ8838 and its opposing, inactive enantiomer ((*S*)-**3.1** and (*R*)-**3.1**, respectively) were docked. In addition to replicating the binding mode of AZ8838, it was anticipated that the binding of (*S*)-**3.1** would provide a baseline for further docking studies.

Initial attempts at docking (*S*)-**3.1** were performed using a large cross-section across PAR2 as the area for docking.¹⁷¹ Unfortunately, contrary to the published crystal structure (**Figure 3.2A**), the docking of (*S*)-**3.1** within this region resulted in the most preferred binding pose occurring outside the transmembrane helix of PAR2 (**Figure 3.2B**).

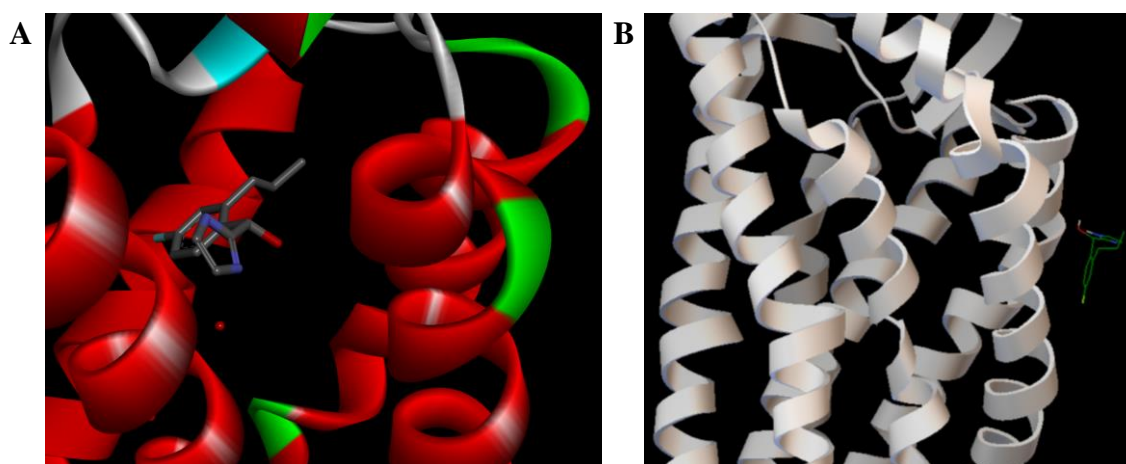


Figure 3.2: Initial docking of (*S*)-**3.1** within the PAR2 crystal structure with AutoDock Vina. **A** Crystal structure of PAR2 binding site with AZ8838.⁴ **B** Generated docking structure of (*S*)-**3.1** using AutoDock Vina with a cross-sectional search area

In an attempt to find a low energy binding mode similar to the published structure, the docking area was limited to an area focussed around the crystallographically determined AZ8838 binding site. It was anticipated that AutoDock Vina would more easily identify a low energy binding pose similar to the published structure. However, while the lowest energy solution lay within the binding site, the orientation of the molecule did not align with reported data and provided a predicted affinity which was less favourable than the previous attempt (**Figure 3.3**).

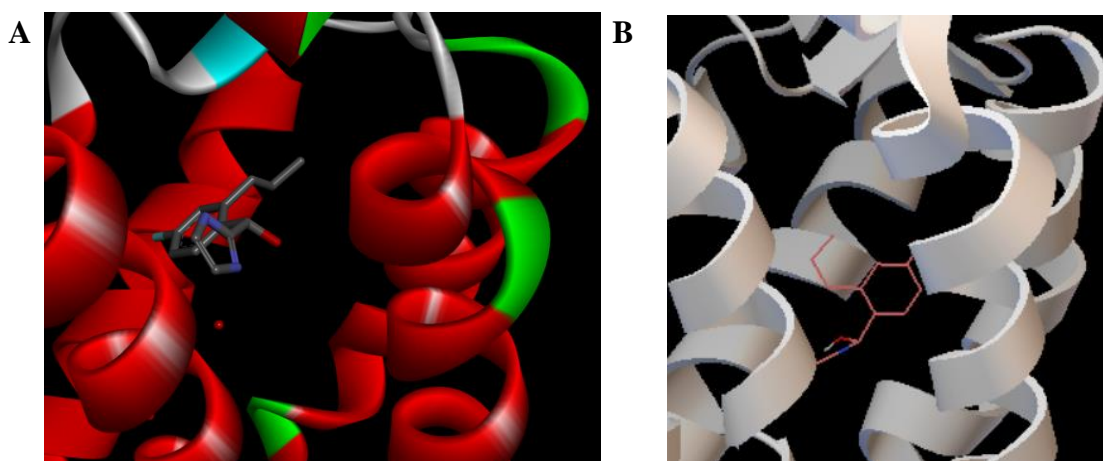


Figure 3.3: Further docking of (*S*)-**3.1** within the PAR2 crystal structure with AutoDock Vina. **A** Crystal structure of PAR2 binding site with AZ8838.⁴ **B** Generated docking pose of (*S*)-**3.1** using AutoDock Vina with search area limited around the binding site.

Ultimately, AutoDock Vina proved to be unsuitable for docking simulations within the PAR2/AZ8838 binding pocket. This was attributed to the method of preparation for files used throughout the docking, namely the removal of water molecules from the crystal structure. Water molecules were required to be removed in order to simplify the calculations for this particular software package. However, interrogation of the binding interactions between AZ8838 and PAR2 show a hydrogen bond interaction between the sp^2 nitrogen of the imidazole with a water molecule in the binding site (**Figure 3.4**). As such, removing the water molecules from the crystal structure could have a significant impact on the binding mode obtained from the simulations.

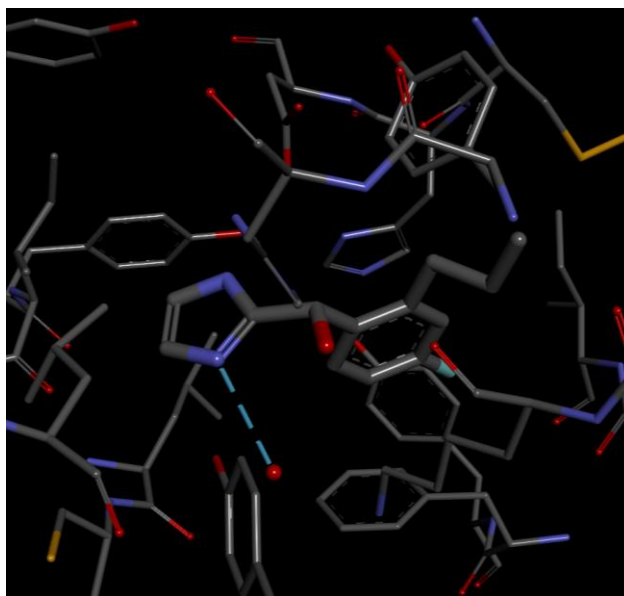


Figure 3.4: Hydrogen bond interaction between AZ8838 and a water molecule in the PAR2 binding site.⁴

Based on this, attempts were made to dock (*S*)-**3.1** while maintaining the presence of water molecules within the crystal structure. However, ultimately AutoDock Vina failed to produce a solution under these circumstances. Given the failure to generate a similar binding mode for (*S*)-**3.1** to the published AZ8838, alternative software was required for the docking studies.

3.3.2 Validation of GOLD

With the use of AutoDock Vina shown to be unsuitable, an alternative was found in GOLD.¹⁷² While the use of other free software such as AutoDock Tools was considered, an active license was available for GOLD which was chosen for the study due to its diverse profile for achieving successful docking within known binding sites across a range of proteins.¹⁷³

Within GOLD, a variety of Fitness scoring functions were available for docking simulations: ChemPLP, GoldScore, ChemScore, Astex Statistical Potential and User Defined. User-defined fitness functions were immediately ruled out, given the time

requirements of optimising the scoring function. From the remaining four functions, there is no clear best function. Unlike the other three functions, the Astex Statistical Potential (ASP) is a knowledge-based scoring function: the scoring function relies on a large sample size of known binding affinities to predict distance-dependent pairwise potential forces for the binding.¹⁷⁴

Of the other three functions, GoldScore is a force-field based scoring function, deriving its binding simulations from force-fields such as AMBER or CHARMM.¹⁷² GoldScore is a scoring function which has been optimised for ligand binding position, rather than binding affinity making it less suitable for the intended analyses. ChemScore and ChemPLP, conversely, are empirical functions which have been designed to reproduce data of experimentally complex structures.^{175–177} This was ideal for the analyses to be carried out in this study, where the first step was the reproduction of the AZ8838 binding mode with (S)-**3.1**.

ChemPLP is an empirical fitness function which derives its scoring functions on parameters from two other fitness functions: ChemScore and Piecewise Linear Potential (PLP) (**Figure 3.5**). Given the consideration for the ChemScore fitness function within ChemPLP, its promising track record in drug validation studies and its high performance as GOLD's default scoring function, it was decided ChemPLP would be used throughout the study for AZ8838 and its analogues.

The final ChemPLP fitness function derives from multiple parameters used within ChemScore as well as the PLP fitness model (**Figure 3.5A**), where the three ChemScore terms relate to distance-dependent hydrogen bonding ($f_{Chem-HB}$), angle-dependent hydrogen bonding ($f_{Chem-Cho}$) and metal bonding ($f_{Chem-met}$). Additionally, the PLP function is derived from clashes between ligand and protein ($f_{lig-clash}$), torsion of the ligand ($f_{lig-tors}$), covalent bonding between ligand and protein ($f_{Chem-cov}$), side-chain flexibility ($f_{Chem-prot}$) and interactions including water molecules (f_{cons}) (**Figure 3.5B**).¹⁷⁷

$$\begin{aligned}
 \mathbf{A} \quad & \text{Fitness}_{\text{ChemPLP}} = \text{Fitness}_{\text{PLP}} - (f_{\text{Chem-HB}} + f_{\text{Chem-Cho}} + f_{\text{Chem-met}}) \\
 \mathbf{B} \quad & \text{Fitness}_{\text{PLP}} = -(w_{\text{PLP}} \cdot f_{\text{PLP}} + w_{\text{lig-clash}} \cdot f_{\text{lig-clash}} + w_{\text{lig-tors}} \cdot f_{\text{lig-tors}} \\
 & + f_{\text{Chem-cov}} + w_{\text{prot}} \cdot f_{\text{Chem-prot}} + w_{\text{cons}} \cdot f_{\text{cons}})
 \end{aligned}$$

Figure 3.5: Equations for the derivation of ChemPLP (**A**) and, correspondingly, PLP (**B**) scoring functions.

Once again, (*S*)-**3.1** was docked into the PAR2 crystal structure to determine if a binding mode which resembled the published structure for AZ8838 could be obtained.⁴ Firstly, a 3D structure for (*S*)-**3.1** was energy minimised using Chem3D. The docking area was then established in a sphere with a radius of 10 Å centred on the location of AZ8838 within the published crystal structure. Following this, the energy minimised structure was docked multiple times yielding multiple binding poses each with their own ChemPLP scores. The resulting structures were overlaid with the published AZ8838 structure (**Figure 3.6**). Fortunately, the binding poses obtained from the simulation very closely resembled that published by Cheng *et al.*, providing some validation of the use of GOLD in conjunction with the ChemPLP algorithm for further docking studies.⁴

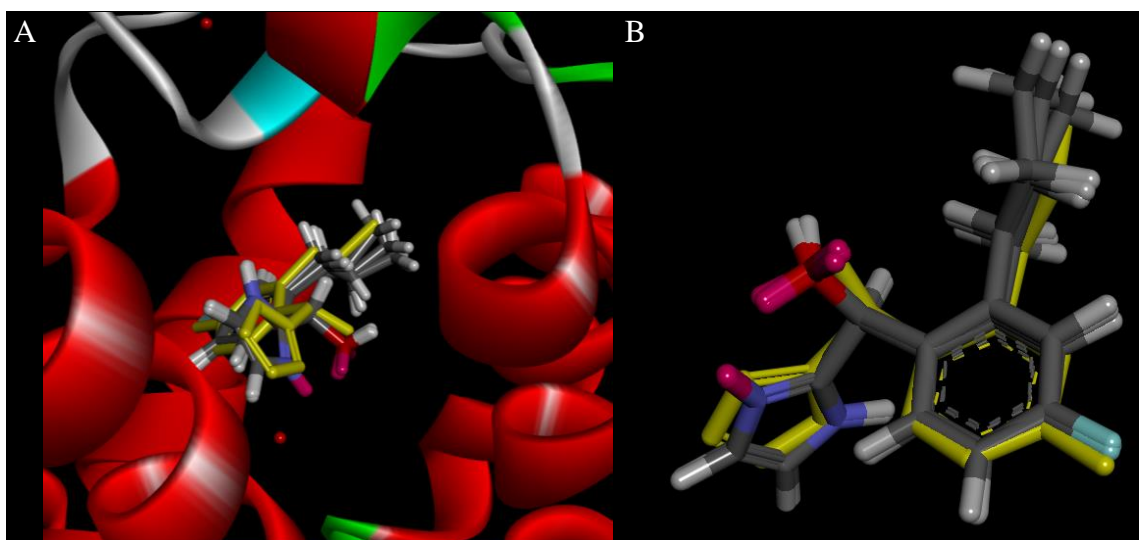


Figure 3.6: Overlaid docking modes of (*S*)-**3.1** with published binding mode of AZ8838 (yellow). **A** Generated binding poses of (*S*)-**3.1** overlaid with AZ8838 (yellow) within the PAR2 binding site. **B** Overlaid binding poses with AZ8838 (yellow) minus protein structure.

With confirmation of the binding mode obtained, a final validation experiment was carried out whereby (*R*)-**3.1** was also docked and compared to (*S*)-**3.1** with the expectation that a lower binding score would be obtained to reflect the lack of activity of the (*R*)-isomer of AZ8838.⁴ By examining the binding mode of (*R*)-**3.1**, it can be seen that the imidazole and phenyl groups remain in roughly the correct space and orientation (**Figure 3.7A**). However, the inversion of the chiral centre leads to the hydroxyl group in the wrong vector for maintaining the hydrogen bond interaction observed with the (*S*)-enantiomer. By plotting the ChemPLP scores for each generated binding mode (9 scores over 3 individual experiments) it can be seen that (*R*)-**3.1** provides a lower binding score than (*S*)-**3.1**, which is reflective of the relative activity of the two enantiomers (**Figure 3.7B**).

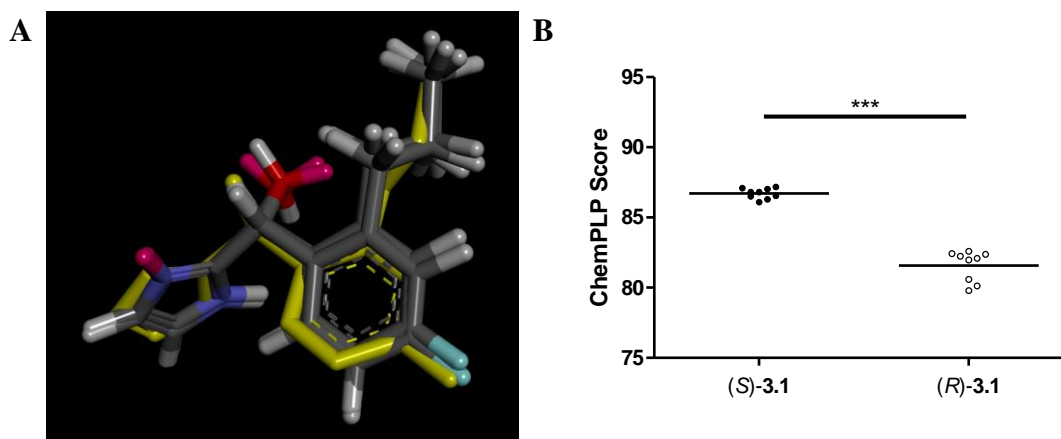


Figure 3.7: Comparison of docking in PAR2 with (S)-3.1 and (R)-3.1. **A** Overlaid binding modes of (R)-3.1 with AZ8838 (yellow). **B** Docking scores for all docked structures of (S)-3.1 and (R)-3.1 represented as a scatter plot. ● = “active” (S) conformation of linker, ○ = “inactive” (R) conformation of linker, — = mean value. Data represents n = 3, with each experiment reporting at least three binding scores for each analogue. *** denotes p < 0.001.

3.3.3 Docking of AZ8838 analogues

With validation experiments in GOLD carried out, a library of AZ8838 analogues could then be docked. In total, the (S)- and (R)-isomers of 27 analogues were docked and compared to the scores generated with 3.1. Within the chemical structure of AZ8838, there were three broad areas targeted for diversification (**Figure 3.8**). Namely, the imidazole group, the linker between the two aromatic rings and the propyl group on the phenyl ring. The imidazole group was chosen for its role in hydrogen bonding interactions within the binding pocket, where it bonds to Asp228 and Tyr82, residing in ECL2 and TM1 respectively.⁴

The linker region, containing a chiral benzylic alcohol, has a pivotal role in the potency of AZ8838, with the (S)-enantiomer as the active form reported by Cheng *et al.*⁴ It was also reported that changing the linker to the (R)-enantiomer completely removed the antagonist properties of AZ8838, showing the importance of the linker, although the corresponding data accompanying this observation was omitted from the publication by Cheng *et al.*⁴

Finally, the propyl chain is known to fit under a disulfide bridge between Cys148 and Cys226.⁴ While this would imply limited scope for expansion of the propyl group, it was decided to explore the tolerance for changes by expanding or reducing the steric requirements of the alkyl chain. While modification of the fluorine was considered for this study, given its role in maintaining interaction with Ile152, utilising the reported synthesis for AZ8838 (*vide infra* **Section 3.4**) would have required significant deviation to access fluorine analogues.⁴ As such, the propyl chain was prioritised for this study.

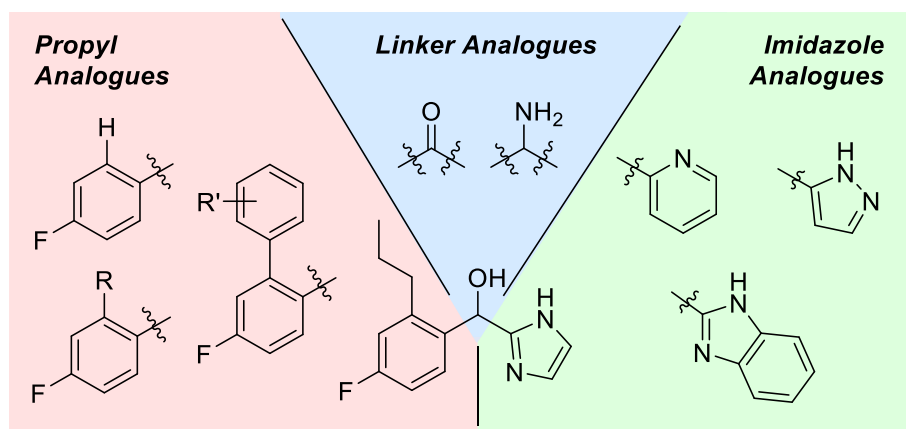


Figure 3.8: Proposed sites within AZ8838 for diversification. R = Br, cyclopropyl, cyclohexyl, Ph, pyridinyl, furanyl. R' = Me, ^tBu, CF₃, NMe₂

3.3.3.1 Imidazole Analogues

Firstly, the imidazole region was explored predominately through the removal of the hydrogen bond interactions inherent in the heteroaromatic ring (**Figure 3.9**). Pyrrole **3.3** and pyridine **3.4** demonstrate the loss of a single hydrogen bond interaction, losing an acceptor and a donor, respectively (**Figure 3.9A**). This is taken further in phenyl analogue **3.5**, where both hydrogen bonding groups are removed whilst aromaticity is maintained (**Figure 3.9A**).

By comparing the ChemPLP docking scores of the (*S*)-analogues to those of (*S*)-**3.1**, it can be noted that each modification in this series is predicted to have a negative impact on

binding affinity within PAR2 (**Figure 3.9B**). In each case, the removal of hydrogen bonding interactions had a negative impact on the simulated binding. Removal of the hydrogen bond accepting nitrogen to form pyrrole (*S*)-**3.3** provides an initial decrease in comparison to (*S*)-**3.1**. The docking score deteriorates further with the removal of the hydrogen bond donating group to form pyridine (*S*)-**3.4** whilst removal of both hydrogen bonding groups provides the lowest docking score of the series in phenyl analogue (*S*)-**3.5**. By interrogating the generated binding modes, each analogue is shown to lose the key hydrogen bonds with Tyr82 or Asp228 (**Figure 3.9C**). Pyrrole (*S*)-**3.3** maintains an interaction with Tyr82, losing Asp228, while the pyridinyl and phenyl analogues lose both interactions (**Figure 3.9C**). However, the further decreases in docking score for **3.4** and **3.5** could also be attributed to increasing the ring size and the subsequent effect this would have on the occupied volume of space within the imidazole pocket.

The importance of stereochemistry is also highlighted, with (*S*)- and (*R*)-enantiomers for **3.3** and **3.5** displaying significantly different distributions of docking scores. Interestingly, the trend for each is different: (*S*)-**3.3** demonstrated a higher binding affinity than (*R*)-**3.3** whilst phenyl analogue (*R*)-**3.5** showed higher binding than its (*S*)-enantiomer. This difference could account for more flexible rotation with **3.5**, with the lack of hydrogen bonding inherent in the phenyl ring allowing the molecule to recover from suboptimal hydrogen bonding with the hydroxyl linker.

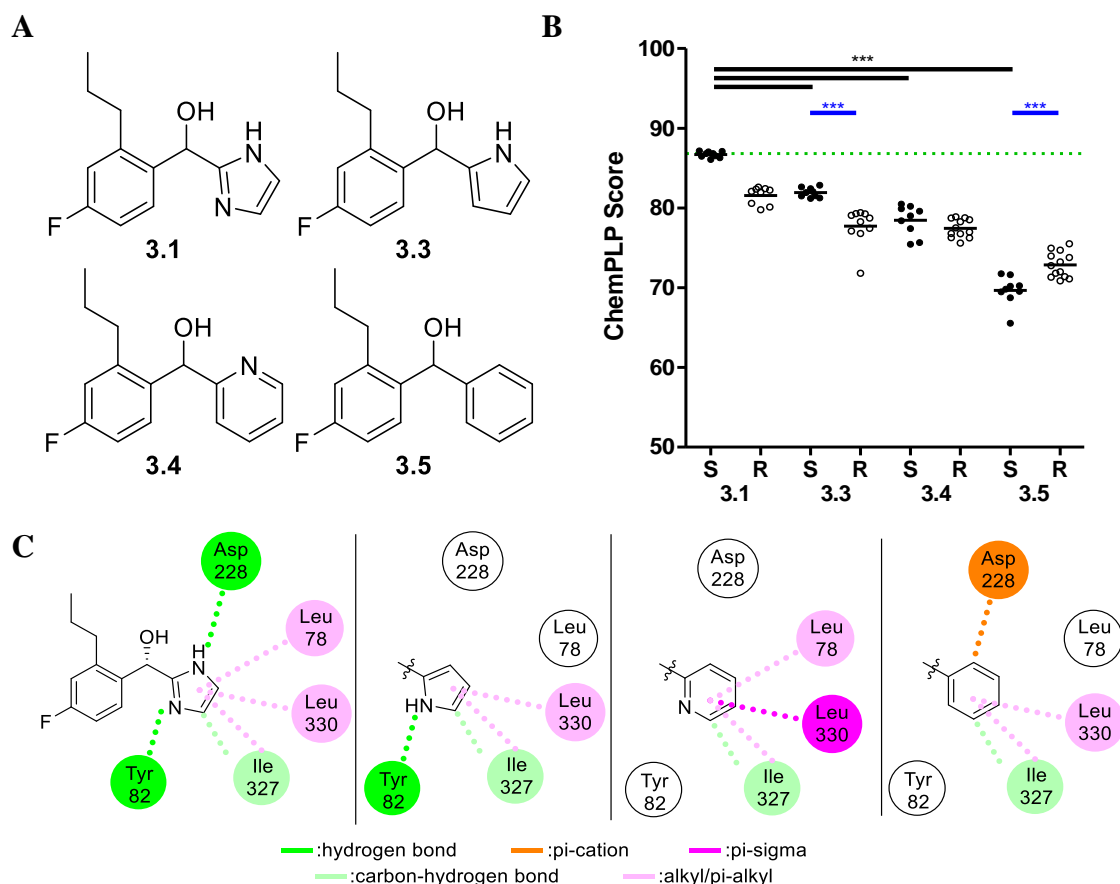


Figure 3.9: Effect of removal of hydrogen bonding functionalities in the imidazole region on binding within PAR2. **A** Chemical structure of three novel AZ8838 analogues (**3.3**, **3.4** and **3.5**). **B** ChemPLP docking score of (*S*)- and (*R*)-enantiomers of **3.3**, **3.4** and **3.5** compared to **3.1** represented as a scatter plot. ● = “active” (*S*) conformation of linker, ○ = “inactive” (*R*) conformation of linker, — = mean value. Data represents $n = 3$, with each experiment reporting at least three binding scores for each analogue. *** denotes $p < 0.001$. **C** Interaction maps showing key protein-ligand interactions within imidazole binding pocket, comparing (*S*) enantiomer of **3.1** with those of **3.3**, **3.4** and **3.5**.

The importance of hydrogen bonding interactions was further explored with additional imidazole analogues (**Figure 3.10A**). Imidazole **3.6** alongside pyrazoles **3.7** and **3.8** represent the movement of hydrogen bonding groups around the ring, in order to identify the optimised vectors within the imidazole binding pocket (**Figure 3.10A**). It was anticipated that small changes to the hydrogen bonding interactions, without removing them, would allow a more detailed picture to be built upon the requirements for efficient binding within the AZ8838 binding pocket of PAR2 and could enable comparison with

known X-ray data through the docking studies. Triazole **3.9** is a further example of a heterocycle of a similar size which maintains at least a hydrogen bond donor and a hydrogen bond acceptor (**Figure 3.10A**). In each case, docking was performed with structures of each tautomer of the compounds where appropriate, due to the inability for GOLD to accommodate tautomerization (**Figure 3.10A**).

By comparing ChemPLP scores to (*S*)-**3.1**, each modification resulted in a significant decrease in the docking score. Imidazole (*S*)-**3.6** and pyrazole (*S*)-**3.7** performed the best in the series, showing similar docking scores to pyrrole (*S*)-**3.4** above (**Figure 3.10B**). Further deviation towards pyrazole (*S*)-**3.8**, with the movement of both nitrogen atoms, further deteriorates the docking score while the incorporation of an additional nitrogen atom in triazole (*S*)-**3.9** provides the lowest scores of the series (**Figure 3.10B**). The decrease in ChemPLP score for this series helps to highlight that the hydrogen bonding interactions with the imidazole moiety are key to binding affinity within the binding pocket and manipulation, through transfer around the ring or removal, is predicted to lead to a reduced binding affinity.

By scrutinising the interactions between each ligand and the binding pocket, the importance of Tyr82 and Asp228 is highlighted further. Each analogue in the series is shown to be losing one or both of the hydrogen bonds with these residues, resulting in the decrease in binding score (**Figure 3.11**).

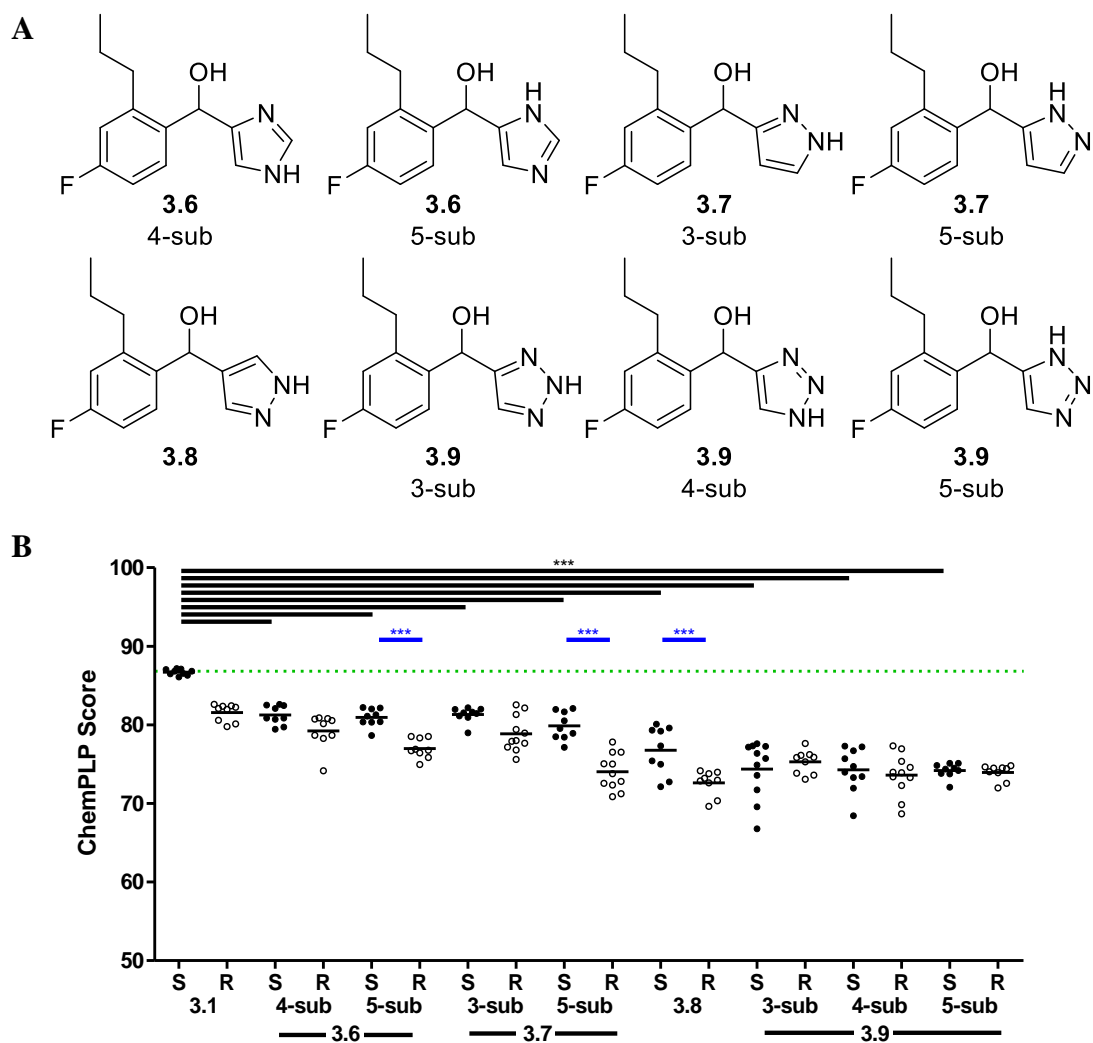


Figure 3.10: Effect of modification of hydrogen bonding vectors within the imidazole on binding within PAR2. **A** Chemical structure of four novel AZ8838 analogues (**3.6**, **3.7**, **3.8** and **3.9**). **B** ChemPLP docking score of (*S*)- and (*R*)-enantiomers of **3.6**, **3.7**, **3.8** and **3.9** compared to **3.1** represented as a scatter plot. ● = “active” (*S*) conformation of linker, ○ = “inactive” (*R*) conformation of linker, — = mean value. Data represents n = 3, with each experiment reporting at least three binding scores for each analogue. *** denotes p < 0.001.

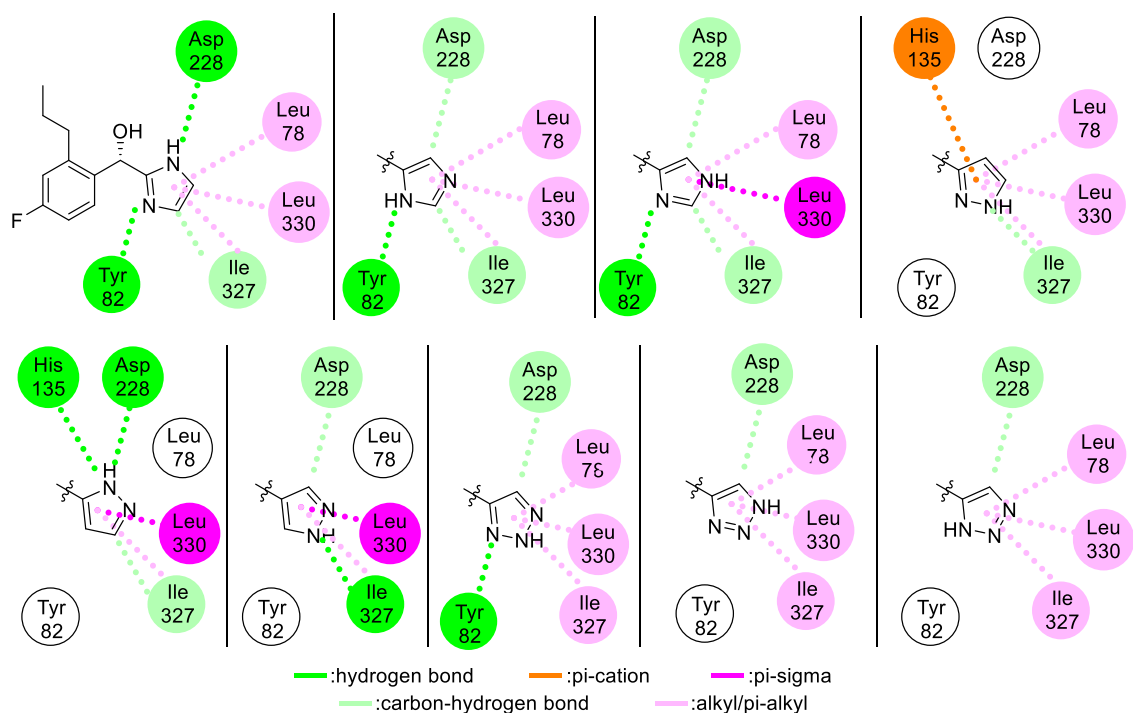


Figure 3.11: Interaction maps showing key protein-ligand interactions within imidazole binding pocket, comparing (*S*) enantiomer of **3.1** with those of **3.6**, **3.7**, **3.8** and **3.9**.

A final series of imidazole analogues were included in the study to explore the steric volume available within the imidazole pocket (**Figure 3.12A**). Benzimidazole analogue **3.10** was designed to incorporate the same hydrogen bonding vectors as AZ8838, in order to ascertain the impact of steric bulk on binding within the imidazole pocket (**Figure 3.12A**). Pyrrolidine **3.11** and bispyrrolidine **3.12** were included retrospectively in this study following their serendipitous synthesis (*vide infra* **Section 3.5.1.5**) and would provide an insight into the 3D space available within the binding pocket with increased sp^3 character (**Figure 3.12A**).

Benzimidazole (*S*)-**3.10** displays a lower binding score than (*S*)-**3.1**, indicating limited space for substitution off of the imidazole 4- and 5-positions (**Figure 3.12B**). Similarly, pyrrolidines (*S,R*)-**3.11** and (*S,S*)-**3.11** display lowered ChemPLP binding scores (**Figure 3.12B**). However, (*S,R*)-**3.11** does show a higher score than the (*S,S*)-enantiomer showing a possibility for recovering the hydrogen bonding with a non-aromatic analogue (**Figure**

3.12B). Finally, (*S*)-**3.12** shows a major loss in predicted binding affinity, although it is accepted that this structure demonstrates a significant deviation from the chemical structure of AZ8838 (**Figure 3.12B**). In addition to the hydrogen bonding requirements within the imidazole pocket (*vide supra* **Figure 3.9** & **Figure 3.10**), these simulations show a low tolerance for steric bulk being added to the imidazole functionality (**Figure 3.12B**).

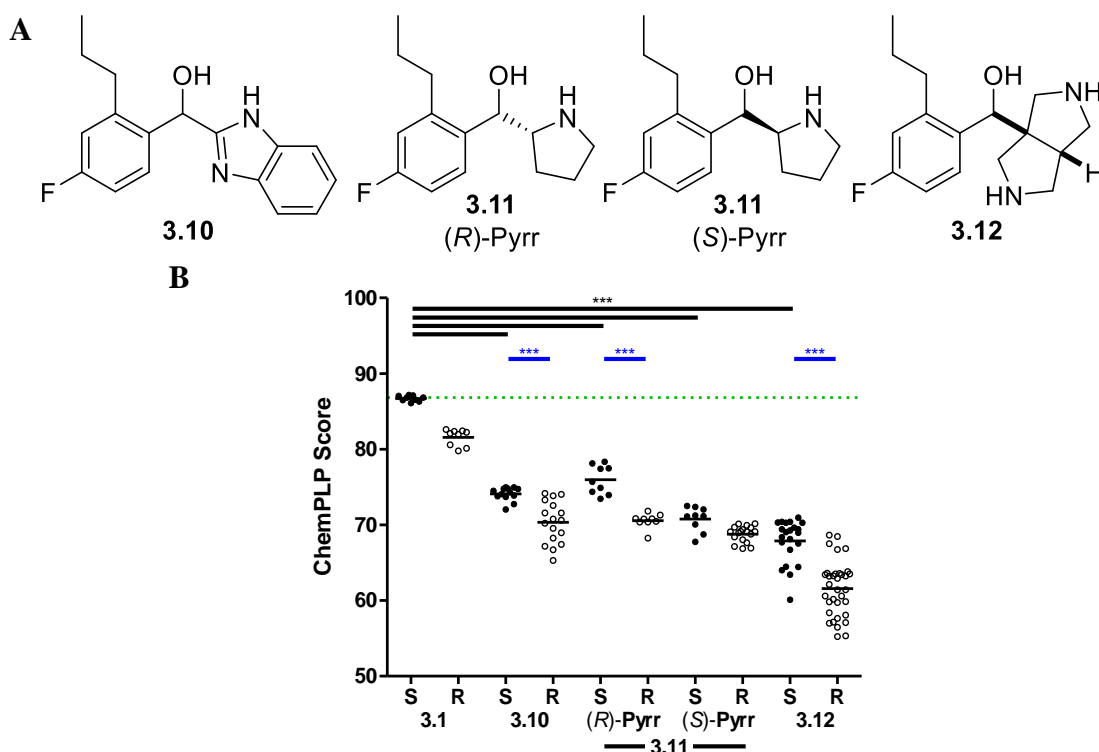


Figure 3.12: Effect of increases in steric volume within the imidazole on binding within PAR2. **A** Chemical structure of three novel AZ8838 analogues (**3.10**, **3.11** and **3.12**). **B** ChemPLP docking score of (*S*)- and (*R*)-enantiomers of **3.10**, **3.11** and **3.12** compared to **3.1** represented as a scatter plot. ● = “active” (*S*) conformation of linker, ○ = “inactive” (*R*) conformation of linker, — = mean value. Data represents n = 3, with each experiment reporting at least three binding scores for each analogue. *** denotes p < 0.001.

The low tolerance for steric bulk is further shown upon interrogation of the binding interactions exerted within the imidazole pocket (**Figure 3.13**). Whilst benzimidazole (*S*)-**3.10** maintains some alkyl- π interactions with Leu330 and Ile327, pyrrolidines (*S,R*)- and

(*S,S*)-**3.11** and bispyrrolidine (*S*)-**3.12** have lost most interactions within the binding pocket, providing the lowest scores for the imidazole analogues.

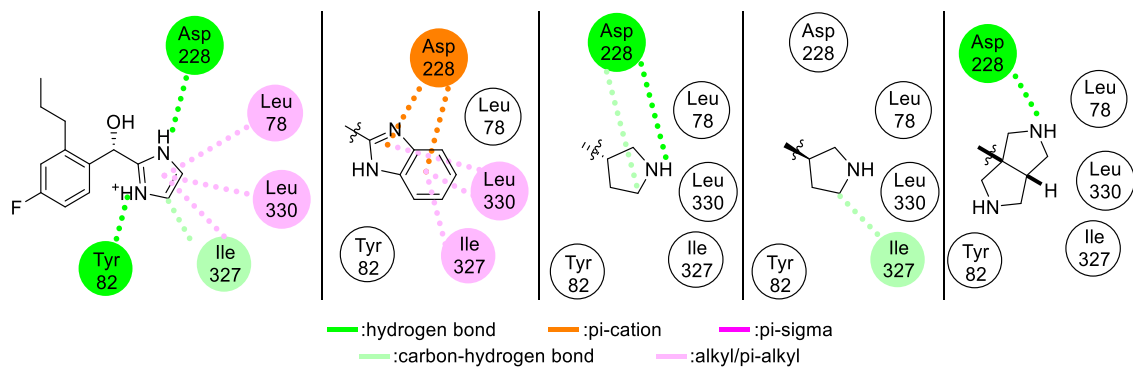


Figure 3.13: Interaction maps showing key protein-ligand interactions within imidazole binding pocket, comparing (*S*) enantiomer of **3.1** with those of **3.10**, **3.11** and **3.12**.

3.3.3.2 Linker Analogues

The design of the imidazole analogues (**Section 3.3.3.1**) was predominately based on the manipulation of the hydrogen bonding character of the heteroaromatic region of AZ8838. This would be further explored in the linker region, given the known importance of the alcohol functionality. It had been reported that the hydroxyl group was forming a hydrogen bond with His135.⁴ It had also been highlighted that the vector along which this interaction can occur is crucial for activity, with the (*S*)-isomer of AZ8838 being active whilst the (*R*)-isomer lost all PAR2 inhibition.⁴ As such, modifications to the hydroxyl linker were designed based on the retention of a hydrogen bond donor or by changing the nature of the interaction and incorporating a hydrogen bond acceptor. With these requirements, ketone analogue **3.45** and amine analogue **3.46** were chosen for docking (**Figure 3.14A**).

The significant change in geometry and hydrogen bond character of the linker induced by oxidising to the ketone with **3.13** resulted in a detrimental change in the binding score when docking in PAR2 (**Figure 3.14B**). This is likely to correlate with the known binding interactions in which the alcohol forms a hydrogen bond with His135 (**Figure 3.14C**).⁴

The importance of maintaining a hydrogen bond-donating group within the linker is further highlighted with amine derivative (*S*)-**3.14**, which displayed a similar binding score to (*S*)-**3.1** by preserving a hydrogen bond donor on a tetrahedral carbon centre (**Figure 3.14B-C**). Curiously, the replacement of the hydroxyl with an amine in **3.14** does not provide the same effect on the inversion of stereochemistry. While it can be seen that (*R*)-**3.14** displays lowered binding scores than (*S*)-**3.14**, the loss is not statistically significant unlike with **3.1** (*vide supra*, **Figure 3.7**).

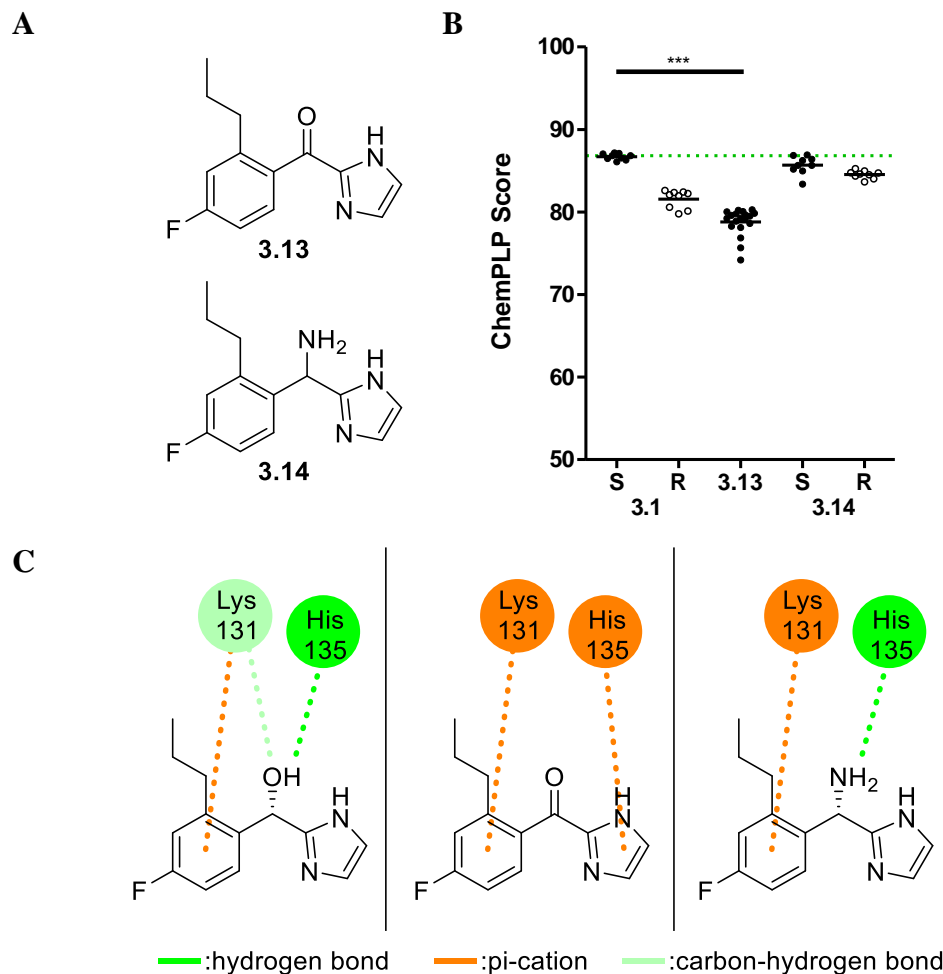


Figure 3.14: Effect of modification to the linker region on docking within PAR2. **A** Chemical structure of two novel AZ8838 analogues (**3.13** and **3.14**). **B** ChemPLP docking score of (*S*)- and (*R*)-enantiomers of **3.13** and **3.14** compared to **3.1** represented as a scatter plot. ● = “active” (*S*) conformation of linker, ○ = “inactive” (*R*) conformation of linker, — = mean value. Data represents n = 3, with each experiment reporting at least three binding scores for each analogue. *** denotes p < 0.001. **C** Interaction maps showing key protein-ligand interactions within imidazole binding pocket, comparing (*S*) enantiomer of **3.1** with those of **3.13** and **3.14**.

3.3.3.3 Propyl Analogues

The propyl analogues were designed to explore the hydrophobic pocket in which the alkyl chain resides. It is known that the propyl group extends under a disulfide bridge between Cys148 and Cys226 (**Figure 3.15**).⁴ However, it is not known how tolerant this region is likely to be towards larger functional groups.

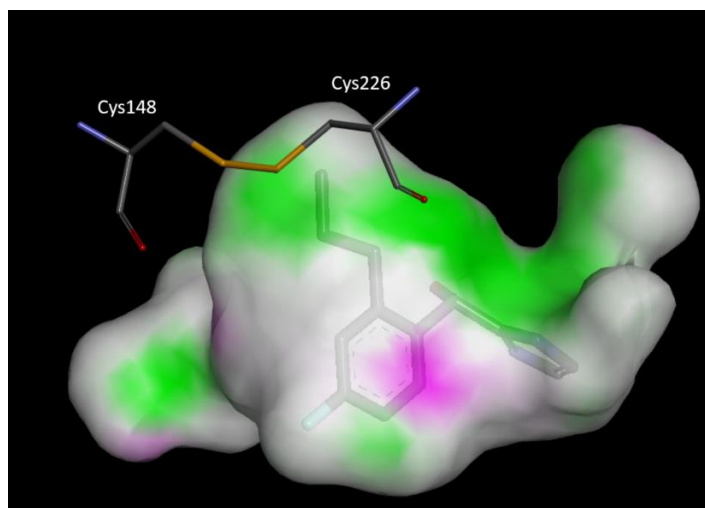


Figure 3.15: AZ8838 within the PAR2 binding pocket and associated disulfide bridge.⁴

The series was designed to occupy a range of space inside the binding pocket and included a reduction in chain length as well as increases in steric bulk with aromatic and substituted-aromatic groups providing increases in size. A selection of hydrogen bonding contributions were also accounted for and tested.

The first set of analogues included the non-aromatic analogues of the propyl group (**Figure 3.16A**). Removing the propyl chain in proto-analogue **3.15** would highlight the importance of substitution at the 2-position on the benzene ring, while the brominated analogue **3.16** would provide a halogenated analogue for exploring the propyl pocket. Cyclopropyl analogue **3.17** was designed to provide a similar volume to the original propyl group but in a restricted conformation, while allyl and vinyl analogues **3.18** and **3.19** introduce sp^2 character into a similar steric space. Finally, cyclohexyl analogue **3.20** presents increased steric volume whilst maintaining the sp^3 nature of the propyl chain.

Reductions in size in (*S*)-**3.15** and (*S*)-**3.16** led to decreases in docking score, highlighting the need for substitution at the 2-position to maintain alkyl-alkyl and pi-alkyl interactions with Tyr134, Trp14, Leu151 and Cys226 (**Figure 3.16B**, **Figure 3.17**). Similarly, cyclopropyl, allyl and vinyl analogues (*S*)-**3.17**, (*S*)-**3.18** and (*S*)-**3.19** also displayed reductions in docking score, although these were improved in comparison to the proto- and bromo-analogues due to the recovery of some of the aforementioned interactions with Tyr134, Trp14, Leu151 and Cys226 (**Figure 3.16B**). Conversely, the cyclohexyl analogue (*S*)-**3.20** displayed an improved docking score over (*S*)-**3.1**, suggesting the possibility for improved binding affinity following expansion at the propyl position (**Figure 3.16B**). The increase in binding is also facilitated by maintaining interactions with each of the key residues in this region of the binding pocket: Tyr134, Trp14, Leu151 and Cys226 (**Figure 3.17**).

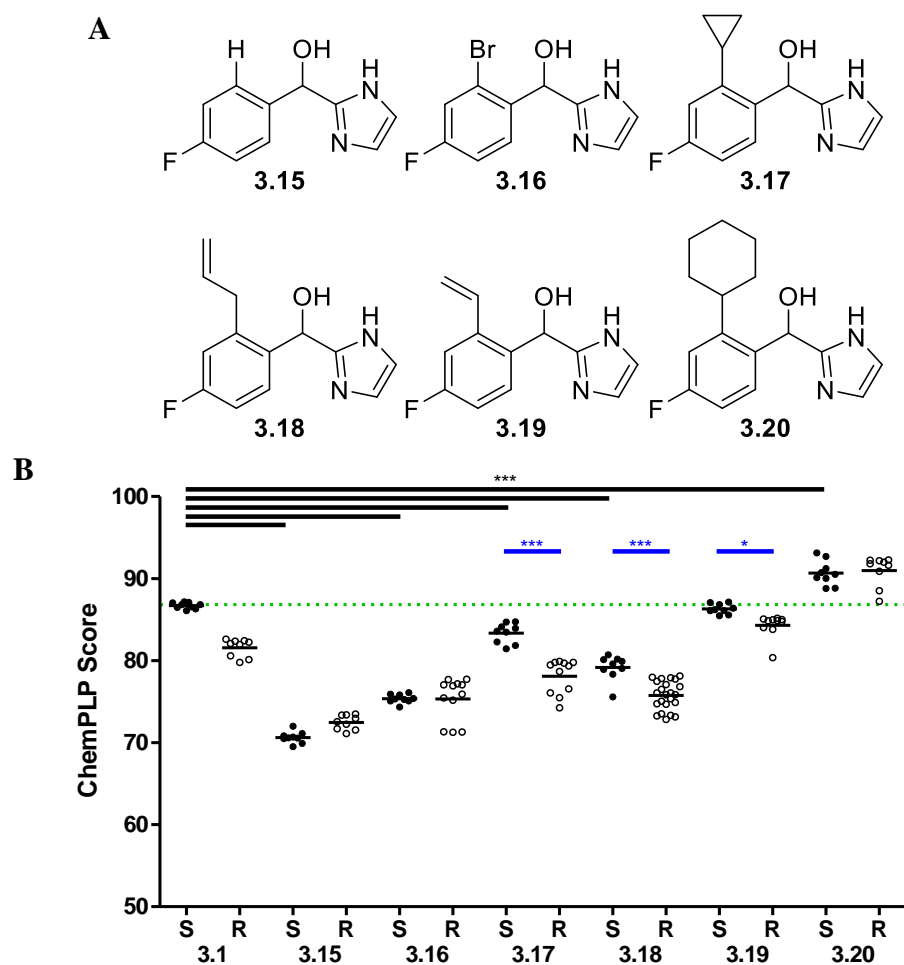


Figure 3.16: Effect of non-aromatic modifications to the propyl region on docking within PAR2. **A** Chemical structure of six novel AZ8838 analogues (**3.15**, **3.16**, **3.17**, **3.18**, **3.19** and **3.20**). **B** ChemPLP docking score of (*S*)- and (*R*)-enantiomers of **3.15**, **3.16**, **3.17**, **3.18**, **3.19** and **3.20** compared to **3.1** represented as a scatter plot. ● = “active” (*S*) conformation of linker, ○ = “inactive” (*R*) conformation of linker, — = mean value. Data represents n = 3, with each experiment reporting at least three binding scores for each analogue. *** denotes p < 0.001, * denotes p < 0.05.

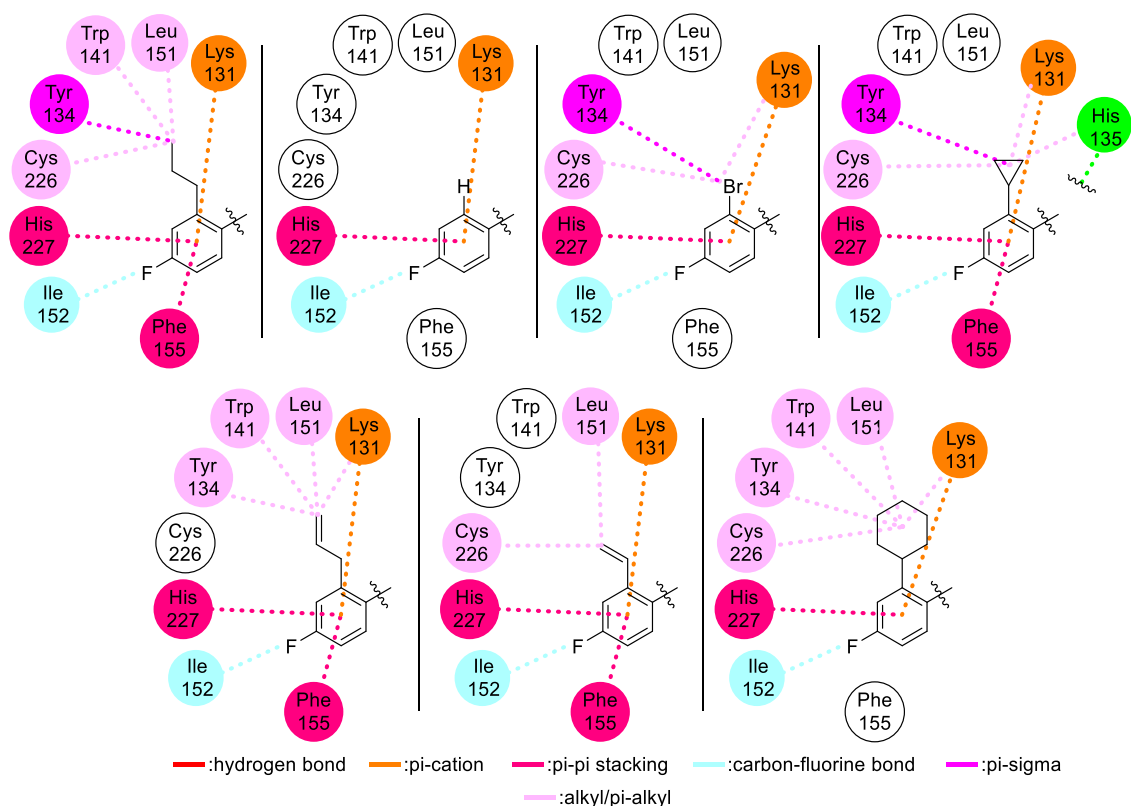


Figure 3.17: Interaction maps showing key protein-ligand interactions within imidazole binding pocket, comparing (*S*) enantiomer of **3.1** with those of **3.15-20**.

Further propyl analogues continued to explore expansion in this region, with phenyl (**3.21**), pyridinyl (**3.22**) and furanyl (**3.23**) analogues all providing data on non-substituted aromatic functional groups within the propyl binding pocket (**Figure 3.18A**). These groups continued to suggest the potential benefits of the expansion of the propyl group, with each analogue demonstrating improved binding over (*S*)-**3.1** (**Figure 3.18B**). In particular, (*S*)-**3.21** provided the highest docking score, highlighting a potential area for further expansion through substitution (**Figure 3.18B**). Of note within these analogues is the occurrence of a pi-sulphur interaction between the new phenyl ring of **3.21** and Cys226, which could account for the significant increase in docking score in comparison to **3.1** (**Figure 3.18C**).

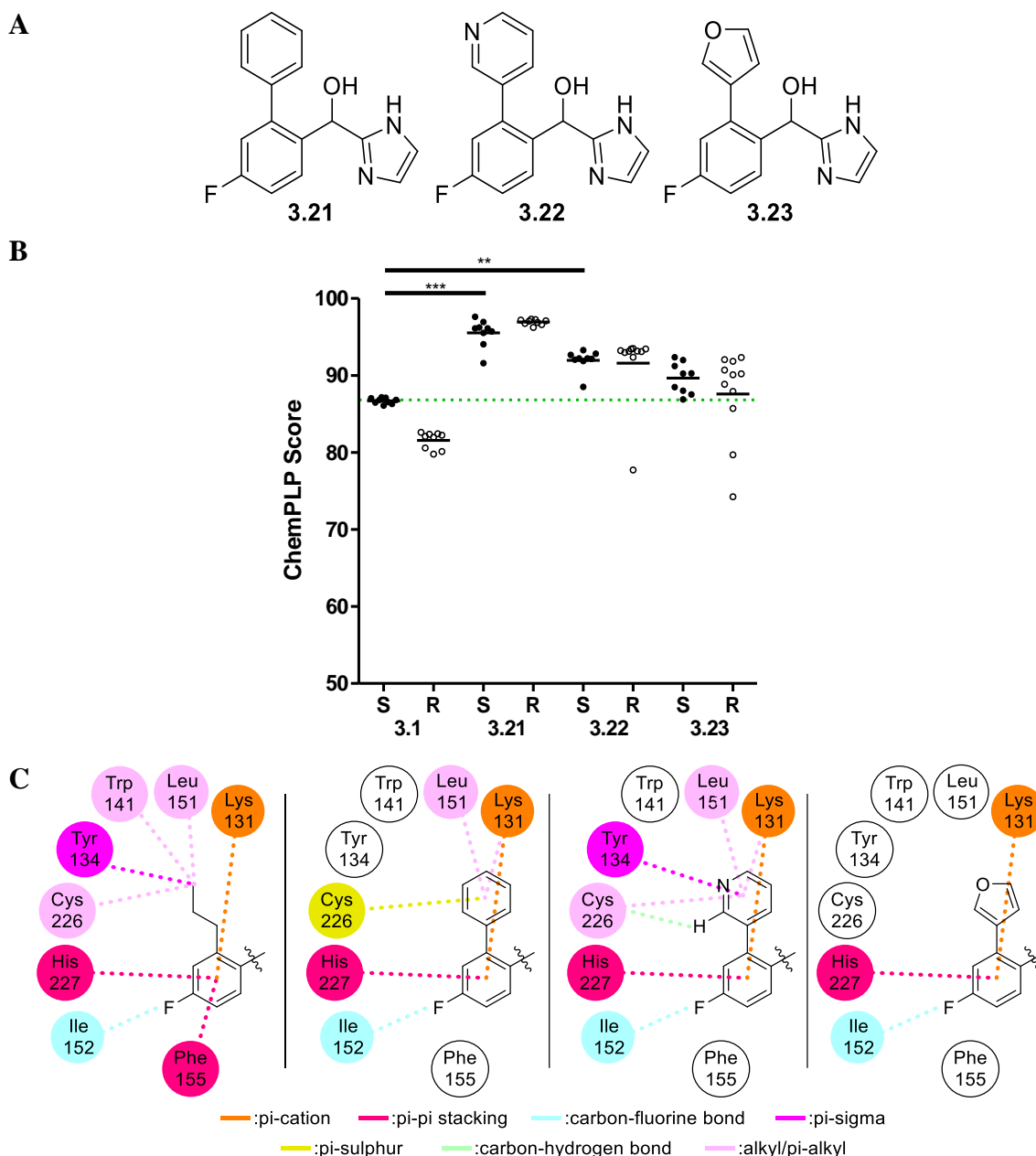


Figure 3.18: Effect of aromatic modifications to the propyl region on docking within PAR2. **A** Chemical structure of three novel AZ8838 analogues (**3.21**, **3.22** and **3.23**). **B** ChemPLP docking score of (*S*)- and (*R*)-enantiomers of **3.21**, **3.22** and **3.23** compared to **3.1** represented as a scatter plot. ● = “active” (*S*) conformation of linker, ○ = “inactive” (*R*) conformation of linker, — = mean value. Data represents $n = 3$, with each experiment reporting at least three binding scores for each analogue. *** denotes $p < 0.001$, ** denotes $p < 0.01$. **C** Interaction maps showing key protein-ligand interactions within imidazole binding pocket, comparing (*S*) enantiomer of **3.1** with those of **3.21-23**.

With phenyl analogue (*S*)-**3.21** suggesting an improved predicted binding affinity over (*S*)-**3.1**, further analogues were designed to explore the remaining space in the pocket. These analogues were also designed with consideration for available starting reagents for synthesis. Tollyl analogues **3.24-26** would provide subtle increases in the volume occupied within the propyl domain whilst trifluoromethyl (**3.27**), *tert*-butyl (**3.28**) and dimethylamino (**3.29**) substitutions at the *para* position would introduce more significant changes in the volume occupied (**Figure 3.19A**).

The tolyl compounds (*S*)-**3.24-26** all showed similar or improved docking scores in comparison to (*S*)-**3.1**, although the scores were lower than that of phenyl analogue (*S*)-**3.21** (**Figure 3.19B**). However, further expansion at the *para* position led to a significant drop off in predicted binding affinity with trifluoromethyl ((*S*)-**3.27**), *tert*-butyl ((*S*)-**3.28**) and dimethylamino ((*S*)-**3.29**) analogues all showing docking scores of less than 70 (**Figure 3.19B**).

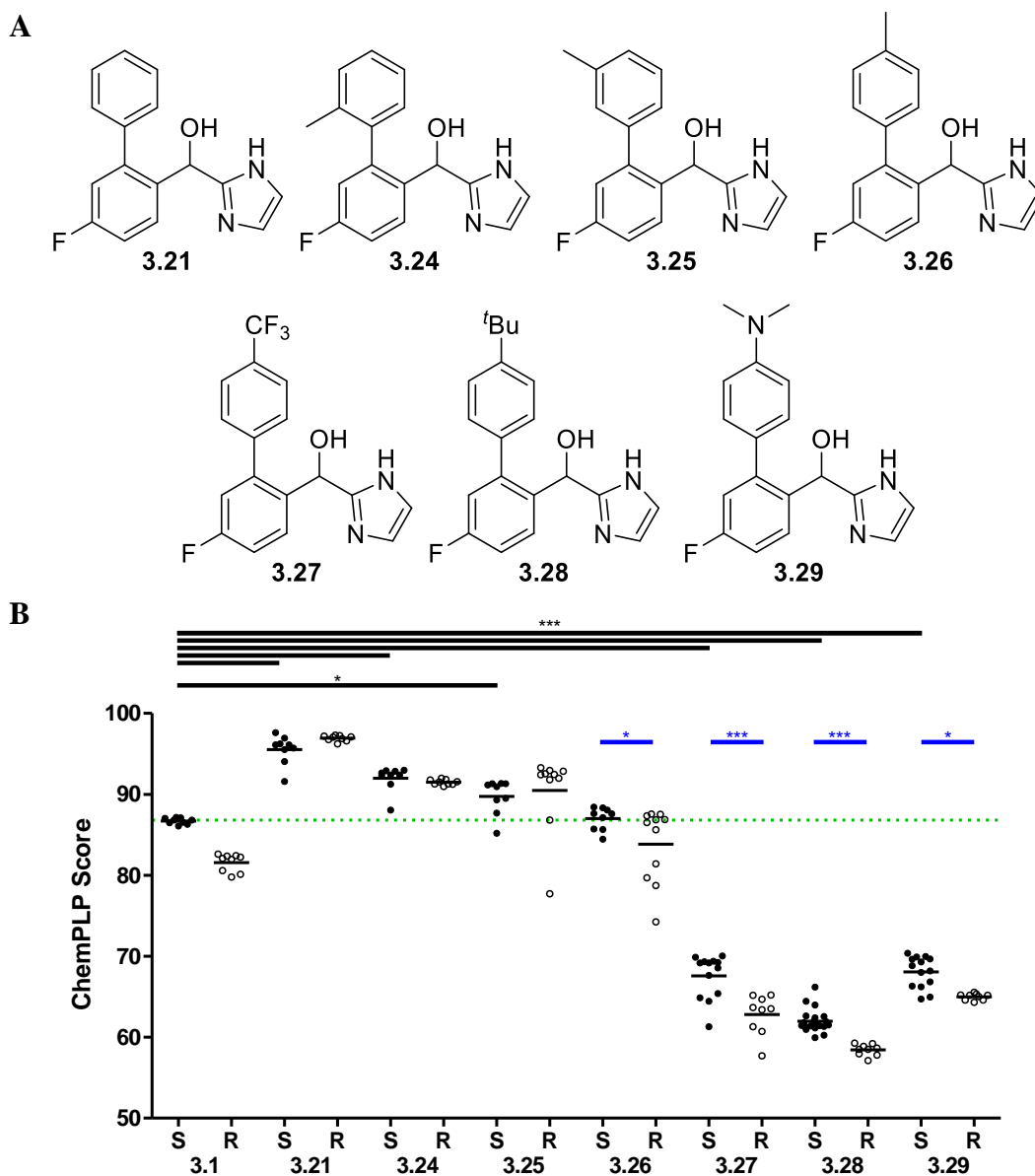


Figure 3.19: Effect of substituted aromatic modifications to the propyl region on docking within PAR2. **A** Chemical structure of seven novel AZ8838 analogues (**3.21**, **3.24**, **3.25**, **3.26**, **3.27**, **3.28** and **3.29**) **B** ChemPLP docking score of (*S*)- and (*R*)-enantiomers of **3.24**, **3.25**, **3.26**, **3.27**, **3.28** and **3.29** compared to **3.1** and **3.21** represented as a scatter plot. ● = “active” (*S*)-conformation of linker, ○ = “inactive” (*R*)-conformation of linker, — = mean value. Data represents $n = 3$, with each experiment reporting at least three binding scores for each analogue.

By interrogating the binding interactions of those analogues with improved or comparable docking scores to **3.1**, the range of interactions on display highlights the potential flexibility within the propyl binding pocket (**Figure 3.20**). The methyl groups within **3.24**-

26 each show a propensity for recovering pi-alkyl and alkyl-alkyl interactions which would be lost upon removal of the propyl substituent for an aromatic group (**Figure 3.20**). Additionally, the additional phenyl ring provides another region for pi-pi stacking and pi-sigma interactions to be built up, shown with **3.26** (**Figure 3.20**).

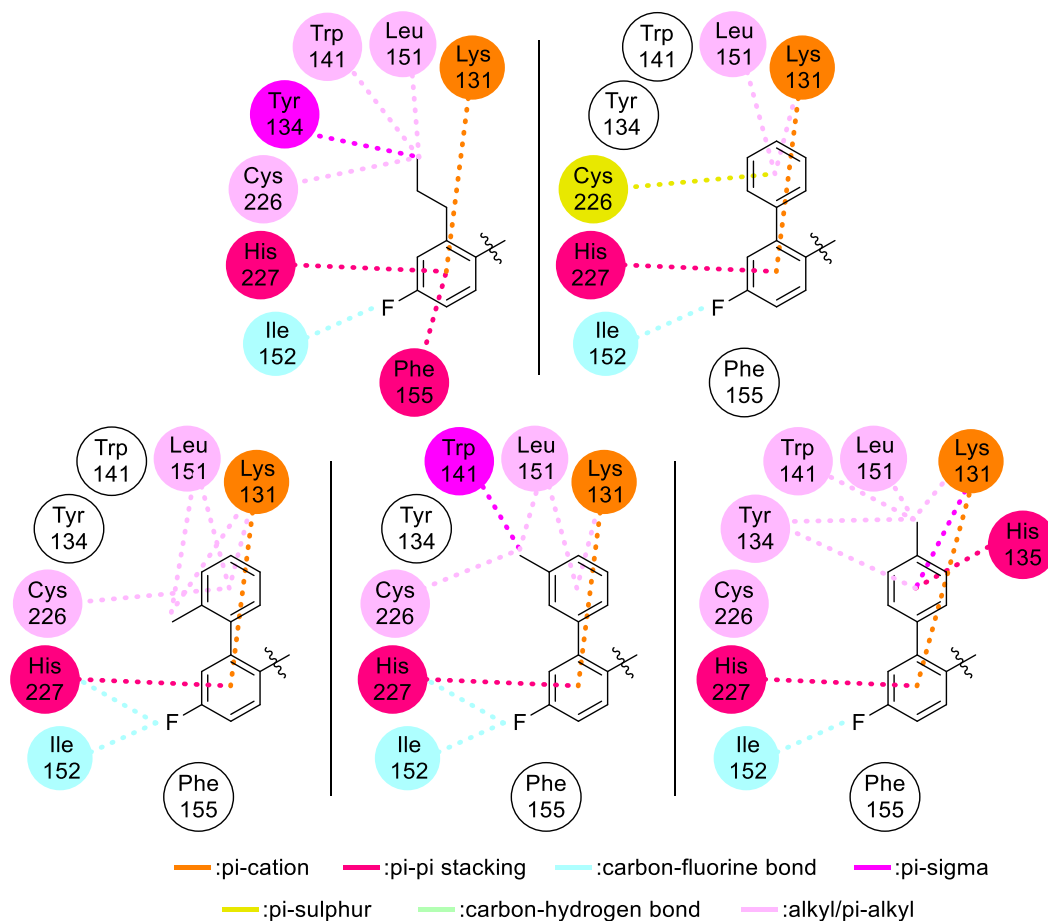


Figure 3.20: Interaction maps showing key protein-ligand interactions within imidazole binding pocket, comparing (S)-enantiomer of **3.1** with those of **3.21** and **3.24-26**. **3.27-29** were not included due to vast differences in docking score/binding mode.

3.3.4 Summary of Docking

Overall, the docking experiments highlighted the importance of the hydrogen bonding interactions displayed by AZ8838 in the binding pocket. The function of the imidazole moiety as a hydrogen bond donating and accepting group was highlighted when modification or removal of the hydrogen bonding functionalities led uniformly to decreased binding scores upon docking (**Figure 3.9**, **Figure 3.10**).

Additionally, the contribution of hydrogen bonding from the linker was highlighted, with inversion of the hydrogen bond character from donator to acceptor in **3.13** showing the propensity for reduced binding in the pocket (**Figure 3.14**). However, this loss of binding could also be attributed to the change in geometry of the oxygen atom as a result of changing from sp^3 hybridisation of the bridging carbon to sp^2 . The importance of the hydrogen bond geometry was further emphasised, with the (*R*)-isomers of many analogues showing similar or slightly lower binding. Exceptions to this are found with the pyridinyl analogue **3.22** and the furanyl analogue **3.23**, where the introduction of other hydrogen bonding groups can potentially compensate for the poor geometry of the linker.

The simulated docking also highlighted a relatively congested binding pocket, with a limited tolerance for increased sterics on the imidazole ring. Extending into a benzimidazole (**3.10**) and increasing the volume occupied with a pyrrolidine or bispyrrolidine (**3.11** and **3.12**) also yielded reduced docking scores (**Figure 3.12**).

Conversely, the docking experiments did suggest a possible region for expansion through modification of the propyl chain. Slight increases to the size of the functional group were anticipated to improve binding when modelled in GOLD, with cyclohexyl (**3.20**), phenyl (**3.21**) and tolyl (**3.24-26**) all providing significant increases to the binding score (**Figure 3.16**, **Figure 3.18** and **Figure 3.19**). However, increasing the size too much had the inverse effect, with larger *para*-substituents like *tert*-butyl, trifluoromethyl and dimethylamino groups on the phenyl ring leading to decreases in docking score (**3.27-29**, **Figure 3.19**).

The relative increase in binding scores for the phenyl and tolyl analogues (**3.21** and **3.24-26**) could suggest a propensity for π - π interactions within the binding pocket. However, the binding modes generated for each of the compounds show the phenyl ring in different orientations within the propyl domain across the series (**Figure 3.21A-H**). This region of the binding pocket is surrounded by multiple aromatic amino acids including Tyr134, His135 and Trp141, which could all be contributing to potential π -interactions with the aromatic analogues when docked to the receptor.⁴

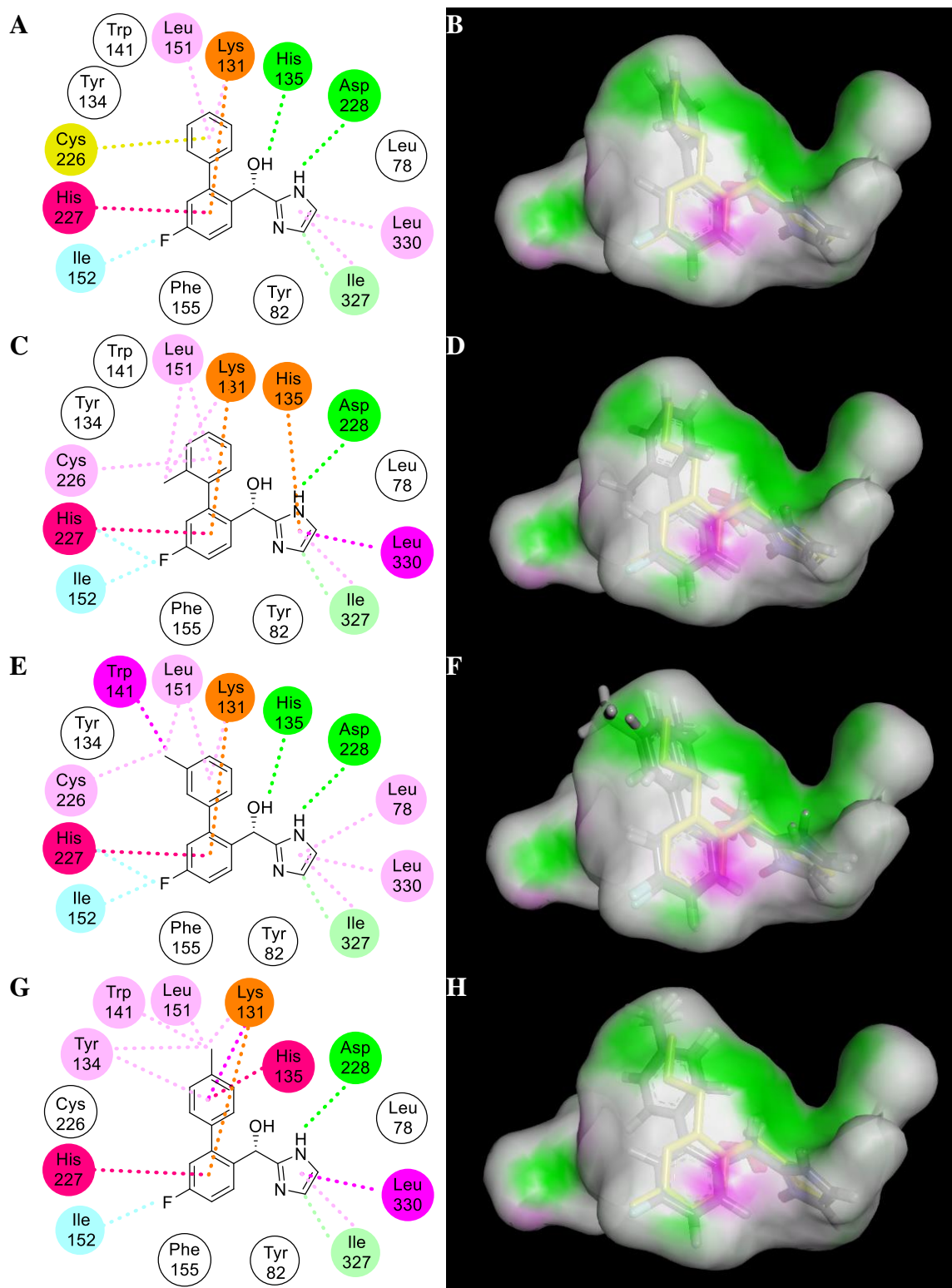


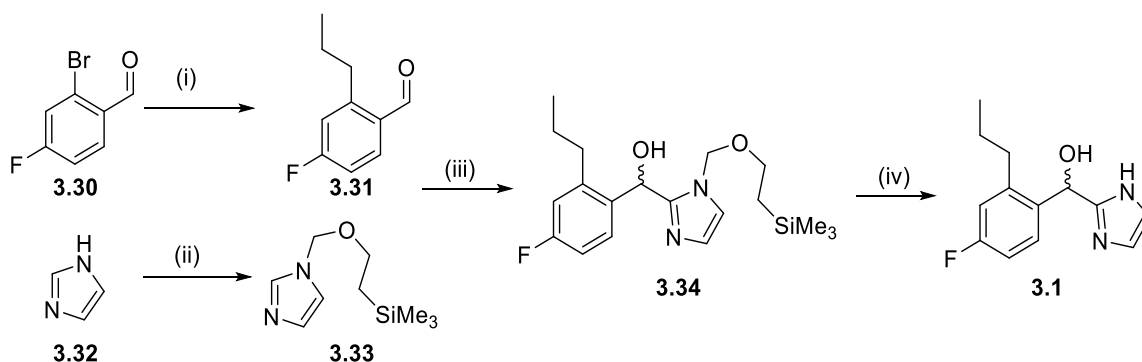
Figure 3.21: Binding mode of aryl analogues (*S*)-3.21 (A-B), (*S*)-3.24 (C-D), (*S*)-3.25 (E-F) and (*S*)-3.26 (G-H) displayed as an interaction map of the AZ8838-PAR2 binding pocket (Left) and overlaid with AZ8838 within the PAR2 binding site represented as its H-Bonding surface (Right).

Among the tolyl compounds, the *ortho*-tolyl analogue (*S*)-**3.79** displayed a unique characteristic with its binding mode which could be further exploited. Upon docking, the methyl group appeared to extend into a secondary binding pocket located deeper in the transmembrane domain (**Figure 3.21C-D**). This, coupled with the increased binding score for the analogue in comparison to (*S*)-**3.1** (*vide supra* **Figure 3.19**), suggests further development of the methyl group could allow access to more potent binding within the AZ8838 pocket.

These results highlight the propyl analogues as the most promising new molecules. In particular, the phenyl and tolyl analogues stand out as, potentially, offering comparable or increased potency relative to (*S*)-**3.1**. However, the results obtained from the docking experiments would be best used to complement biological data. As such, the analogues would be carried on to *in vitro* biological assays following synthesis to evaluate their PAR2 inhibition.

3.4 Synthesis of (±)-AZ8838

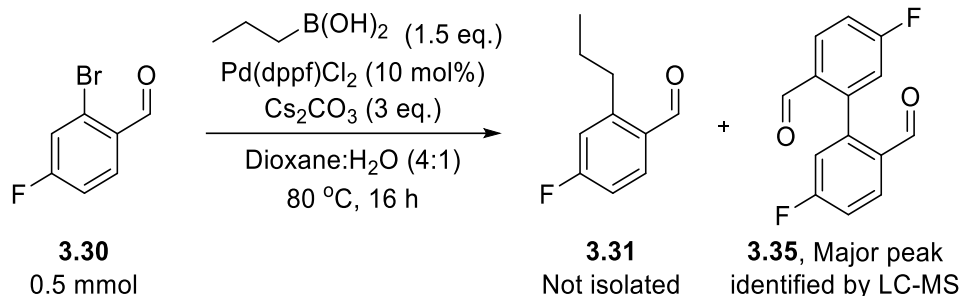
Prior to testing any AZ8838 analogues, it was necessary to obtain access to a stock of AZ8838. In addition to its favourable properties, AZ8838 was thought to be chemically tractable, hence was amenable to analogue synthesis and this initial phase of the study would then enable downstream analogue generation. The initial synthetic route used to access a racemic mixture of AZ8838, **3.1**, was that used by Cheng *et al.* (**Scheme 3.1**).⁴ Firstly, a Suzuki-Miyaura cross-coupling would be carried out with benzaldehyde **3.30** to access propylbenzaldehyde intermediate **3.31** (**Scheme 3.1(i)**).⁴ Concurrently, protection of imidazole, **3.32**, with a trimethoxysilylethyl methyl (SEM) protecting group to provide protected intermediate **3.33** would be performed (**Scheme 3.1(ii)**).⁴ Treatment of **3.33** with *n*-butyllithium would then allow addition into benzaldehyde **3.31** to furnish protected intermediate **3.34** (**Scheme 3.1(iii)**).⁴ Finally, acid deprotection would furnish the desired AZ8838, **3.1**, as a racemic mixture (**Scheme 3.1(iv)**).⁴



Scheme 3.1: Reported synthetic route towards AZ8838 (**3.1**) as used by Cheng *et al.*⁴ (i) PrB(OH)₂, PdCl₂(dppf), Cs₂CO₃, dioxane, H₂O, 80 °C, 16 h. (ii) SEM-Cl, NaH, THF, 0 °C-RT, 16 h. (iii) *n*BuLi, THF, -78 °C-RT, 1 h. (iv) TFA, DCM, reflux, 3 h.

However, initial attempts at reproducing the synthesis were met with extremely low yields (**Scheme 3.2**). Using the literature conditions, the Suzuki-Miyaura cross-coupling of benzaldehyde **3.30** with propyl boronic acid failed to yield any of the desired propyl

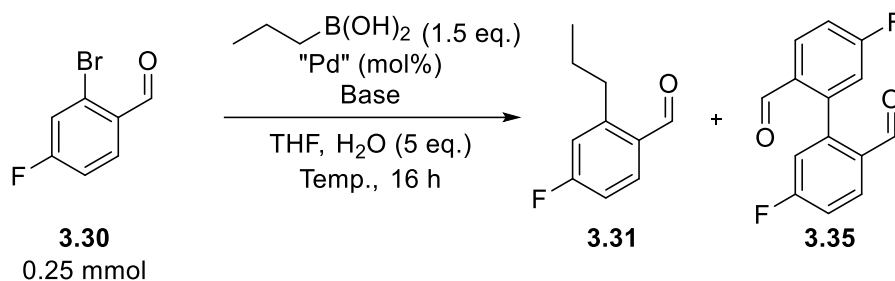
benzaldehyde. Additionally, homo-coupled benzaldehyde **3.35** was identified within the reaction mixture as the major product.



Scheme 3.2: Initial attempt at Suzuki-Miyaura Cross-Coupling towards **3.31**

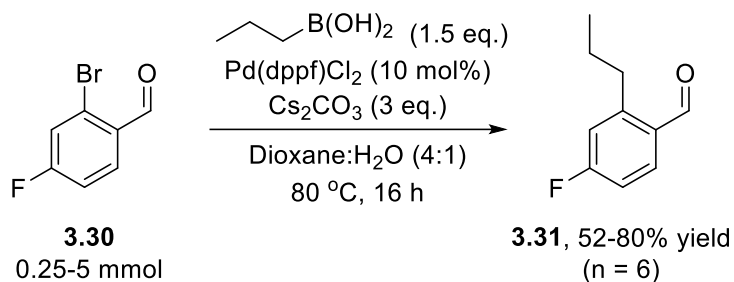
Attempts were then made to optimise the Suzuki-Miyaura reaction, considering a variety of parameters (**Table 3.2**). Using methodology available in our laboratories as a starting point, changes to temperature (Entries 1-3), catalyst loading (Entries 4-5), palladium source (Entries 6-7) and base (Entries 8-9) were all considered and compared to the literature conditions (Entry 10).¹⁷⁸ The reactions were carried out on a 0.25 mmol scale and analysed using 1,4-dinitrobenzene as a ¹H NMR standard at 0.0625 M to establish conversions. Specifically, the benzaldehyde peaks of **3.30**, **3.31** and **3.35** were used as the analyte peaks, with the integral of the **3.35** peak being halved prior to compiling the data.

While variation in the total content of the reactions was noted, the experiments did allow identification of 50 °C, 5 mol% of Pd(dppf)Cl₂ and potassium phosphate as ideal conditions for full consumption of aryl bromide **3.30** and a good ratio of product **3.31** to homocoupled system **3.35** at 4:1 (Entry 4). However, this was not significantly different from the literature conditions, Entry 10, which had shown full conversion of **3.30** previously (**Table 3.2**).

Table 3.2: Optimisation of Suzuki-Miyaura Cross-Coupling towards **3.31**

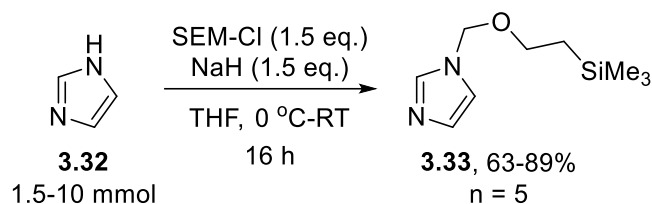
Entry	Catalyst	Cat. loading	Base	Temp (°C)	3.30 (%)	3.31 (%)	3.35 (%)
1	Pd(dppf)Cl ₂	10	K ₃ PO ₄	22	48	4	1
2	Pd(dppf)Cl ₂	10	K ₃ PO ₄	50	0	36	13
3	Pd(dppf)Cl ₂	10	K ₃ PO ₄	80	0	20	8
4	Pd(dppf)Cl ₂	5	K ₃ PO ₄	50	0	40	10
5	Pd(dppf)Cl ₂	3	K ₃ PO ₄	50	28	38	1
6	Pd(PPh ₃) ₄	5	K ₃ PO ₄	50	76	0	0
7	Pd(OAc) ₂ .2SPhos	5	K ₃ PO ₄	50	70	1	0
8	Pd(dppf)Cl ₂	5	K ₂ CO ₃	50	62	19	5
9	Pd(dppf)Cl ₂	5	Cs ₂ CO ₃	50	38	21	0
Literature Conditions							
10	Pd(dppf)Cl ₂ (10 mol%), Cs ₂ CO ₃ (3 eq.) Dioxane:H ₂ O (4:1), 80 °C, 16 h				2	29	8

On further inspection, the initial reactions were performed using an older sample of Pd(dppf)Cl₂ which had lost its characteristic orange colour. Ultimately, using a fresh source of palladium with the original literature conditions for the reaction restored the yields to levels comparable with Cheng *et al.*, allowing access to the desired propyl benzaldehyde intermediate **3.31** in good yields (**Scheme 3.3**).⁴



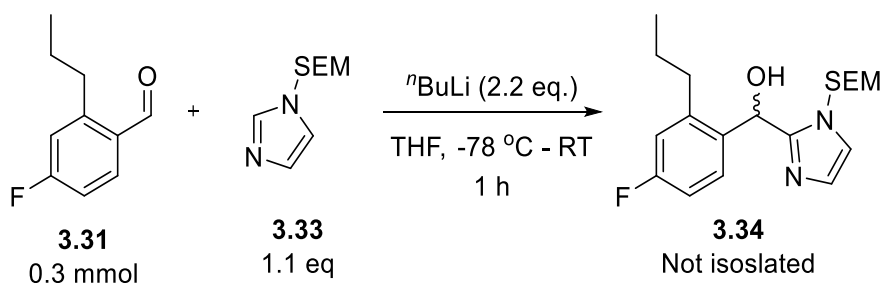
Scheme 3.3: Synthesis of benzaldehyde intermediate **3.31**

The SEM protection of imidazole, **3.32**, proceeded readily utilising sodium hydride as the base to deprotonate the imidazole before reacting with SEM-Cl, yielding the protected intermediate **3.33** in good to excellent yields (**Scheme 3.4**).⁴



Scheme 3.4: Synthesis of SEM-protected imidazole **3.33**

Cheng *et al.* reported the lithiation step, whereby imidazole **3.33** is deprotonated at the 2-position with *n*-butyllithium before undergoing nucleophilic attack onto the aldehyde of intermediate **3.31**, in moderate yields of 54%.⁴ However, under the same conditions, in our hands the product **3.34** was only observed in trace amounts (**Scheme 3.5**).



Scheme 3.5: Initial attempt at the synthesis of **3.34**

While the scale was reduced in comparison to the published methods (0.3 mmol in comparison to the reported 1.8 mmol), it was thought the cause of the low yield could potentially be from the excess *n*-butyllithium reacting nucleophilically with benzaldehyde **3.31**. By reducing the stoichiometry of *n*-butyllithium to ensure full consumption in the deprotonation of **3.33**, it was thought that comparable yields to the literature could be achieved. Given the lower equivalents of *n*-butyllithium, it was decided to confirm successful lithiation of **3.33**. The solution of imidazole **3.33** and *n*-butyllithium was quenched in deuterated water and, after extracting into deuterated chloroform, a ^1H NMR was taken. Loss of the characteristic methine peak at the 2-position, located at 7.59 ppm, confirmed successful deprotonation in solution (**Figure 3.22**).

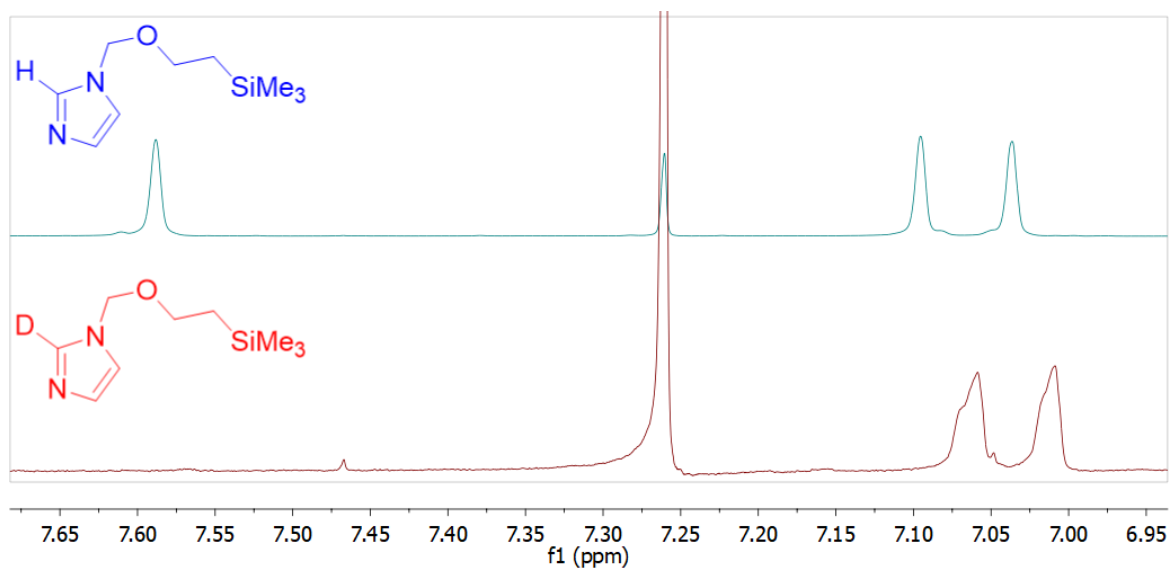
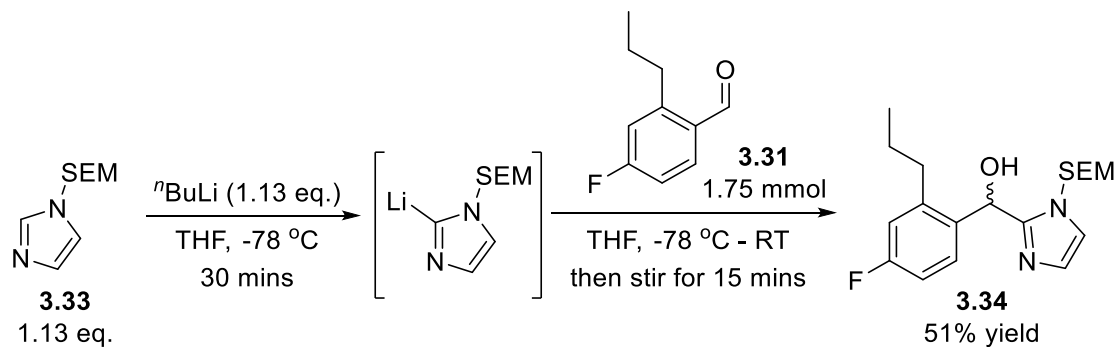


Figure 3.22: Confirmation of deprotonation at the 2-position of **3.33**

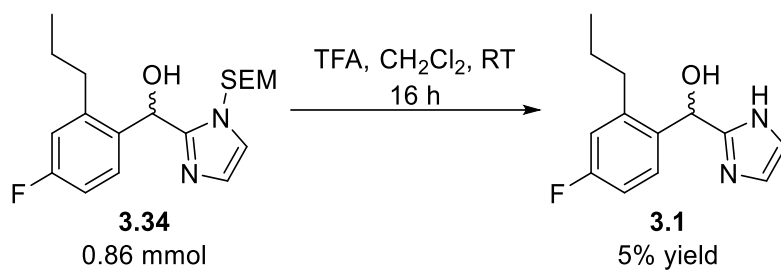
With the deprotonation of SEM-protected intermediate **3.33** proceeding with full conversion, reaction with aldehyde **3.31** was then carried out *in situ* providing access to protected intermediate **3.34** in 51% yield, comparable to the yield reported by Cheng *et al.* (**Scheme 3.6**).⁴



Scheme 3.6: Lithiation of **3.33** towards **3.34**

Following the preparation of target secondary alcohol **3.34**, deprotection of the SEM protecting group also proved to be problematic. Initial deprotection conditions using

trifluoroacetic acid (TFA) showed complete consumption of **3.34** but with extremely low yields following purification by reverse-phase preparative HPLC (**Scheme 3.7**). Regardless, 15 mg of (\pm)-AZ8838 (**3.1**) was obtained and sufficient for using the compound as a comparator in the biological assays.



Scheme 3.7: Deprotection of intermediate **3.34** to yield (\pm)-AZ8838, **3.1**

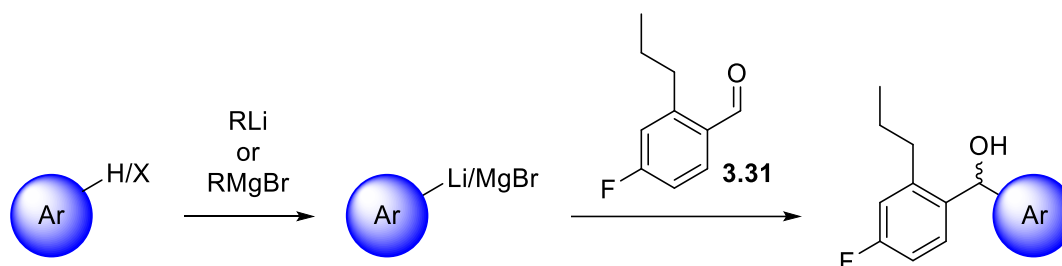
Due to time constraints for the synthesis of analogues of AZ8838, **3.1** was used as a racemic mixture as opposed to the active (*S*)-enantiomer.⁴ Generation of new analogues was also carried out towards racemates rather than enantiomerically pure compounds, with the intention to compare racemic mixtures initially in the biological assays.

3.5 Synthesis of AZ8838 analogues

With access to **3.1** achieved and enablement of the synthetic chemistry carried out, synthesis of the AZ8838 analogues docked above (*vide supra*, **Section 3.3.3**) could then be synthesised.

3.5.1 Synthesis of Imidazole Analogues

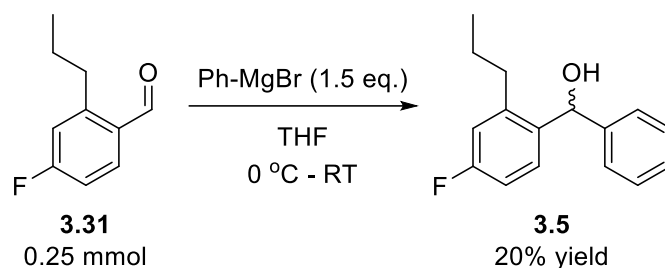
Initially, the imidazole analogues (**3.3-10**) were chosen for synthesis. This was thought to be a good starting point, with the introduction of the imidazole moiety occurring late in the synthesis of AZ8838. Thus, a general approach for heterocycle modification was produced whereby aryl moieties could be introduced by reacting as a Grignard reagent or organolithium species with benzaldehyde **3.31** to yield a range of novel AZ8838 analogues (**Scheme 3.8**). The late-stage functionalisation of these syntheses would allow a stock of intermediate **3.31** to be built up before derivatisation with the novel moieties.



Scheme 3.8: General synthesis of AZ8838 analogues, diversifying at the imidazole functionality

3.5.1.1 Phenyl analogue **3.5**

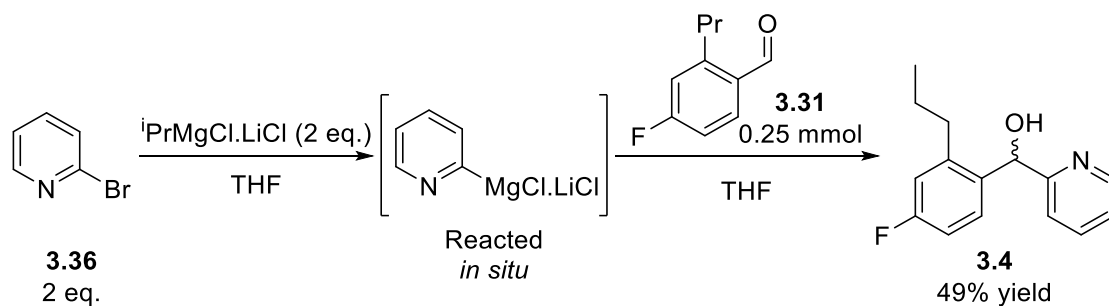
As a means of testing the nucleophilic attack onto benzaldehyde **3.31** using Grignard reagents, phenyl magnesium bromide was initially used as a commercially available organometallic reagent to provide phenyl analogue **3.5**. The Grignard reaction with benzaldehyde **3.31** provided analogue **3.5** in 21% yield (**Scheme 3.9**). Despite the low yields, the material obtained was a sufficient quantity for biological analyses to be performed and no further optimisation of the reaction was carried out.



Scheme 3.9: Grignard reaction towards phenyl analogue **3.5**

3.5.1.2 Pyridinyl analogue **3.4**

Following successful addition of a commercial Grignard reagent into benzaldehyde **3.31**, attempts were then made to transform aryl bromides into Grignard reagents. Initially, 2-bromopyridine (**3.36**) was used, treating with $i\text{PrMgCl}\cdot\text{LiCl}$ to facilitate bromine/magnesium exchange and provide a pyridine-2-yl Grignard species (**Scheme 3.10**).¹⁷⁹ The Grignard was then reacted *in situ* with benzaldehyde **3.31** to provide pyridine analogue **3.4** in 49% yield (**Scheme 3.10**).

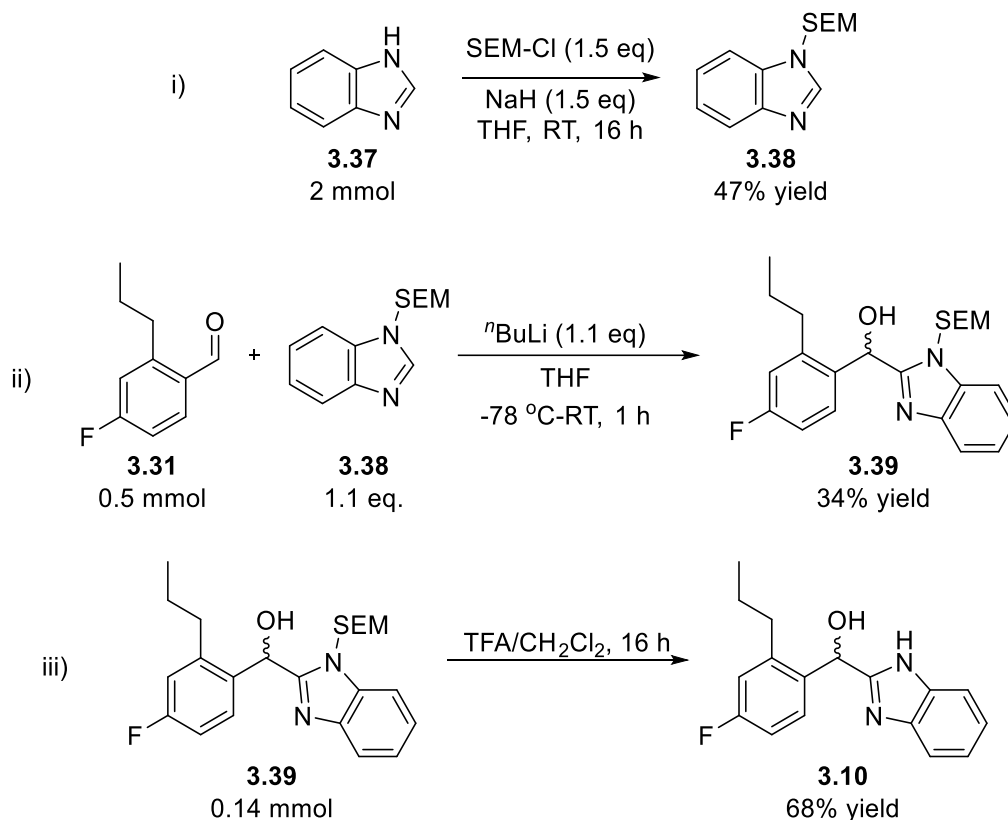


Scheme 3.10: Synthesis of **3.4** via bromine/magnesium exchange of **3.36**

3.5.1.3 Benzimidazole analogue **3.10**

Incorporation of a benzimidazole functionality was carried out by using the same methodology as the synthesis for AZ8838 (**3.1**, **Scheme 3.3-7**).⁴ Firstly, benzimidazole **3.37** was protected using SEM-Cl to yield **3.38** in 47% yield (**Scheme 3.11(i)**). Following this, the position 2 carbon was deprotonated using *n*-butyllithium, allowing nucleophilic

addition into benzaldehyde **3.31** to provide protected intermediate **3.39** in 34% yield (**Scheme 3.11(ii)**). Finally, deprotection of intermediate **3.39** with TFA yielded the desired benzimidazole analogue, **3.10**, in 68% yield (**Scheme 3.11(iii)**).



Scheme 3.11: 3-step synthesis of benzimidazolyl analogue **3.10**

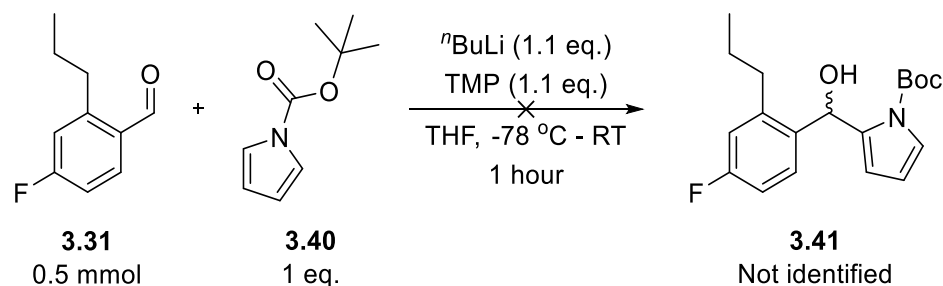
3.5.1.4 Other Heterocyclic Analogues

The initial synthetic strategy used for the syntheses was the same as the above imidazole analogues, with late-stage functionalisation at the imidazole occurring as the final step, excluding necessary deprotections.

Pyrrrole **3.3**

Synthesis of pyrrolyl analogue **3.3** was attempted *via* the lithiation of *tert*-butyl 1*H*-pyrrole-1-carboxylate (**3.40**) at the 2-position followed by a nucleophilic attack into the

carbonyl of benzaldehyde **3.4**.¹⁸⁰ However, after one hour the reaction mixture consisted mostly of unreacted benzaldehyde **3.4** (**Scheme 3.12**), with no indication of successful formation of **3.41** by NMR or LC-MS despite full consumption of **3.40** within the reaction mixture.

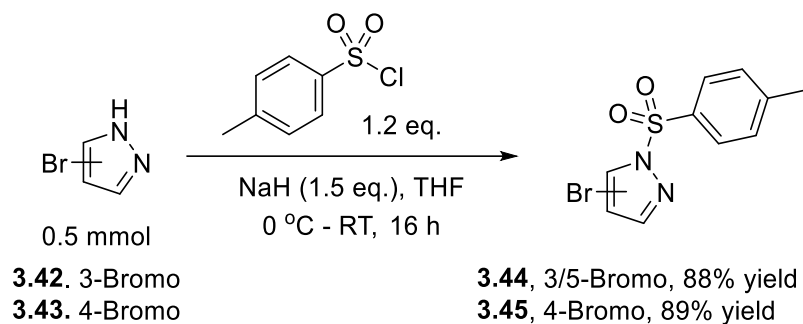


Scheme 3.12: Attempted synthesis of pyrrolyl analogue **3.41**

Ultimately, with no signs of product formation alongside ongoing issues with other compounds in the series, the synthesis of **3.3** was abandoned.

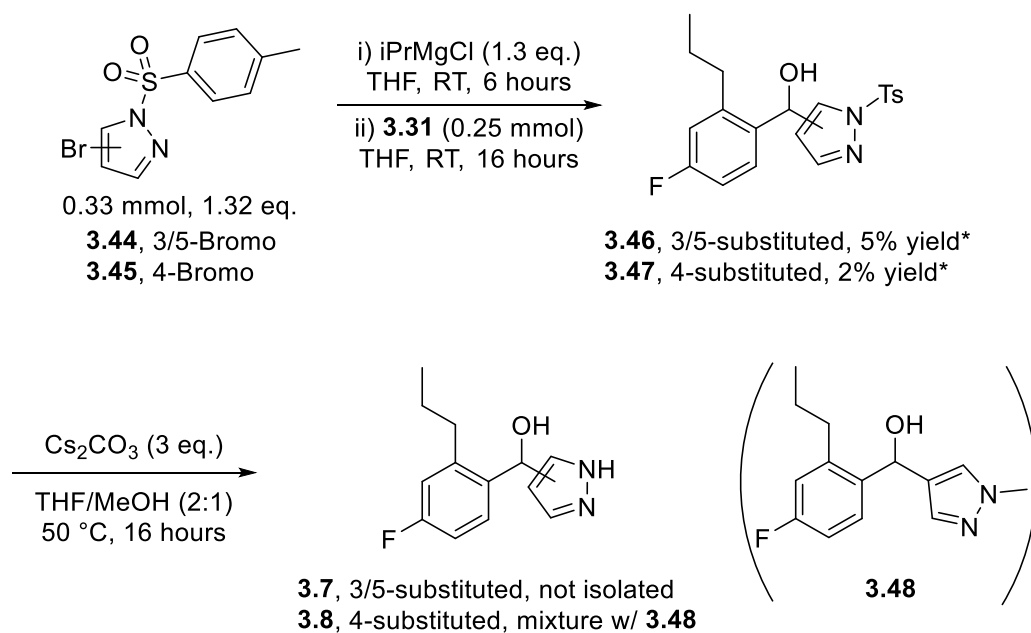
Pyrazoles **3.7** & **3.8**

Initially, attempts to introduce pyrazoles were performed using tosyl-protected bromopyrazoles. With the low yields experienced for SEM deprotection in the synthesis of **3.1** (**Scheme 3.7**), an alternative was explored with the tosyl protecting group. The protected intermediates **3.44** and **3.45** were synthesised in good yields by treating bromopyrazoles (**3.42-43**) with sodium hydride and tosyl chloride (**Scheme 3.13**).¹⁸¹



Scheme 3.13: Tosyl protection of bromopyrazoles **3.42** and **3.43**

The subsequent Grignard reaction with benzaldehyde **3.31** yielded very low quantities of the desired protected intermediates **3.46** and **3.47**, which were not purified (**Scheme 3.14**). Attempts at deprotection of the crude **3.47** showed traces of the desired pyrazole product **3.8**. However, this was isolated as a mixture with the *N*-methylated analogue **3.48**, as also identified by LC-MS (**Figure 3.23**), with evidence suggesting that the two compounds would have been inseparable considering the low yield obtained. Additionally, deprotection of the crude **3.46** failed to yield pyrazole **3.7**.



Scheme 3.14: Attempted synthesis of **3.7** and **3.8** via Grignard reaction between tosyl-protected bromopyrazoles **3.44-45** and **3.31**

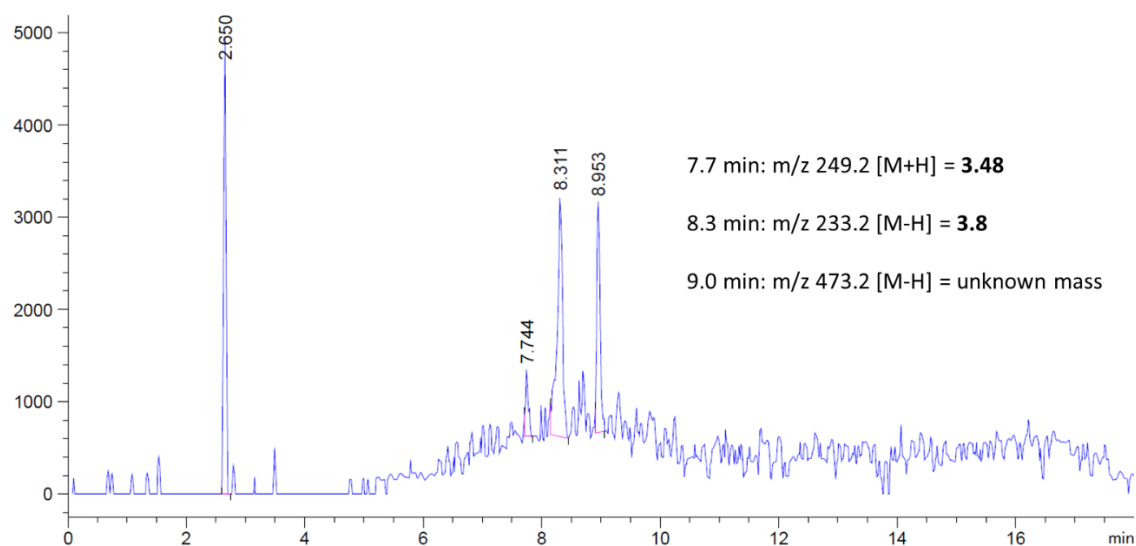
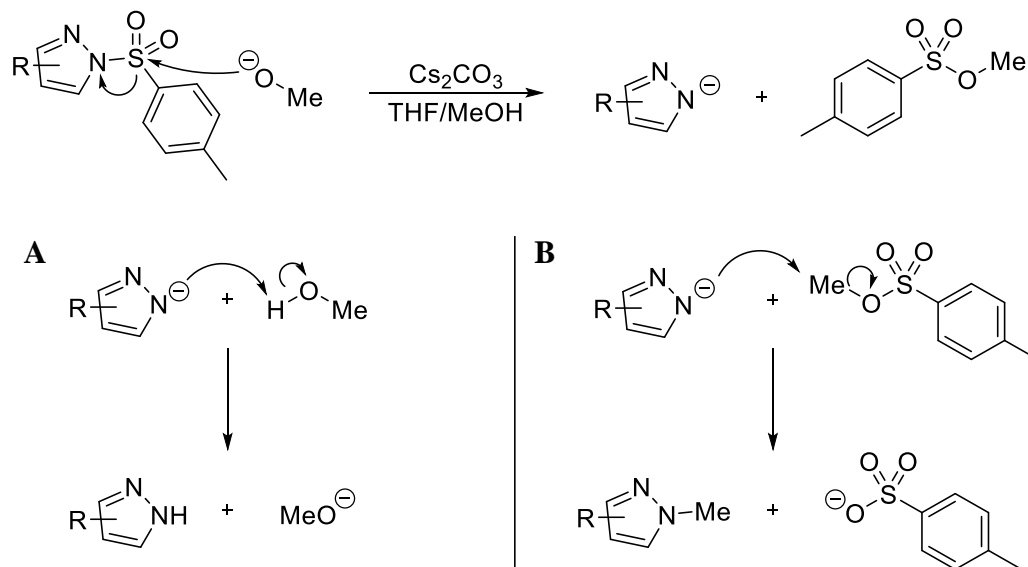


Figure 3.23: LC-MS trace for crude **3.8**, showing mass spectrum in the negative scan with annotated masses for each peak of interest.

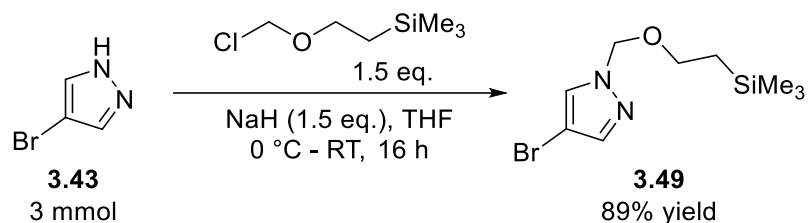
The N-methylation towards pyrazole **3.48** was thought to occur following the initial cleavage of the N-S bond. Initially, the attack of a methoxy anion will result in the

formation of methyl *p*-toluenesulfonate. Ideally, the pyrrole anion is then protonated by an additional molecule of methanol (**Scheme 3.15A**). However, it has been shown that alkyl *p*-toluenesulfonates can act as alkylating agents, yielding the methylated pyrrole and *p*-toluenesulfonate, which would be subsequently protonated to provide *p*-toluenesulfonic acid (**Scheme 3.15B**).¹⁸²



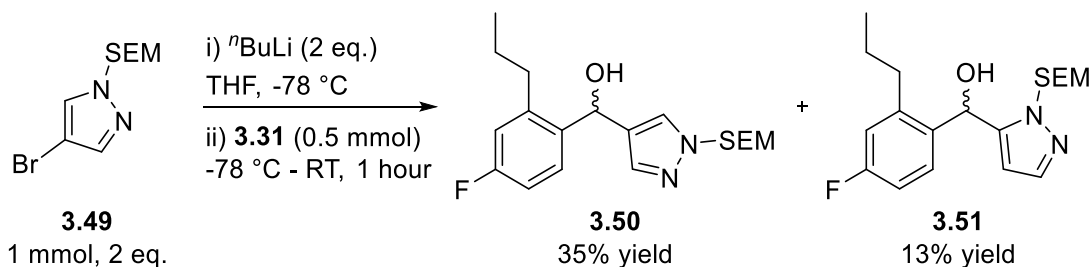
Scheme 3.15: Proposed mechanism for deprotection of N-tosylated heterocycles resulting in the desired product (**A**) or methylated side-product (**B**)

Despite initial low yields using the SEM protecting group and organolithium chemistry, it was decided to change the strategy and utilise lithium-halogen exchange with the SEM protected bromopyrazole. As such, pyrazole **3.43** was firstly protected using SEM-Cl, providing **3.49** in 66% yield using the previously established protocol with sodium hydride (**Scheme 3.16**).⁴



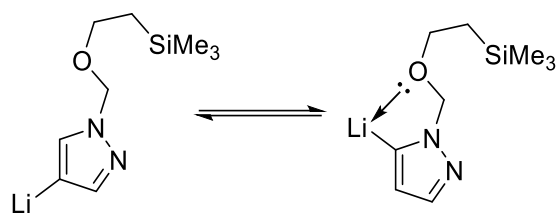
Scheme 3.16: SEM-protection of 4-bromopyrazole **3.43**

The lithium-halogen exchange reaction was performed using *n*-butyllithium to provide the required organolithium species, which was then reacted *in situ* with aldehyde **3.31** to provide the desired 4-substituted pyrazole analogue, **3.50**, in 30% yield (**Scheme 3.17**). Additionally, 5-substituted pyrazole **3.51** was also identified and isolated from the reaction mixture in 7% yield.



Scheme 3.17: $n\text{-BuLi}$ -mediated coupling of bromopyrazole **3.49** with **3.31** to yield protected pyrazoles **3.50** and **3.51**

The formation of **3.51** was unexpected but was thought to occur by the transfer of the anionic charge on the organolithium species from the 4- to the 5-position of the ring (**Scheme 3.18**). This site would allow additional stabilisation of the organolithium with the lone pair of the SEM oxygen atom being able to chelate to the lithium cation. The SEM protecting group has been shown to stabilise an *ortho* charge in other applications such as directed lithiation for the synthesis of organohalides, where it showed improved stabilisation over the Boc protecting group.¹⁸³



Scheme 3.18: Stabilisation of organolithium species via the oxygen atom of the SEM protecting group

This change in localisation of the charge was supported by the structure of **3.51**. By comparing 2D NMR experiments with those of **3.50**, not only was a difference in structure confirmed but also specifically the 5-substituted product was formed over the 3-substituted product, for which the organolithium intermediate would have no further stabilisation from the SEM group.

HSQC experiments were firstly used to fully assign each intermediate before further analysis using HMBC (**Appendix I/II**). HMBC experiments for **3.51** displayed a series of 2/3/4-bond interactions from both the methine linker and the first methylene of the SEM group with the 5-position of the imidazole (**Figure 3.24, Appendix II**). Conversely, in **3.50** the correlations between the SEM methylene and the pyrazole carbons were not observed, while the linking methine displays interactions with all 3 of the pyrazole carbons (**Figure 3.24, Appendix I**).

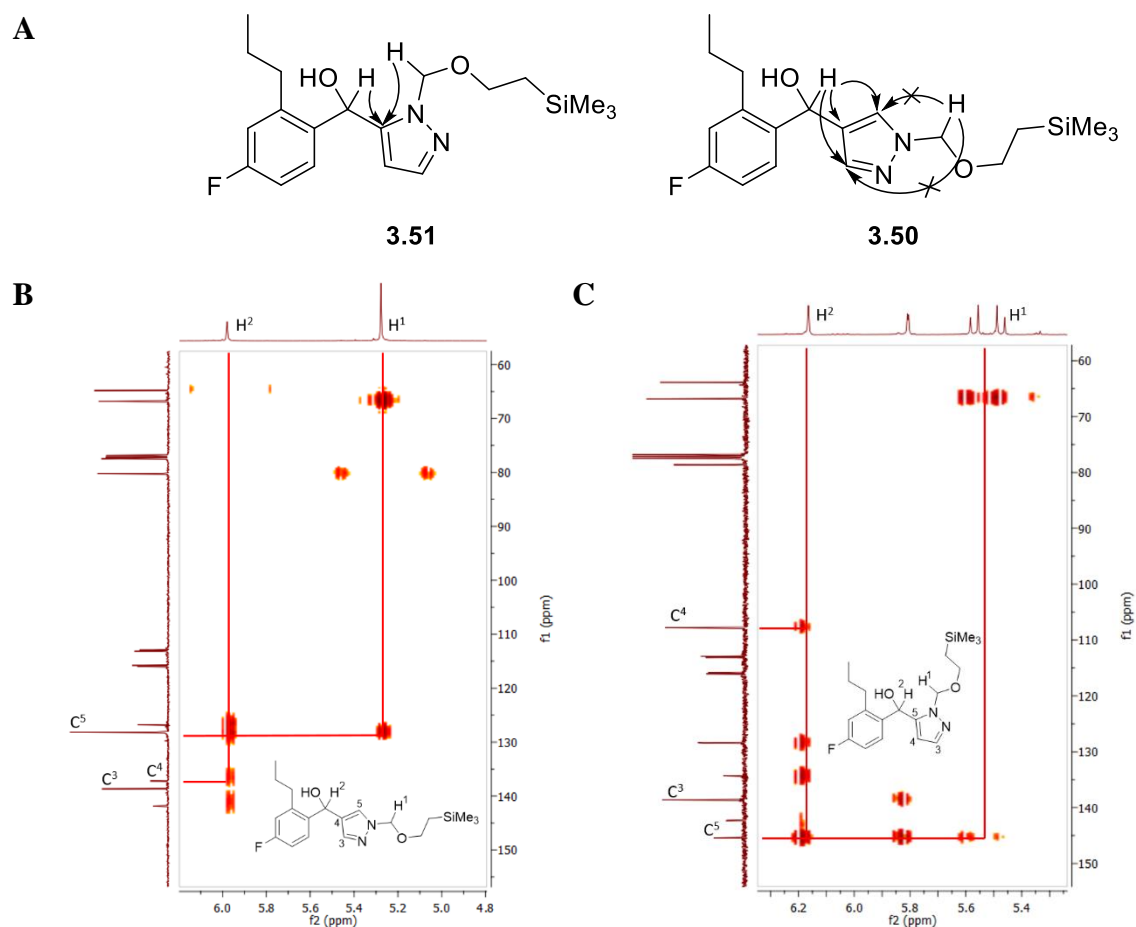
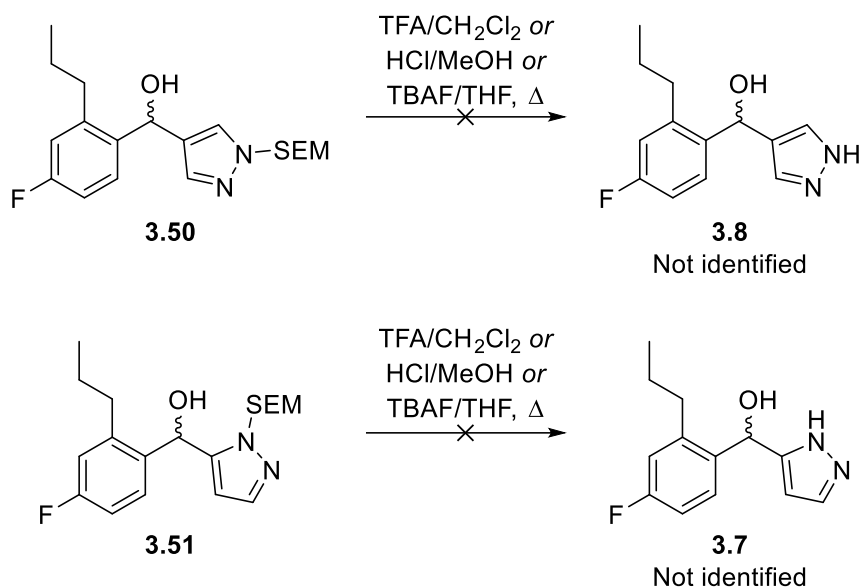


Figure 3.24: Highlighted interactions in **3.50** and **3.51** identified through HMBC NMR experiments

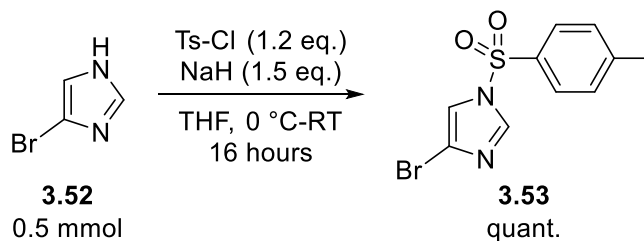
However, attempts at deprotection, despite showing full consumption of the protected intermediates **3.50** and **3.51**, were unable to deliver the desired pyrazole analogues **3.8** and **3.7**, respectively (**Scheme 3.19**). Following multiple attempts leading to decomposition of the reaction material, this approach towards building the pyrazole analogues **3.17** and **3.18** was abandoned.



Scheme 3.19: Failed deprotection reactions towards pyrazole analogues **3.8** and **3.7**

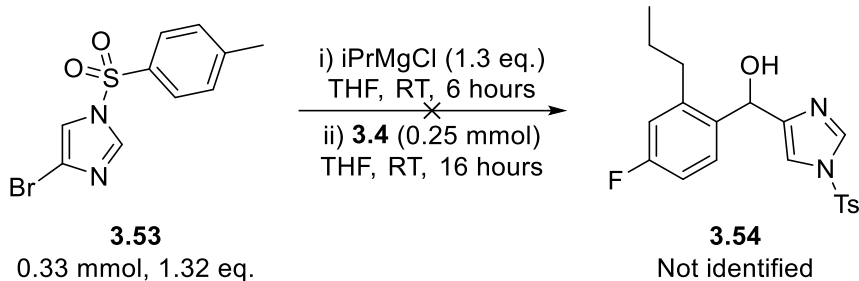
4-Imidazole **3.6**

Imidazole analogue **3.6** was initially proposed to be synthesised using an analogous route to **3.7-8**. In preparation for the route, 4-Bromoimidazole **3.52** was protected with a tosyl group, yielding **3.53** in quantitative yield (**Scheme 3.20**).



Scheme 3.20: Tosyl-protection of 4-bromoimidazole **3.52** towards **3.53**

However, continuing this route had multiple issues. Firstly, the Grignard reaction with **3.53** failed to yield the desired intermediate, **3.54** (**Scheme 3.21**), continuing the trend shown during the attempted syntheses of **3.7** and **3.8** (**Scheme 3.14**)



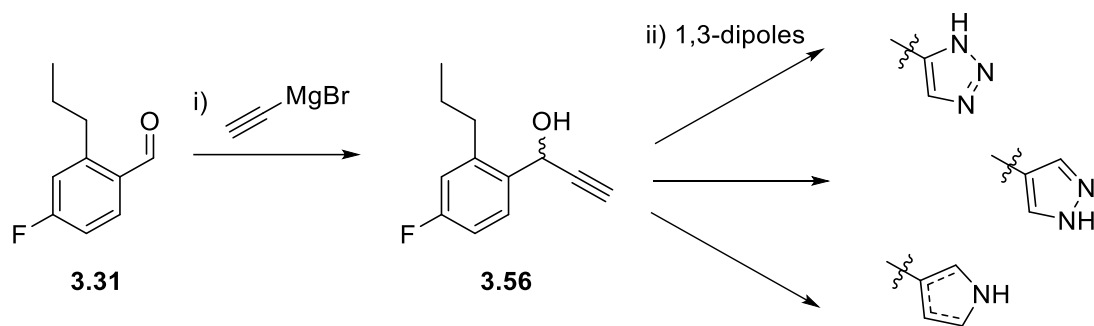
Scheme 3.21: Failed Grignard reaction of **3.53** towards intermediate **3.54**

Triazole **3.9**

Consideration was given to attempting the synthesis of triazole analogue **3.9** using the same, previously attempted route *via* organolithium or Grignard chemistry. However, given the previous failures in these syntheses, and the need to synthesise a protected bromotriazole intermediate, the route would be reconsidered.

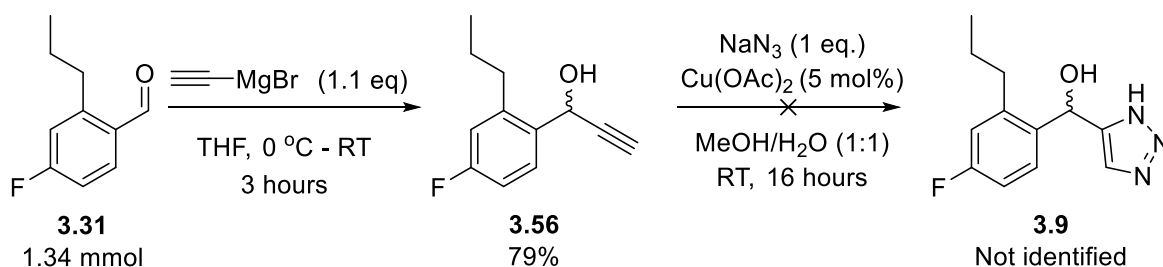
3.5.1.5 Building the heterocycles

With the challenges experienced in isolating the desired heterocyclic analogues of AZ8838 (**3.3**, **3.6-9**), the synthetic route was redesigned with the aim of building the heterocycles through the use of cycloaddition reactions. Starting with benzaldehyde **3.31**, it was thought an alkyne could be introduced using a propargyl Grignard reagent and the desired functionalities installed using [3+2] dipolar cycloadditions with 1,3-dipoles (**Scheme 3.22**).



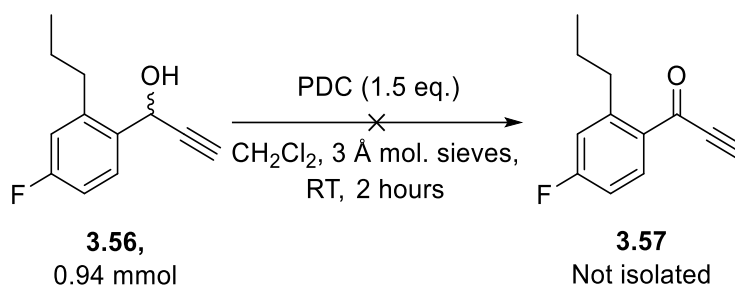
Scheme 3.22: Planned synthetic route towards heterocyclic analogues of AZ8838.

Triazole analogue **3.9** was chosen as the first target, utilising a Click reaction as the [3+2] dipolar cycloaddition.¹⁶⁶ The initial Grignard reaction successfully provided the alkynyl analogue **3.56** in good yields (**Scheme 3.23**, Step 1). However, subsequent attempts at the Click reaction using sodium azide were met with no formation of the desired triazole **3.9** (**Scheme 3.23**, Step 2).¹⁶⁶



Scheme 3.23: Initial attempt at the synthesis of triazole **3.9** via [3+2] dipolar cycloadditions

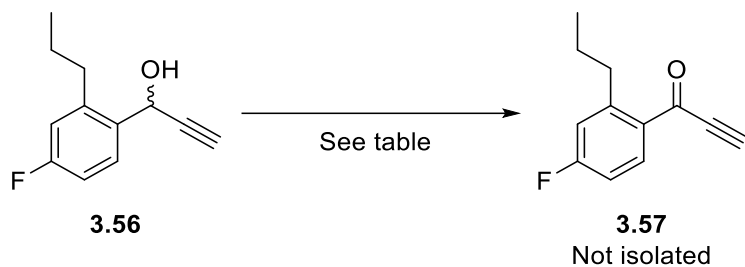
It was thought the presence of the free alcohol functionality may have been interfering in the reaction. To combat this, it was decided to first oxidise the alcohol to the ketone prior to the Click reaction, using oxidation as a form of protecting group. Initial attempts at the oxidation of **3.56** were performed using pyridinium dichromate (PDC) as the oxidising agent (**Scheme 3.24**). However, this ultimately failed to yield the desired ketone **3.57**.



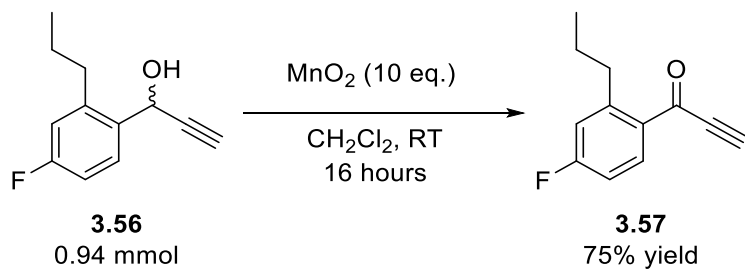
Scheme 3.24: Attempted oxidation of **3.56** using PDC

By changing the oxidising agent to manganese dioxide, it was anticipated the benzylic alcohol could be more readily oxidised. Using THF as the initial solvent at room temperature, no conversion of **3.56** was observed (**Table 3.3**, Entry 1). This continued after heating to 60 °C (Entry 2). However, by changing the solvent to toluene and heating further to 80 °C and then 100 °C, a new species was seen to be formed (Entries 3-4) although the starting material **3.56** remained the major component of the reaction mixture. Finally, by changing the solvent to CH₂Cl₂, alcohol **3.56** was observed to be fully consumed (Entry 5). Repeating the reaction using a fresh batch of **3.56** provided ketone **3.57** in 75% yield (**Scheme 3.25**).

Table 3.3: Optimisation of manganese dioxide oxidation towards ketone **3.57**

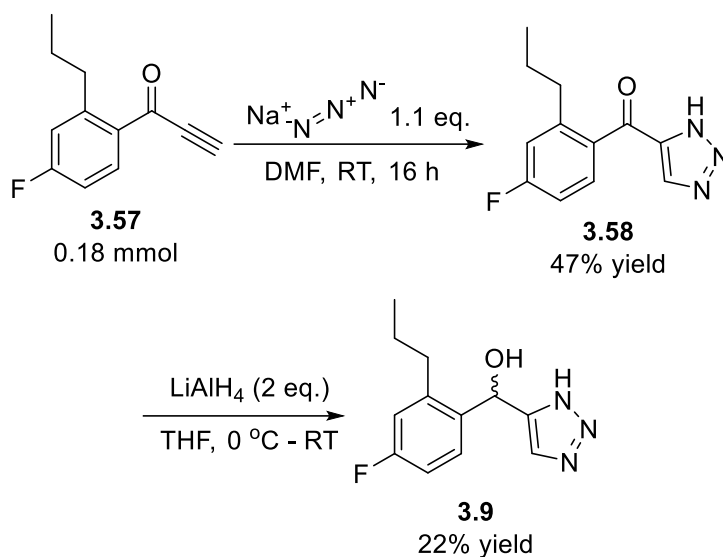


Entry	[MnO ₂]	Solvent	Temp.	Time	TLC
1	5 eq.	THF	Room Temp	Overnight	No conversion
2	10 eq.	THF	60 °C	2 hours	No conversion
3	10 eq.	Toluene	80 °C	2 hours	Low conversion
4	10 eq.	Toluene	100 °C	16 hours	Low conversion
5	10 eq.	CH ₂ Cl ₂	Room Temp	2 hours	Full Conversion



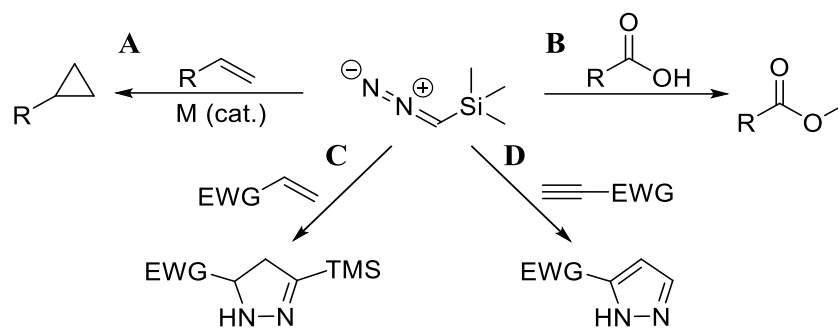
Scheme 3.25: Oxidation of **3.56** towards ketone **3.57**

With ketone **3.57** in hand, the desired [3+2] cycloadditions could be attempted once again. Triazole **3.58** was synthesised using sodium azide as the 1,3-dipole in a metal-free azide-alkyne cycloaddition reaction with a 47% yield, with subsequent reduction of the ketone with lithium aluminium hydride (LAH) providing access to triazole analogue **3.9** in 26% yield (**Scheme 3.26**).



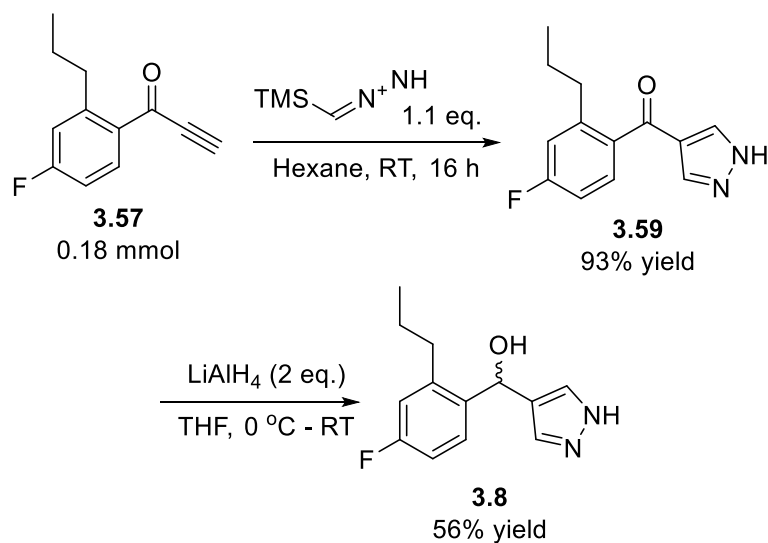
Scheme 3.26: Synthesis of triazole analogue **3.9**

Concurrently, pyrazole **3.59** was synthesised using trimethylsilyl diazomethane as the 1,3-dipole.¹⁸⁴ Trimethylsilyl diazomethane has been more commonly used as a source of a carbene for cyclopropanation reactions or as a methyl source for the methyl esterification of carboxylic acids.^{185,186} Its use as a 1,3-dipole is becoming more widespread, given the increased stability and safety benefits of trimethylsilyl diazomethane in comparison to the traditionally used diazomethane. Examples have been shown using trimethylsilyl diazomethane to produce pyrazolines and pyrazoles upon reaction with electron deficient alkenes and alkynes, respectively.



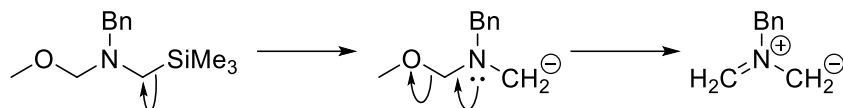
Scheme 3.27: Sample reactions of trimethylsilyl diazomethane including metal catalysed cyclopropanation of alkenes (A), methyl esterification of carboxylic acids (B) and 1,3-dipolar cycloaddition towards substituted pyrazolines (C) and pyrazoles (D)

The corresponding [3+2] dipolar cycloaddition with alkyne **3.57** yielded 4-substituted pyrazole **3.59** exclusively in 93% yield, with the 3-substituted pyrazole not present at all (**Scheme 3.28**). The following LAH-mediated reduction of the ketone was carried out in 52% yield to provide pyrazole **3.8** (**Scheme 3.28**).



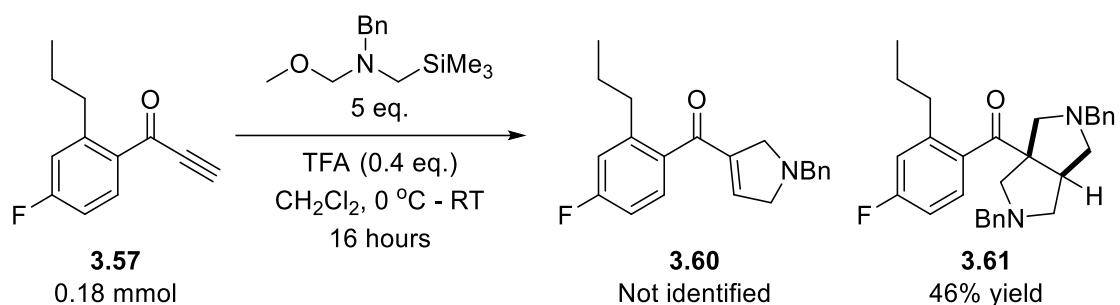
Scheme 3.28: Synthesis of pyrazole analogue **3.8**

To complement the previous targets, a subsequent [3+2] cycloaddition was performed using an azomethine ylide generated from *N*-benzyl-1-methoxy-*N*-((trimethylsilyl)methyl)methanamine *in situ* (**Scheme 3.29**).¹⁸⁷



Scheme 3.29: Generation of reactive azomethine ylide from *N*-benzyl-1-methoxy-*N*-((trimethylsilyl)methyl)methanamine

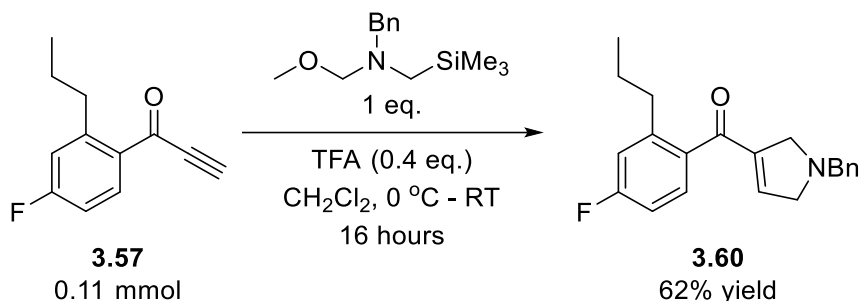
An excess of the azomethine ylide was reacted *in situ* with alkyne **3.57** in an attempt to access pyrroline **3.60** (**Scheme 3.30**). However, the resulting alkene in the pyrroline moiety proved to be a reactive dipolarophile for further cycloaddition, resulting in the fused bis-pyrrolidine **3.61** as the major product (**Scheme 3.30**). Pyrrolines with lowered LUMO have been shown to be synthetically useful as dipolarophiles and dienophiles previously.¹⁸⁸ Additionally, the production of fused pyrrolidines has also been documented, with the fused system being identified as a side product in the synthesis of pyrrolines *via* [3+2] dipolar cycloaddition.¹⁸⁹



Scheme 3.30: [3+2] dipolar cycloadditions leading to bis-pyrrolidine **3.61**

To gain access to pyrroline **3.60**, the equivalents of the azomethine precursor were lowered to stoichiometric quantities. It was reasoned that this change would limit the

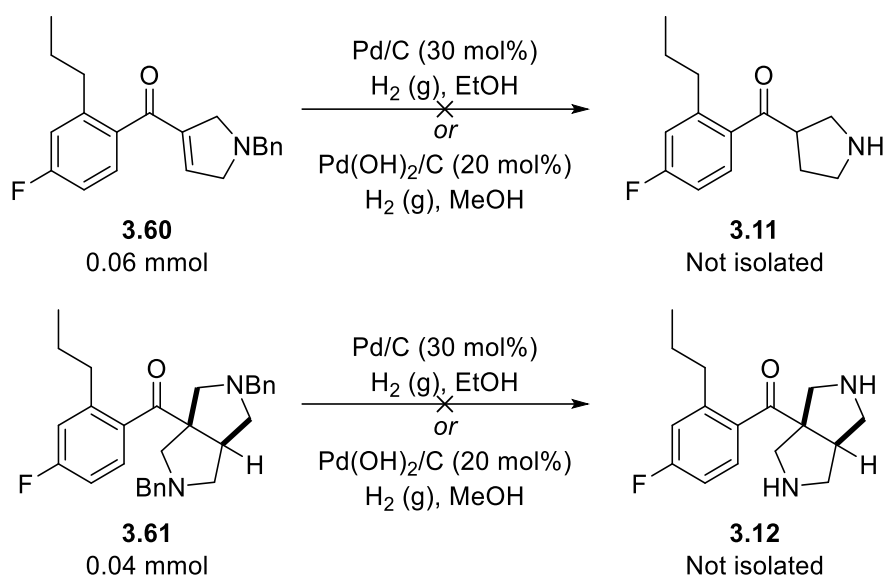
additional [3+2] dipolar cycloaddition towards bispyrrolidine **3.61** and allow isolation of pyrroline **3.60**. Accordingly, pyrroline **3.60** was obtained in 62% yield (**Scheme 3.31**).



Scheme 3.31: Synthesis of pyrroline **3.60** using reduced equivalents of azomethine precursor

With the production of bispyrrolidine **3.61**, access had been gained to an intermediate which showed enriched sp^3 character. It was decided to attempt the reduction of the alkene in pyrroline **3.60** to obtain a matched pair with **3.61** for biological testing. This was a significant deviation from the planned target synthesis, but it was thought that the concurrent reduction of the alkene and deprotection of the benzyl protecting groups would provide facile access to the new target molecules.

Initially, the hydrogenation was carried out using palladium on carbon in a hydrogen atmosphere (**Scheme 3.32**). With starting materials remaining, the palladium source was changed to palladium hydroxide on carbon but, again, this failed to yield the desired products **3.11** and **3.12** (**Scheme 3.32**). With other priorities still pending, synthesis of these compounds was halted.



Scheme 3.32: Failed reductions towards pyrrolidine **3.11** and bis-pyrrolidine **3.12**

3.5.2 Synthesis of Linker Analogues

As with the imidazole analogues synthesised above, it was anticipated that synthesis of carbonyl analogue **3.13** and amine analogue **3.14** (**Figure 3.25**) could be readily accessed *via* slight modification of the established synthetic route.

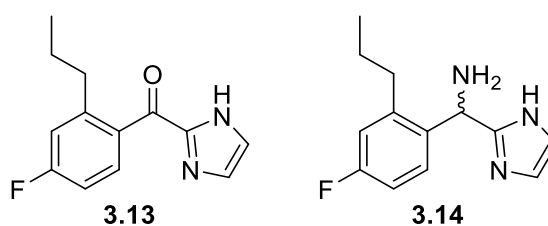
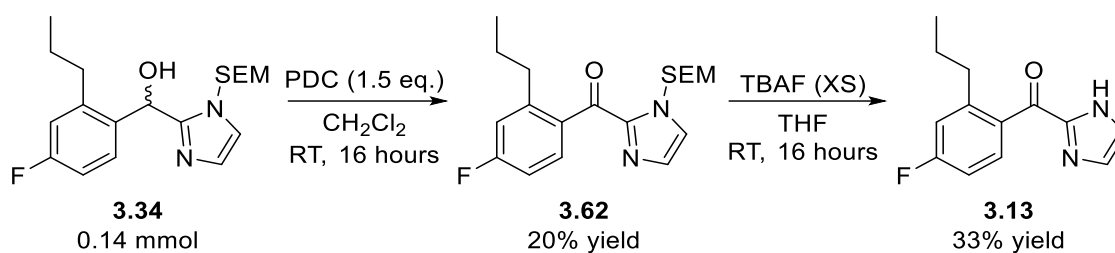


Figure 3.25: Proposed linker analogues exploring modifications to the hydroxyl group

3.5.2.1 Ketone analogue

The ketone analogue **3.13** was synthesised readily by a small modification to the existing route towards AZ8838. Starting with protected intermediate **3.34**, the alcohol was oxidised to the corresponding ketone, **3.62** using PDC, before removing the SEM protecting group

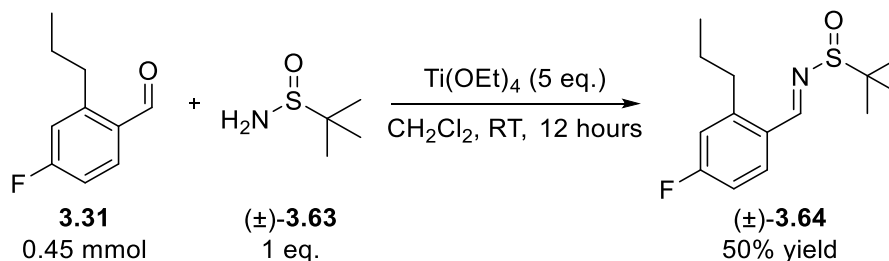
using TBAF in THF to access the desired ketone analogue in low, but usable, yields of 7% over two steps (**Scheme 3.33**).



Scheme 3.33: Synthesis of carbonyl analogue **3.13** from common AZ8838 intermediate **3.34**

3.5.2.2 Amine analogue

The route chosen for the synthesis of aminated analogue **3.14** was based on the chiral nature of the series. By utilising Ellman auxiliaries, initial synthesis could be carried out racemically while also allowing access to a chirally pure species through an analogous route using an enantiopure sulfinamide species if needed upon biological testing. Starting from benzaldehyde intermediate **3.31**, the aldehyde was transformed into Ellman imine (\pm)-**3.64** by treating with racemic 2-methylpropane-2-sulfinamide (\pm)-**3.63** in the presence of titanium ethoxide (**Scheme 3.34**).¹⁹⁰



Scheme 3.34: Synthesis of racemic Ellman imine (\pm)-**3.49**

Upon installation of the auxiliary, attempts were made to install the protected imidazole using *n*-butyllithium, but this ultimately did not provide the desired product. Deprotection of the crude product was also attempted, but the resulting crude reaction mixture did not

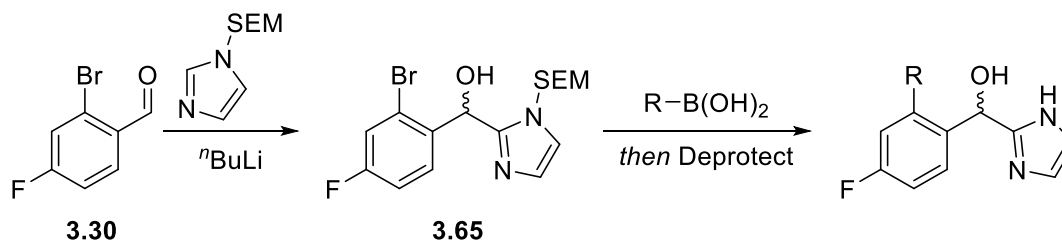
contain traces of **3.14**. Given time constraints, the route towards this analogue was deprioritised.

3.5.3 Synthesis of Propyl Analogues

Modifications of the phenyl ring were focused primarily on the propyl chain. Given the synthetic route used, this site could hypothetically be modified with very little change from the established synthetic route. Additionally, a wide variety of functional groups would be accessible given the range of boronic acids commercially available.

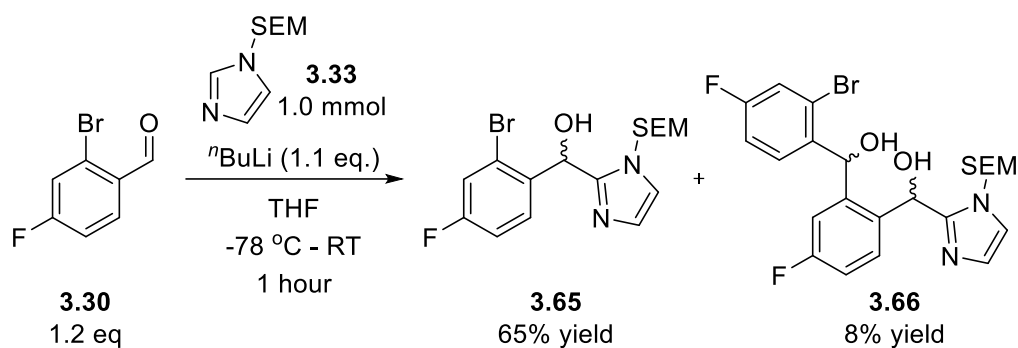
3.5.3.1 Reversing the Synthetic Route

While diversification at the propyl position could be carried out using the previously established synthetic route, doing so in this manner would require the divergent step to be carried out first followed by furnishing the rest of the molecule. By reversing the synthetic steps (**Scheme 3.35**), it was proposed that late stage functionalisation could be carried out. If successful, this would allow more compounds to be accessed readily with greater efficiency.



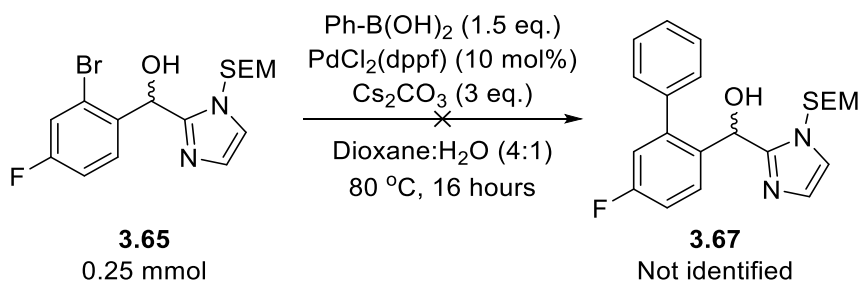
Scheme 3.35: General scheme for the synthesis of AZ8838 analogues via a reversed synthetic route

The initial lithiation reaction between benzaldehyde **3.30** and imidazole **3.33** occurred in moderate yield, providing access to **3.65** in 36% yield (**Scheme 3.36**). In addition to the desired bromo intermediate **3.65**, a side product was also formed due to lithium-halogen exchange with the bromine. This resulted in further nucleophilic attack onto bromobenzaldehyde **3.30**, providing diol **3.66** in isolable quantities.



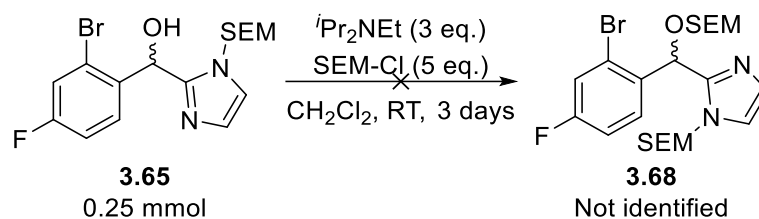
Scheme 3.36: Attempted coupling of imidazole **3.33** and bromobenzaldehyde **3.30** to yield **3.65** and side-product **3.66**

With bromo-intermediate **3.65** in hand, a test Suzuki-Miyaura cross-coupling was carried out using phenylboronic acid (**Scheme 3.37**). However, the desired product **3.67** was not identified in the reaction mixture.



Scheme 3.37: Failed Suzuki-Miyaura cross-coupling reaction of **3.65** towards **3.67**

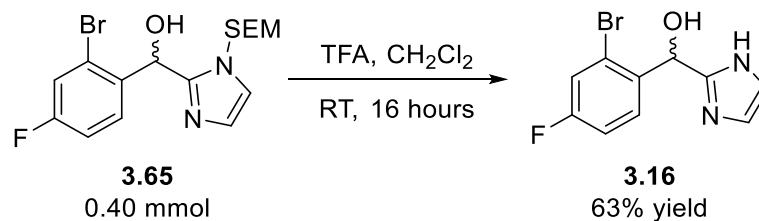
It was thought that the presence of the free hydroxyl was interfering in the reaction. As such, protection of the alcohol before undergoing the Suzuki reaction was attempted using $i\text{Pr}_2\text{NEt}$ and SEM-Cl. After 3 days, full consumption of the starting alcohol was observed but the desired protected alcohol **3.68** was not identified in the reaction mixture (**Scheme 3.38**).



Scheme 3.38: Failed protection of **3.65** with SEM-Cl

Given the difficulties experienced with furnishing the imidazole moiety before utilising the cross-coupling chemistry, it was decided to return to the previously established route despite the inherent inefficiencies with functionalising the propyl position early in the synthesis.

Despite the complications with reversing the route to allow divergent late-stage modification of the propyl region, the bromo-intermediate **3.65** was deprotected using TFA in CH_2Cl_2 to provide **3.16** in 63% yield, which was submitted for biological testing as a propyl analogue (**Scheme 3.39**).



Scheme 3.39: Deprotection of **3.65** to provide bromo-analogue **3.16**

3.5.3.2 Original Route

By returning to the previously established route for analogue synthesis, it was required to generate a series of substituted benzaldehydes to access structurally diverse analogues. These analogues were designed to explore the hydrophobic pocket in which the propyl chain resides, by utilising reductions and increases in steric bulk to investigate the

available hydrophobic space. An initial eleven species were targeted, based on available boronic acids (**Figure 3.26**).

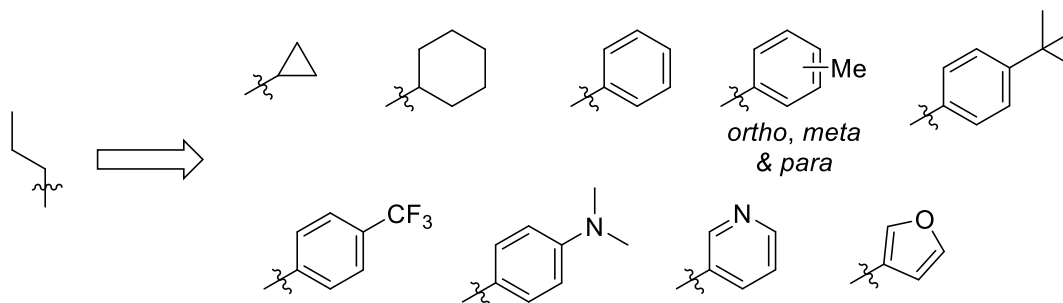
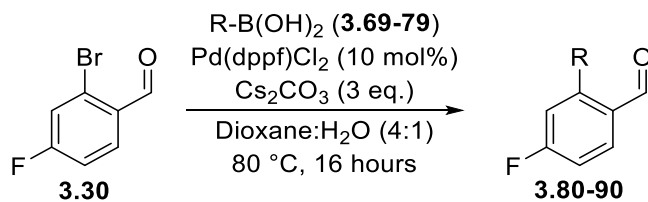


Figure 3.26: Initial targets for propyl analogue synthesis of **3.1**

The initial library of eleven boronic acids (**3.69-79**) was used within Suzuki-Miyaura cross-coupling reactions towards benzaldehydes **3.80-90** (**Table 3.4**). The conditions used for the reactions were adapted from the synthesis of AZ8838 (**3.1**) by Cheng *et al.*⁴ While most of the Suzuki reactions were moderate to high yielding, the reaction with cyclohexyl boronic acid (**3.70**) failed to provide the corresponding benzaldehyde, **3.81**, following purification (Entry 2). Full consumption of bromobenzaldehyde **3.30** was observed. However, NMR and LC-MS showed a lack of target product **3.81**. This could likely be caused by protodeboronation of **3.70**, leading to a species incapable of undergoing a Suzuki reaction. Alternatively, the boronic acid could be undergoing β -hydride elimination during coupling or impeding transmetalation. Each of these possibilities are well-documented issues with sp^3 boronic acids.¹⁹¹

Table 3.4: Suzuki-Miyaura Cross-Couplings towards diverse benzaldehyde intermediates **3.80-90**

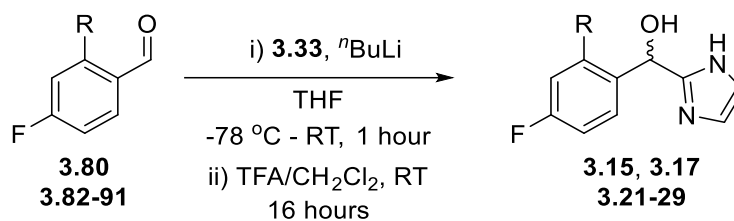
Entry	3.3 (mmol)	R	Boronic Acid	Product Yield
1	1.0		3.69 , 1.5 eq.	3.80 , 77% yield
2	1.0		3.70 , 1.5 eq.	3.81 Not isolated
3	0.5		3.71 , 2.0 eq.	3.82 , 76% yield
4	1.0		3.72 , 1.5 eq.	3.83 , 55% yield
5	1.0		3.73 , 1.5 eq.	3.84 , 68% yield
6	1.0		3.74 , 1.5 eq.	3.85 , 52% yield
7	1.0		3.75 , 1.5 eq.	3.86 , 50% yield
8	1.0		3.76 , 1.5 eq.	3.87 , 74% yield
9	1.0		3.77 , 1.5 eq.	3.88 , 34% yield
10	1.0		3.78 , 1.5 eq.	3.89 , 67% yield
11	1.0		3.79 , 3.0 eq.	3.90 , 66% yield

Following the successful synthesis of benzaldehydes **3.80/82-90**, a modified lithiation protocol was devised. Firstly, the organolithium step and deprotection steps were carried out with no purification in between. This was intended to allow higher throughput generation of the desired AZ8838 analogues.

Secondly, with the exclusion of **3.25** and **3.26**, the limiting reagent was changed to SEM-protected imidazole **3.34**. With the increasing polarity following the deprotection of the SEM-protecting groups towards the final compounds (**3.77-87**), it was anticipated that purification of the desired analogues from leftover imidazole could prove more difficult than separation from leftover benzaldehydes. By changing the limiting reagent, it was thought that the imidazole would be fully consumed and any residual benzaldehyde derivatives would be readily washed off from the solid product due to their increased solubility in non-polar solvents or removed by flash chromatography. For the most part, this hypothesis proved to be correct with the final desired compounds **3.15/17/21/24-28** all being isolated in moderate-to-good yields over two steps (**Table 3.5**, Entries 1-7, 11).

However, the organolithium reactions to provide dimethylaminophenyl analogue **3.29**, pyridinyl analogue **3.22** and furanyl analogue **3.23** all failed to yield the desired products (**Table 3.5**, Entries 8-10).

Table 3.5: ⁿBuLi-mediated couplings towards propyl analogues of AZ8838. ***3.15** was synthesised in two steps, with the SEM-protected intermediate **3.15'** isolated in quantitative yield (Section 6.3.4.4).



Entry	R	Benzaldehyde	3.6	ⁿ BuLi	Product
1		3.80 0.55 mmol	0.50 mmol	0.50 mmol	3.17 26% yield
2		3.82 0.55 mmol	0.50 mmol	0.50 mmol	3.21 26% yield
3		3.83 0.55 mmol	0.50 mmol	0.50 mmol	3.24 8% yield
4		3.84 0.50 mmol	0.55 mmol	0.55 mmol	3.25 22% yield
5		3.85 0.50 mmol	0.55 mmol	0.55 mmol	3.26 36% yield
6		3.86 0.44 mmol	0.40 mmol	0.40 mmol	3.28 67% yield
7		3.87 0.55 mmol	0.50 mmol	0.50 mmol	3.27 25% yield
8		3.88 0.55 mmol	0.50 mmol	0.50 mmol	3.29 Not isolated
9		3.89 0.55 mmol	0.50 mmol	0.50 mmol	3.22 Not isolated
10		3.90 0.55 mmol	0.50 mmol	0.50 mmol	3.23 Not isolated
11	H	3.91 0.55 mmol	0.50 mmol	0.50 mmol	3.15 26% yield*

3.5.3.3 Resynthesis of 3.79

Following initial biological testing (*vide infra*, **Section 3.6**), it was necessary to resynthesise and further characterise *o*-tolyl analogue **3.24**. Initial characterisation of **3.24** confirmed the presence of the desired mass by LC-MS, but the NMR analysis indicated the presence of additional signals. However, the extra peaks did not integrate with the rest of the NMR, leading to the initial assumption that the molecule was potentially rotameric. The sites of restricted rotation were thought to be the two C-C single bonds from the benzene ring (**Figure 3.27**).

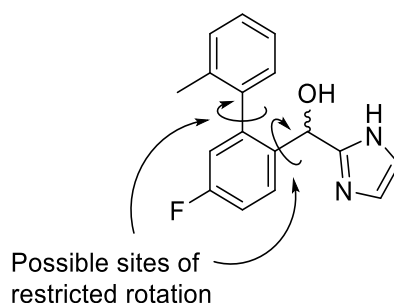
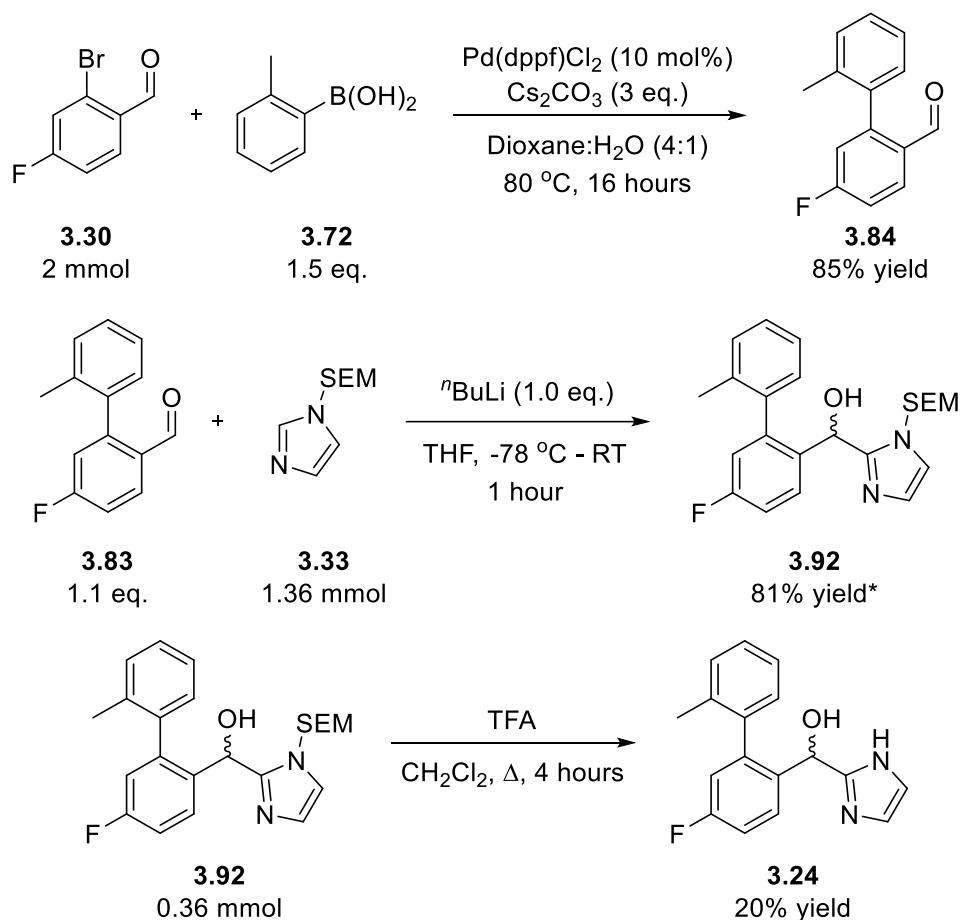


Figure 3.27: Rotameric nature of **3.24**

To rule out the possibility of side-product formation, it was decided to employ variable-temperature NMR. However, before using variable temperature NMR techniques it was necessary to access more of the analogue to provide high concentrations for analysis. The initial Suzuki-Miyaura cross-coupling was carried out on a 2.0 mmol scale, providing benzaldehyde **3.84** in 85% yield (**Scheme 3.40**). Subsequently, the *n*-butyllithium-mediated coupling of **3.84** and **3.33** was carried out on a 1.5 mmol scale, yielding 500 mg of **3.92** as a crude product (**Scheme 3.40**). While not purified, **3.92** was confirmed to contain similar extra peaks to **3.24** as described above. Finally, the deprotection of the crude sample of **3.92** was carried out initially on two 150 mg replicates, providing a total of 20 mg of **3.24** (**Scheme 3.40**). The lowered yield in the final step was thought to be due to the harsh nature of the conditions used. Initial attempts at deprotection were carried out

in TFA overnight and these provided full conversion of the protected starting material **3.92** but no indication of the presence of **3.79**.



Scheme 3.40: Synthesis of *o*-tolyl analogue **3.24**

Having gained access to **3.24**, variable temperature NMR experiments could be carried out. It was thought that by increasing the temperature, the signal from the two rotamers could be averaged out, and a single spectrum obtained. By heating the sample from 23 °C sequentially up to 100 °C while conducting ^1H NMR experiments, the slow convergence of some peaks can be observed (**Figure 3.28, Appendix III**). Firstly, the doublet signal obtained for the N-H peak is shown to converge and shift rightward with heating (**Figure**

3.28A). Additionally, two doublet-of-doublets, thought to represent the hydroxyl hydrogen atom and the methine linker, converge to form a triplet at high temperatures (**Figure 3.28B**).

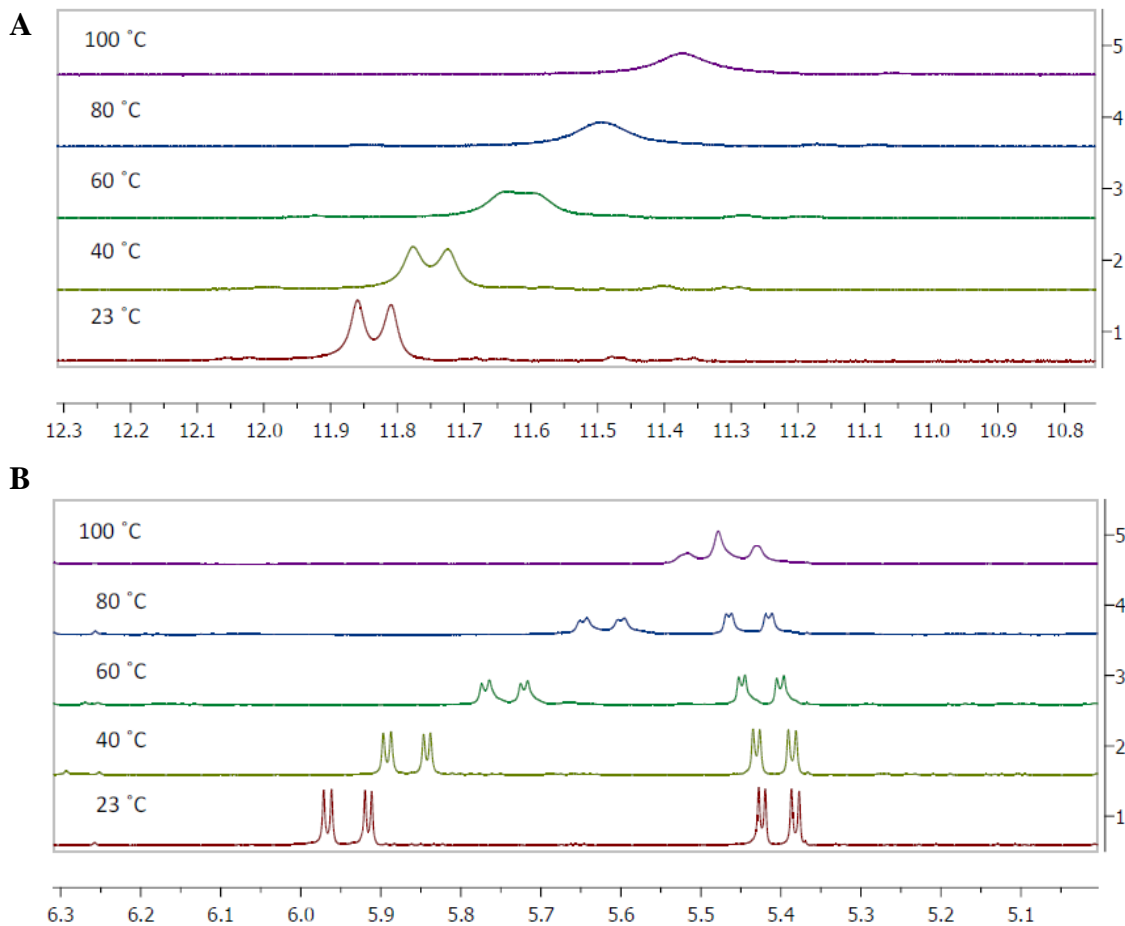


Figure 3.28: Variable temperature NMR experiments for **3.24**. **A** Convergence of N-H peak (11.83 ppm, d, $J = 25.4$ Hz). **B** Convergence of linking methine peaks (5.94 ppm, dd, $J = 25.4, 4.5$ Hz and 5.40 ppm, dd, $J = 20.9, 4.4$ Hz).

However, the tolyl methyl peak and, in the ^{19}F NMR, the C-F peak all remained split at high temperatures (**Figure 3.29A-B, Appendix III**). Following the variable temperature experiments, the product was demonstrated to be homogenous by TLC and by LC-MS analysis. The retention of some split peaks with heating whilst others converged suggests the rotameric nature of the molecule, coupled with the chiral linker, could result in axial

chirality around the phenyl-phenyl bond, resulting in a diastereomeric mixture which would be consistent with the observed NMR data.

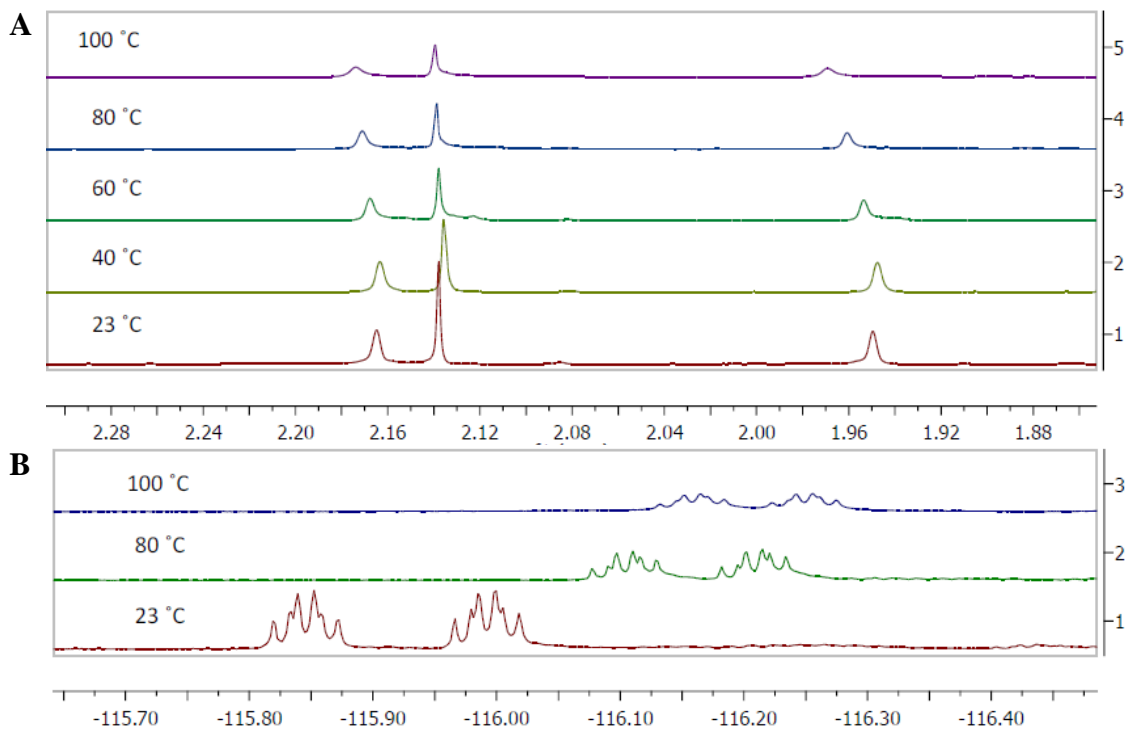


Figure 3.29: Variable temperature NMR experiments of **3.24**. **A** Lack of convergence for split tolyl -CH₃ peak (¹H NMR, 2.16 ppm, s and 1.95 ppm, s). **B** Partial convergence of fluorine peak (¹⁹F NMR, -116.12 - -116.30 ppm, m).

3.5.4 Alkenyl analogues

Following the synthesis of eight analogues of the propyl moiety (**Section 3.5.3**), two further analogues were chosen for synthesis in allyl analogue **3.18** and vinyl analogue **3.19** (**Figure 3.30**). The alkenyl analogues were hypothesised to occupy a similar chemical volume to the propyl chain but in a different orientation.

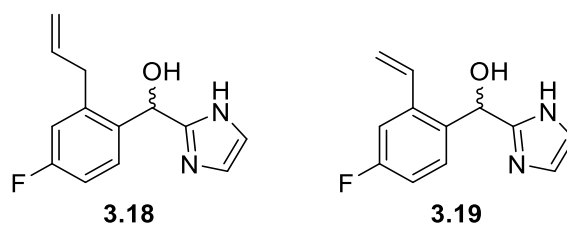
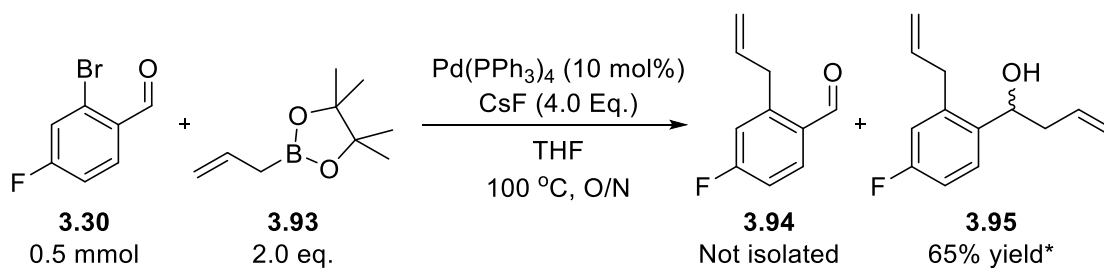


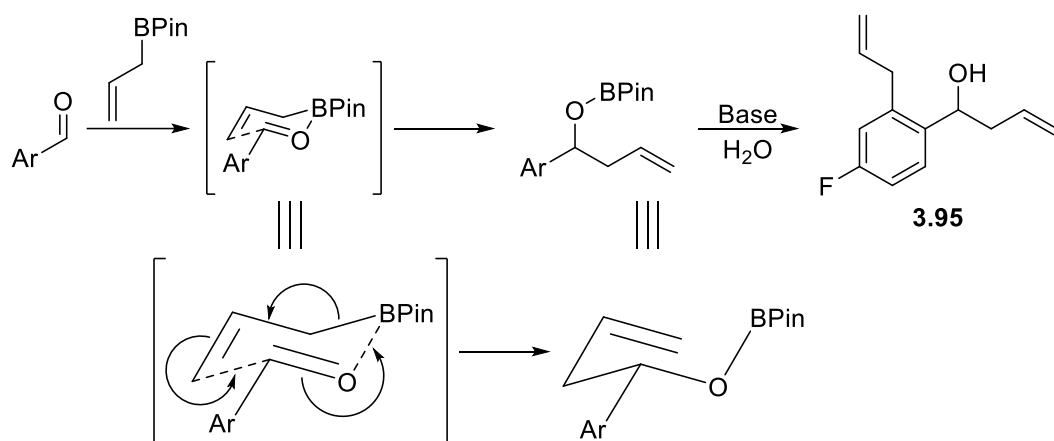
Figure 3.30: Allyl and vinyl analogues of AZ8838, **3.18** and **3.19**

Access to these compounds was proposed using an analogous route to the other propyl analogues. Accessing allyl analogue **3.18** was attempted using an analogous route, starting with the Suzuki-Miyaura cross-coupling between benzaldehyde **3.30** and allyl boronic acid pinacol ester **3.93** to form allylbenzaldehyde **3.94**. Unfortunately, **3.94** was not identified within the reaction mixture, with allyl alcohol **3.95** being isolated in 65% yield (**Scheme 3.41**).



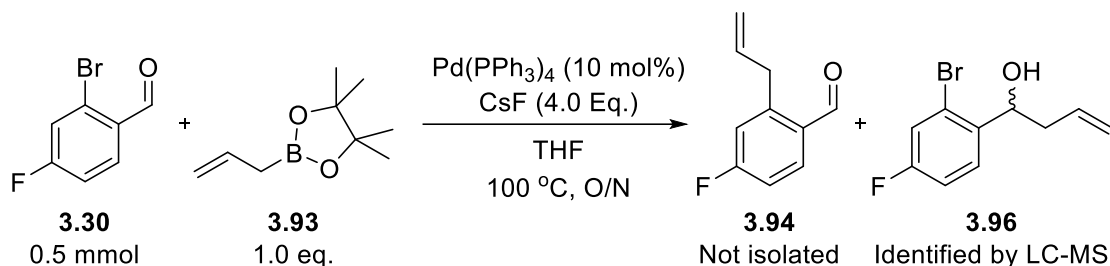
Scheme 3.41: Attempted Suzuki-Miyaura Cross-Coupling towards **3.94** resulting in the formation of **3.95**

The additional allylation was hypothesised to occur by an allylation procedure analogous to the Roush Asymmetric Allylation, excepting the chiral nature of the boronic ester used in the asymmetric reaction.¹⁹² Mechanistically, the oxygen of the aldehyde chelates to the boron followed by breaking of the C=O bond to form an O-B bond and C-C bond (**Scheme 3.42**).



Scheme 3.42: Proposed mechanism of Roush-like Allylation towards allyl alcohol **3.95**

In order to limit the allylation reaction with the aldehyde, the stoichiometry of **3.94** was reduced to stoichiometric quantities with the hope that the Suzuki reaction would be the more favourable process. However, the allylation reaction proved to be more favourable, with allyl alcohol **3.96** being the only observable product of the reaction (**Scheme 3.43**).

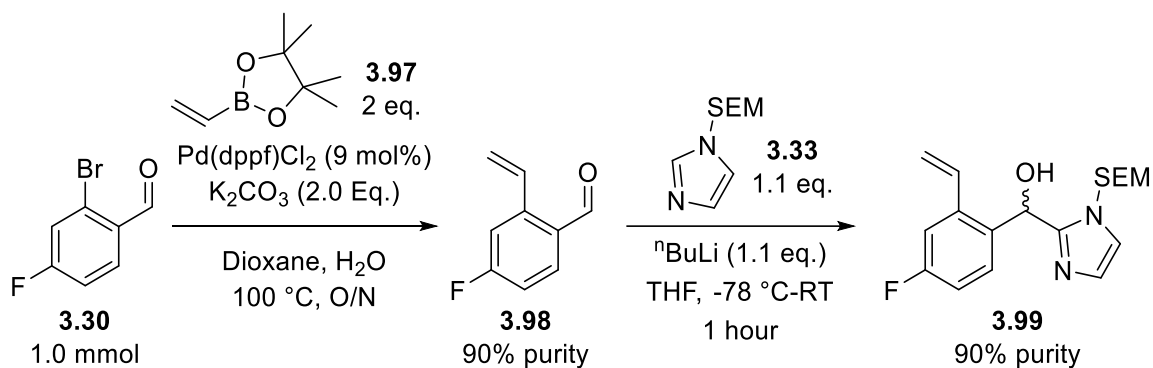


Scheme 3.43: Revised reaction conditions for Suzuki-Miyaura reaction resulting in the formation of **3.96**

With the problems associated with incorporating the allyl group at the start of the synthesis and the observed issues with Suzuki reactions following imidazole coupling (**Scheme 3.37**), the allyl analogue **3.18** was abandoned.

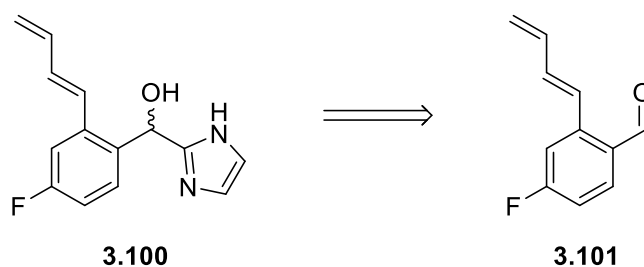
To synthesise vinyl analogue **3.18**, bromobenzaldehyde **3.30** was firstly coupled with vinylboronic acid pinacol ester **3.97** to provide vinylbenzaldehyde **3.98**. While **3.98** was not fully purified, the presence of **3.98** was confirmed in 90% purity within the reaction

mixture by ^1H NMR (**Scheme 3.44**). The crude benzaldehyde was then coupled with **3.33**, making the assumption that intermediate **3.99** would be more readily purified (**Scheme 3.44**).



Scheme 3.44: Suzuki-Miyaura cross-coupling and organolithium coupling towards vinyl intermediate **3.99**

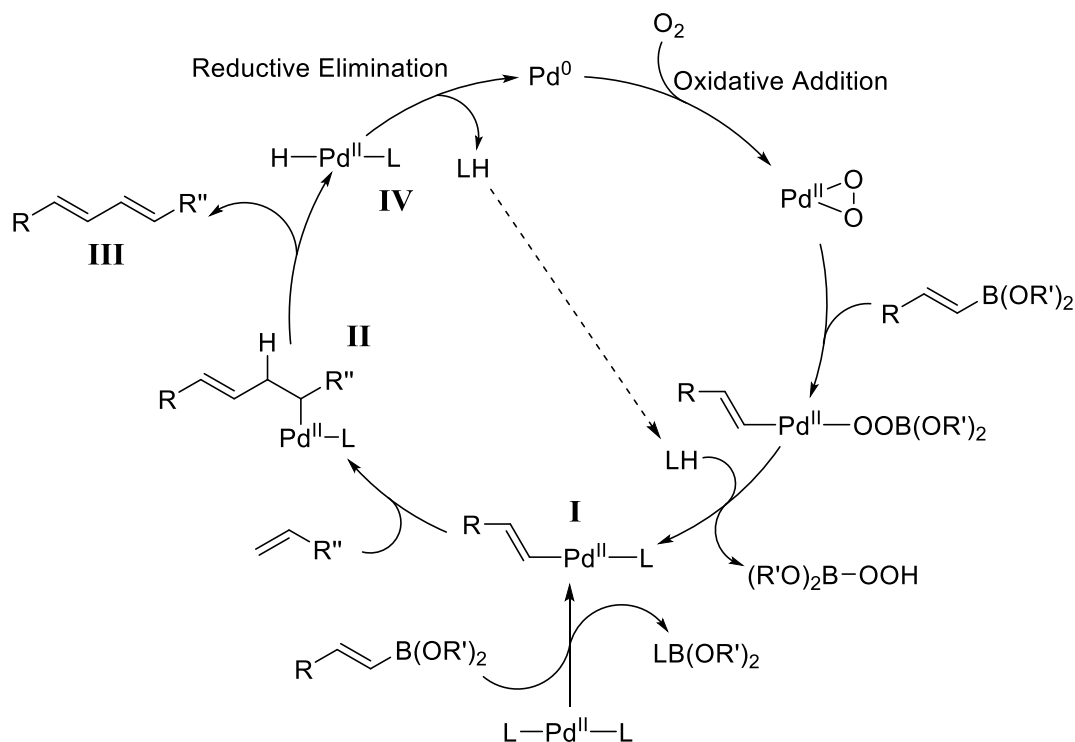
However, the isolated secondary alcohol **3.99** retained a 10% impurity which, following interpretation of NMR and LC-MS data, was confirmed to be the diene structure **3.100**, accessed *via* benzaldehyde **3.101** (**Scheme 3.45**). These molecules appeared to coelute with their vinyl analogues by LC-MS, HPLC and TLC, making purification challenging.



Scheme 3.45: Side-product **3.100** and preceding intermediate **3.101** formed during the Suzuki reaction towards **3.99**

Diene **3.101** was hypothesised to be forming due to an additional cross-coupling reaction between the desired alkene intermediate **3.98** and the excess vinyl boronic acid pinacol

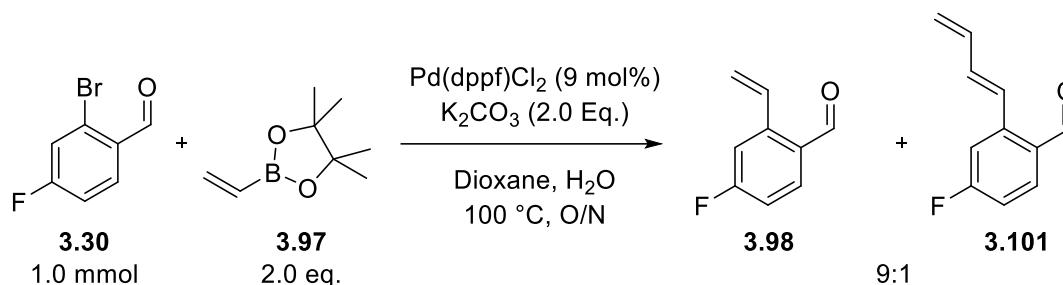
ester **3.97**. While sp^2 - sp^2 cross-couplings of this nature between alkenes have been described, they have typically been shown to require an oxygen atmosphere to allow oxidative addition of a Pd^0 catalyst (**Scheme 3.46**).^{193,194} It was proposed that the additional C-C bond could be formed following in a base-free cross-coupling reaction following initial transmetalation with an alkyl boronic acid, forming Pd^{II} intermediate **I**.¹⁹³ The second alkyl unit could then be introduced *via* chelation to the palladium centre and subsequent migratory insertion to yield intermediate **II**.¹⁹³ Finally, β -hydride elimination can yield the cross-coupled diene, **III**, and palladium intermediate **IV** which would be reduced to allow the catalytic cycle to continue upon reoxidation.¹⁹³



Scheme 3.46: Proposed mechanism for palladium-mediated cross-coupling of alkenyl boronic acids and functionalised alkenes.¹⁹³

The Suzuki reaction performed above was carried out in an inert atmosphere, but the synthesis of diene **3.101** could suggest the presence of oxygen within the reaction vessel.

To prevent the side-product **3.101** from being formed during the Suzuki reaction to form **3.98**, the amount of the vinyl boronic acid pinacol ester was reduced to a stoichiometric quantity. However, this ultimately yielded the same 9:1 ratio of alkene to diene (**Scheme 3.47**). These compounds again proved to be inseparable as the aldehyde and after reacting with the imidazole, therefore the route towards **3.19** was abandoned.



Scheme 3.47: Revised Suzuki reaction resulting in **3.98** and **3.101**

3.5.5 Summary of Synthesis

Out of a total twenty-six target molecules, fifteen entirely novel analogues of AZ8838 (**3.1**) have been synthesised as racemic mixtures (**Figure 3.31**). These analogues cover three key regions of AZ8838, with five analogues exploring changes to the imidazole, one modification to the alcohol linker and nine exploring changes to the propyl group on the phenyl ring.

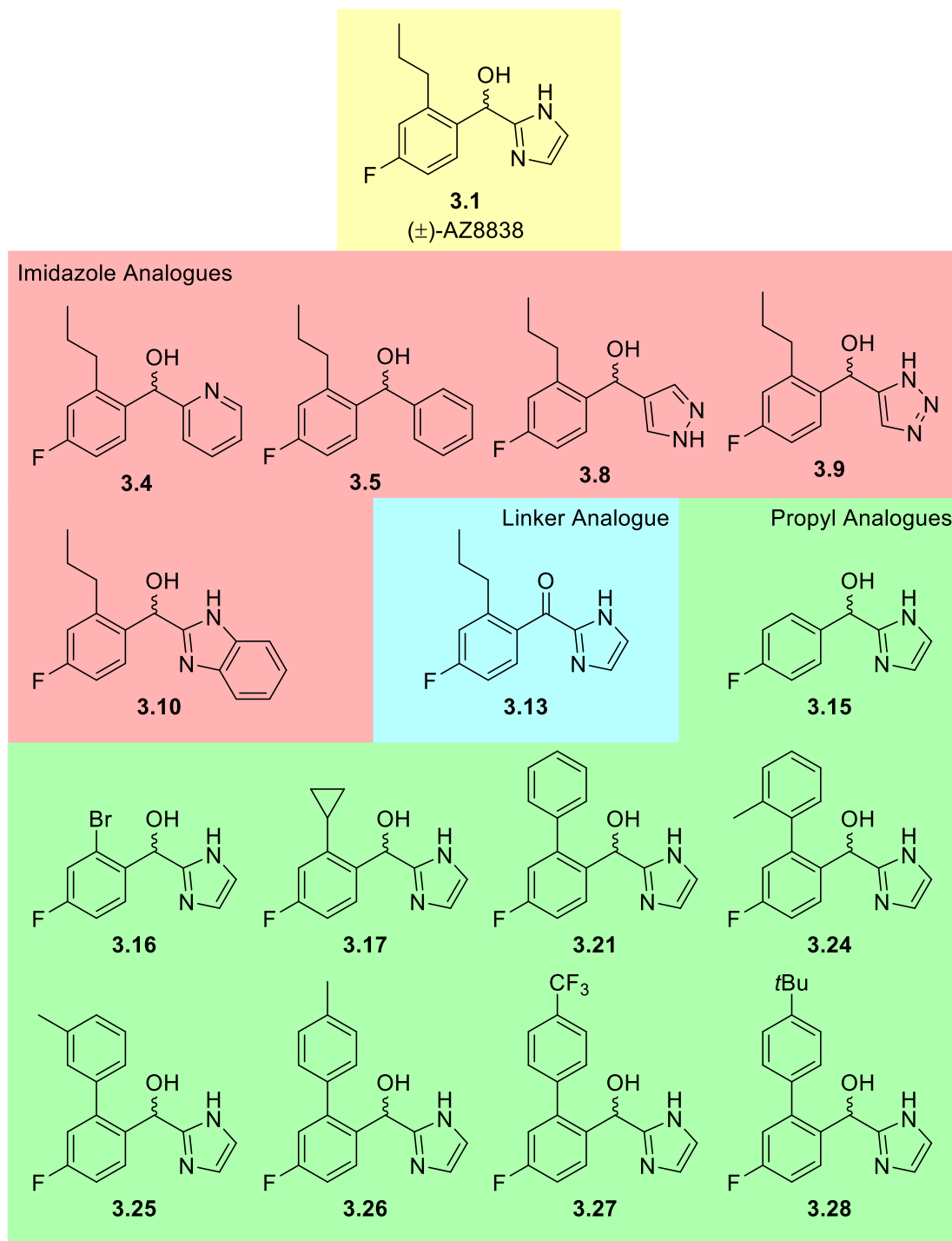


Figure 3.31: Synthesised analogues of AZ8838 (**3.1**) covering SAR of three main regions of the molecule: imidazole (red), linker alcohol (yellow) and propyl position (green).

3.6 Biological Data

Having secured access to a range of AZ8838 analogues, the assessment of their pharmacological profile could then be carried out using *in vitro* assays. The assay intended for use was a luminescence assay within NCTC2544 cells, a skin epithelial-like cell line, stably transfected with PAR2 and NF- κ B constructs.

A known downstream signal of PAR2 activation, NF- κ B is a complex of proteins which control DNA transcription (**Figure 3.32**). NF- κ B has an established role in pro-inflammatory signalling, where it functions in response to stimuli including stress, radiation or bacterial/viral invasion in addition to responding to damage sustained from free radicals.¹⁹⁵ Additionally, NF- κ B has been shown to be active in a range of diseases including asthma, atherosclerosis, arthritis, neurodegenerative diseases and cancer, where its aberrant functions contribute to cell proliferation, inflammation and promotion of tumorigenesis.^{195–198} This highlights the physiological relevance of NF- κ B for investigation of PAR2 antagonists, given the essential roles of NF- κ B, in addition to the consequences of its aberrant activation, and its role in downstream signalling from PAR2.¹⁹⁹

Within the reporter cells, activation of NF- κ B causes the transcription of a luciferase enzyme which will, in turn, respond to a luciferase substrate, resulting in a quantifiable luminescent output. As such, the luminescent output can be directly correlated with PAR2 activation by the natural PAR2 agonist protease, trypsin.²⁰⁰

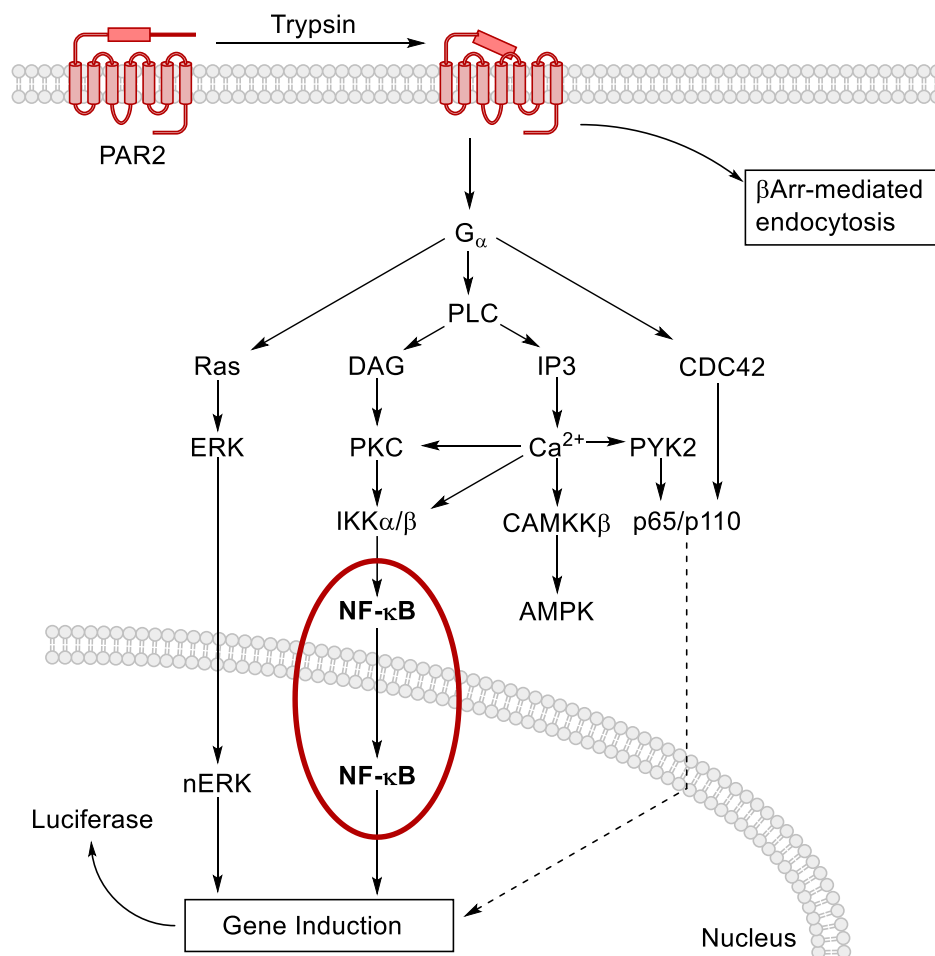


Figure 3.32: Canonical signalling occurring as a result of PAR2 activation.

3.6.1 Confirmation of **3.1** Function

Prior to analysing the generated compounds within the NF κ B assay, confirmation of the activity of the synthesised batch of **3.1** was carried out. **3.1** was firstly analysed at three concentration points, 3 μ M, 10 μ M and 30 μ M, to confirm inhibition in comparison with a commercial sample of **3.1** (**Figure 3.33**). It can be noted that AZ8838 and **3.1** both display similar pharmacological properties within this assay. Both caused concentration-dependent decreases in trypsin-mediated luminescent responses, confirming the literature precedent for PAR2 inhibition with AZ8838 (**Figure 3.33**). Additionally, both compounds failed to initiate a response in the cells following addition on their own, suggesting they did not exhibit agonist pharmacology (**Figure 3.33**, AZ and **3.1**).

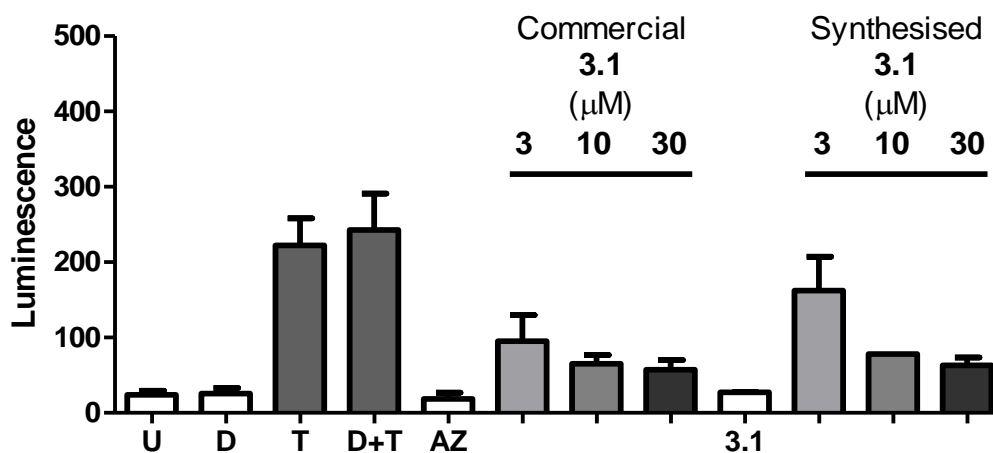


Figure 3.33: Initial screening of a commercial sample and the synthesised sample of **3.1** within the NFκB luciferase reporter assay. The graph shows the luminescent response on an arbitrary scale. U = untreated cells, D = DMSO treatment, T = trypsin treatment (100 nM), C = combined DMSO pretreatment followed by trypsin treatment. AZ/**3.1** = treatment with commercial/synthesised **3.1**. Where concentration is noted, cells were pretreated with the noted drug followed by treatment with trypsin (100 nM). Data represents N = 2 for AZ8838 and **3.1** and N = 3 for controls, with mean ± SEM.

Following the initial testing in the assays, full concentration-response curves were generated using concentrations ranging from 0.01-30 μM for both AZ8838 and **3.1**. Here, both samples of drug displayed similar levels of inhibition, with IC₅₀ values of 1.3 μM for the commercial sample of AZ8838 and 2.1 μM for the synthesised **3.1**, values which fall within error of each other (**Figure 3.34**, **Table 3.6**). These values confirm the literature findings of AZ8838-mediated inhibition of PAR2, and also validate the assay for use within this study.⁴

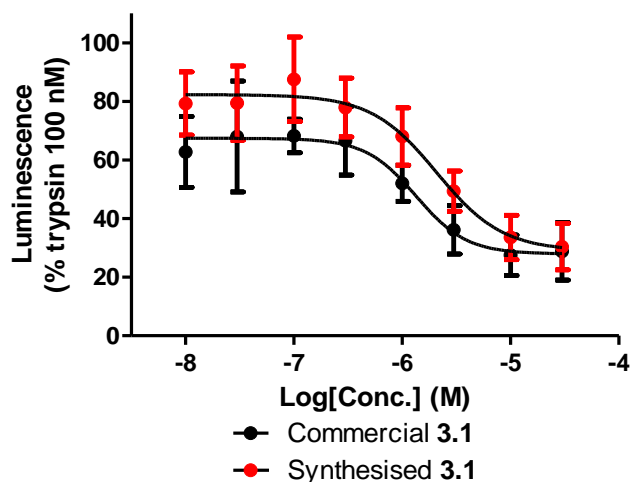


Figure 3.34: Concentration-response curves for inhibition of trypsin-mediated PAR2 activation in NFκB luciferase reporter assays using PAR2 antagonists AZ8838 and **3.1**. Data represents N = 5 for AZ8838 and N = 6 for **3.1**, with mean ± SEM, normalised to the uninhibited trypsin response.

Table 3.6: IC₅₀ values obtained following inhibition of trypsin-mediated PAR2 function

Drug	Log[IC ₅₀]	IC ₅₀ (μM)
Commercial 3.1	-5.87 ± 0.22	1.3
Synthesised 3.1	-5.68 ± 0.22	2.1

3.6.2 Initial Screening of AZ8838 Library

In order to rapidly assay the AZ8838 analogues, an initial triage of the library was performed whereby the inhibition of the analogues was confirmed, as above, at three high concentrations points: 3 μM, 10 μM and 30 μM.

3.6.2.1 Imidazole Analogues

Analogues **3.4**, **3.5**, **3.8**, **3.9** and **3.10** incorporate a range of modifications to the hydrogen bonding and steric character within the imidazole region of AZ8838. Hydrogen bonding was removed to form pyridine, by removing a hydrogen bond donor, and phenyl, by removing both the hydrogen bond donor and acceptor, analogues **3.4** and **3.5**.

Modification of the hydrogen bond vectors provided pyrazole and triazole **3.8** and **3.9** and additional steric bulk was introduced with benzimidazole **3.10** (**Figure 3.35A**). Each of these analogues did not display measurable concentration-dependent effects on luminescent responses to trypsin within the assay (**Figure 3.35B**). However, phenyl analogue **3.5** and benzimidazole analogue **3.10** displayed a slightly reduced luminescent intensity. As such, these analogues were chosen for further study (*vide infra*, **Section 3.6.3**).

The failure of pyrazole **3.8** and triazole **3.9** to elicit an antagonistic effect provides further evidence, in addition to the previous *in silico* study (*vide supra*, **Section 3.3**), that the hydrogen bonds exerted by the imidazole region are crucial for efficient binding within the AZ8838 pocket. Pyrazole **3.8** demonstrates the movement of both hydrogen bonding nitrogen atoms around the ring, while triazole **3.9**, in addition to including an additional nitrogen atom, has the position of one nitrogen atom moved around the ring. The movement of these atoms is clearly disrupting the inhibitive properties of AZ8838, in accordance with the *in silico* data shown previously.

Pyridinyl analogue **3.4** features both the removal of a hydrogen bond donating nitrogen atom and an increase in ring size in comparison to **3.1**. *In silico* work had shown that this combination would result in a depreciation in binding, which was confirmed with the loss of inhibitive properties *in vitro*.

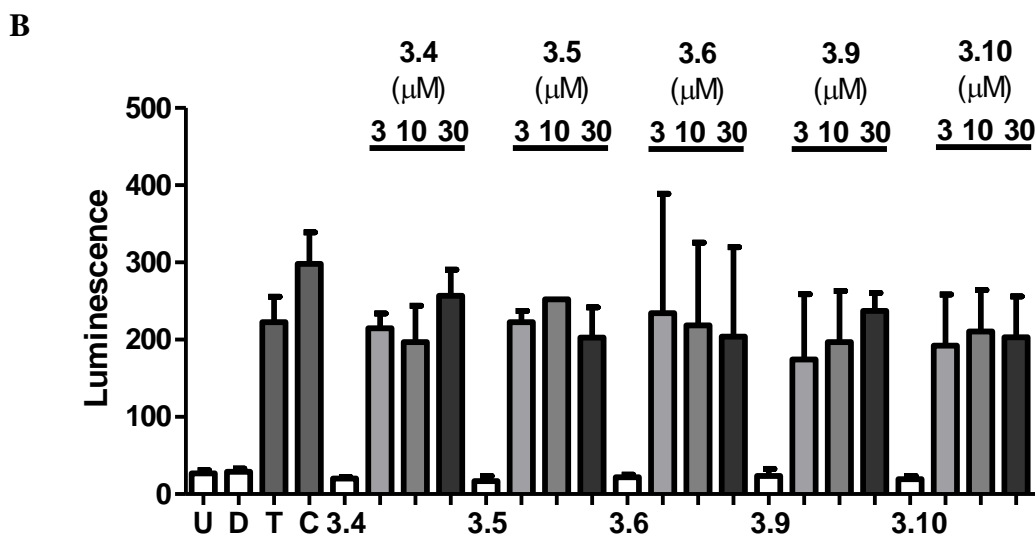
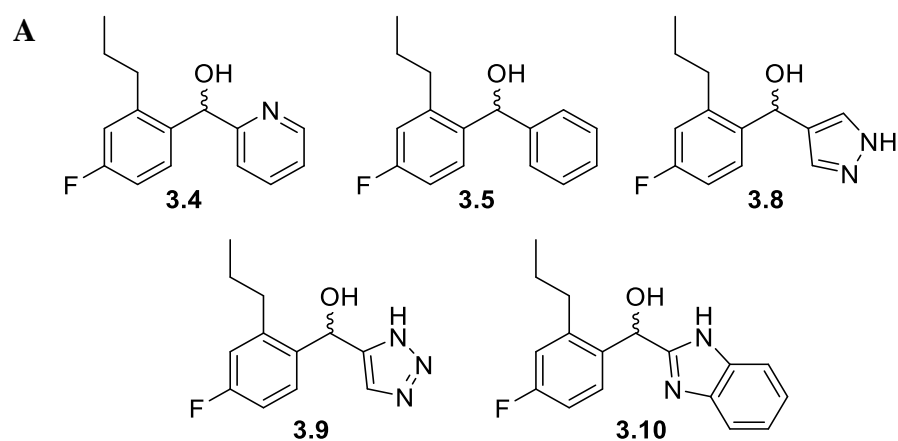


Figure 3.35: Initial screening of imidazolyl analogues **3.4**, **3.5**, **3.8**, **3.9** and **3.10** within NFκB luciferase reporter assay. **A** Chemical structure of analogues. **B** Graph shows the luminescent response on an arbitrary scale. U = untreated cells, D = DMSO treatment, T = trypsin treatment (100 nM), C = combined DMSO pretreatment followed by trypsin treatment. **3.X** = treatment with analogue **3.X** (30 μM). Where concentration is noted, cells were pretreated with the noted drug (3-30 μM) followed by treatment with trypsin (100 nM). Data represents N = 2 for **3.4**, **3.5**, **3.8**, **3.9** and **3.10** and N = 7 for controls, with mean ± SEM.

In addition to the imidazole analogues tested above, fragment-like intermediates were also included in the study with alkynyl intermediates **3.56** and **3.57**, triazole intermediate **3.58** and pyrazole intermediate **3.59** (Figure 3.36A). The intermediates generally succeeded in reducing the response to trypsin treatments, with the exception of triazole intermediate **3.58** (Figure 3.36B). However, while this would suggest **3.56**, **3.57** and **3.59** would be

potential candidates for PAR2 inhibition, it should be noted that one of the two replicates were carried out in insensitive cells which displayed vastly reduced responses to trypsin as shown by the large error bars (**Figure 3.36B**, T and C). This, coupled with the late stage at which the intermediates were tested, meant the compounds would not be studied further.

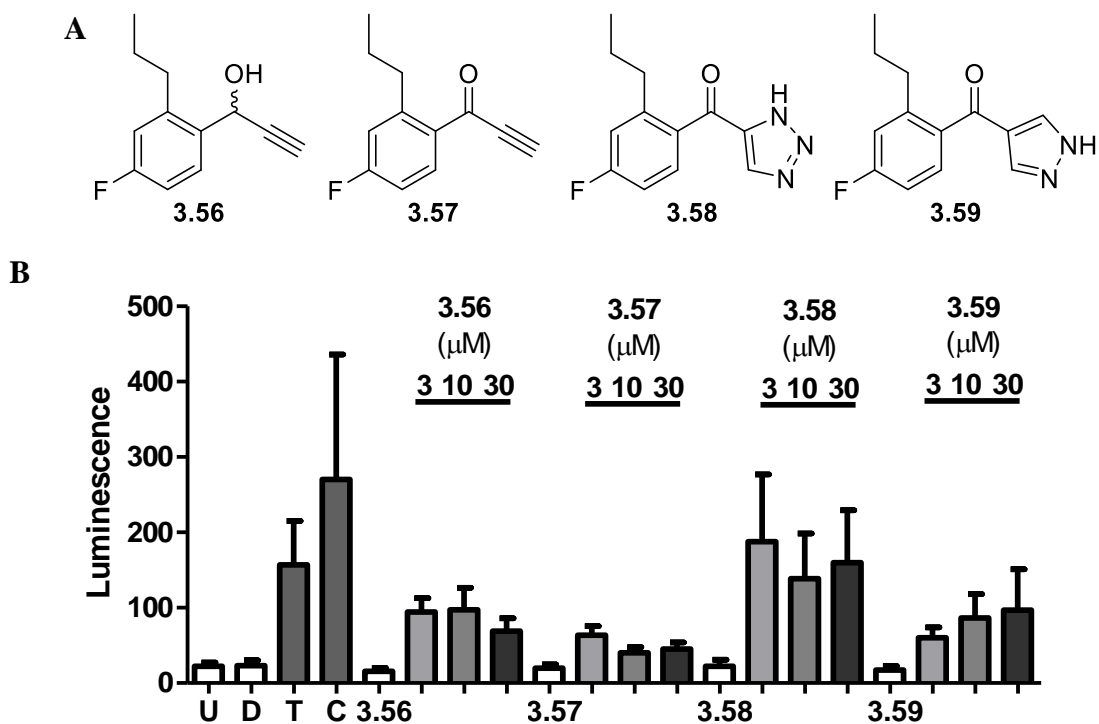


Figure 3.36: Initial screening of intermediates **3.56**, **3.57**, **3.58** and **3.59** within NFκB luciferase reporter assay. **A** Chemical structure of intermediates. **B** Graph shows the luminescent response on an arbitrary scale. U = untreated cells, D = DMSO treatment, T = trypsin treatment (100 nM), C = combined DMSO pretreatment followed by trypsin treatment. **3.X** = treatment with analogue **3.X** (30 μM). Where concentration is noted, cells were pretreated with the noted drug (3-30 μM) followed by treatment with trypsin (100 nM). Data represents N = 2 with mean ± SEM.

3.6.2.2 Linker Analogue

Ketone analogue **3.13** (**Figure 3.37A**) yielded a modest concentration-dependent decrease in the luminescent response (**Figure 3.37B**). However, it was decided the responses shown were not sufficiently distinct from the controls to warrant further study. As shown above with the imidazole analogues, this data was indicative of the importance of hydrogen

bonds within the AZ8838 binding site. The hydroxyl linker forms a hydrogen bond with His135 which, containing an imidazole functionality, is capable of hydrogen bond acceptance and donation. However, the change from the hydroxyl to a carbonyl within the linker does not only modify the hydrogen bond character of the group, it also impacts the geometry of the linker region. This change in vector for the hydrogen bond could impact the hydrogen bonding whilst also distorting the location of the imidazole and phenyl groups.

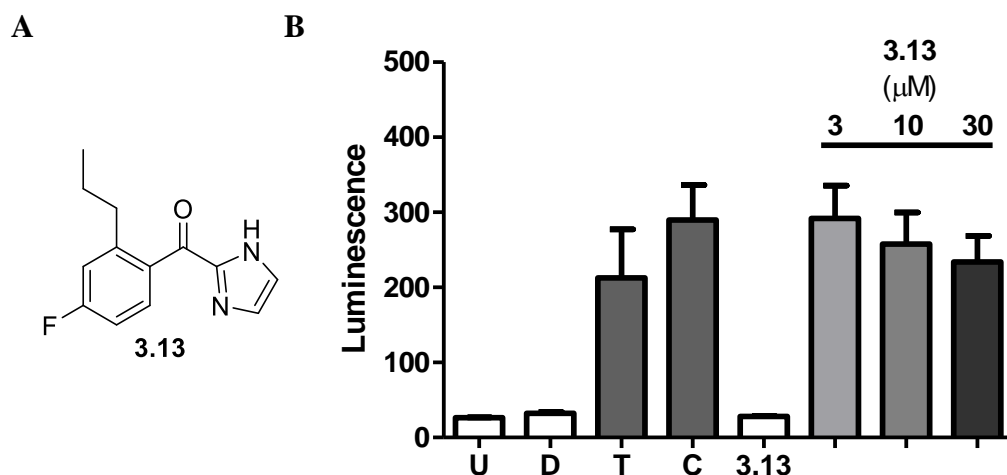


Figure 3.37: Initial screening of linker analogue **3.13** within NFκB luciferase reporter assay. **A** Chemical structure of **3.13**. **B** Graph shows the luminescent response on an arbitrary scale. U = untreated cells, D = DMSO treatment, T = trypsin treatment (100 nM), C = combined DMSO pretreatment followed by trypsin treatment. **3.13** = treatment with analogue **3.13** (30 μM). Where concentration is noted, cells were pretreated with the noted drug (3-30 μM) followed by treatment with trypsin (100 nM). Data represents N = 2 with mean ± SEM.

3.6.2.3 Propyl Analogues

In silico studies for the AZ8838 analogues highlighted the analogues where the propyl region was modified as the most promising for identification of improved PAR2 inhibitors due to the increased binding affinity upon increasing the steric bulk at the propyl position (*vide supra*, Section 3.3.3.3). Initially, simple changes to the propyl group were analysed with proto analogue **3.15**, bromo analogue **3.16**, cyclopropyl analogue **3.17** and phenyl analogue **3.21** (Figure 3.38A). Removal of the propyl group to form proto and bromo

analogues **3.15** and **3.16** removed the propensity for inhibition of PAR2, with both compounds unable to suppress the trypsin-mediated luminescence (**Figure 3.38B**). However, cyclopropyl analogue **3.17** yielded concentration-dependent inhibition of PAR2 while phenyl analogue **3.21** caused the signal to reduce, but not in a concentration-dependent manner (**Figure 3.38B**).

The proto- and bromo-analogues **3.15** and **3.16** demonstrated the lowest *in silico* binding of the AZ8838 library. This trend is continued *in vitro*, with **3.15-16** displaying no PAR2 antagonistic properties within the NF κ B reporter assay. These results highlight the importance of maintaining a hydrophobic presence at the 2-propyl position of AZ8838.

Conversely, the cyclopropyl group within analogue **3.17** facilitated a concentration-dependent inhibition of PAR2 function. The cyclopropyl group represents a pseudo-isomeric functional group maintaining a hydrophobic presence within the propyl region. However, a cyclopropyl group displays similar properties to an alkenyl group, with the increased π -character of its C-C bonds. This property could lead to more favourable interactions with aromatic amino acids within the binding pocket.

Finally, phenyl analogue **3.21** displayed no concentration-dependent effects on PAR2 function. Introduction of the phenyl group, and similarly sized aromatic moieties, showed the most promise as potent binders during the *in silico*. However, the *in vitro* result would indicate that this region of the binding pocket is more constrained than initially predicted. Whilst the aromatic substituents could impart favourable π - π interactions as alluded to above, the volume of space occupied could be preventing access to the binding site.

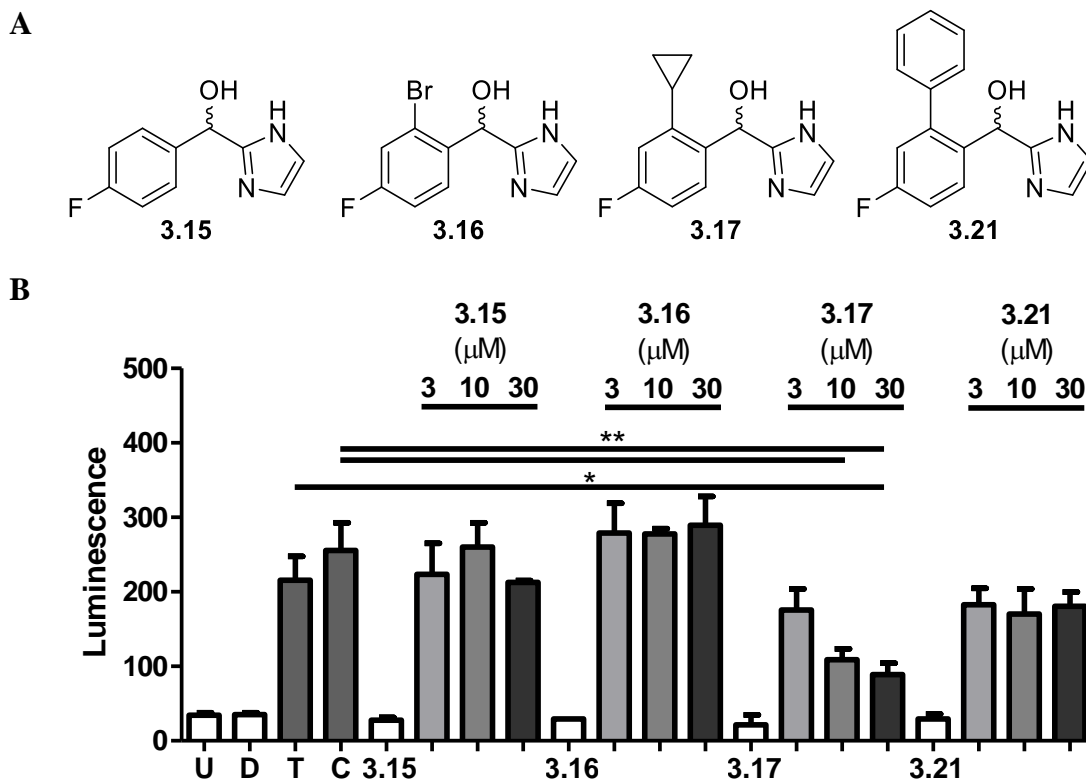


Figure 3.38: Initial screening of propyl analogues **3.15**, **3.16**, **3.17** and **3.21** within NFκB luciferase reporter assay. **A** Chemical structure of analogues. **B** Graph shows the luminescent response on an arbitrary scale. U = untreated cells, D = DMSO treatment, T = trypsin treatment (100 nM), C = combined DMSO pretreatment followed by trypsin treatment. **3.X** = treatment with analogue **3.X** (30 μM). Where concentration is noted, cells were pretreated with the noted drug (3-30 μM) followed by treatment with trypsin (100 nM). Data represents N = 2 for **3.15**, **3.16**, **3.17** and **3.21** and N = 4 for controls with mean ± SEM.

Finally, additional phenyl analogues were tested with tolyl analogues **3.24-26**, trifluoromethyl analogue **3.27** and *tert*-butyl analogue **3.28** (**Figure 3.39A**). These analogues each failed to provide concentration-dependent inhibition of PAR2 function (**Figure 3.39B**). The lack of inhibition observed could correlate with phenyl analogue **3.21** above, with the volume of space occupied by the phenyl ring and included substituents being too large to allow access into the binding site.

However, *o*-tolyl analogue **3.24** did display concentration-dependent activation of PAR2 in cooperation with trypsin (**Figure 3.39B**). This aberrant behaviour within the series could be explained by the secondary pocket the methyl group of **3.24** was observed to

reach into during the *in silico* studies (*vide supra*, **Section 3.3.4**). However, researching this was considered outwith the scope of the current study given time constraints.

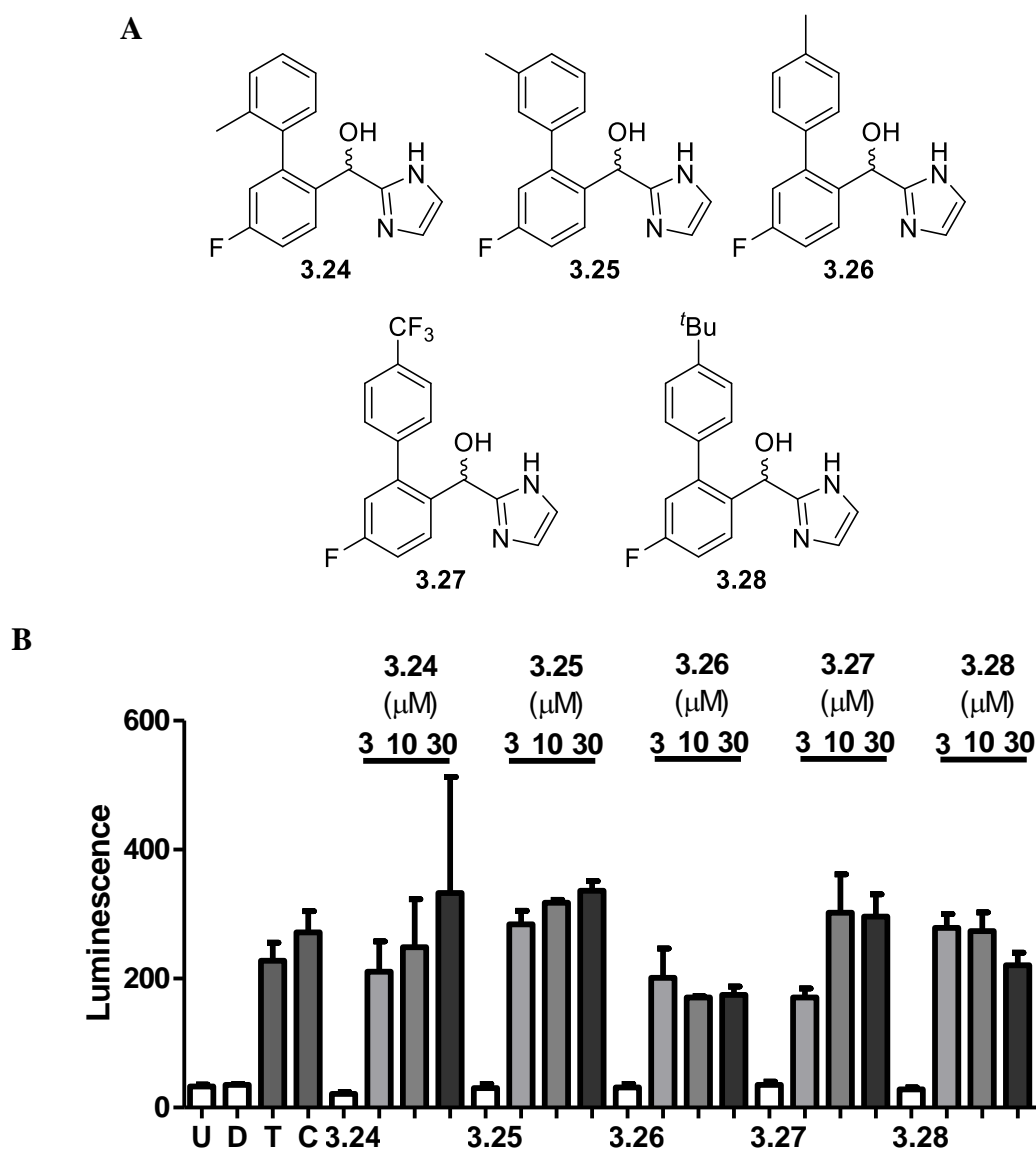


Figure 3.39: Initial screening of propyl analogues **3.24**, **3.25**, **3.26**, **3.27** and **3.28** within NFκB luciferase reporter assay. **A** Chemical structure of analogues. **B** Graph shows the luminescent response on an arbitrary scale. U = untreated cells, D = DMSO treatment, T = trypsin treatment (100 nM), C = combined DMSO pretreatment followed by trypsin treatment. **3.X** = treatment with analogue **3.X** (30 μM). Where concentration is noted, cells were pretreated with the noted drug (3-30 μM) followed by treatment with trypsin (100 nM). Data represents N = 2 for **3.24**, **3.25**, **3.26**, **3.27** and **3.28** and N = 5 for controls with mean ± SEM.

3.6.3 Further Analysis

With initial screening carried out, a small number of AZ8838 analogues were chosen for further study. From the selection of imidazole analogues, phenyl analogue **3.5** and benzimidazole analogue **3.10** were highlighted for reducing the trypsin-mediated luminescent output from the assay at maximal concentrations. To analyse this further, the concentrations used for inhibition were expanded in order to identify a concentration-response curve (**Figure 3.40A-B**). Unfortunately, repeating treatments with **3.5** and **3.10** at a wider range of concentrations resulted in no observable inhibition of trypsin-mediated activity (**Figure 3.40A-B**). As such, pursuit of these compounds as PAR2 inhibitors was halted.

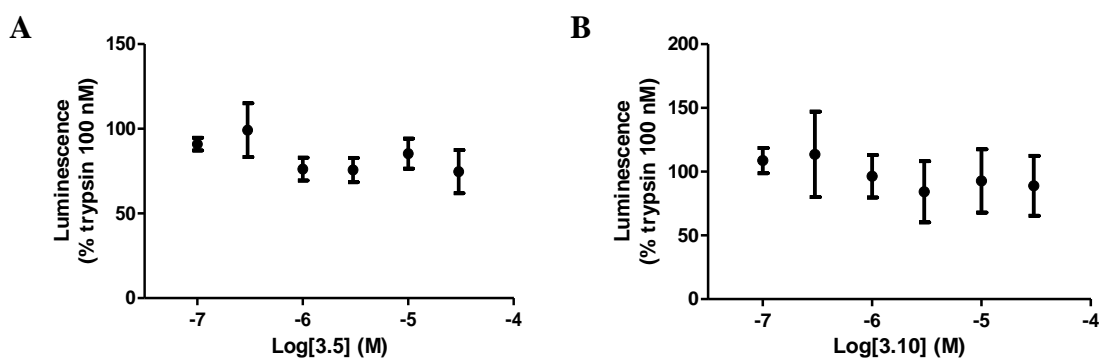


Figure 3.40: Concentration-response curve for inhibition of trypsin-mediated PAR2 activation in NF κ B luciferase reporter assays using AZ8838 analogues (A) **3.5** and (B) **3.10**. Data represents N = 4 for **3.5** and N = 3 for **3.10** with mean \pm SEM, normalised to the uninhibited trypsin response.

Within the propyl analogues, the cyclopropyl analogue, **3.17**, displayed the most promise as a PAR2 inhibitor, previously displaying a clear concentration-dependent inhibition of trypsin (**Figure 3.38**). By extending the concentration-range used for the study to allow testing from 0.01-30 μ M, a clear concentration-dependent relationship between **3.17** and trypsin-mediated luminescence is shown (**Figure 3.41**). The resulting concentration-response curve shows cyclopropyl analogue **3.17** as a submicromolar inhibitor of PAR2, with IC₅₀ of 0.86 μ M (**Table 3.7**). While this would demonstrate improved inhibition over **3.1**, the values are ultimately comparable (**Table 3.7**).

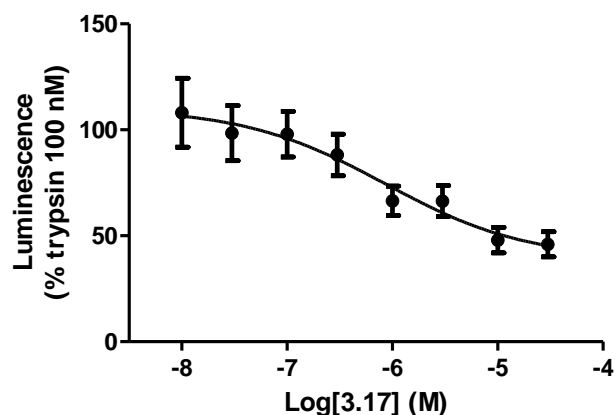


Figure 3.41: Concentration-response curve for inhibition of trypsin-mediated PAR2 activation in NFκB luciferase reporter assays using AZ8838 analogue **3.17**. Data represents N = 6 with mean ± SEM, normalised to the uninhibited trypsin response.

Table 3.7: IC₅₀ values for AZ8838 and **3.1** generated previously (**Figure 3.34**) and **3.17**, generated above.

Compound	Log[IC ₅₀] (M)	IC ₅₀ (μM)
Commercial 3.1	-5.87 ± 0.22	1.3
Synthesised 3.1	-5.68 ± 0.22	2.1
3.17	-6.07 ± 0.44	0.86

3.6.4 Summary of Biological Experiments

Assaying of the AZ8838 library eliminated many compounds from further study very rapidly, with all but three analogues displaying ineffective inhibition of PAR2. Of the remaining three, phenyl analogue **3.5** and benzimidazole analogue **3.10** did not provide concentration-dependent inhibition of trypsin-mediated PAR2 function. However, cyclopropyl analogue **3.17** displayed a full concentration-response curve for inhibition of PAR2 yielding improved IC₅₀ over AZ8838 with 0.86 μM. While this data is promising in isolation, the assumption made is that the binding site of **3.17** is PAR2 within this assay. This assumption would need to be confirmed through further study, given there is a significant number of signals between PAR2 activation and NFκB function/luciferase release (**Figure 3.32**). By treating with **3.17**, subsequent activation of other signalling

molecules in the cascade independently of PAR2 would provide confirmation of the **3.17** binding site.

This evidence leads to the conclusion that the SAR surrounding the tested regions of AZ8838 within PAR2 is generally restrictive (**Figure 3.42**). Modifications of the imidazole and the linker led, universally, to lower inhibition of PAR2 function *in vitro* with lower binding also observed *in silico*, showing the importance for maintaining the hydrogen bonding relationships within the binding pocket. Additionally, there was little scope for expansion of the imidazole, with increases in ring size and substitution all reducing simulated binding scores and impacting the potency as a PAR2 inhibitor.

Examining the propyl region highlighted differences between the *in silico* and *in vitro* experiments. *In silico* docking highlighted expansion of the propyl group towards small aromatic substitutions as the best path towards improved binding. However, the failure of phenyl analogue **3.21** and substituted aromatics **3.25-28** demonstrated that the aromatic substitution was not appropriate for the binding pocket, possibly preventing access into the binding site. However, sp² character was shown to be favourable, with cyclopropyl analogue **3.17** displaying inhibition of PAR2 which was comparable with AZ8838. While cyclopropyl groups do not contain a formal carbon-carbon double bond, they have been shown to possess higher π character in their C-C bonds, allowing the strained bond angles of 60°. ^{201,202}

On the other hand, *ortho*-tolyl analogue **3.24**, whilst not activating PAR2 on its own, was cooperating with PAR2 agonists to yield concentration-dependent increases in the luminescence observed. The activation could be occurring as a result of accessing the deeper pocket shown during *in silico* studies and could represent an opportunity for accessing PAR2 agonists.

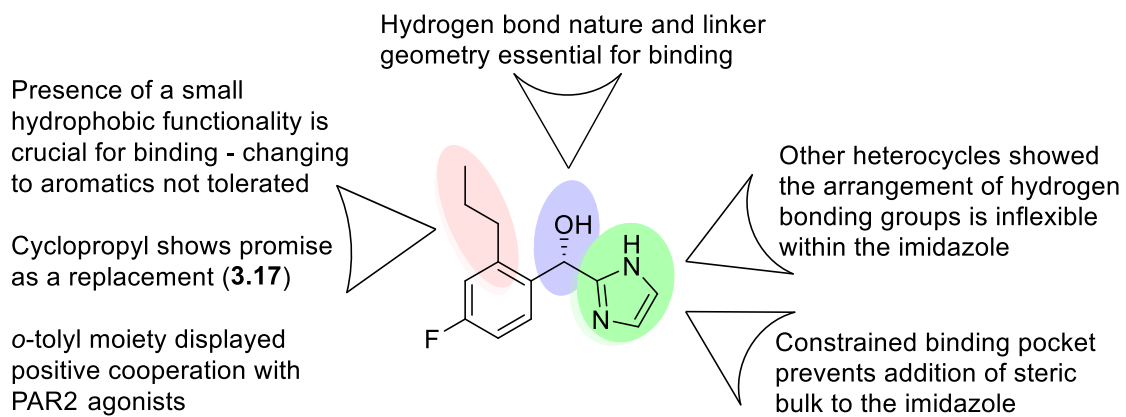


Figure 3.42: SAR developed for AZ8838 within the PAR2 binding site.

Chapter 4 Conclusions

Allosteric modulation of the PARs has been shown herein to be a promising strategy for novel drugs, with inhibition of both PAR1 and PAR2 being described following a fast-follower drug discovery approach centred on two PAR antagonists. However, the SAR for literature antagonists has also been shown to be highly restrictive.


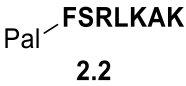
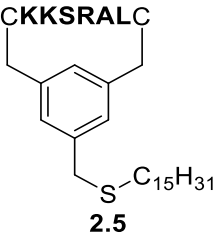
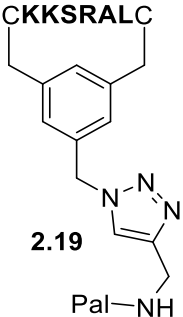
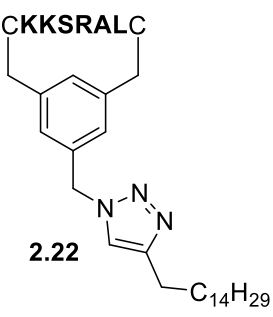
4.1 Allosteric Modulation of PAR1

This study highlighted the vulnerabilities with a pepducin-based strategy for PAR1 modulation, with specific concerns being raised over the PAR1 antagonist PZ-128 (**2.1**). It was demonstrated that **2.1** had conflicting pharmacological data, with off-target effects observed during calcium signalling assays, ERK activation and platelet aggregation (*vide supra*, **Section 2.4**).^{124,127,129} Many of the off-target effects were shown to be dependent on the pepducin structure, with a number of experiments using a control compound, **2.2**, resulting in no pharmacological effects. Additionally, the salt-form of the pepducin used was also shown to not impact the pharmacological outcome, as the negative control **2.2** was also used as a TFA salt. Exceptions to this included platelet aggregation, phosphatidylserine exposure and MTT assays, where both **2.1** and **2.2** elicited effects on platelet function and cell viability.

However, the specific pharmacological binding site of **2.1** was not confirmed. While the inhibitive exploration of the G_q signalling cascade highlighted PLC β as a potential binding site for the activation of Ca²⁺ release, **2.1** was also shown to affect cell death pathways with the exposure of phosphatidylserine during flow cytometry experiments as well as impacting cell viability, as witnessed *via* an MTT assay. However, it was noted that the concentrations used herein are in excess of the concentrations measured within the clinical trial studies, where allergic responses to **2.1** were shown with concentrations of 4.7-21.5 μ M.¹³⁴ In comparison, signalling and cell viability effects as a result of **2.1** treatment in HEK-293 cells or in mouse platelets were observed at 30 μ M or higher, meaning these results could have low relevance for the use of **2.1** in the clinic, where maximal concentrations fall below 30 μ M.

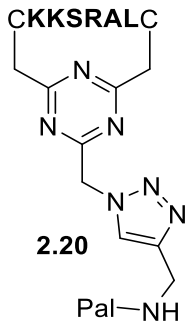
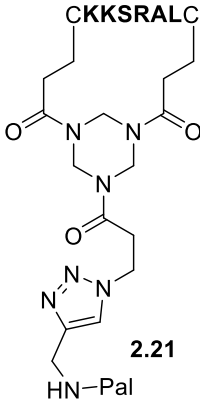
The novel **2.1**-analogues were also displaying off-target effects, further supporting the theory that sequence specificity was responsible for the agonistic events occurring following treatments with **2.1**. Ultimately, the pursuit of improved pharmacology within the pepducin analogues herein resulted in very little progress. Whilst the off-target effects could be reduced, especially with phenyl linker analogues **2.5**, **2.19** and **2.22**, this was not successfully paired with improved inhibition of PAR1 (**Table 4.2**).

Table 4.1: Pharmacological Data for **2.1**, **2.2** and phenyl analogues **2.5/19/22**.

					
EC ₅₀	27 μM	N/A	672 μM	160 μM	N/A
IC ₅₀	26 μM	N/A	N/A	N/A	N/A

Meanwhile, the triazine and triazinane analogues proved to be more potent inhibitors of PAR1 than their phenyl counterparts, with **2.20** and **2.21** displaying modest levels of PAR1 inhibition, this was accompanied by comparable levels of agonistic function to **2.1** (**Table 4.2**).

Table 4.2: Pharmacological Data for extended analogues **2.20** and **2.21**.

		
EC ₅₀	39 μM	54 μM
IC ₅₀	38 μM	22 μM

4.2 Allosteric Modulation of PAR2

The SAR of AZ8838 within its PAR2 binding pocket was explored through *in silico* screening and *in vitro* assay of a range of AZ8838 analogues. The library focused on three specific areas within AZ8838: the imidazole ring, the linking hydroxyl group and the propyl substitution on the phenyl ring.

Initial *in silico* profiling of the library suggested the imidazole ring and the hydroxyl linker were not amenable for modification towards improved binding. Conversion of the hydroxyl to a carbonyl and movement or removal of the hydrogen bonding nitrogens within the imidazole ring led to reductions in the predicted binding score. Additionally, adding steric bulk to the imidazole ring at the C₄ and C₅ positions resulted in a decreased binding score.

Conversely, the propyl region showed promise within the *in silico* studies, with increases in the steric bulk to a phenyl ring showing improved binding, alongside the similarly sized pyridinyl and furanyl substitutions. Methyl substitutions onto the secondary phenyl ring at the *ortho*- and *meta*- positions also led to increased binding scores, with the *ortho*-tolyl analogue also highlighting a potential pocket in the binding site for further binding.

Of the 27 analogues tested in *in silico* assays, 15 were successfully prepared using analogous routes to that reported for AZ8838 (**Figure 4.1**).⁴ Deviation from this route was taken for the inclusion of oxidation chemistry in the synthesis of the linker analogue, while [3+2] dipolar cycloadditions were utilised for the synthesis of two imidazole analogues.

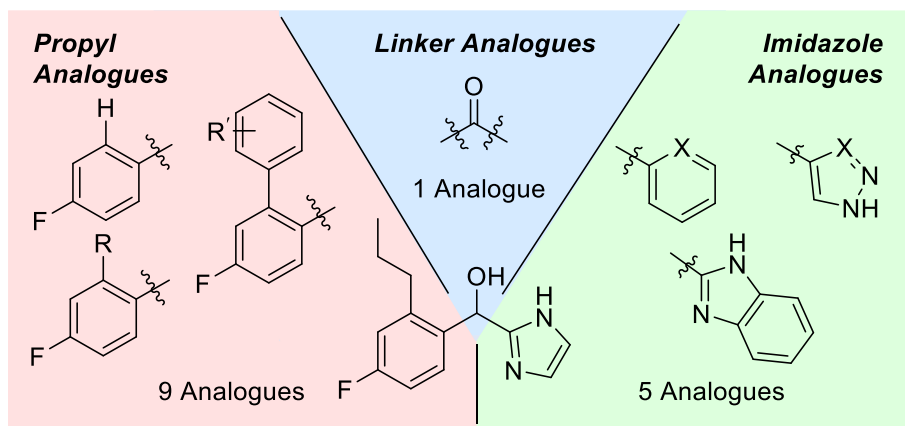


Figure 4.1: Successfully synthesised analogues of AZ8838. R = H, Br, cyclopropyl or Ph. R' = *o/m/p*-Me, *p*'-Bu or *p*-CF₃, X = CH or N.

In vitro assessment of the analogues confirmed the low flexibility for changes to the imidazole region, with no analogues successfully inhibiting PAR2 function. Further, modification of the hydrogen bond donating hydroxyl group also resulted in no inhibition. These results highlighted the importance of hydrogen bonding within the binding pocket and the low flexibility for changing the nature of arrangement of such bonding.

Additionally, the scope for expansion at the propyl position was limited, more so than expected. *In silico* analysis highlighted expansion of the propyl group to simple aromatic moieties as the optimal route towards stronger simulated binding. However, this was not replicated within the *in vitro* studies, with the phenyl analogues all displaying poor inhibition of PAR2 and the cyclopropyl analogue as the only compound showing comparable or improved potency over AZ8838.

Chapter 5 Future Work

5.1 PAR1 Pepducins

5.1.1 Completing the study of PZ-128

While the evidence shown herein demonstrates a propensity for PZ-128 (**2.1**) to activate pathways relating to platelet aggregation and, indeed, activated platelet aggregation in a non-PAR1 system (mouse platelets), one major piece of work remains to bring the study to a close. Specifically, aggregation studies in human platelets or, ideally, in whole blood. These studies would provide a physiologically relevant answer to the question of **2.1** operating in a pro-platelet manner, rather than inhibiting platelet function as reported.^{2,127,138} If **2.1** would activate platelet function, significant scrutiny would need to be turned on the reported finding for PZ-128 as this would directly contradict the intended purpose for the drug, which has been making progress through clinical trials until recently.

5.1.2 Advancing the PAR1-derived pepducin strategy

With regards to the development of novel PAR1 pepducins based on the compounds used in the current study, one path forward for the series could be to change the peptide sequence. With the problematic behaviour displayed by PZ-128 and the sequence-dependent nature under which this behaviour occurs, it could be surmised that the issue lies in the peptide sequence utilised with the pepducins.

One possible avenue for counteracting this could be to utilise a peptide sequence not from the loop of PAR1 but from a natural partner which binds to the intracellular surface of PAR1: the heterotrimeric G-protein. However, while this approach could result in more promising interactions with PAR1, the resulting pepducins would also likely demonstrate low specificity due to the diverse nature of G-protein associations.

5.2 PAR2 small molecule modulators

Regrettably, time constraints led to a limited exploration of the SAR surrounding AZ8838. With more time, more extensive studies into the simulated binding and biological assaying could be carried out to identify areas for improvement within the AZ8838 structure.

5.2.1 *In silico* studies

While the accuracy of the *in silico* studies herein was shown to be limited when compared with the *in vitro* experiments, a further study could identify areas for expansion. As part of this further study, comparing the binding results under different force fields used within GOLD to the *in vitro* results obtained herein could identify a more suitable protocol for screening further analogues *in silico*. This extended *in silico* study would then allow an informed decision to be made over analogues which could be targeted for synthesis and further *in vitro* assaying.

Additionally, expansion of the *o*-tolyl analogue, **3.24**, would be of interest due to the unique profile for its cooperative function with trypsin. The methyl group was shown *in silico* to be extending towards a putative second pocket in the crystal structure, perhaps further expansion at this site could identify further analogues and confirm the presence of a switch in the molecules pharmacological character. *In vitro* analysis of such compounds could highlight potential positive allosteric modulators of PAR2.

5.2.2 Synthetic chemistry

With only 15 of the targeted 27 analogues being successfully synthesised, time could be taken to optimise the procedures and secure access of further analogues of AZ8838. The common problems included ⁿBuLi-mediated coupling and deprotection. The coupling reactions typically failed for more polar molecules which contained groups capable of chelating the lithium cation, with coupling onto pyridinyl-, furanyl- and dimethylaminophenyl-benzaldehyde all yielding no signs of successful reaction. However, access to these analogues would not be of high importance given the failures of the aromatic substitutions at the propyl position.

Additionally, TFA proved to be a harsh reagent for the deprotection of the SEM group for many imidazole analogues. Time could be spent to optimise the TBAF conditions used for deprotection, which successfully yielded one analogue, to access a gentler deprotection strategy.

5.2.3 Enantiopure synthesis

Following the initial screening and identification of a single promising PAR2 inhibitor, steps could be taken to obtain the individual enantiomers of **3.1** and **3.17**. This would enable comparison between the active (*S*)-enantiomer of AZ8838 and the individual enantiomers of **3.17**. The reported synthesis utilised chiral preparative HPLC to access AZ8838. However, an alternative approach could be to access a ketone intermediate and use a chiral reducing agent to access the required (*S*)-enantiomers, such as in the Noyori asymmetric hydrogenation using BINAP (**Figure 5.1A**).²⁰³ Another consideration could be chiral resolution of the final products using enzymes or kinetic resolution using a non-enzymatic catalyst (**Figure 5.1B**).^{204,205} However, this approach may meet difficulties given the bisaryl nature of the AZ8838 analogues, which does not feature prominently in the literature for these transformations.

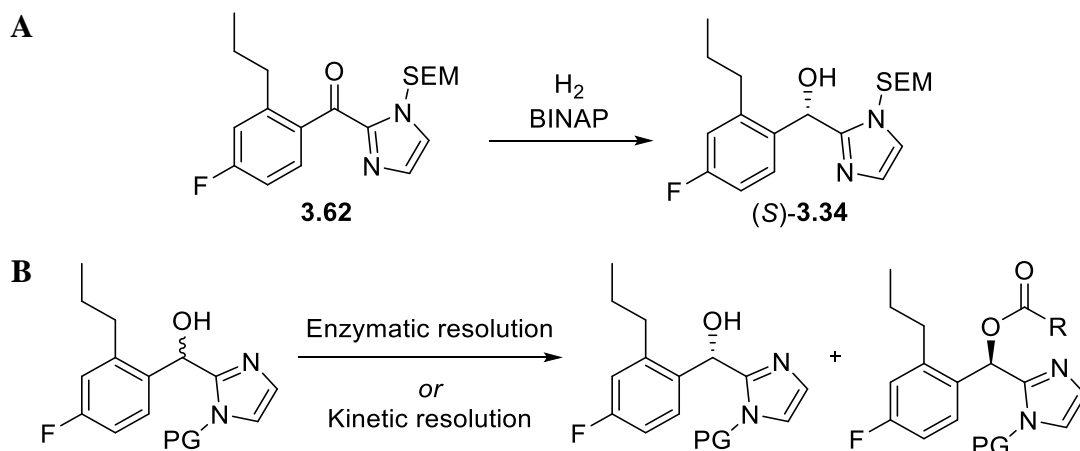


Figure 5.1: Possible processes for isolation of enantiopure analogues of AZ8838. **A** Chiral hydrogenation of a ketone intermediate to access the active (*S*)-enantiomer of the alcohol. **B** Chiral resolution of an intermediate prior to deprotection to access desired (*S*)-enantiomer of the alcohol and (*R*)-enantiomer as an ester.

5.2.4 Further biological testing

A weakness of the luciferase reporter assay used is the number of other potential binding sites for a drug between the target, PAR2, and the output, NFκB/luciferase release. To provide confirmation of the binding site for **3.17**, further biological assaying would be required. Primarily, studies could be carried out in the same luciferase assay, utilising agonists of different proteins within the signalling cascade to ensure **3.17** or **3.1** are not inhibiting at an off-target site, similar to the work carried out on PAR1 in **Section 2.4.4**. Additionally, utilising different signalling outputs within the cascade would also provide further confirmation of the PAR2 binding site. For example, calcium assays have been used within PAR2 and would provide a readily available, robust assay for measuring the impact on PAR2 signalling through a different output. Finally, binding assays could be designed to allow recruitment of **3.1/3.17** within PAR2 to be monitored, utilising, for example, radioligand binding.

Chapter 6 Materials and Methods

6.1 Allosteric Modulation of PAR1 – Chemical Synthesis

6.1.1 General Techniques

- i. All reagents, catalysts and solvents were obtained from commercial suppliers and were used without further purification unless otherwise stated
- ii. Purification was carried out according to standard laboratory methods.²⁰⁶

6.1.1.1 Experimental Details

- i. Solid-phase peptide synthesis was performed on a PTI Tribute-UV peptide synthesizer Glassware was oven-dried at 150 °C and purged with N₂ before use.
- ii. Lyophilizations were performed on a Christ Alpha 2-4 LDplus apparatus.

6.1.1.2 Purification of Products

- i. Thin-layer chromatography was carried out using Merck silica plates coated with fluorescent indicator UV254. These were analysed under 254 nm UV light or developed using a solution of ninhydrin.
- ii. Purification of the peptidic compounds was performed on an Agilent Technologies 1260 infinity preparative system using both UV and ELSD detectors with a Phenomenex Gemini C18 column (110 Å, 10 µm, 250×20 mm). Auto-collection of fractions was used based on the UV measurements at 214 or 254 nm, using a standard protocol: 100% buffer A (acetonitrile/H₂O 5:95 with 0.1% TFA) for 5 min followed by and linear gradient of buffer B (acetonitrile/H₂O 95:5 with 0.1% TFA) into buffer A (20-100%) over 65 min at a flow rate of 12.5 mL·min⁻¹.

6.1.1.3 Analysis of Products

- i. Analytical high pressure liquid chromatography (HPLC) was carried out on a Shimadzu instrument comprising a communication module (CBM-20A), autosampler (SIL-20HT), pump modules (LC-20AT), UV/Vis detector (SPD-20A) and system controller (Labsolutions V5.54 SP), with a Phenomenex Gemini C18 column (110 Å, 5 µm, 250×4.60 mm). UV measurements were recorded at 214 and 254 nm, using a standard protocol: 100% buffer A for 2 min followed by

a linear gradient of buffer B into buffer A (0-100%) over 28 min at a flow rate of 1.0 mL·min⁻¹ using the same buffers as described for peptidic compound purification.

- ii. Liquid chromatography-mass spectrometry (LCMS) was carried out on a Thermo Scientific LCQ Fleet quadrupole mass spectrometer with a Dionex Ultimate 3000 LC using a Dr. Maisch Reprosil Gold 120 C18 column (110 Å, 3 µm, 150×4.0 mm) and a 0-100% linear gradient of buffer B into buffer A at a flow rate of 1.0 mL·min⁻¹ and using the same buffers as described for purification of peptidic compounds.

6.1.2 General Procedures

General Procedure for Automated Peptide Synthesis

Peptides were synthesized on a PTI Tribute-UV peptide synthesizer. Tentagel S Ram resin (1.14 g, 0.25 mmol, 1.0 equiv.) was allowed to swell (3 x 8 mL, each 10 min). Removal of the Fmoc group was achieved by treatment of the resin with 20% piperidine in DMF using the RV_top_UV_Xtend protocol from the Tribute-UV peptide synthesizer followed by a DMF washing step (5 x 8 mL, each 30 sec). Fmoc-protected amino acids (4 equiv.) were coupled for 20 min using HCTU (4 equiv) and DIPEA (8 equiv.) in DMF (8 mL), as a coupling system, with 2 min pre-activation. After every coupling, the resin was washed with DMF (6 x 8 mL, each 30 sec). After the last amino acid coupling, the resin was washed with DMF (5 x 8 mL, each 30 sec), CH₂Cl₂ (5 x 8 mL, each 30 sec) and dried over a nitrogen flow for 10 min and further dried *in vacuo*.

Manual procedure for Fmoc-removal

The resin (0.73 g resin, 0.125 mmol) was swollen in DMF (5 mL for 2 min). After draining the solvent, the resin was shaken with piperidine/DMF (1:4, v/v, 3 x 5 mL, each 10 min), washed with DMF (5 x 5 mL, each 30 sec).

Manual procedure for Palmitoyl chloride coupling

The Fmoc deprotected resin (0.125 mmol) was washed with CH₂Cl₂ (5 x 5 mL, each 30 sec). After draining the solvent, the resin was shaken with palmitoyl chloride (152 µL, 0.5

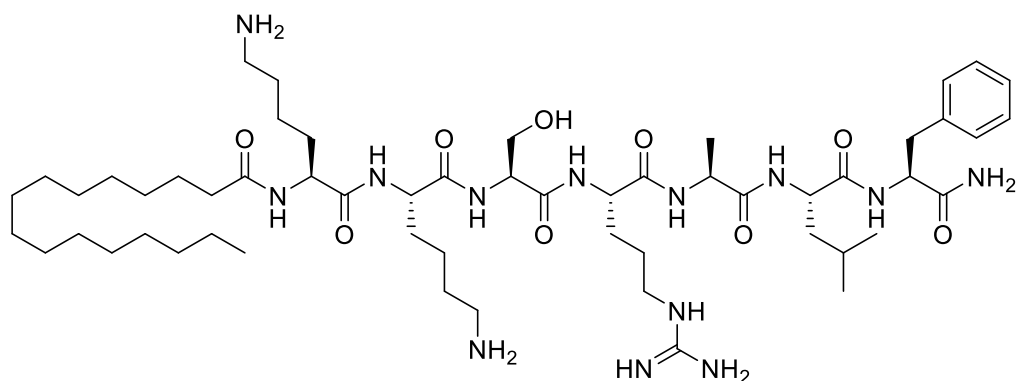
mmol, 4 equiv.) and DIPEA (174 μ L, 1.0 mmol, 8 equiv.) in CH_2Cl_2 (5 mL) for 1 hour. Next, the resin was washed with CH_2Cl_2 (5 x 5 mL, each 30 sec).

Procedure for Peptide cleavage and deprotection

Peptide cleavage and deprotection were achieved by treatment of the resin with TFA/ H_2O /TIS (5 mL, 95:2.5:2.5, v/v/v/v) for 3 hours. Next, the peptide was precipitated by dropwise addition of the TFA mixture to a cold (4 $^\circ\text{C}$) solution of MTBE/hexanes (1:1, 45 mL). After centrifugation (3500 rpm, 5 min) the supernatant was decanted and the pellet was re-suspended in MTBE/hexanes (1:1, v/v) and centrifuged again. Finally, the pellet was washed twice with MTBE/hexanes (1:1, v/v), each time collected by centrifugation, dissolved in t BuOH/ H_2O (1:1, v/v) and lyophilized to yield the crude peptide.

6.1.3 Characterisation Data

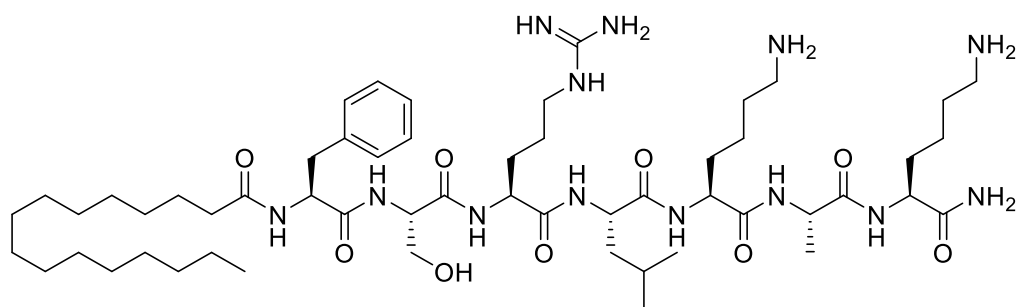
PZ-128 (2.1)



By performing the above described general peptide synthesis procedures followed by manual Fmoc-removal, after the introduction of a palmitoyl chain and peptide cleavage and deprotection, lyophilized **2.1** was obtained. Next, crude **2.1** was dissolved in HPLC buffer A/B/DMSO (45:45:10, v/v/v) and purified by preparative HPLC. Fractions corresponding to **2.1** were pooled and lyophilized to yield the TFA salt of **2.1** as a white fluffy solid (30 mg, 0.021 mmol, 8.4% yield).

LCMS (ESI) m/z calcd for $\text{C}_{55}\text{H}_{100}\text{N}_{13}\text{O}_9$ $[\text{M}+\text{H}]^+$ 1086.78, found 1086.83.

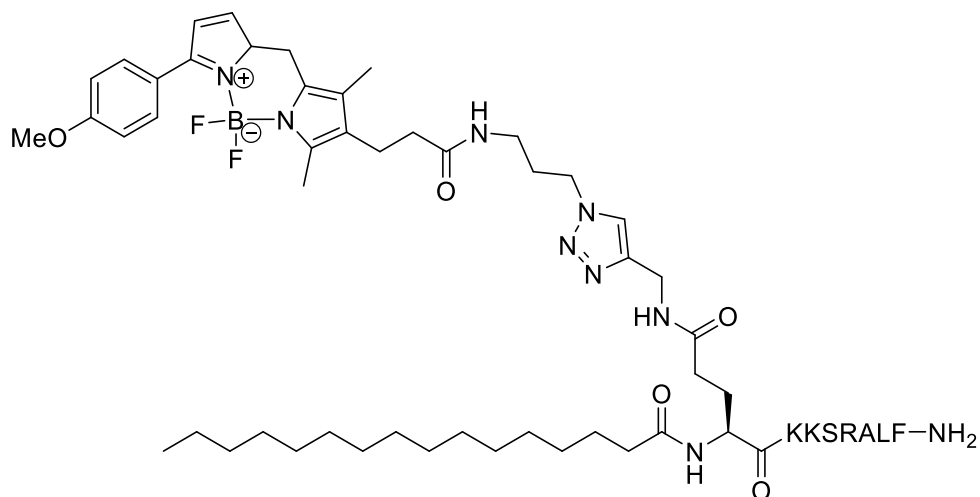
Scrambled PZ-128 Analogue (2.2)



By performing the above described general peptide synthesis procedures followed by manual Fmoc-removal, after introduction of a palmitoyl chain and peptide cleavage and deprotection, lyophilized **2.2** was obtained. Next, crude **2.2** was dissolved in HPLC buffer A/B/DMSO (45:45:10, v/v/v) and purified by preparative HPLC. Fractions corresponding to **2.2** were pooled and lyophilized to yield the TFA salt of **2.2** as a white fluffy solid (10 mg, 0.007 mmol, 2.8% yield).

LCMS (ESI) m/z calcd for $C_{55}H_{100}N_{13}O_9$ $[M+H]^+$ 1086.78, found 1086.83.

BODIPY-TMR-modified PZ-128 (2.29)



An alkynylated analogue of PZ-128 (7.56 mg, 4.8 μ mol, 1.2 eq.) and BODIPY-TMR azide (1.92 mg, 4.0 μ mol, 1.0 eq.) were added to an eppendorf tube alongside $CuSO_4 \cdot 5H_2O$ (0.30 mg, 1.2 μ mol, 0.3 equiv.), TBTA (0.32 mg, 0.60 μ mol, 0.15 equiv.) and sodium

ascorbate (0.72 mg, 3.6 μmol , 0.90 equiv.) and dissolved in *t*BuOH/H₂O (1.5 mL, 3:2 v/v). The eppendorf tube was then shaken for 1 hour after which the reaction mixture was purified by preparative HPLC. Fractions corresponding to the triazole product were combined and lyophilised, yielding the TFA salt of **2.17** as a purple fluffy solid (5.3 mg, 2.6 μmol , 65% yield).

LCMS (ESI) *m/z* calc. for C₈₇H₁₃₈BF₂N₂₁O₁₃ [M+2H]²⁺ 867.04, found 867.33.

6.2 Allosteric Modulation of PAR1 – Biological Methods

6.2.1 Reagents

Human embryonic kidney cells (HEK293 cells) were purchased from ATCC (293 [HEK293](ATCC® CRL1573™)).

Platelet studies were carried out using washed platelet preparations from whole blood isolated from male C57 black 6 (C57BL/6) mice aged between 8-12 weeks. Mice were bred and maintained in the University of Strathclyde animal facilities according to United Kingdom Home Office regulations. Platelet isolations for this study were carried out by Dr Margaret Rose Cunningham and Ms Jordanna Magee.

Pepducin analogues used in this study (**2.5-7**, **2.15-21**) were synthesised by Dr Helmus Van de Langemheen and Mr Joachim Bijl within the laboratory of Prof Robert Liskamp (University of Glasgow). Pepducins were provided as lyophilised trifluoroacetic acid salts which were then diluted to 10 mM in DMSO for further use. Stock solutions were maintained at -20 °C.

Control compound **2.3** (SCH79797) was used as a dihydrochloride salt purchased from Santa Cruz Biotech. (CA, USA). Peptide control **2.4** was synthesised within the Liskamp lab (University of Glasgow) for an unrelated project and initially provided as a blind control with no disclosed structure.

All reagents used in the experiments detailed in this study are presented in **Table 6.1**. Details that relate to the antibodies used in Western blotting experiments are shown in **Table 6.2**. Chemical structures for pepducins used in the study are shown in Table 3.

Table 6.1: Reagents used for experiments

Experiment	Supplier	Products
Cell Culture	- Thermo Fischer Scientific (Paisley, UK))	- Dulbecco's Modified Eagle Medium (DMEM) (Gibco, product number 41966-029), Nunc TM Cell-Culture Treated Multidishes (24 well, 12 well plates)
	- Gentaur Ltd (London, UK)	- Foetal calf serum (Biosera, product number FB-1090/500)
	-Lonza (Verviers, Belgium)	- Penicillin-Streptomycin solution (Product number 17-602E, 10,000 U/mL Penicillin/10,000 µg/mL Streptomycin)
	-Merck (previously Sigma Aldrich, Dorset, UK)	- Corning [®] 75 cm ² Cell Culture Flask (product number 430641U), TPP [®] tissue culture plates (96 well, 6 well)
	- Sarstedt (Leicester, UK)	- Serological pipettes (5/10/25 mL)
Protein Quantification	- Thermo Fisher Scientific (Paisley, UK)	- Pierce TM BCA Protein Assay Kit (product number 23227)
Western Blotting	- Carl Roth GmbH (Germany)	- Rotiphorese [®] Gel 30 (37,5:1, product number 3029.1)
	- GE Healthcare (Buckinghamshire, UK)	- Bovine serum albumin (product number K45-001)
	- Whatmann (Kent, UK)	- 17 CHR Chromatography paper (product number 3017-915)
	- Merck (Dorset, UK)	- Hydrogen peroxide (30% w/w solution), luminol, p-coumaric acid, sodium dodecyl sulphate (SDS), Tween-20, Trizma base
	- Thermo Fisher Scientific (Paisley, UK)	- GE Healthcare Amersham TM Hybond TM PO.45 µM PVDF membrane (product code 15259894), NuPage LDS sample

		buffer (4x Novex, product number NP0008), PageRuler™ Plus Prestained Protein ladder (product number 26619), ammonium persulfate (APS), N,N,N',N'-tetramethylethylenediamine (TEMED), sodium chloride
	-VWR International Ltd (UK)	- Glycine, methanol
	-Santa Cruz Biotech (CA, USA)	- UltraCruz autoradiography film (Product number sc-201696)
Calcium Signalling	- Molecular Devices (Berkshire, UK)	- FlexStation pipette tips (black)
	- Corning (MA, USA)	- 96-well Corning CellBIND plates, black with clear bottom
	- Merck (Dorset, UK)	- Adenosine diphosphate (ADP, calcium chloride, D-(+)-glucose, dimethyl sulfoxide, magnesium sulphate, potassium chloride, potassium dihydrogen phosphate, sodium bicarbonate, sodium chloride, sodium hydrogen phosphate
	- Thermo Fisher Scientific (Paisley, UK)	- Fluo-4 Direct Calcium Assay Kit (containing Fluo-4 Direct Dye, Probenecid and Calcium Assay Buffer)
Fura-2 Ratiometric Imaging	- VWR International Ltd (UK)	- No. 0 circular glass 13 mm diameter coverslips, 0.8-1.0 mm thick glass microscopy slides
	- Thermo Fisher Scientific (Paisley, UK)	- Fura-2, AM, cell permeant
MTT Assay	- Merck (Dorset, UK)	- 3-(4,5-Dimethyl-2-thiazolyl)-2,5-diphenyl-2H-tetrazolium bromide (MTT)
Flow Cytometry	- BD Biosciences (Oxford, UK)	- BD Pharmingen™ APC Annexin V

Table 6.2: Western Blot Antibodies

Antibody Name	Company	Dilution
pERK mouse monoclonal	Santa Cruz Biotech (CA, USA)	2:15000
ERK-1 (K-23) rabbit polyclonal	Santa Cruz Biotech (CA, USA)	1:15000
Anti-Mouse IgG	Jackson Immuno Research (Cambridge, UK)	2:15000
Anti-Rabbit IgG	Jackson Immuno Research (Cambridge, UK)	2:15000

Cell culture media consists of DMEM (4.5 g/L D-Glucose, L-Glutamine and Pyruvate, 500 mL), Penicillin/Streptomycin (5 mL) and FCS (50 mL). Serum-free media consists of DMEM (4.5 g/L D-Glucose, L-Glutamine and Pyruvate, 500 mL) and Penicillin/Streptomycin (5 mL).

Calcium assay buffer consists of 137 mM NaCl, 5.4 mM KCl, 0.25 mM Na₂HPO₄, 0.56 mM glucose, 0.44 mM KH₂PO₄, 1 mM CaCl₂, 1 mM MgSO₄ and 4.2 mM NaHCO₃ in distilled water.

Enhanced Chemiluminescence (ECL) solution consists of 1.25 mM luminol, 0.58 mM coumaric acid, 50 mM tris and 32 µL/100 mL hydrogen peroxide in distilled water.

Annexin binding buffer consists of 10 mM HEPES/NaOH (pH = 7.4), 140 nM NaCl and 2.5 mM CaCl₂.

6.2.2 Equipment

- i. 96-well calcium signalling experiments were carried out on a FlexStation 3 plate reader (Molecular Devices).
- ii. Fura-2 ratiometric analysis was carried out using an Olympus BX50 widefield epifluorescence microscope with an Olympus UMPlanFl 20x/0.5 water dipping lens fitted with a fast wavelength switchable 340/380 nm light emitting diode (LED) illuminator (CoolLED). Fluorescent emissions were detected by a Hamamatsu ORCA-Flash 4.0 camera.

6.2.3 Biological Methods

6.2.3.1 Cell Culture of HEK-293 cells

Human Embryonic Kidney 293 (HEK-293) cells were cultured in cell culture media at 37 °C and 5% CO₂ in a humidified atmosphere. During cell culture passage, versene (2 mL) was used to free cells from the surface of the flask. The cells were then taken up in 8 mL of cell culture media, transferred to a 15 mL centrifuge tube and spun down at 1000 rpm for 3 minutes. The supernatant was removed and the pellet resuspended in cell culture media prior to reseeding in a T75 flask at the desired dilution (typically 1:5 or 1:10 dilution) as well as into plates for experiments. HEK-293 cells were used from passage 20-80.

6.2.3.2 PAR1 Signal Transduction Assays

Calcium Assays - HEK-293

HEK-293 cells were cultured in a Corning Black 96-well Assay Plate with Clear, Flat Bind and a CellBIND Surface in cell culture media to near confluence. Cell culture media was then removed and serum-free media (100 µL) added to quiesce cell growth. After 2 hours of incubation at 37 °C the serum-free media was removed and 90 µL of 1× Fluo-4 Direct calcium dye added to each well (20 mL of calcium assay buffer and 200 µL of probenecid (0.27 mM) added to a bottle of Fluo-4 Direct Calcium Assay Reagent). The cells were then incubated at 37 °C for 1 hour before carrying out the assay. The automated pipetting system within the plate reader was used to dispense 10 µL of pepducin/control solutions (made to 10× required final concentration) to the wells. Fluorescence readings were taken (Ex: 494 Em: 516) every 3 seconds over a period of 120 seconds, with the sample solutions being added after 17 seconds.

For inhibitory assays, a further addition of 11 µL of agonist (made to 10× required final concentration) was carried out, with fluorescence readings taken as described above.

For prolonged exposure experiments, the time over which scans were taken was increased to 1800 seconds.

For desensitisation studies, once the plate had been incubated for one hour post-addition of the dye, 10 μ L of thrombin solution was added to each well to desensitise PAR1. 30 mins after addition of thrombin, 11 μ L of agonist solutions were added at 10x the final concentration.

SoftMax Pro v5.4.5 was used to obtain and process the raw fluorescence readings.

Data Analysis

SoftMax Pro v5.4.5 was used to process the raw fluorescence data into Max-Min (the value of the maximal response minus the value of the minimal response) for each well. These data points were then taken into GraphPad Prism 5.0 where appropriate curves were generated for each dataset.

Agonist dose response curves were generated using Log[Agonist] vs Response with equation: $Y = Bottom + (Top + Bottom)/(1 + 10^{(LogEC_{50} - X)})$. For control curves with TFLLR-NH₂ and thrombin, the bottom value was constrained to 0 yielding the equation $Y = Top/(1 + 10^{(LogEC_{50} - X)})$.

For agonist dose-response curves with pepducins, Max-Min readings were normalised against readings obtained with thrombin at 5 U/mL. The Top value was constrained to 100 and the Bottom value constrained to 0, yielding the equation: $Y = 100/(1 + 10^{(LogEC_{50} - X)})$.

Dose-response curves for inhibition were fitted using GraphPad Prism's nonlinear regression analysis model for Log[Inhibitor] vs Response with equation: $Y = Bottom + (Top - Bottom)/(1 + 10^{(X - LogIC_{50})})$. Max-Min data was normalised against the response obtained with thrombin at 5 U/mL.

Schild data was fitted to a Gaddum/Schild shift model with GraphPad Prism 5.0 with the following equations:

$$EC_{50} = 10^{Log(EC_{50})}$$

$$Antag = 1 + \left(\frac{B}{(10^{-pA2})} \right)^{SchildSlope}$$

$$LogEC = Log(EC_{50} \times Antag)$$

$$Y = Bottom + \frac{Top - Bottom}{1 + 10^{(LogEC - X) \times HillSlope}}$$

Where pA2 is the negative log of the concentration of antagonist at which the EC₅₀ has shifted by a factor of 2.

PZ-128 Schild data was also fitted to an Allosteric EC₅₀ shift model using GraphPad Prism 5.0 with the following equations ¹⁵²:

$$EC_{50} = 10^{Log(EC_{50})}$$

$$KB = 10^{LogKB}$$

$$\alpha = 10^{Log(\alpha)}$$

$$Antag = \frac{1 + \frac{B}{KB}}{1 + \frac{\alpha \times B}{KB}}$$

$$LogEC = Log(EC_{50} \times Antag)$$

$$Y = Bottom + \frac{Top - Bottom}{1 + 10^{(LogEC - X) \times HillSlope}}$$

Where α is the cooperativity constant for the interaction between allosteric modulator and the receptor.

6.2.3.3 Western Blotting – PAR-dependent MAPK activity measurement

Cell-lysate preparation

Cells were grown in a 24 well plate to >90% confluence in cell culture media. Media was then removed and serum-free media added to quiesce cell growth. After 24 hours incubation, the cells were treated with agonists for the time specified. At the end of the allotted time, the media was removed and the cells washed briefly in cold PBS. The PBS was removed and clear lysis buffer added to lyse the cells. The cells were then scraped off the bottom of the well using a rubber plunger and transferred via syringe to an Eppendorf

vial. 5 mL of each sample were then transferred to a 96-well plate to perform a BCA assay. Sample volumes were then adjusted to 75 μ L to normalise the protein concentrations and 4 \times NuPage lysis buffer (25 μ L) added. The vials were boiled for 2 minutes before storing in a freezer at -20 °C.

SDS-PAGE Electrophoresis

The gel cast was assembled with 1.0 mm spacers and tested for leaks. Once the cast was satisfactorily assembled, 10% resolving gel was prepared for separation. This was prepared using Tris/SDS buffer solution (1.5 M Tris base, 0.4% (w/v) SDS pH adjusted to 8.8 with HCl), 33.3% (v/v) acrylamide/Bis-acrylamide solution, 40% (v/v) ddH₂O and 0.03% (v/v) TEMED. Ammonium persulphate (APS, 10% v/v) was then added to initiate the crosslinking process. The resulting solution was immediately transferred to the gel cast using a pipette and a layer of isopropanol added to provide an anaerobic atmosphere for the cross-linking reaction. Once set, the isopropanol was removed by absorption with filter paper.

4% stacking gel was prepared from 25% (v/v) stacking buffer (0.5 M Tris base, 0.4% w/v SDS pH adjusted to 6.8 with HCl), 10% (v/v) acrylamide/Bis-acrylamide solution, 65% (v/v) ddH₂O, 0.13% (v/v) TEMED and 10% APS (w/v in ddH₂O). Immediately after the addition of APS, the stacking gel was added on top of the resolving gel and the gel comb inserted carefully to ensure no air bubbles in the wells. This was allowed to set before removing the comb.

The gel cast was removed from the casting assembly and put into a gel tank. Running buffer (0.025 M tris base, 0.19 M glycine, 0.1% (w/v) SDS) was poured into the tank and the gel submerged. Cell lysates were boiled at 90 °C for five minutes before loading into the wells using a syringe alongside protein standards. Lysate samples were loaded at a volume of 15 μ L alongside 5 μ L of the molecular ladder. Gels were electrophoresed at 100 V until the marker had run off the gel.

PVDF membrane was cut to the required size and soaked in methanol for 2 minutes. Two pieces of thick filter paper were cut and soaked in transfer buffer (0.025 M tris base, 0.19

M glycine in 4:1 water/methanol solution). The gels were then removed from the electrophoresis tank and carefully removed from the plates. The gel and PVDF membrane were sandwiched within the transfer cassette between layers of filter paper and sponge. The transfer cassette was loaded into the gel tank along with an ice tank. The cold transfer buffer solution was then added alongside a cooling block and electrophoresis performed at 300 mA for 105 minutes. The PVDF membrane was removed from the sandwich and blocked with 1% BSA in TBS-tween buffer (0.15 M NaCl, 0.02 M tris base and 0.27 mM Tween-20 in water) for 2 hours. The buffer was removed and the PVDF membrane treated with 3 mL of 0.2% BSA in TBS-tween solution along with 3 μ L of the primary antibody (1:1000 dilution). This was left to incubate overnight.

The PVDF membrane was then washed with TBS-tween buffer for 90 minutes, renewing the solution every 15 minutes, to remove any remaining unbound antibodies. The buffer was removed and the membrane treated with 10 mL 0.2% BSA in TBS-tween and 3 μ L of secondary antibody before incubating for 90 minutes. The membrane was washed with TBS-tween solution once more to remove any remaining antibodies. The blot was incubated in ECL solution for 2 minutes before being placed in a cassette and developed.

Densitometry Analysis

Developed film was scanned into a computer at 600 dpi resolution. The image was then loaded into ImageJ and the colours inverted. The integrated density of each band was calculated using ImageJ for pERK and Total ERK and the %phosphorylation calculated for each sample using the equation: $\%phosphorylation = \left(\frac{IntDensity_{pERK}}{IntDensity_{TotERK}} \right) \times 100$. A bar graph of the percentage phosphorylation was then produced using GraphPad Prism 5.0.

6.2.3.4 Calcium Assays – Mouse Platelets

Platelet Isolation from Mouse Blood

Blood was drawn by cardiac puncture under terminal anaesthesia into acid citrate dextrose (20 mM citric acid, 110 mM sodium citrate, 5 mM glucose). This solution was then diluted

to 2 mL in modified Tyrode's-HEPES buffer (135 mM NaCl, 3 mM KCl, 10 mM HEPES, 5 mM glucose, and 1 mM MgCl₂·6 H₂O, pH 7.3) and centrifuged at 1000 rpm for 7 minutes. Platelet-rich plasma was removed, and the remaining blood diluted once again to 2 mL and centrifuged once more. The platelet rich plasma was removed once again and both samples combined. Platelets were isolated by centrifuging at 1500 rpm for 12 minutes in the presence of PGE₁ (140 nM), indomethacin (10 μM) and apyrase (0.02 U/mL). Pelleted platelets were resuspended in Tyrode's-HEPES and rested for 30 minutes at 30 °C in the presence of 10 μM indomethacin and 0.02 U/mL apyrase.

Activation of Calcium Signalling

Platelet suspension in Tyrode's-HEPES buffer was added to a Corning Black 96-well Assay Plate with Clear, Flat Bind and a CellBIND Surface (45 μL per well) alongside 45 μL of 2x Cal-6 dye solution. The plate was then wrapped in tin-foil and incubated at 37 °C for 2 hours. After incubation, the plate was spun down at 1000 rpm for 2 mins before placing in a Flexstation 3 Plate Reader. The automated pipetting system was then used to add agonists in 10 μL solutions, prepared in Tyrode's-HEPES buffer, to the plate. Meanwhile, fluorescence readings were taken (Ex: 485 Em: 538) over 120 seconds with agonist addition starting at 17 seconds.

Platelet Aggregation Assays

Platelets (90 μL, normalised to 5×10^5) were added as a suspension to a black 96-well plate. Platelets were then treated with concentration-gradients of compounds (10 μL, 10× required final conc.) and the resulting aggregation measured using light transmission aggregometry at 405 nm every 10 s for 10 mins.

Data Analysis

SoftMax Pro v5.4.5 was used to process the raw fluorescence data into Max-Min (the value of the maximal response minus the value of the minimal response) for each well. These data points were then taken into GraphPad Prism 5.0 where appropriate curves were generated for each dataset.

Max-Min readings were normalised against readings obtained with thrombin at 5 U/mL. Agonist dose response curves were then generated using Log[Agonist] vs Normalised Response with equation: $Y = Bottom + (Top + Bottom)/(1 + 10^{(LogEC_{50}-X)})$. The Top value was constrained to 100 and the Bottom value constrained to 0, yielding the equation: $Y = 100/(1 + 10^{(LogEC_{50}-X)})$.

6.2.3.5 Fura-2 AM Ratiometric Calcium Imaging

Coverslips cultured with HEK-293 cells were gathered into one well of the plate and washed three times with Hanks balanced salt solution (HBSS). Following the final wash, Fura-2 AM (Invitrogen) was loaded as a 1 μ M solution in 1.5 mL of HBSS. The plate was then wrapped in tin foil and incubated at 37 °C with 5% CO₂ for 1 hour before washing three more times prior to imaging.

Coverslips were placed individually in a perfusion bath and imaged using an Olympus BX50 widefield epifluorescence microscope with a Olympus UMPlanFl 20x/0.5 water dipping lens. Excitation of Fura-2 AM was provided by a fast wavelength switchable 340/380 nm light emitting diode (LED) illuminator (CoolLED) with consecutive exposure times of 100 ms for each LED and an imaging rate of 0.5 Hz. Emitted fluorescence was detected by a Hamamatsu ORCA-Flash 4.0 camera and recorded using WinFluor. Specimens were perfused (3 mL/min) firstly with HBSS to establish a baseline calcium level for analysis then perfused separately with solutions of thrombin (1 U/mL, Sigma), PZ-128 (30 μ M) and PZ-Scrambled (30 μ M) in HBSS with a final wash of HBSS to remove the drugs from the perfusion bath.

Data Analysis

Cells were highlighted as regions of interest on the output images using WinFluor alongside one region taken as a background signal. The fluorescent signals were plotted against time for each region of interest and the data then exported into separate MS Excel files for fluorescence signals resulting from 340 nm and 380 nm excitation. The Excel files were then processed using a custom MATLAB script (Peter Tinning) to output data

and graphs for the peak fluorescent ratio change normalised to the baseline and corresponding change in calcium concentration for each region of interest.

The data obtained from MATLAB for fluorescent ratio and calcium concentrations were then transposed into GraphPad Prism to produce graphs comparing the differing responses of thrombin, PZ-128 and PZ-Scram. Data was presented here as mean \pm standard error.

6.2.3.6 MTT Cell Viability Assay

HEK-293 cells were cultured in a clear 96-well assay plate in cell culture media to near confluence. Treatments were carried out progressively in 12 μ L samples at 10 \times the final concentration made up in cell culture media, starting with 24 hour treatments, 5 hour treatments and 2 hour treatments. 24 hours after the initial treatment, the cell-culture media was removed and fresh cell-culture media added (100 μ L). To each well was added 10 μ L of MTT in H₂O (10 mM) and the plate incubated for 2 hours. The media was then removed and DMSO (100 μ L) added to the plate before incubating for 5 mins. The plate was then read, with absorbance being read at 570 nm.

The resulting absorbance values were normalised against the readings obtained from cells treated with media alone and expressed as % viable cells, with media control assumed as 100% cell viability.

6.2.3.7 Flow Cytometric Analyses

During cell passage, cells were spun down and resuspended in 10 mL of cell culture media. Cells were then counted using a haemocytometer and subsequently diluted to 1 \times 10⁶ cells/mL. 1 mL of cell suspension was added to each of 6 FACS tubes. Stimulations were then carried out by adding stock solutions of drugs directly to the cell suspensions and incubating for 1 hour at 37 °C. Following stimulation, the cells were centrifuged at 1400 rpm for 5 mins, the supernatant removed, and the cells washed with 1 mL of PBS. The cells were then centrifuged as above, the supernatant PBS removed and 100 μ L of annexin binding buffer added. APC Annexin V was then added (5 μ L) and the tubes wrapped in foil and incubated at room temperature for 20 mins. Data was acquired on a BD FACSCanto flow cytometer and subsequently analysed using FACSDiva v6.1 (Becton

Dickinson, NJ, USA). A total of 10000 events were measured per sample and gating was set up in APC-A. The number of events falling within the gated region as a percentage of total events was then calculated for each treatment.

6.2.3.8 Statistics

All data shown in figures and tables are the means \pm SEM of at least 3 separate experiments. Where appropriate, statistical significance was calculated using a One-Way ANOVA with a Tukey *Post Hoc* test or a Two-Way ANOVA with a Bonferroni correction comparing two factors.

6.3 Small Molecule Allosteric Inhibitors of PAR2

6.3.1 General Techniques

- i. All reagents, catalysts and solvents were obtained from commercial suppliers and were used without further purification unless otherwise stated.
- ii. Purification was carried out according to standard laboratory methods.²⁰⁶

6.3.1.1 Purification of Solvents

- i. THF was obtained from a PureSolv SPS-400-5 solvent purification system and transferred to and stored in a septum-sealed, oven-dried flask over previously activated 4 Å molecular sieves and purged with and stored under N₂ (g).
- ii. CH₂Cl₂, Et₂O, EtOAc, MeCN and petroleum ether 40-60 °C for purification purposes were used as obtained from suppliers without further purification.

6.3.1.2 Experimental Details

- i. Reactions were carried out using conventional glassware or in sealed microwave vials for air sensitive reactions.
- ii. Glassware was oven-dried at 150 °C and purged with N₂ before use.
- iii. Room temperature was generally 20 °C.
- iv. Reactions carried out at elevated temperatures were heated within a heated sand bath using a temperature-regulated hotplate/stirrer.

6.3.1.3 Purification of Products

- i. Thin layer chromatography was carried out using Merck silica plates coated with fluorescent indicator UV254. These were analysed under 254 nm UV light or developed using solutions of vanillin, ninhydrin or potassium permanganate.
- ii. Normal phase flash chromatography was carried out manually using ZEOprep 60 HYD 40-63 µm silica gel.
- iii. Reverse-phase preparative HPLC was performed using a Gilson preparative HPLC system of 322 pumps coupled to a 151 UV/vis 163 spectrometer, 234 Autoinjector and a GX-271 liquid handler using a Waters XBridge Prep C18 5 µm OBD 19 x 15 mm column at room temperature. Purifications were performed using gradient methods ranging from 10-90% MeCN in H₂O over 20 minutes at a flow rate of 10

mL/min, with UV monitoring at 254 nm. Analysis was conducted using Trilution v2.0 software.

6.3.1.4 Analysis of Products

- i. Fourier Transformed Infra-Red (FTIR) spectra were obtained on a Shimadzu IRAffinity-1S machine.
- ii. ^1H , ^{13}C and ^{19}F NMR spectra were obtained on either a:
 - a. Bruker DRX 500 spectrometer (Avance III HD console, Ascend 500 MHz magnet, BBO smart probe) at 500 MHz, 126 MHz and 471 MHz, respectively
 - b. Bruker AV 400 spectrometer at 400 MHz, 101 MHz and 376 MHz, respectively
 - c. Bruker AV 600 spectrometer at 600 MHz for ^1H and 151 MHz for ^{13}C

Chemical shifts are reported in ppm and coupling constants are reported in Hz with CDCl_3 referenced at 7.26 ppm (^1H) and 77.1 ppm (^{13}C), DMSO-d_6 referenced at 2.50 ppm (^1H) and 39.5 ppm (^{13}C), MeOD referenced at 4.87 ppm (^1H) and 49 ppm (^{13}C) and Acetone-d_6 referenced at 2.05 ppm (^1H) and 29.84 ppm (^{13}C).

- iii. High-resolution mass spectra (HRMS) were obtained through analysis at the EPSRC UK National Mass Spectrometry Facility at Swansea University.
- iv. Liquid-chromatography mass spectra (LCMS) were recorded on an Agilent 6130 single quadrupole with APCI/ESI dual source, on a ThermoQuest Finnigan LCQ DUO electrospray.
- v. Analytical HPLC data was obtained on an Agilent 1200 series HPLC using a Machery-Nagel Nucleodur C18 column. Analysis was performed using a gradient method, eluting with 5 – 80% $\text{MeCN}/\text{H}_2\text{O}$ over 16 minutes at a flow rate of 2 mL/min.

6.3.2 Computational Studies

Preparation of Ligand Files

The ligand files were generated initially in ChemDraw Professional, copied into Chem3D and energy minimisation of the structure was performed. The resulting structural data was saved as a Spatial Data File (.sdf) prior to performing the docking simulation.

Performing the Docking Simulation

The docking simulations for AZ8838-analogues within PAR2 were performed using GOLD (Cambridge Crystallographic Data Centre). The region of interest for the docking studies was defined within all amino acid residues that remained within 10 Å of the docked ligand in the original crystal structure. The “allow early termination” command was deactivated, and all other parameters were used as the GOLD defaults. For each molecule docked within the study, the final ChemPLP Scores for each docking pose were collated and presented as a raw value using GraphPad Prism 5.0.

Statistics

Where appropriate, statistical significance was calculated using a One-Way ANOVA with a Dunnett *Post Hoc* test to compare each entry to a single control ((S)-**3.1**) or a Bonferroni *Post Hoc* test to compare chiral pairs of molecules or different tautomeric forms.

6.3.3 General Procedures

General Procedure A: Suzuki-Miyaura Cross Couplings between boronic acids and 2-bromo-4-fluorobenzaldehyde

2-bromo-4-fluorobenzaldehyde (1 eq.), alkyl/aryl boronic acid (1.5 eq.), caesium carbonate (2-3 eq.) and [1,1'-Bis(diphenylphosphino)ferrocene]-dichloropalladium(II) (10 mol%) were added to a dry microwave vial which was sealed and purged with nitrogen gas. Dioxane (*volume*) and water (*volume*) were then added and the reaction mixture was heated to 80 °C and stirred for 16 hours. The reaction mixture was diluted with EtOAc (10 mL) and washed with saturated sodium chloride solution (3x 15 mL). The organics were dried using Na₂SO₄, filtered and concentrated *in vacuo* to afford the crude product. The

crude residue was then purified by flash chromatography. Pure fractions were collected and evaporated to dryness, yielding the desired product.

General Procedure B: SEM protection of heteroaromatics

Sodium hydride (1.5 eq.) was added to a dry round bottom flask and purged with nitrogen gas. THF (*volume*) was then added to form a suspension, which was stirred at 0 °C. Heteroaryl compound (1 eq.) was added slowly to the suspension and the temperature slowly raised to room temperature. The resulting mixture was stirred at room temperature for 30 minutes before adding (2-(chloromethoxy)ethyl)trimethylsilane (1.5 eq.) slowly at 0 °C. The temperature was allowed to rise to room temperature gradually, stirring the reaction for 16 hours. The reaction mixture was then concentrated *in vacuo* and diluted with EtOAc (100 mL). The resulting solution was washed with water (3x 50 mL), the organics dried over Na₂SO₄, filtered and concentrated *in vacuo* to provide the crude product. The crude residue was purified by flash chromatography. Fractions containing pure product were combined and concentrated *in vacuo* to provide the desired product.

General Procedure C: Organolithium mediated coupling of heterocycle with 4-fluoro-2-propylbenzaldehyde

Protected heterocycle (1.14 eq.) and THF (*volume*) were added to a dry microwave vial and stirred at -78 °C. ⁿBuLi (1.14 eq.) was then added slowly to the reaction mixture which was stirred at -78 °C for 30 mins. A solution of 4-fluoro-2-propylbenzaldehyde (1 eq.) as a solution in THF (*volume*) was then added slowly at -78 °C. The solution was allowed to come to room temperature and then the reaction stirred for one hour. The reaction mixture was quenched with saturated NH₄Cl solution and extracted into EtOAc (3x 10 mL). The organics were collected and washed with water then saturated NaCl solution. The organics were dried with Na₂SO₄, filtered and concentrated *in vacuo* to provide the crude product as a yellow oil. The residue was purified by flash chromatography to provide the desired product.

General Procedure D: Deprotection of SEM protecting groups using TFA

SEM-protected intermediate (1 eq.) was dissolved in CH₂Cl₂ (2 mL) and stirred at room temperature. Trifluoroacetic acid (2 mL) was then added and the solution left to stir overnight. The crude reaction mixture was then evaporated to dryness, diluted with CH₂Cl₂ (5 mL) and washed with sodium bicarbonate (3x 5 mL). The organics were dried using Na₂SO₄, filtered and concentrated *in vacuo* to yield the crude product. The desired product was then obtained by purification using either:

- Reverse-phase preparative HPLC **or**
- Filtering off the solid and washing with hexane

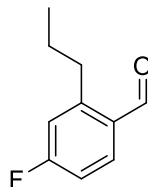
General Procedure E: Organolithium mediated coupling of 1-((2-(trimethylsilyl)ethoxy)methyl)-1*H*-imidazole with 4-fluoro-2-alkyl/arylbenzaldehydes followed by deprotection.

1-((2-(trimethylsilyl)ethoxy)methyl)-1*H*-imidazole (*Eq.*) and THF (*Volume*) were added to a dry microwave vial and stirred at -78 °C. ⁿBuLi (*Eq.*) was then added slowly to the reaction mixture which was stirred at -78 °C for 30 mins. A solution of substituted benzaldehyde (*Eq.*) as a solution in THF (*Volume*) was then added slowly at -78 °C. The solution was warmed to room temperature and stirred for one hour. The reaction mixture was quenched with saturated NH₄Cl solution and extracted into EtOAc (3x 10 mL). The organics were collected and washed with water then saturated NaCl solution. The organics were dried with Na₂SO₄, filtered and concentrated *in vacuo* to provide the crude product as a yellow oil. The crude was then added to a microwave vial and dissolved in CH₂Cl₂ (2 mL) before adding TFA (2 mL) and stirring for 16 hours at room temperature. The reaction mixture was quenched with saturated sodium bicarbonate solution (2 mL) and diluted in CH₂Cl₂ (10 mL). The organics were then washed with sodium bicarbonate (10 mL) and sodium carbonate solution (2x 10 mL), dried with Na₂SO₄, filtered and concentrated *in vacuo* to yield the crude product. The crude was then diluted in CH₂Cl₂ (2 mL) and hexane (2 mL) and concentrated under a constant flow of air until a solid crashed out. The solid was filtered off and washed with hexane to yield the desired product.

6.3.4 Characterisation Data

6.3.4.1 Characterisation Data for Synthesis of 3.1

4-Fluoro-2-propylbenzaldehyde (3.31)⁴



Prepared according to **General Procedure A** using 2-bromo-4-fluorobenzaldehyde (1015 mg, 5 mmol), propylboronic acid (659 mg, 7.5 mmol), caesium carbonate (3260 mg, 10 mmol) and [1,1'-Bis(diphenylphosphino)ferrocene]-dichloropalladium(II) (408 mg, 0.5 mmol) in dioxane (8 mL) and water (2 mL). The crude residue was purified by flash chromatography, eluting with 0-5% EtOAc in petroleum ether, yielding 4-fluoro-2-propylbenzaldehyde (410 mg, 49% yield) as a yellow oil.

IR (ν_{\max} , cm^{-1}) 2978, 2400, 2380, 1703, 1380, 1238

¹H NMR (400 MHz, CDCl_3) δ 10.22 (s, 1H), 7.86 (dd, $J = 8.6, 6.0$ Hz, 1H), 7.06-6.94 (m, 2H), 3.01 (m, 2H), 1.67 (m, 2H), 1.00 (t, $J = 7.3$ Hz, 3H)

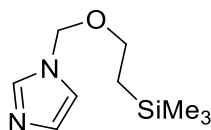
¹³C NMR (101 MHz, CDCl_3) δ 190.03, 165.29 (d, $J = 256.7$ Hz), 148.49 (d, $J = 9.0$ Hz), 133.74 (d, $J = 10.3$ Hz), 129.87, 117.11 (d, $J = 21.5$ Hz), 113.18 (d, $J = 22.4$ Hz), 33.69, 24.49, 13.29

¹⁹F NMR (376 MHz, CDCl_3) -103.99 (ddd, $J = 9.7, 8.0, 6.1$ Hz)

LCMS (ESI) m/z $[\text{M}+\text{MeOH}+\text{H}]^+$ calcd for $\text{C}_{11}\text{H}_{16}\text{FO}_2$ 199.1, found 199.1

Consistent with previously reported data.

1-((2-(Trimethylsilyl)ethoxy)methyl)-1*H*-imidazole (3.33)⁴



Prepared according to **General Procedure B** using sodium hydride (600 mg, 15 mmol), THF (50 mL) and 1*H*-imidazole (681 mg, 10 mmol). The crude residue was purified by flash chromatography, eluting in 50-100% EtOAc in petroleum ether, yielding 1-((2-(trimethylsilyl)ethoxy)methyl)-1*H*-imidazole (1.24 g, 63% yield) as a pale yellow oil.

IR (ν_{\max} , cm^{-1}) 2951, 1247, 1091

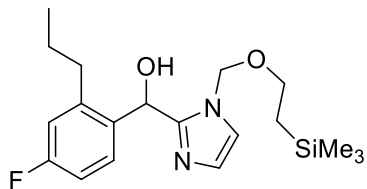
¹H NMR (500 MHz, CDCl_3) δ 7.59 (s, 1H), 7.10 (s, 1H), 7.04 (s, 1H), 5.27 (s, 2H), 3.56 – 3.39 (m, 2H), 0.97 – 0.82 (m, 2H), -0.02 (s, 9H)

¹³C NMR (126 MHz, CDCl_3) δ 138.85, 131.53, 120.31, 77.34, 67.78, 19.14, -0.01

LCMS (ESI) m/z $[\text{M}+\text{H}]^+$ calcd for $\text{C}_9\text{H}_{19}\text{N}_2\text{OSi}$ 199.13, found 199.3

Consistent with previously reported data.

(4-Fluoro-2-propylphenyl)(1-((2-(trimethylsilyl)ethoxy)methyl)-1*H*-imidazol-2-yl)methanol (3.34)⁴



Prepared according to **General Procedure C** using 1-((2-(trimethylsilyl)ethoxy)methyl)-1*H*-imidazole (397 mg, 2.0 mmol) in THF (4 mL), ⁿBuLi (1.015 mL, 2.0 mmol) and 4-fluoro-2-propylbenzaldehyde (290mg, 1.75 mmol) as a solution in THF (4 mL). The crude residue was purified by flash chromatography, eluting in 0-50% EtOAc in petroleum ether to afford (4-fluoro-2-propylphenyl)(1-((2-(trimethylsilyl)ethoxy)methyl)-1*H*-imidazol-2-yl)methanol (322 mg, 51% yield) as a clear oil.

IR (ν_{\max} , cm^{-1}) 3157, 2956, 1249, 1097

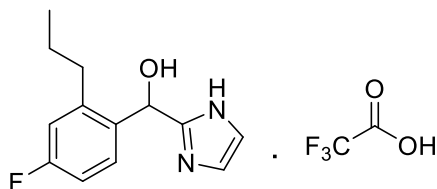
¹H NMR (500 MHz, CDCl_3) δ 7.31 (dd, $J = 8.6, 6.0$ Hz, 1H), 6.94 (dd, $J = 10.2, 2.7$ Hz, 2H), 6.89 – 6.83 (m, 2H), 6.18 (s, 1H), 5.11 (d, $J = 10.7$ Hz, 1H), 5.01 (d, $J = 10.7$ Hz, 1H), 3.29 (dd, $J = 9.2, 7.3$ Hz, 2H), 2.68 (dt, $J = 9.0, 6.1$ Hz, 2H), 1.67 – 1.42 (m, 2H), 0.98 (t, $J = 7.3$ Hz, 3H), 0.87 – 0.71 (m, 2H), -0.00 (s, 9H)

¹³C NMR (126 MHz, CDCl_3) δ 162.41 (d, $J = 245.9$ Hz), 149.37, 143.55 (d, $J = 7.4$ Hz), 134.47 (d, $J = 3.0$ Hz), 128.91 (d, $J = 8.4$ Hz), 126.74, 120.47, 116.14 (d, $J = 21.0$ Hz), 112.58 (d, $J = 20.9$ Hz), 75.06, 66.19, 65.90, 34.27, 23.89, 17.71, 14.10, -1.48

¹⁹F NMR (471 MHz, CDCl_3) δ -115.06 – -115.14 (m)

LCMS (ESI) m/z $[\text{M}+\text{H}]^+$ calcd for $\text{C}_{19}\text{H}_{30}\text{FN}_2\text{O}_2\text{Si}$ 365.21, found 365.2

(4-Fluoro-2-propylphenyl)(1*H*-imidazol-2-yl)methanol (3.1)⁴



Prepared according to **General Procedure D** using (4-fluoro-2-propylphenyl)(1-((2-(trimethylsilyl)ethoxy)methyl)-1*H*-imidazol-2-yl)methanol (315 mg, 0.86 mmol), CH₂Cl₂ (2 mL) and trifluoroacetic acid (2 mL). The crude was purified by reverse phase preparative HPLC to yield (4-fluoro-2-propylphenyl)(1*H*-imidazol-2-yl)methanol as the trifluoroacetic acid salt (15 mg, 0.04 mmol, 5% yield) as a white solid.

IR (ν_{max} , cm⁻¹) 3726, 3111, 2924, 1249

¹H NMR (500 MHz, Acetone-d₆) δ 7.57 (s, 2H), 7.48 (dd, $J = 8.6, 6.0$ Hz, 1H), 7.05 (dd, $J = 10.2, 2.6$ Hz, 1H), 7.00 (td, $J = 8.5, 2.7$ Hz, 1H), 6.48 (s, 1H), 2.79 – 2.53 (m, 2H), 1.63 – 1.51 (m, 2H), 0.93 (t, $J = 7.3$ Hz, 3H)

¹³C NMR (126 MHz, Acetone-d₆) δ 163.75 (d, $J = 245.1$ Hz), 151.36, 144.71 (d, $J = 7.7$ Hz), 133.40 (d, $J = 2.5$ Hz), 130.71 (d, $J = 8.7$ Hz), 120.40, 120.24, 117.01 (d, $J = 20.7$ Hz), 113.88 (d, $J = 24.3$ Hz), 65.11, 34.78, 24.69, 14.18

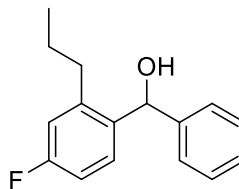
¹⁹F NMR (471 MHz, Acetone-d₆) δ -70.75 (s), -110.10 – -110.17 (m)

HRMS (ESI) m/z [M+H]⁺ calcd for C₁₃H₁₆FN₂O 235.1241, found 235.1243

Consistent with previously reported data.

6.3.4.2 Characterisation Data for Synthesis of Imidazole Analogues

(4-Fluoro-2-propylphenyl)(phenyl)methanol (3.5)



4-Fluoro-2-propylbenzaldehyde (42 mg, 0.25 mmol) was added to an oven dried microwave vial as a solution in THF (1 mL) and cooled to 0 °C. Phenyl magnesium bromide (100 μ L, 0.3 mmol) was then added dropwise to the reaction mixture under nitrogen, stirring continuously. The reaction was warmed to room temperature and stirred for 2 hours before quenching with ammonium chloride (2 mL). The product was extracted into ethyl acetate (3x 5 mL) before drying the organics using Na_2SO_4 and filtering. The resulting solution was concentrated *in vacuo* to provide the crude product. Purification was carried out by Flash chromatography, eluting with 0-20% ethyl acetate/petroleum ether (40-60 °C), to yield (4-fluoro-2-propylphenyl)(phenyl)methanol (13 mg, 0.05 mmol, 20% yield) as a yellow oil.

IR (ν_{max} , cm^{-1}) 3358, 2850, 1222

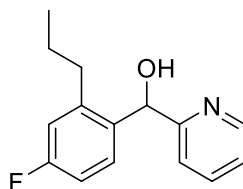
^1H NMR (500 MHz, CDCl_3) δ 7.30 (dd, $J = 8.2, 6.1$ Hz, 1H), 7.25 – 7.19 (m, 4H), 7.19 – 7.14 (m, 1H), 6.87 – 6.72 (m, 2H), 5.94 (s, 1H), 2.56 – 2.41 (m, 2H), 1.51 – 1.33 (m, 2H), 0.82 (t, $J = 7.3$ Hz, 3H).

^{13}C NMR (126 MHz, CDCl_3) δ 162.21 (d, $J = 245.5$ Hz), 143.35, 142.62 (d, $J = 7.2$ Hz), 136.87 (d, $J = 2.9$ Hz), 128.76 (d, $J = 8.3$ Hz), 128.51, 127.62, 126.82 (d, $J = 2.9$ Hz), 115.92 (d, $J = 21.0$ Hz), 112.83 (d, $J = 20.9$ Hz), 72.26, 34.35, 23.98, 14.07

^{19}F NMR (471 MHz, CDCl_3) δ -115.45 – -115.48 (m)

LCMS (ESI) m/z : $[\text{M-OH}+\text{NH}_3]^+$ calcd for $\text{C}_{16}\text{H}_{19}\text{FN}$ 244.1496, found 244.1

(4-Fluoro-2-propylphenyl)(pyridin-2-yl)methanol (3.4)



2-Bromopyridine (78 mg, 0.5 mmol) was added to a dried microwave vial and dissolved in THF (0.5 mL) before cooling to 0 °C. *i*-PrMgCl.LiCl (1.7 M in THF, 0.3 mL, 0.5 mmol) was then added slowly under nitrogen and the resulting solution raised out of the ice bath and stirred at room temperature for 6 hours. 4-Fluoro-2-propylbenzaldehyde (42 mg, 0.25 mmol) was then added dropwise under nitrogen and the solution stirred at room temperature for 30 minutes. The reaction mixture was quenched with water (2 mL) and extracted into CH₂Cl₂ (5 mL). The organics were washed with water (3x 5 mL) before drying using Na₂SO₄, filtering and concentrating *in vacuo* to provide the crude product. The crude was purified by Flash chromatography, eluting with 0-30% ethyl acetate/petroleum ether (40-60 °C), yielding (4-fluoro-2-propylphenyl)(pyridin-2-yl)methanol (30 mg, 0.12 mmol, 49% yield) as a brown oil.

IR (ν_{\max} , cm⁻¹) 3701, 2951, 1249

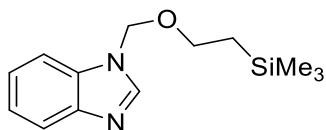
¹H NMR (500 MHz, CDCl₃) δ 8.58 (d, *J* = 4.8 Hz, 1H), 7.61 (t, *J* = 7.7 Hz, 1H), 7.23 – 7.16 (m, 1H), 7.11 (dd, *J* = 8.5, 6.1 Hz, 1H), 6.99 (d, *J* = 7.9 Hz, 1H), 6.90 (dd, *J* = 10.1, 2.6 Hz, 1H), 6.83 (td, *J* = 8.4, 2.6 Hz, 1H), 5.96 (s, 1H), 2.75 – 2.63 (m, 2H), 1.68 – 1.51 (m, 2H), 0.94 (t, *J* = 7.3 Hz, 3H).

¹³C NMR (126 MHz, CDCl₃) δ 162.29 (d, *J* = 245.8 Hz), 161.11, 149.18, 147.79, 136.85, 130.19 (d, *J* = 8.4 Hz), 123.73, 122.41, 121.32, 116.10 (d, *J* = 20.9 Hz), 113.08 (d, *J* = 21.1 Hz), 71.30, 34.62, 24.42, 14.06

¹⁹F NMR (471 MHz, CDCl₃) δ -115.09 – -115.13 (m)

LCMS (ESI) *m/z*: [M+H]⁺ calcd for C₁₅H₁₇FNO 246.13, found 246.1

1-((2-(Trimethylsilyl)ethoxy)methyl)-1*H*-benzo[*d*]imidazole (3.38)²⁰⁷



Prepared according to **General Procedure B** using sodium hydride (120 mg, 3.0 mmol), THF (6 mL) and benzimidazole (236 mg, 2.0 mmol) as a solution in THF (4 mL). The crude residue was purified by flash chromatography eluting with 0-70% EtOAc/petroleum ether to provide 1-((2-(trimethylsilyl)ethoxy)methyl)-1*H*-benzo[*d*]imidazole (235 mg, 0.95 mmol, 47% yield) as a white solid.

IR (ν_{\max} , cm^{-1}) 2951, 1247, 1082

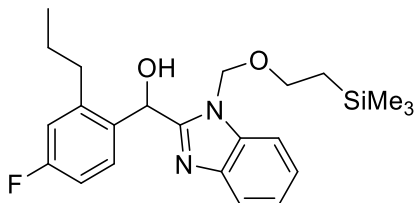
¹H NMR (500 MHz, CDCl_3) δ 8.02 (s, 1H), 7.87 (dd, $J = 6.4, 2.2$ Hz, 1H), 7.58 (dd, $J = 6.5, 2.1$ Hz, 1H), 7.40 – 7.33 (m, 2H), 5.55 (s, 2H), 3.61 – 3.51 (m, 2H), 1.01 – 0.90 (m, 2H), 0.00 (s, 9H).

¹³C NMR (126 MHz, CDCl_3) δ 145.47, 144.49, 135.11, 124.87, 124.10, 121.80, 111.70, 75.62, 67.87, 19.12, -0.01

LCMS (ESI) m/z $[\text{M}+\text{H}]^+$ calcd for $\text{C}_{13}\text{H}_{21}\text{N}_2\text{OSi}$ 249.14, found 249.3

Consistent with previously reported data.

(4-Fluoro-2-propylphenyl)(1-((2-(trimethylsilyl)ethoxy)methyl)-1H-benzo[d]imidazol-2-yl)methanol (3.39)



Prepared according to **General Procedure C** using 1-((2-(trimethylsilyl)ethoxy)methyl)-1H-benzo[d]imidazole (142 mg, 0.57 mmol) in THF (1 mL), ⁿBuLi (1.97 M in THF) (290 μL, 0.57 mmol) and 4-fluoro-2-propylbenzaldehyde (83 mg, 0.5 mmol) as a solution in THF (1 mL). The crude residue was purified by flash chromatography eluting with 0-20% EtOAc/petroleum ether to yield (4-fluoro-2-propylphenyl)(1-((2-(trimethylsilyl)ethoxy)methyl)-1H-benzo[d]imidazol-2-yl)methanol (70 mg, 0.17 mmol, 34% yield) as a yellow oil.

IR (ν_{\max} , cm^{-1}) 3192, 2954, 1263, 1095

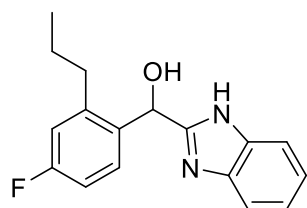
¹H NMR (500 MHz, CDCl_3) δ 7.65 (d, $J = 7.3$ Hz, 1H), 7.47 (d, $J = 7.3$ Hz, 1H), 7.39 – 7.32 (m, 2H), 7.20 (dd, $J = 8.6, 6.0$ Hz, 1H), 7.06 (dd, $J = 9.9, 2.6$ Hz, 1H), 6.81 (td, $J = 8.4, 2.6$ Hz, 1H), 6.46 (s, 1H), 5.34 (d, $J = 11.2$ Hz, 1H), 5.21 (d, $J = 11.2$ Hz, 1H), 3.39 – 3.30 (m, 2H), 3.02 – 2.86 (m, 2H), 1.87 – 1.68 (m, 2H), 1.10 (t, $J = 7.3$ Hz, 3H), 0.88 – 0.81 (m, 2H), -0.00 (s, 9H)

¹³C NMR (126 MHz, CDCl_3) δ 162.71 (d, $J = 247.0$ Hz), 156.05, 144.13 (d, $J = 7.5$ Hz), 141.33, 135.83, 133.92 (d, $J = 3.0$ Hz), 129.44 (d, $J = 8.5$ Hz), 123.43, 122.69, 119.60, 116.50 (d, $J = 21.1$ Hz), 113.07 (d, $J = 21.1$ Hz), 109.93, 72.84, 66.49, 66.34, 34.56, 24.18, 17.84, 14.24 (d, $J = 9.0$ Hz), -1.45

¹⁹F NMR (471 MHz, CDCl_3) δ -114.02 (ddd, $J = 10.4, 8.1, 6.1$ Hz)

HRMS (ESI) m/z $[\text{M}+\text{H}]^+$ calcd for $\text{C}_{23}\text{H}_{32}\text{FN}_2\text{O}_2\text{Si}$, found 415.2212, found 415.2213

(1*H*-Benzo[*d*]imidazol-2-yl)(4-fluoro-2-propylphenyl)methanol (3.10)



Prepared according to **General Procedure D** using (4-fluoro-2-propylphenyl)(1-((2-(trimethylsilyl)ethoxy)methyl)-1*H*-benzo[*d*]imidazol-2-yl)methanol (40 mg, 0.14 mmol, CH₂Cl₂ (2 mL) and TFA (1 mL). The crude was then diluted in CH₂Cl₂ (2 mL) and hexane (2 mL) and concentrated under a constant flow of air until a solid crashed out. The solid was filtered off and washed with hexane to yield (1*H*-benzo[*d*]imidazol-2-yl)(4-fluoro-2-propylphenyl)methanol (27 mg, 0.09 mmol, 68% yield) as a white solid.

IR (ν_{\max} , cm⁻¹) 3253, 2794, 1226

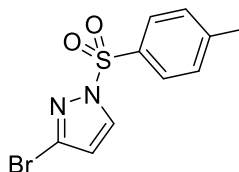
¹H NMR (500 MHz, DMSO) δ 15.03 (s, 1H), 7.78 – 7.70 (m, 2H), 7.54 – 7.49 (m, 2H), 7.39 (dd, J = 8.6, 6.0 Hz, 2H), 7.13 (dd, J = 10.2, 2.6 Hz, 1H), 7.07 (td, J = 8.5, 2.7 Hz, 1H), 6.43 (s, 1H), 2.85 – 2.61 (m, 2H), 1.59 – 1.43 (m, 2H), 0.89 (t, J = 7.3 Hz, 3H)

¹³C NMR (126 MHz, DMSO) δ 162.64 (d, J = 245.0 Hz), 156.15, 144.40 (d, J = 7.6 Hz), 133.79, 132.03, 131.03 (d, J = 8.9 Hz), 126.01, 116.74 (d, J = 21.1 Hz), 114.67, 113.62 (d, J = 21.2 Hz), 65.47, 34.13, 24.27, 14.33

¹⁹F NMR (471 MHz, DMSO) δ -113.37 – -113.53 (m)

HRMS (ESI) m/z [M+H] calcd for C₁₇H₁₈FN₂O 285.1398, found 285.1404

Synthesis of 3-bromo-1-tosyl-1H-pyrazole (3.44)²⁰⁸



3-Bromo-1H-pyrazole (74 mg, 0.5 mmol) was dissolved in THF (2 mL) and cooled to 0 °C before adding sodium hydride (30 mg, 0.75 mmol). The reaction mixture was stirred for 10 mins before addition of tosyl chloride (114 mg, 0.6 mmol) and the reaction was stirred overnight, raising to room temperature slowly. The reaction was concentrated *in vacuo*, diluted with EtOAc (5 mL) and washed with water (3x 5 mL). The organics were dried with Na₂SO₄, filtered and concentrated *in vacuo* to yield 3-bromo-1-tosyl-1H-pyrazole (131 mg, 0.44 mmol, 88% yield) as a white powder.

IR (ν_{\max} , cm⁻¹) 1371, 667

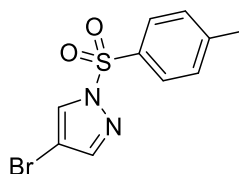
¹H NMR (500 MHz, CDCl₃) δ 7.99 (d, J = 2.7 Hz, 1H), 7.90 (d, J = 8.3 Hz, 2H), 7.34 (d, J = 8.3 Hz, 2H), 6.40 (d, J = 2.7 Hz, 1H), 2.43 (s, 3H)

¹³C NMR (126 MHz, CDCl₃) δ 146.51, 133.55, 133.06, 132.88, 130.33, 128.52, 112.26, 21.89

LCMS (ESI) m/z [M+H] calcd for C₁₀H₁₀BrN₂O₂S 301.0/303.0, found 301.1 and 303.1

Consistent with previously reported data.

Synthesis of 4-bromo-1-tosyl-1H-pyrazole (3.45)²⁰⁹



4-Bromo-1H-pyrazole (74 mg, 0.5 mmol) was dissolved in THF (2 mL) and cooled to 0 °C before adding sodium hydride (30 mg, 0.75 mmol). The reaction mixture was stirred for 10 mins before addition of tosyl chloride (114 mg, 0.6 mmol) and the reaction was stirred overnight, raising to room temperature slowly. The reaction was concentrated *in vacuo*, diluted with EtOAc (5 mL) and washed with water (3x 5 mL). The organics were dried with Na₂SO₄, filtered and concentrated *in vacuo* to yield 4-bromo-1-tosyl-1H-pyrazole (134 mg, 0.44 mmol, 89% yield) as a white powder.

IR (ν_{\max} , cm⁻¹) 1396, 1377, 528

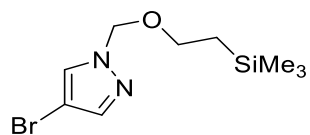
¹H NMR (500 MHz, CDCl₃) δ 8.04 (s, 1H), 7.83 (d, J = 8.3 Hz, 2H), 7.58 (s, 1H), 7.28 (d, J = 8.3 Hz, 2H), 2.36 (s, 3H)

¹³C NMR (126 MHz, CDCl₃) δ 146.43, 145.63, 133.42, 130.41, 130.20, 128.36, 97.45, 21.77

LCMS (ESI) m/z [M+H] calcd for C₁₀H₁₀BrN₂O₂S 301.0/303.0, found 301.1 and 303.1

Consistent with previously reported data.

4-Bromo-1-((2-(trimethylsilyl)ethoxy)methyl)-1H-pyrazole (3.49)^{210,211}



Prepared according to **General Procedure B** using sodium hydride (180 mg, 4.5 mmol), THF (10 mL) and 4-bromo-1H-pyrazole (441 mg, 3 mmol). The crude residue was purified by flash chromatography, eluting in 0-20% EtOAc in petroleum ether to provide 4-bromo-1-((2-(trimethylsilyl)ethoxy)methyl)-1H-pyrazole (740 mg, 89% yield) as a yellow oil.

IR (ν_{\max} , cm^{-1}) 1453, 1432, 734

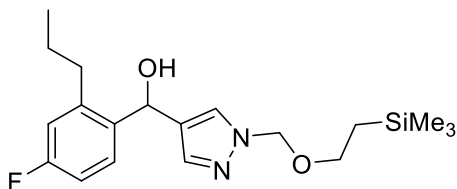
¹H NMR (500 MHz, CDCl_3) δ 7.59 (s, 1H), 7.49 (s, 1H), 5.38 (s, 2H), 3.65 – 3.44 (m, 2H), 1.00 – 0.78 (m, 2H), -0.02 (s, 9H).

¹³C NMR (126 MHz, CDCl_3) δ 141.84, 130.95, 96.08, 82.15, 68.46, 19.22, -0.01

LCMS (ESI) m/z [M+H] calcd for $\text{C}_9\text{H}_{18}\text{BrN}_2\text{OSi}$ 277.0/279.0, found 277.2 and 279.1

Consistent with previously reported data.

(4-Fluoro-2-propylphenyl)(1-((2-(trimethylsilyl)ethoxy)methyl)-1H-pyrazol-4-yl)methanol (3.50)



4-Bromo-1-((2-(trimethylsilyl)ethoxy)methyl)-1H-pyrazole (277 mg, 1.0 mmol) was dissolved in THF (1.5 mL) and added to a dried and purged (N₂) microwave vial. The solution was cooled to -78 °C and ⁿBuLi (1.97 M in THF) (510 μL, 1.0 mmol) was added slowly under N₂. The resulting solution was stirred for 5 mins at -78 °C before adding 4-fluoro-2-propylbenzaldehyde (83 mg, 0.5 mmol) as a solution in THF (1 mL) dropwise. The reaction mixture was stirred for 5 minutes at -78 °C before warming to room temperature and stirring for a further 15 minutes. The reaction was then quenched with water (2 mL) and extracted with diethyl ether (3x 5 mL). The organics were combined and concentrated to yield the crude product. The crude was purified by flash chromatography eluting with 0-50% EtOAc/petroleum ether to yield (4-fluoro-2-propylphenyl)(1-((2-(trimethylsilyl)ethoxy)methyl)-1H-pyrazol-4-yl)methanol (64 mg, 0.18 mmol, 35% yield) as a yellow oil.

IR (ν_{max}, cm⁻¹) 2955, 2872, 1247, 1085

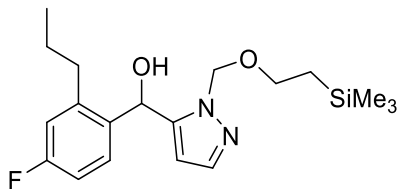
¹H NMR (400 MHz, CDCl₃) δ 7.47 (dd, *J* = 8.5, 6.0 Hz, 1H), 7.31 (s, 1H), 7.27 (s, 1H), 6.91 – 6.82 (m, 2H), 5.98 (s, 1H), 5.28 (s, 2H), 3.54 – 3.43 (m, 2H), 2.57 – 2.46 (m, 2H), 1.58 – 1.45 (m, 2H), 0.94 – 0.80 (m, 5H), -0.06 (s, 9H)

¹³C NMR (101 MHz, CDCl₃) δ 162.19 (d, *J* = 245.4 Hz), 141.88 (d, *J* = 6.9 Hz), 138.66, 137.21, 128.19 (d, *J* = 7.7 Hz), 128.19 (d, *J* = 7.7 Hz), 126.78, 115.87 (d, *J* = 21.1 Hz), 113.02 (d, *J* = 20.8 Hz), 80.24, 66.81, 64.82, 34.31, 24.07, 17.79, 14.08, -1.41

¹⁹F NMR (471 MHz, CDCl₃) δ -115.41 (ddd, *J* = 10.5, 8.5, 6.2 Hz)

HRMS (ESI) *m/z* [M+H] calcd for C₁₉H₃₀FN₂O₂Si 365.2055, found 365.2057

(4-Fluoro-2-propylphenyl)(1-((2-(trimethylsilyl)ethoxy)methyl)-1H-pyrazol-5-yl)methanol (3.51)



(4-Fluoro-2-propylphenyl)(1-((2-(trimethylsilyl)ethoxy)methyl)-1H-pyrazol-5-yl)methanol was isolated during the synthesis of **3.50** following flash chromatography (0-50% EtOAc/petroleum ether) as a yellow oil (23.1 mg, 0.06 mmol, 13% yield).

IR (ν_{\max} , cm^{-1}) 2957, 2874, 1265, 1250, 1078

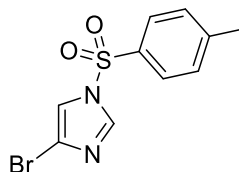
^1H NMR (500 MHz, CDCl_3) δ 7.55 (dd, $J = 8.6, 6.0$ Hz, 1H), 7.33 (d, $J = 1.8$ Hz, 1H), 6.98 – 6.87 (m, 2H), 6.16 (s, 1H), 5.81 (d, $J = 1.6$ Hz, 1H), 5.57 (d, $J = 11.2$ Hz, 1H), 5.47 (d, $J = 11.2$ Hz, 1H), 3.55 (dd, $J = 9.0, 7.9$ Hz, 2H), 2.56 – 2.40 (m, 2H), 1.61 – 1.42 (m, 2H), 0.88 (dd, $J = 11.6, 4.3$ Hz, 5H), -0.02 (s, 9H)

^{13}C NMR (101 MHz, CDCl_3) δ 162.56 (d, $J = 246.1$ Hz), 145.42, 142.29 (d, $J = 7.4$ Hz), 138.62, 134.31, 128.42 (d, $J = 8.6$ Hz), 115.95 (d, $J = 21.0$ Hz), 113.03 (d, $J = 21.1$ Hz), 107.78, 78.61, 66.83, 63.87, 34.32, 23.68, 17.99, 14.11, -1.39

^{19}F NMR (471 MHz, CDCl_3) δ -114.87 (ddd, $J = 10.4, 8.7, 6.1$ Hz)

HRMS (ESI) m/z $[\text{M}+\text{H}]$ calcd for $\text{C}_{19}\text{H}_{30}\text{FN}_2\text{O}_2\text{Si}$ 365.2055, found 365.2057

4-Bromo-1-tosyl-1H-imidazole (3.53)²¹²



4-Bromo-1H-imidazole (74 mg, 0.5 mmol) was dissolved in THF (2 mL) and cooled to 0 °C before adding sodium hydride (30 mg, 0.75 mmol). The reaction mixture was stirred for 10 mins before addition of tosyl chloride (114 mg, 0.6 mmol) and the reaction was stirred overnight, raising to room temperature slowly. The reaction was concentrated *in vacuo*, diluted with EtOAc (5 mL) and washed with water (3x 5 mL). The organics were dried with Na₂SO₄, filtered and concentrated *in vacuo* to yield 3-bromo-1-tosyl-1H-pyrazole (154 mg, 0.5 mmol, quant.) as a white powder.

IR (ν_{\max} , cm⁻¹) 1371, 1359, 534

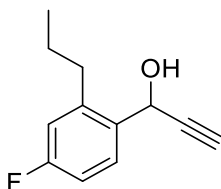
¹H NMR (500 MHz, CDCl₃) δ 7.88 (s, 1H), 7.83 (d, *J* = 8.3 Hz, 2H), 7.38 (d, *J* = 8.3 Hz, 2H), 7.26 (s, 1H), 2.45 (s, 3H)

¹³C NMR (126 MHz, CDCl₃) δ 146.93, 136.25, 134.28, 130.64, 127.58, 118.61, 116.45, 21.78

LCMS (ESI) *m/z* [M+H] calcd for C₁₀H₁₀BrN₂O₂S 300.96, found 301.0 and 303.0

Consistent with previously reported data.

1-(4-Fluoro-2-propylphenyl)prop-2-yn-1-ol (3.56)



4-Fluoro-2-propylbenzaldehyde (220 mg, 1.3 mmol) was added to a dried and purged microwave vial as a solution in THF (1.5 mL) and cooled to 0 °C. Ethynylmagnesium bromide (5.2 mL, 2.5 mmol, 1.1 eq.) was then added dropwise at 0 °C. The reaction mixture was warmed to room temperature and stirred for 3 hours then quenched with saturated ammonium chloride solution (3 mL). The resulting solution was extracted into ethyl acetate (3x 15 mL) and the organics combined, dried with Na₂SO₄ and filtered. The filtrate was concentrated *in vacuo* yielding 1-(4-fluoro-2-propylphenyl)prop-2-yn-1-ol (200 mg, 1.04 mmol, 79% yield) as a yellow oil.

IR (ν_{\max} , cm⁻¹) 3361, 3302, 2110, 1234

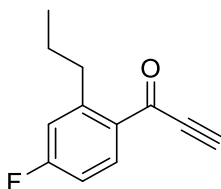
¹H NMR (500 MHz, CDCl₃) δ 7.71 (dd, J = 8.3, 5.9 Hz, 1H), 6.99 – 6.91 (m, 2H), 5.65 (d, J = 2.1 Hz, 1H), 2.80 – 2.69 (m, 2H), 2.68 (d, J = 2.2 Hz, 1H), 1.74 – 1.64 (m, 2H), 1.03 (t, J = 7.3 Hz, 3H)

¹³C NMR (126 MHz, CDCl₃) δ 162.64 (d, J = 246.9 Hz), 142.90 (d, J = 7.6 Hz), 133.41 (d, J = 2.9 Hz), 128.73 (d, J = 8.7 Hz), 116.05 (d, J = 21.2 Hz), 112.89 (d, J = 21.2 Hz), 83.50, 74.68, 60.91, 34.04, 23.98, 13.91

¹⁹F NMR (471 MHz, CDCl₃) δ -113.87 (ddd, J = 10.5, 8.7, 6.1 Hz)

HRMS (ESI) m/z [M-H] calcd for C₁₂H₁₂FO 191.0872, found 191.0869.

1-(4-Fluoro-2-propylphenyl)prop-2-yn-1-one (3.57)



1-(4-Fluoro-2-propylphenyl)prop-2-yn-1-ol (180 mg, 0.94 mmol) was added as a solution in dichloromethane (5 mL) to a microwave vial containing manganese dioxide (817 mg, 9.4 mmol). The reaction mixture was then stirred at room temperature for 16 hours before diluting in dichloromethane and filtering through a pad of celite. After washing with further dichloromethane, organics were concentrated *in vacuo* to yield 1-(4-fluoro-2-propylphenyl)prop-2-yn-1-one as a yellow oil (134 mg, 0.70 mmol, 75% yield).

IR (ν_{\max} , cm^{-1}) 3294, 1651, 2092, 1226, 999

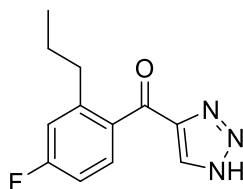
^1H NMR (500 MHz, CDCl_3) δ 8.26 (dd, $J = 8.7, 5.9$ Hz, 1H), 7.02 – 6.89 (m, 2H), 3.40 (s, 1H), 3.01 – 2.85 (m, 2H), 1.68 – 1.45 (m, 2H), 0.95 (t, $J = 7.3$ Hz, 3H).

^{13}C NMR (101 MHz, CDCl_3) δ 176.74, 164.81 (d, $J = 256.5$ Hz), 148.83 (d, $J = 8.6$ Hz), 136.38 (d, $J = 9.7$ Hz), 130.44, 117.72 (d, $J = 21.4$ Hz), 112.46 (d, $J = 21.7$ Hz), 81.03, 79.14, 35.74, 23.55, 13.51

^{19}F NMR (471 MHz, CDCl_3) δ -104.54 (ddd, $J = 9.6, 7.8, 6.2$ Hz)

HRMS (ESI) m/z $[\text{M}+\text{H}]$ calcd for $\text{C}_{12}\text{H}_{12}\text{FO}$ 191.0872, found 191.0867.

(4-Fluoro-2-propylphenyl)(1*H*-1,2,3-triazol-4-yl)methanone (3.58)



1-(4-Fluoro-2-propylphenyl)prop-2-yn-1-one (34 mg, 0.18 mmol) was added as a solution in DMF (2 mL) to a sealed microwave vial containing sodium azide (12.6 mg, 0.19 mmol). The reaction mixture was then stirred for 16 hours before diluting with H₂O (2 mL) and EtOAc (5 mL). After separation, the organics were washed twice with brine (10 mL) and twice with saturated LiCl solution (10 mL). The organics were then dried with using Na₂SO₄, filtered and concentrated to yield (4-fluoro-2-propylphenyl)(1*H*-1,2,3-triazol-4-yl)methanone (19.9 mg, 0.09 mmol, 47% yield) as a yellow oil.

IR (ν_{\max} , cm⁻¹) 3120, 1662, 1234

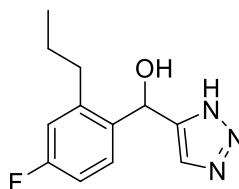
¹H NMR (400 MHz, CDCl₃) δ 8.29 (s, 1H), 7.71 (dd, J = 8.4, 5.9 Hz, 1H), 7.07 (dd, J = 9.9, 2.3 Hz, 1H), 7.00 (td, J = 8.3, 2.3 Hz, 1H), 2.85 – 2.75 (m, 2H), 1.71 – 1.57 (m, 2H), 0.94 (t, J = 7.3 Hz, 3H).

¹³C NMR (101 MHz, CDCl₃) δ 187.47, 163.86 (d, J = 253.0 Hz), 146.23 (d, J = 8.3 Hz), 145.86, 133.25, 132.51, 131.82 (d, J = 9.4 Hz), 117.06 (d, J = 21.3 Hz), 111.97 (d, J = 21.7 Hz), 34.81, 24.17, 13.42

¹⁹F NMR (471 MHz, CDCl₃) δ -108.08 – -108.35 (m)

HRMS (ESI) m/z [M+H] calcd for C₁₂H₁₃FN₃O 234.1043, found 234.1041.

(4-Fluoro-2-propylphenyl)(1*H*-1,2,3-triazol-4-yl)methanol (3.9)



(4-Fluoro-2-propylphenyl)(1*H*-1,2,3-triazol-4-yl)methanone (10 mg, 0.05 mmol) was added to a dried and purged microwave vial as a solution in THF (2 mL) before adding LiAlH₄ (1 M in Et₂O) (180 μL, 0.18 mmol) at 0 °C under nitrogen. The reaction mixture was then warmed to room temperature and stirred for 30 mins. The reaction was quenched with H₂O (2 mL) and extracted in EtOAc (10 mL). Organics were then washed with brine (2x 10 mL), dried with Na₂SO₄ and filtered. The filtrate was concentrated *in vacuo* and the crude residue taken up in CH₂Cl₂ (2 mL) and hexane (2 mL). The resulting solution was concentrated under constant flow of air until a solid precipitated. The solid was filtered and washed with hexane to provide (4-fluoro-2-propylphenyl)(1*H*-pyrazol-4-yl)methanol (2.6 mg, 0.01 mmol, 22% yield) as a white solid.

IR (ν_{\max} , cm⁻¹) 3136, 1230

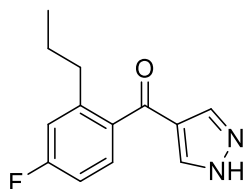
¹H NMR (500 MHz, DMSO) δ 14.79 (s, 1H), 7.60 (s, 1H), 7.55 – 7.47 (m, 1H), 7.05 – 6.92 (m, 2H), 6.02 (s, 1H), 5.94 (s, 1H), 2.66 – 2.52 (m, 2H), 1.55 – 1.39 (m, 2H), 0.87 (t, J = 7.3 Hz, 3H).

¹³C NMR (101 MHz, DMSO) δ 165.59, 161.15 (d, J = 241.9 Hz), 141.79 (d, J = 6.9 Hz), 128.70 (d, J = 8.4 Hz), 115.22 (d, J = 21.0 Hz), 112.40 (d, J = 20.7 Hz), 63.83, 33.50, 23.50, 13.84. Two carbon atoms were unaccounted for due to peak broadening.

¹⁹F NMR (471 MHz, DMSO) δ -116.08 – -116.54 (m)

HRMS (ESI) m/z [M-OH] calcd for C₁₂H₁₃FN₃ 218.1099, found 218.1090

(4-Fluoro-2-propylphenyl)(1H-pyrazol-4-yl)methanone (3.59)



1-(4-Fluoro-2-propylphenyl)prop-2-yn-1-one (34 mg, 0.18 mmol) was added to a sealed microwave vial before adding (diazomethyl)trimethylsilane (2.0 M in hexanes) (100 μ L, 0.19 mmol) and hexane (1 mL). The reaction mixture was stirred at room temperature for 16 hours before concentrating *in vacuo* to yield (4-fluoro-2-propylphenyl)(1H-pyrazol-4-yl)methanone (39 mg, 0.17 mmol, 93% yield) as a yellow oil.

IR (ν_{\max} , cm^{-1}) 3327, 1112

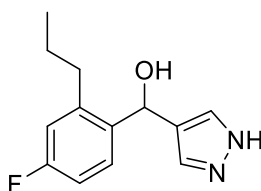
^1H NMR (500 MHz, CDCl_3) δ 7.49 (s, 1H), 7.40 (dd, $J = 8.5, 5.9$ Hz, 1H), 6.87 (dd, $J = 9.9, 2.5$ Hz, 1H), 6.77 (td, $J = 8.3, 2.5$ Hz, 1H), 6.50 (s, 1H), 2.63 – 2.54 (m, 2H), 1.50 – 1.37 (m, 2H), 0.72 (t, $J = 7.3$ Hz, 3H)

^{13}C NMR (126 MHz, CDCl_3) δ 189.39, 164.15 (d, $J = 251.5$ Hz), 146.15 (d, $J = 8.0$ Hz), 134.25, 131.74 (d, $J = 8.9$ Hz), 131.54 (d, $J = 9.2$ Hz), 117.45 (dd, $J = 21.1, 17.8$ Hz), 112.44 (dd, $J = 29.5, 21.6$ Hz), 110.08, 35.34, 24.87, 14.14

^{19}F NMR (471 MHz, CDCl_3) δ -108.75 – -109.17 (m).

HRMS (ESI) m/z [$\text{M}+\text{H}$] calcd for $\text{C}_{13}\text{H}_{14}\text{FN}_2\text{O}$ 233.1090, found 233.1090.

(4-Fluoro-2-propylphenyl)(1H-pyrazol-4-yl)methanol (3.8)



(4-fluoro-2-propylphenyl)(1H-pyrazol-4-yl)methanone (20 mg, 0.09 mmol) was added to a dried and purged microwave vial as a solution in THF (2 mL) before adding LiAlH₄ (1 M in Et₂O) (180 μL, 0.18 mmol) at 0 °C under nitrogen. The reaction mixture was then warmed to room temperature and stirred for 30 mins. The reaction was quenched with H₂O (2 mL) and extracted in EtOAc (10 mL). Organics were then washed with brine (2x 10 mL), dried with Na₂SO₄ and filtered. The filtrate was concentrated *in vacuo* and the crude residue taken up in CH₂Cl₂ (2 mL) and hexane (2 mL). The resulting solution was concentrated under constant flow of air until a solid precipitated. The solid was filtered and washed with hexane to provide (4-fluoro-2-propylphenyl)(1H-pyrazol-4-yl)methanol (11 mg, 0.05 mmol, 56% yield) as a white solid.

IR (ν_{\max} , cm⁻¹) 3157, 1226, 1031

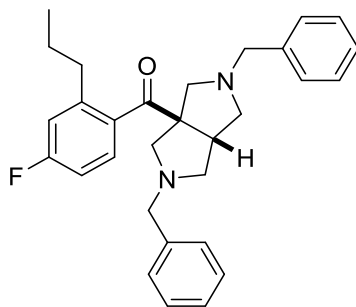
¹H NMR (500 MHz, Acetone-d₆) δ 7.61 (dd, $J = 8.3, 6.2$ Hz, 1H), 7.52 (d, $J = 1.9$ Hz, 1H), 6.97 – 6.88 (m, 2H), 6.13 (s, 1H), 6.04 (d, $J = 1.8$ Hz, 1H), 2.75 – 2.57 (m, 2H), 1.62 – 1.47 (m, 2H), 0.92 (t, $J = 7.3$ Hz, 3H)

¹³C NMR (126 MHz, Acetone-d₆) δ 170.92, 162.73 (d, $J = 242.6$ Hz), 143.27 (d, $J = 7.3$ Hz), 138.87 (d, $J = 2.8$ Hz), 132.82, 129.64 (d, $J = 8.3$ Hz), 116.08 (d, $J = 20.9$ Hz), 113.03 (d, $J = 21.0$ Hz), 103.37, 66.97, 34.86, 24.74, 14.31

¹⁹F NMR (471 MHz, Acetone-d₆) δ -117.96 – -118.12 (m)

HRMS (ESI) m/z [M-H] calcd for C₁₃H₁₄FN₂O 233.1090, found 233.1089.

(2,5-dibenzylhexahydropyrrolo[3,4-c]pyrrol-3a(1H)-yl)(4-fluoro-2-propylphenyl)methanone (3.61)



1-(4-Fluoro-2-propylphenyl)prop-2-yn-1-one (34 mg, 0.18 mmol) was added to a sealed microwave vial before adding CH_2Cl_2 (1 mL). The solution was then cooled to 0 °C and *N*-benzyl-1-methoxy-*N*-((trimethylsilyl)methyl)methanamine (214 mg, 0.9 mmol) and TFA (20 μL) were added. The reaction mixture was then warmed to room temperature and stirred for 16 hours before concentrating *in vacuo* to provide the crude product. The crude residue was then purified by flash chromatography, eluting with 0-30% EtOAc/petroleum ether to yield (2,5-dibenzylhexahydropyrrolo[3,4-c]pyrrol-3a(1H)-yl)(4-fluoro-2-propylphenyl)methanone (37.8 mg, 0.08 mmol, 46% yield) as a yellow oil.

IR (ν_{max} , cm^{-1}) 1681, 1236

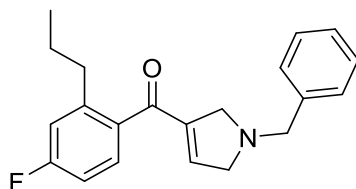
^1H NMR (400 MHz, CDCl_3) δ 7.38 (dd, $J = 8.6, 5.7$ Hz, 1H), 7.36 – 7.23 (m, 10H), 6.95 (dd, $J = 10.1, 2.5$ Hz, 1H), 6.85 (td, $J = 8.3, 2.5$ Hz, 1H), 3.70 – 3.56 (m, 4H), 3.23 – 3.13 (m, 1H), 2.91 (d, $J = 9.2$ Hz, 2H), 2.81 (t, $J = 8.1$ Hz, 2H), 2.75 (d, $J = 9.2$ Hz, 2H), 2.65 – 2.56 (m, 2H), 2.49 (dd, $J = 8.7, 4.7$ Hz, 2H), 1.62 (m, 2H), 0.96 (t, $J = 7.3$ Hz, 3H).

^{13}C NMR (101 MHz, CDCl_3) δ 209.16, 162.52 (d, $J = 249.1$ Hz), 143.84 (d, $J = 7.2$ Hz), 138.55, 134.88 (d, $J = 2.4$ Hz), 127.89, 127.72, 127.37 (d, $J = 8.8$ Hz), 126.41, 116.36 (d, $J = 20.8$ Hz), 111.41 (d, $J = 21.4$ Hz), 65.93, 63.04, 59.05, 58.61, 46.84, 34.90, 23.98, 13.54

^{19}F NMR (376 MHz, CDCl_3) δ -111.04 – -111.49 (m)

HRMS (ESI) m/z [M+H] calcd for $\text{C}_{30}\text{H}_{34}\text{FN}_2\text{O}$ 457.2655, found 457.2650.

(1-Benzyl-2,5-dihydro-1H-pyrrol-3-yl)(4-fluoro-2-propylphenyl)methanone (3.60)



1-(4-fluoro-2-propylphenyl)prop-2-yn-1-one (20 mg, 0.11 mmol) was added to a sealed microwave vial before adding CH_2Cl_2 (500 μL). The solution was then cooled to 0 °C and *N*-benzyl-1-methoxy-*N*-((trimethylsilyl)methyl)methanamine (25 mg, 0.11 mmol) and TFA (20 μL) were added. The reaction mixture was then warmed to room temperature and stirred for 16 hours before concentrating *in vacuo* to provide the crude product. The crude residue was then purified by flash chromatography, eluting with 0-40% EtOAc/petroleum ether to yield (1-benzyl-2,5-dihydro-1H-pyrrol-3-yl)(4-fluoro-2-propylphenyl)methanone (22 mg, 0.07 mmol, 62% yield) as a yellow oil.

IR (ν_{max} , cm^{-1}) 1635, 1031, 738

^1H NMR (500 MHz, CDCl_3) δ 7.34 – 7.18 (m, 6H), 6.90 (dd, $J = 10.0, 2.5$ Hz, 1H), 6.82 (td, $J = 8.3, 2.6$ Hz, 1H), 6.27 – 6.23 (m, 1H), 3.80 (s, 4H), 3.67 (s, 2H), 2.63 – 2.52 (m, 2H), 1.51 (dq, $J = 14.8, 7.4$ Hz, 2H), 0.85 (t, $J = 7.3$ Hz, 3H).

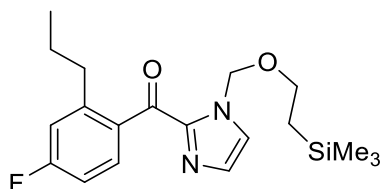
^{13}C NMR (126 MHz, CDCl_3) δ 193.35, 163.55 (d, $J = 250.2$ Hz), 144.82 (d, $J = 7.7$ Hz), 143.42, 143.16, 134.44 (d, $J = 2.4$ Hz), 130.33 (d, $J = 8.9$ Hz), 128.99, 128.75, 128.52, 127.34, 117.01 (d, $J = 21.1$ Hz), 111.99 (d, $J = 21.6$ Hz), 60.67, 60.08, 58.11, 35.04, 24.50, 13.93

^{19}F NMR (471 MHz, CDCl_3) δ -110.00 – -110.41 (m)

HRMS (ESI) m/z $[\text{M}+\text{H}-\text{H}_2]^+$ calcd for $\text{C}_{21}\text{H}_{21}\text{FNO}$ 322.1602, found 322.1610 (Possible aromatization of pyrroline)

6.3.4.3 Characterisation Data for Synthesis of Linker Analogues

(4-Fluoro-2-propylphenyl)(1-((2-(trimethylsilyl)ethoxy)methyl)-1*H*-imidazol-2-yl)methanone (3.62)



(4-Fluoro-2-propylphenyl)(1-((2-(trimethylsilyl)ethoxy)methyl)-1*H*-imidazol-2-yl)methanol (50 mg, 0.14 mmol) was added to a microwave vial with dichloromethane (2 mL) and 3 Å molecular sieves. Pyridinium dichromate (79 mg, 0.21 mmol) was then added and the reaction stirred for 16 hours. The reaction mixture was then concentrated *in vacuo* onto silica and purified by flash chromatography eluting with 0-30% ethyl acetate in petroleum ether (40-60 °C) to provide (4-fluoro-2-propylphenyl)(1-((2-(trimethylsilyl)ethoxy)methyl)-1*H*-imidazol-2-yl)methanone as a colourless oil (10 mg, 0.03 mmol, 20% yield).

IR (ν_{\max} , cm^{-1}) 1712, 1234, 1095

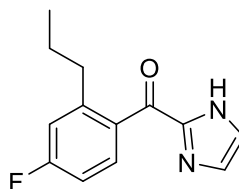
^1H NMR (500 MHz, CDCl_3) δ 7.61 (dd, $J = 8.5, 5.9$ Hz, 1H), 7.36 (s, 1H), 7.23 (s, 1H), 6.99 (dd, $J = 10.0, 2.5$ Hz, 1H), 6.94 (td, $J = 8.3, 2.6$ Hz, 1H), 5.87 (s, 2H), 3.69 – 3.61 (m, 2H), 2.70 (dd, $J = 8.7, 6.9$ Hz, 2H), 1.71 – 1.51 (m, 2H), 1.00 – 0.94 (m, 2H), 0.91 (t, $J = 7.3$ Hz, 3H), -0.01 (s, 9H)

^{13}C NMR (101 MHz, CDCl_3) δ 187.14, 164.13 (d, $J = 250.7$ Hz), 146.04 (d, $J = 7.8$ Hz), 143.69, 133.97 (d, $J = 2.6$ Hz), 132.73 (d, $J = 9.1$ Hz), 130.36, 124.94, 117.02 (d, $J = 21.4$ Hz), 112.24 (d, $J = 21.9$ Hz), 67.18, 35.48, 24.60, 18.05, 14.16, -1.33. One carbon not observed due to solvent peak.

^{19}F NMR (471 MHz, CDCl_3) δ -109.24 (ddd, $J = 10.1, 8.8, 6.5$ Hz)

HRMS (ESI) m/z $[\text{M}+\text{H}]$ calcd for $\text{C}_{19}\text{H}_{28}\text{FN}_2\text{O}_2\text{Si}$ 363.1904, found 363.1901.

(4-Fluoro-2-propylphenyl)(1H-imidazol-2-yl)methanone (3.13)



(4-Fluoro-2-propylphenyl)(1-((2-(trimethylsilyl)ethoxy)methyl)-1H-imidazol-2-yl)methanone (10 mg, 0.3 mmol) was added to a microwave vial as a solution in THF (1 mL). TBAF in THF (1 M, 1 mL) was then added and the reaction stirred for 16 hours. The reaction mixture was concentrated *in vacuo* and taken up in ethyl acetate (5 mL) before washing with brine (3x 5 mL), drying with Na₂SO₄ and filtering. The organics were then concentrated onto silica and purified by flash chromatography, eluting with 0-100% ethyl acetate in petroleum ether (40-60 °C) to provide (4-fluoro-2-propylphenyl)(1H-imidazol-2-yl)methanone (2.4 mg, 0.01 mmol, 33% yield) as a pale yellow oil.

IR (ν_{\max} , cm⁻¹) 3367, 1701, 1641, 1232

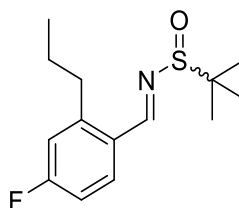
¹H NMR (600 MHz, Acetone-d₆) δ 8.04 (dd, $J = 8.6, 6.1$ Hz, 1H), 7.50 (s, 1H), 7.25 (s, 1H), 7.12 (dd, $J = 10.2, 2.6$ Hz, 1H), 7.07 (td, $J = 8.5, 2.6$ Hz, 1H), 2.81 – 2.76 (m, 2H), 1.64 – 1.56 (m, 2H), 0.88 (t, $J = 7.3$ Hz, 3H)

¹³C NMR (126 MHz, Acetone-d₆) δ 185.38, 164.55 (d, $J = 248.3$ Hz), 146.94 (d, $J = 8.1$ Hz), 146.48, 134.82 (d, $J = 2.8$ Hz), 134.49 (d, $J = 9.0$ Hz), 131.46, 123.18, 117.34 (d, $J = 21.3$ Hz), 112.45 (d, $J = 21.4$ Hz), 36.03, 25.45, 14.33

¹⁹F NMR (471 MHz, Acetone-d₆) δ -111.92 (ddd, $J = 9.5, 7.8, 6.0$ Hz)

HRMS (ESI) m/z [M+H] calcd for C₁₃H₁₄FN₂O 233.1085, found 233.1087.

(±)-N-(4-Fluoro-2-propylbenzylidene)-2-methylpropane-2-sulfinamide (3.64)



4-Fluoro-2-propylbenzaldehyde (75.3 mg, 0.45 mmol) was added to a round bottom flask as a solution in CH₂Cl₂ (5 mL) along with titanium ethoxide (476 μL, 2.3 mmol, 5 eq.). 2-methylpropane-2-sulfinamide (54.5 mg, 0.45 mmol, 1 eq.) was then added slowly and the reaction mixture stirred for 12 hours at room temperature. A saturated solution of sodium bicarbonate was added to the reaction mixture until a solid precipitated, which was filtered off on a pad of celite before washing with CH₂Cl₂. The organics were concentrated *in vacuo* and the resulting residue taken up in ethyl acetate (10 mL) and washed with brine. Organics were dried (Na₂SO₄), filtered and concentrated to yield (±)-N-(4-fluoro-2-propylbenzylidene)-2-methylpropane-2-sulfinamide (60 mg, 0.22 mmol, 50% yield) as an amorphous solid.

IR (ν_{\max} , cm⁻¹) 1587, 1247

¹H NMR (500 MHz, CDCl₃) δ 8.74 (s, 1H), 7.90 (dd, $J = 8.6, 6.1$ Hz, 1H), 6.94 – 6.87 (m, 2H), 3.00 – 2.66 (m, 2H), 1.62 – 1.52 (m, 2H), 1.19 (s, 9H), 0.91 (t, $J = 7.3$ Hz, 3H)

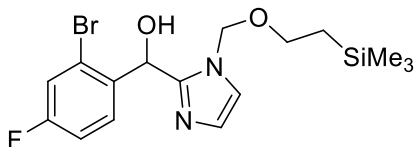
¹³C NMR (101 MHz, CDCl₃) δ 164.39 (d, $J = 253.7$ Hz), 159.63, 146.73 (d, $J = 8.3$ Hz), 131.28 (d, $J = 9.3$ Hz), 127.71 (d, $J = 2.5$ Hz), 116.58 (d, $J = 21.1$ Hz), 113.29 (d, $J = 22.1$ Hz), 57.15, 34.18, 24.33, 22.07, 13.29

¹⁹F NMR (471 MHz, CDCl₃) δ -107.30 (ddd, $J = 9.3, 8.1, 6.4$ Hz)

HRMS (ESI) m/z [M-H+H₂SO₄]⁻ calcd for C₁₄H₁₉FNO₅S₂ 366.0851, found 366.1815

6.3.4.4 Characterisation Data for Synthesis of Propyl Analogues

Synthesis of (2-bromo-4-fluorophenyl)(1-((2-(trimethylsilyl)ethoxy)methyl)-1*H*-imidazol-2-yl)methanol (3.65)



Prepared according to **General Procedure C** using 1-((2-(trimethylsilyl)ethoxy)methyl)-1*H*-imidazole (198 mg, 1.0 mmol), THF (2 mL), ⁿBuLi (560 μL, 1.1 mmol) and 2-bromo-4-fluorobenzaldehyde (244 mg, 1.2 mmol) in THF (2 mL). The crude residue was purified by flash chromatography, eluting in 0-50% EtOAc in petroleum ether to afford (2-bromo-4-fluorophenyl)(1-((2-(trimethylsilyl)ethoxy)methyl)-1*H*-imidazol-2-yl)methanol (261 mg, 65% yield) as a yellow oil.

IR (ν_{\max} , cm⁻¹) 3134, 1249, 1220, 1095, 750

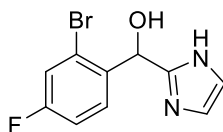
¹H NMR (500 MHz, CDCl₃) δ 7.59 (dd, J = 8.7, 6.1 Hz, 1H), 7.30 (dd, J = 8.1, 2.5 Hz, 1H), 7.03 (td, J = 8.4, 2.5 Hz, 1H), 6.96 (s, 1H), 6.83 (s, 1H), 6.20 (s, 1H), 5.28 (d, J = 10.8 Hz, 1H), 5.19 (d, J = 10.8 Hz, 1H), 3.39 (t, J = 8.4 Hz, 2H), 0.93 – 0.76 (m, 2H), -0.00 (s, 9H)

¹³C NMR (126 MHz, CDCl₃) δ 163.24 (d, J = 250.8 Hz), 149.75, 137.78 (d, J = 3.3 Hz), 131.69 (d, J = 8.4 Hz), 128.60, 124.24 (d, J = 9.6 Hz), 121.91, 121.23 (d, J = 24.5 Hz), 116.17 (d, J = 20.8 Hz), 76.55, 68.63, 67.76, 19.20, -0.01

¹⁹F NMR (471 MHz, CDCl₃) δ -112.45 – -112.55 (m)

HRMS (ESI) m/z [M+H] calcd for C₁₆H₂₃BrFN₂O₂Si 401.0691, found 401.0690 and 403.0667

(2-Bromo-4-fluorophenyl)(1H-imidazol-2-yl)methanol (3.16)



Prepared according to **General Procedure D** using (2-bromo-4-fluorophenyl)(1-((2-(trimethylsilyl)ethoxy)methyl)-1H-imidazol-2-yl)methanol (160 mg, 0.40 mmol), CH₂Cl₂ (2 mL) and TFA (2 mL). The crude was then diluted in CH₂Cl₂ (2 mL) and hexane (2 mL) and concentrated under a constant flow of air until a solid crashed out. The solid was filtered off and washed with hexane to yield (2-bromo-4-fluorophenyl)(1H-imidazol-2-yl)methanol (72 mg, 0.25 mmol, 63% yield) as a white solid.

IR (ν_{\max} , cm⁻¹) 3184, 1219, 744

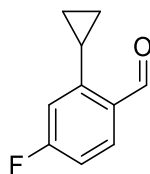
¹H NMR (500 MHz, DMSO) δ 111.95 (s, 1H), 7.70 – 7.61 (m, 1H), 7.50 (dd, $J = 8.5, 2.1$ Hz, 1H), 7.29 (dd, $J = 11.7, 5.3$ Hz, 1H), 6.88 (s, 2H), 6.32 (s, 1H), 5.95 (s, 1H)

¹³C NMR (126 MHz, DMSO) δ 161.38 (d, $J = 247.4$ Hz), 148.82, 138.98 (d, $J = 3.1$ Hz), 130.85 (d, $J = 8.6$ Hz), 122.48 (d, $J = 9.8$ Hz), 119.43 (d, $J = 24.5$ Hz), 115.11 (d, $J = 20.8$ Hz), 68.33. C₄ and C₅ of imidazole not observed due to peak broadening.

¹⁹F NMR (471 MHz, DMSO) δ -113.56 – -113.68 (m)

HRMS (ESI) m/z [M+H] calcd for C₁₀H₉BrFN₂O 270.9882, found 270.9884 and 272.9863

2-Cyclopropyl-4-fluorobenzaldehyde (3.80)²¹³



Prepared according to **General Procedure A** using 2-bromo-4-fluorobenzaldehyde (203 mg, 1.0 mmol), cyclopropylboronic acid (129 mg, 1.5 mmol), caesium carbonate (977 mg, 3.0 mmol) and [1,1'-Bis(diphenylphosphino)ferrocene]-dichloropalladium(II) (82 mg, 0.1 mmol) in dioxane (1600 μ L) and water (400 μ L). The crude residue was purified by flash chromatography, eluting with 0-30% CH_2Cl_2 /petroleum ether, yielding 2-cyclopropyl-4-fluorobenzaldehyde (127 mg, 0.77 mmol, 77% yield) as a pale yellow oil.

IR (ν_{max} , cm^{-1}) 2926, 2870, 1236

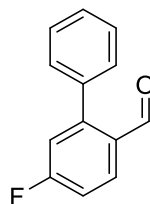
^1H NMR (500 MHz, CDCl_3) δ 10.43 (s, 1H), 7.77 (dd, $J = 8.6, 6.1$ Hz, 1H), 6.91 (td, $J = 8.3, 2.5$ Hz, 1H), 6.70 (dd, $J = 10.2, 2.4$ Hz, 1H), 2.73 – 2.49 (m, 1H), 1.16 – 0.93 (m, 2H), 0.80 – 0.64 (m, 2H)

^{13}C NMR (126 MHz, CDCl_3) δ 191.11, 166.47 (d, $J = 255.7$ Hz), 150.04 (d, $J = 9.1$ Hz), 133.32 (d, $J = 10.3$ Hz), 131.67 (d, $J = 2.6$ Hz), 113.58 (d, $J = 22.0$ Hz), 113.50 (d, $J = 22.4$ Hz), 11.91, 9.13

^{19}F NMR (471 MHz, CDCl_3) δ -103.37 – -103.57 (m)

HRMS (ESI) m/z $[\text{M}-\text{H}]^+$ calcd for $\text{C}_{10}\text{H}_8\text{FO}$ 163.0559, found 163.0563

5-Fluoro-[1,1'-biphenyl]-2-carbaldehyde (3.82)²¹⁴



Prepared according to **General Procedure A** using 2-bromo-4-fluorobenzaldehyde (102 mg, 0.5 mmol), phenylboronic acid (122 mg, 1 mmol), caesium carbonate (489 mg, 1.5 mmol) and [1,1'-Bis(diphenylphosphino)ferrocene]-dichloropalladium(II) (40.8 mg, 0.05 mmol) in dioxane (800 μ L) and water (200 μ L). The crude residue was purified by flash chromatography, eluting with 0-20% CH_2Cl_2 /petroleum ether, yielding 5-fluoro-[1,1'-biphenyl]-2-carbaldehyde (76 mg, 0.38 mmol, 76% yield) as a pale yellow oil.

IR (ν_{max} , cm^{-1}) 3129, 2926, 2852, 1685, 1602, 1570, 1271

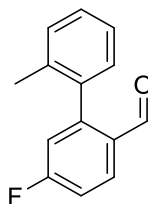
^1H NMR (500 MHz, CDCl_3) δ 9.78 (s, 1H), 7.95 (dd, $J = 8.7, 6.0$ Hz, 1H), 7.40 – 7.32 (m, 3H), 7.30 – 7.21 (m, 2H), 7.06 (td, $J = 8.2, 2.0$ Hz, 1H), 7.01 (dd, $J = 9.3, 2.4$ Hz, 1H).

^{13}C NMR (126 MHz, CDCl_3) δ 190.66, 165.46 (d, $J = 256.6$ Hz), 148.80 (d, $J = 9.3$ Hz), 136.60, 130.62 (d, $J = 10.0$ Hz), 130.37 (d, $J = 2.7$ Hz), 129.89, 128.66, 128.61, 117.42 (d, $J = 22.0$ Hz), 115.29 (d, $J = 22.0$ Hz)

^{19}F NMR (471 MHz, CDCl_3) δ -103.63 (td, $J = 8.2, 6.5$ Hz)

HRMS (ESI) m/z $[\text{M}+\text{H}]$ calcd for $\text{C}_{13}\text{H}_{10}\text{FO}$ 201.0710, found 201.0713

5-Fluoro-2'-methyl-[1,1'-biphenyl]-2-carbaldehyde (3.83)²¹⁵



Prepared according to **General Procedure A** using 2-bromo-4-fluorobenzaldehyde (203 mg, 1 mmol), o-tolylboronic acid (204 mg, 1.5 mmol), caesium carbonate (977.5 mg, 3 mmol) and [1,1'-Bis(diphenylphosphino)ferrocene]-dichloropalladium(II) (82 mg, 0.1 mmol) in dioxane (1600 μ L) and water (400 μ L). The crude residue was purified by flash chromatography, eluting with 0-20% CH_2Cl_2 /petroleum ether, yielding 5-fluoro-[1,1'-biphenyl]-2-carbaldehyde (118 mg, 0.55 mmol, 55% yield) as a pale yellow oil.

IR (ν_{max} , cm^{-1}) 2954, 2848, 1693, 1606, 1577, 1269

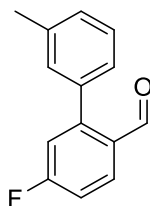
^1H NMR (500 MHz, CDCl_3) δ 9.55 (s, 1H), 7.95 (dd, $J = 8.7, 6.0$ Hz, 1H), 7.27 – 7.14 (m, 3H), 7.10 – 7.04 (m, 2H), 6.89 (dd, $J = 9.1, 2.5$ Hz, 1H), 2.01 (s, 3H)

^{13}C NMR (126 MHz, CDCl_3) δ 189.48, 164.62 (d, $J = 257.4$ Hz), 147.49 (d, $J = 9.2$ Hz), 135.24, 134.94, 129.54 (d, $J = 2.8$ Hz), 129.22, 129.05 (d, $J = 10.0$ Hz), 128.87, 127.69, 124.80, 116.51 (d, $J = 21.6$ Hz), 114.36 (d, $J = 21.9$ Hz), 19.14

^{19}F NMR (471 MHz, CDCl_3) δ -103.39 (td, $J = 8.5, 6.1$ Hz)

HRMS (ESI) m/z $[\text{M}+\text{H}]$ calcd for $\text{C}_{14}\text{H}_{12}\text{FO}$ 215.0867, found 215.0872

5-Fluoro-3'-methyl-[1,1'-biphenyl]-2-carbaldehyde (3.84)



Prepared according to **General Procedure A** using 2-bromo-4-fluorobenzaldehyde (203 mg, 1 mmol), *m*-tolylboronic acid (204 mg, 1.5 mmol), caesium carbonate (977.5 mg, 3 mmol) and [1,1'-Bis(diphenylphosphino)ferrocene]-dichloropalladium(II) (82 mg, 0.1 mmol) in dioxane (1600 μ L) and water (400 μ L). The crude residue was purified by flash chromatography, eluting with 0-20% CH_2Cl_2 /petroleum ether, yielding 5-fluoro-[1,1'-biphenyl]-2-carbaldehyde (146 mg, 0.68 mmol, 68% yield) as a pale yellow oil.

IR (ν_{max} , cm^{-1}) 3035, 2920, 2850, 1689, 1602, 1573, 1274

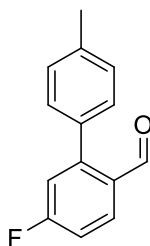
^1H NMR (500 MHz, CDCl_3) δ 9.79 (s, 1H), 7.94 (dd, $J = 8.6, 6.0$ Hz, 1H), 7.25 (t, $J = 7.6$ Hz, 1H), 7.16 (d, $J = 7.7$ Hz, 1H), 7.09 – 6.98 (m, 4H), 2.31 (s, 3H).

^{13}C NMR (126 MHz, CDCl_3) δ 189.77, 164.39 (d, $J = 256.6$ Hz), 147.97 (d, $J = 9.2$ Hz), 137.34, 135.50, 129.53, 129.45 (d, $J = 10.1$ Hz), 129.33 (d, $J = 2.7$ Hz), 128.33, 127.42, 126.01, 116.30 (d, $J = 22.0$ Hz), 114.11 (d, $J = 21.9$ Hz), 20.34

^{19}F NMR (471 MHz, CDCl_3) δ -103.77 (td, $J = 8.7, 6.1$ Hz)

HRMS (ESI) m/z $[\text{M}+\text{H}]$ calcd for $\text{C}_{14}\text{H}_{12}\text{FO}$ 215.0867, found 215.0871

5-Fluoro-4'-methyl-[1,1'-biphenyl]-2-carbaldehyde (3.85)²¹⁵



Prepared according to **General Procedure A** using 2-bromo-4-fluorobenzaldehyde (203 mg, 1 mmol), *p*-tolylboronic acid (204 mg, 1.5 mmol), caesium carbonate (977.5 mg, 3 mmol) and [1,1'-bis(diphenylphosphino)ferrocene]-dichloropalladium(II) (82 mg, 0.1 mmol) in dioxane (1600 μ L) and water (400 μ L). The crude residue was purified by flash chromatography, eluting with 0-20% CH_2Cl_2 /petroleum ether, yielding 5-fluoro-4'-methyl-[1,1'-biphenyl]-2-carbaldehyde (112 mg, 0.52 mmol, 52% yield) as a pale yellow oil.

IR (ν_{max} , cm^{-1}) 2922, 2850, 1687, 1602, 1587, 1269

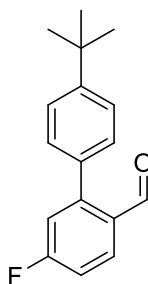
^1H NMR (500 MHz, CDCl_3) δ 9.79 (s, 1H), 7.94 (dd, $J = 8.6, 6.0$ Hz, 1H), 7.20 – 7.12 (m, 4H), 7.06 – 6.97 (m, 2H), 2.32 (s, 3H)

^{13}C NMR (126 MHz, CDCl_3) δ 190.87, 165.48 (d, $J = 256.3$ Hz), 148.88 (d, $J = 9.2$ Hz), 138.68, 133.68, 130.60 (d, $J = 10.0$ Hz), 130.40 (d, $J = 2.6$ Hz), 129.82, 129.32, 117.36 (d, $J = 21.9$ Hz), 115.06 (d, $J = 22.0$ Hz), 21.19

^{19}F NMR (471 MHz, CDCl_3) δ -103.81 (dd, $J = 8.4, 6.2$ Hz)

HRMS (ESI) m/z $[\text{M}+\text{H}]$ calcd for $\text{C}_{14}\text{H}_{12}\text{FO}$ 215.0867, found 215.0869

4'-(tert-Butyl)-5-fluoro-[1,1'-biphenyl]-2-carbaldehyde (3.86)



Prepared according to **General Procedure A** using 2-bromo-4-fluorobenzaldehyde (203 mg, 1 mmol), (4-(*tert*-butyl)phenyl)boronic acid (267 mg, 1.5 mmol), caesium carbonate (977.5 mg, 3 mmol) and [1,1'-Bis(diphenylphosphino)ferrocene]-dichloropalladium(II) (82 mg, 0.1 mmol) in dioxane (1600 μ L) and water (400 μ L). The crude residue was purified by flash chromatography, eluting with 0-20% CH_2Cl_2 /petroleum ether, yielding 4'-(*tert*-butyl)-5-fluoro-[1,1'-biphenyl]-2-carbaldehyde (256 mg, 0.50 mmol, 50% yield) as a pale yellow oil.

IR (ν_{max} , cm^{-1}) 2966, 2860, 1680, 1602, 1577, 1269

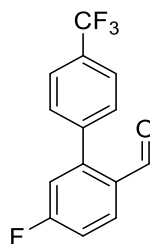
^1H NMR (500 MHz, CDCl_3) δ 9.82 (s, 1H), 7.96 (dd, $J = 8.5, 6.0$ Hz, 1H), 7.41 (d, $J = 8.2$ Hz, 2H), 7.21 (d, $J = 8.2$ Hz, 2H), 7.08 – 7.01 (m, 2H), 1.28 (s, 9H).

^{13}C NMR (126 MHz, CDCl_3) δ 190.98, 165.49 (d, $J = 256.3$ Hz), 151.86, 148.88 (d, $J = 9.4$ Hz), 133.62, 130.54 (d, $J = 10.0$ Hz), 130.44 (d, $J = 2.5$ Hz), 129.70, 125.58, 117.36 (d, $J = 21.9$ Hz), 115.06 (d, $J = 22.0$ Hz), 34.73, 31.31

^{19}F NMR (471 MHz, CDCl_3) δ -103.83 (td, $J = 8.5, 6.3$ Hz)

HRMS (ESI) m/z [M+H] calcd for $\text{C}_{17}\text{H}_{18}\text{FO}$ 257.1342, found 257.1340

5-Fluoro-4'-(trifluoromethyl)-[1,1'-biphenyl]-2-carbaldehyde (3.87)²¹⁶



Prepared according to **General Procedure A** using 2-bromo-4-fluorobenzaldehyde (203 mg, 1 mmol), (4-(trifluoromethyl)phenyl)boronic acid (285 mg, 1.5 mmol), caesium carbonate (977.5 mg, 3 mmol) and [1,1'-Bis(diphenylphosphino)ferrocene]-dichloropalladium(II) (82 mg, 0.1 mmol) in dioxane (1600 μ L) and water (400 μ L). The crude residue was purified by flash chromatography, eluting with 0-40% CH_2Cl_2 /petroleum ether, yielding 5-fluoro-4'-(trifluoromethyl)-[1,1'-biphenyl]-2-carbaldehyde (256 mg, 0.50 mmol, 50% yield) as a pale yellow oil.

IR (ν_{max} , cm^{-1}) 3128, 3053, 2858, 2763, 1687, 1602, 1571, 1321, 1274

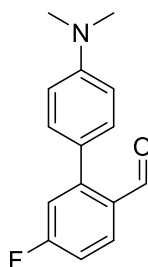
^1H NMR (500 MHz, CDCl_3) δ 9.86 (s, 1H), 8.08 (dd, $J = 8.7, 5.9$ Hz, 1H), 7.76 (d, $J = 8.1$ Hz, 2H), 7.52 (d, $J = 8.0$ Hz, 2H), 7.23 (td, $J = 8.3, 2.3$ Hz, 1H), 7.12 (dd, $J = 9.0, 2.5$ Hz, 1H)

^{13}C NMR (126 MHz, CDCl_3) δ 189.77, 165.49 (d, $J = 257.6$ Hz), 146.95 (d, $J = 8.6$ Hz), 140.37, 131.20 (d, $J = 9.7$ Hz), 130.90 (q, $J = 32.9$ Hz), 130.34, 130.18, 125.59, 123.92 (q, $J = 272.5$ Hz), 117.50 (d, $J = 22.4$ Hz), 116.04 (d, $J = 21.8$ Hz)

^{19}F NMR (471 MHz, CDCl_3) δ -62.72 (s), -103.01 (td, $J = 8.5, 6.0$ Hz)

LCMS (ESI) m/z $[\text{M}+\text{O}-\text{H}]^-$ calcd for $\text{C}_{14}\text{H}_7\text{F}_4\text{O}_2$ 283.0, found 283.0

4'-(Dimethylamino)-5-fluoro-[1,1'-biphenyl]-2-carbaldehyde (3.88)²¹⁷



Prepared according to **General Procedure A** using 2-bromo-4-fluorobenzaldehyde (203 mg, 1 mmol), (4-(dimethylamino)phenyl)boronic acid (248 mg, 1.5 mmol), caesium carbonate (977.5 mg, 3 mmol) and [1,1'-Bis(diphenylphosphino)ferrocene]-dichloropalladium(II) (82 mg, 0.1 mmol) in dioxane (1600 μ L) and water (400 μ L). The crude residue was purified by flash chromatography, eluting with 0-40% CH_2Cl_2 /petroleum ether, yielding 4'-(dimethylamino)-5-fluoro-[1,1'-biphenyl]-2-carbaldehyde (82 mg, 0.34 mmol, 34% yield) as a brown oil.

IR (ν_{max} , cm^{-1}) 2850, 1683, 1602, 1581, 1271, 1192

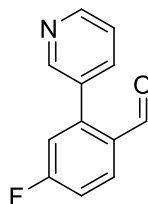
^1H NMR (500 MHz, CDCl_3) δ 9.97 (s, 1H), 8.04 (dd, $J = 8.6, 6.1$ Hz, 1H), 7.31 – 7.19 (m, 2H), 7.22 – 7.01 (m, 2H), 6.82 (d, $J = 8.7$ Hz, 2H), 3.06 (s, 6H)

^{13}C NMR (126 MHz, CDCl_3) δ 191.52, 165.55 (d, $J = 255.6$ Hz), 150.62, 149.27 (d, $J = 9.5$ Hz), 130.98, 130.62 (d, $J = 10.1$ Hz), 130.26 (d, $J = 2.5$ Hz), 123.95, 116.95 (d, $J = 21.4$ Hz), 114.21 (d, $J = 22.1$ Hz), 112.04, 40.32

^{19}F NMR (471 MHz, CDCl_3) δ -104.31 (ddd, $J = 9.5, 7.8, 6.1$ Hz)

LCMS (ESI) m/z $[\text{M}+\text{H}]^+$ calcd for $\text{C}_{15}\text{H}_{15}\text{FNO}$ 244.11, found 244.2

Synthesis of 4-fluoro-2-(pyridin-3-yl)benzaldehyde (3.89)²¹⁸



Prepared according to **General Procedure A** using 2-bromo-4-fluorobenzaldehyde (203 mg, 1 mmol), pyridin-3-ylboronic acid (184 mg, 1.5 mmol), caesium carbonate (977.5 mg, 3 mmol) and [1,1'-Bis(diphenylphosphino)ferrocene]-dichloropalladium(II) (82 mg, 0.1 mmol) in dioxane (1600 μ L) and water (400 μ L). The crude residue was purified by flash chromatography, eluting with 0-40% CH_2Cl_2 /petroleum ether, yielding 4-fluoro-2-(pyridin-3-yl)benzaldehyde (134 mg, 0.67 mmol, 67% yield) as a brown oil.

IR (ν_{max} , cm^{-1}) 3066, 1674, 1604, 1581, 1273, 1199

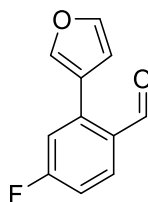
^1H NMR (500 MHz, CDCl_3) δ 9.92 (s, 1H), 8.76 (d, $J = 4.0$ Hz, 1H), 8.70 (s, 1H), 8.13 (dd, $J = 8.7, 5.9$ Hz, 1H), 7.77 (dt, $J = 7.8, 1.8$ Hz, 1H), 7.49 (dd, $J = 7.7, 4.9$ Hz, 1H), 7.29 (td, $J = 8.3, 2.4$ Hz, 1H), 7.15 (dd, $J = 8.9, 2.5$ Hz, 1H)

^{13}C NMR (126 MHz, CDCl_3) δ 189.55, 165.58 (d, $J = 258.2$ Hz), 149.44, 149.40, 144.27 (d, $J = 9.2$ Hz), 137.45, 132.89, 131.87 (d, $J = 10.0$ Hz), 130.47 (d, $J = 2.7$ Hz), 123.42, 117.92 (d, $J = 22.5$ Hz), 116.30 (d, $J = 21.7$ Hz)

^{19}F NMR (471 MHz, CDCl_3) δ -102.56 (td, $J = 8.3, 6.3$ Hz)

LCMS (ESI) m/z $[\text{M}+\text{H}]^+$ calcd for $\text{C}_{12}\text{H}_9\text{FNO}$ 202.07, found 202.2

4-Fluoro-2-(furan-3-yl)benzaldehyde (3.90)²¹⁹



Prepared according to **General Procedure A** using 2-bromo-4-fluorobenzaldehyde (203 mg, 1 mmol), furan-3-ylboronic acid (333 mg, 3.0 mmol), caesium carbonate (977.5 mg, 3 mmol) and [1,1'-Bis(diphenylphosphino)ferrocene]-dichloropalladium(II) (82 mg, 0.1 mmol) in dioxane (1600 μ L) and water (400 μ L). The crude residue was purified by flash chromatography, eluting with 0-40% CH_2Cl_2 /petroleum ether, yielding 4-fluoro-2-(furan-3-yl)benzaldehyde (125 mg, 0.66 mmol, 66% yield) as a brown oil.

IR (ν_{max} , cm^{-1}) 3128, 2858, 1685, 1600, 1573, 1284

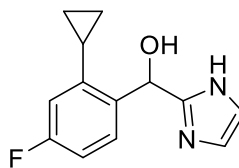
^1H NMR (500 MHz, CDCl_3) δ 10.14 (s, 1H), 8.02 (dd, $J = 8.6, 6.5$ Hz, 1H), 7.61 – 7.50 (m, 2H), 7.18 – 7.08 (m, 2H), 6.58 (m, 1H).

^{13}C NMR (126 MHz, CDCl_3) δ 190.46 (s), 165.78 (d, $J = 256.4$ Hz), 143.83 (s), 141.49 (s), 139.26 (d, $J = 9.9$ Hz), 130.90 (d, $J = 10.1$ Hz), 130.58 (d, $J = 2.9$ Hz), 121.67 (s), 117.11 (d, $J = 22.2$ Hz), 115.31 (d, $J = 21.9$ Hz), 111.94 (s).

^{19}F NMR (471 MHz, CDCl_3) δ -103.54 (td, $J = 8.5, 6.1$ Hz)

LCMS (ESI) product did not ionise

(2-Cyclopropyl-4-fluorophenyl)(1*H*-imidazol-2-yl)methanol (3.17)



Prepared according to **General Procedure E** using 1-((2-(trimethylsilyl)ethoxy)methyl)-1*H*-imidazole (99 mg, 0.5 mmol), THF (1 mL), ⁿBuLi (254 μL, 0.5 mmol) and 2-cyclopropyl-4-fluorobenzaldehyde (90 mg, 0.55 mmol) as a solution in THF (1 mL). The deprotection was performed in a microwave vial with the crude, CH₂Cl₂ (2 mL) and TFA (2 mL), yielding (2-cyclopropyl-4-fluorophenyl)(1*H*-imidazol-2-yl)methanol (25 mg, 0.13 mmol, 26% yield) as a white solid.

IR (ν_{max} , cm⁻¹) 3190, 2802, 2657, 1282

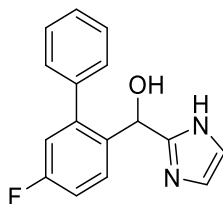
¹H NMR (500 MHz, DMSO) δ 11.89 (s, 1H), 7.55 (dd, $J = 8.6, 6.3$ Hz, 1H), 7.03 (td, $J = 8.6, 2.7$ Hz, 2H), 6.81 (s, 1H), 6.78 (dd, $J = 10.7, 2.7$ Hz, 1H), 6.23 (d, $J = 3.8$ Hz, 1H), 6.12 (d, $J = 4.2$ Hz, 1H), 2.25 – 2.15 (m, 1H), 1.03 – 0.94 (m, 1H), 0.90 – 0.83 (m, 1H), 0.77 (td, $J = 10.0, 5.5$ Hz, 1H), 0.59 (td, $J = 9.5, 5.7$ Hz, 1H)

¹³C NMR (126 MHz, DMSO) δ 162.00 (d, $J = 241.9$ Hz), 150.22, 143.32 (d, $J = 7.6$ Hz), 139.10 (d, $J = 2.7$ Hz), 128.66 (d, $J = 8.5$ Hz), 127.41, 116.26, 112.33 (d, $J = 20.9$ Hz), 111.81 (d, $J = 21.7$ Hz), 66.26, 12.63, 8.68, 7.40

¹⁹F NMR (471 MHz, DMSO) δ -115.84 – -115.96 (m)

HRMS (ESI) m/z [M+H]⁺ calcd for C₁₃H₁₄FN₂O 233.1085, found 233.1085

(5-Fluoro-[1,1'-biphenyl]-2-yl)(1*H*-imidazol-2-yl)methanol (3.21)



Prepared according to **General Procedure E** using 1-((2-(trimethylsilyl)ethoxy)methyl)-1*H*-imidazole (99 mg, 0.5 mmol), THF (1 mL), ⁿBuLi (254 μ L, 0.5 mmol) and 5-fluoro-[1,1'-biphenyl]-2-carbaldehyde (110 mg, 0.55 mmol) as a solution in THF (1 mL). The deprotection was performed in a microwave vial with the crude, CH₂Cl₂ (2 mL) and TFA (2 mL), yielding (5-fluoro-[1,1'-biphenyl]-2-yl)(1*H*-imidazol-2-yl)methanol (34 mg, 0.13 mmol, 26% yield) as a white solid.

IR (ν_{max} , cm⁻¹) 3215, 2546, 1296

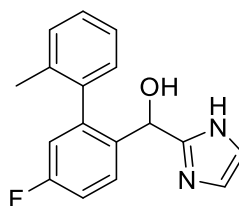
¹H NMR (500 MHz, DMSO) δ 12.16 (s, 1H), 7.67 – 7.58 (m, 3H), 7.56 – 7.44 (m, 3H), 7.27 (td, J = 8.6, 2.7 Hz, 1H), 7.11 (dd, J = 9.9, 2.7 Hz, 1H), 6.97 (s, 2H), 6.13 (d, J = 4.0 Hz, 1H), 5.77 (d, J = 4.0 Hz, 1H)

¹³C NMR (126 MHz, DMSO) δ 161.25 (d, J = 243.8 Hz), 150.57, 142.66 (d, J = 7.7 Hz), 139.55, 137.44 (d, J = 3.0 Hz), 130.89 (d, J = 8.6 Hz), 129.92, 128.65, 128.05, 116.05 (d, J = 21.3 Hz), 114.82 (d, J = 21.1 Hz), 65.96. C₄ and C₅ of imidazole not observed due to peak broadening.

¹⁹F NMR (471 MHz, DMSO) -115.39 – -115.48 (m)

HRMS (ESI) m/z [M+H]⁺ calcd for C₁₆H₁₄FN₂O 269.1085, found 269.1084

(5-Fluoro-2'-methyl-[1,1'-biphenyl]-2-yl)(1*H*-imidazol-2-yl)methanol (3.24)



Prepared according to **General Procedure E** using 1-((2-(trimethylsilyl)ethoxy)methyl)-1*H*-imidazole (99 mg, 0.5 mmol), THF (1 mL), ⁿBuLi (254 μL, 0.5 mmol) and 5-fluoro-2'-methyl-[1,1'-biphenyl]-2-carbaldehyde (118 mg, 0.55 mmol) as a solution in THF (1 mL). The deprotection was performed in a microwave vial with the crude, CH₂Cl₂ (2 mL) and TFA (2 mL), yielding (5-fluoro-2'-methyl-[1,1'-biphenyl]-2-yl)(1*H*-imidazol-2-yl)methanol (11 mg, 0.04 mmol, 8% yield) as a white solid.

IR (ν_{\max} , cm⁻¹) 3347, 1618, 1570, 1242

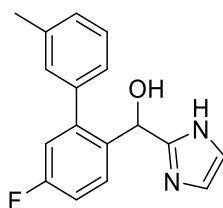
¹H NMR (500 MHz, DMSO) δ 11.78 (m, 1H), 7.61 (m, 1H), 7.34 – 6.87 (m, 8H), 5.91 (m, 0.5H), 5.86 (m, 0.5H), 5.37 (m, 0.5H), 5.33 (m, 0.5H), 2.11 (s, 1.5H), 1.90 (s, 1.5H)

¹³C NMR (126 MHz, Acetone-d₆) δ 160.66 (d, $J = 243.7$ Hz), 149.86, 149.42, 141.37 (d, $J = 7.8$ Hz), 138.89, 138.67, 137.32 (d, $J = 2.8$ Hz), 137.26 (d, $J = 3.0$ Hz), 136.19, 135.15, 130.02 (d, $J = 8.7$ Hz), 129.86, 129.73, 128.92, 127.68, 127.63, 125.27, 125.19, 115.34 (d, $J = 20.6$ Hz), 114.18 (d, $J = 21.6$ Hz), 65.82, 65.78, 19.93, 19.72

¹⁹F NMR (471 MHz, DMSO) δ -115.85 (td, $J = 9.1, 6.4$ Hz), -115.99 (td, $J = 9.1, 6.4$ Hz)

HRMS (ESI) m/z [M+H]⁺ calcd for C₁₇H₁₆FN₂O 283.1247, found 283.1246

(5-Fluoro-3'-methyl-[1,1'-biphenyl]-2-yl)(1*H*-imidazol-2-yl)methanol (3.25)



Prepared according to **General Procedure E** using 1-((2-(trimethylsilyl)ethoxy)methyl)-1*H*-imidazole (111 mg, 0.56 mmol), THF (1 mL), ⁿBuLi (284 μL, 0.56 mmol) and 5-fluoro-3'-methyl-[1,1'-biphenyl]-2-carbaldehyde (107 mg, 0.50 mmol) as a solution in THF (1 mL). The deprotection was performed in a microwave vial with the crude, CH₂Cl₂ (2 mL) and TFA (2 mL), yielding (5-fluoro-3'-methyl-[1,1'-biphenyl]-2-yl)(1*H*-imidazol-2-yl)methanol (30 mg, 0.11 mmol, 22% yield) as a white solid.

IR (ν_{\max} , cm⁻¹) 3213, 1680, 1209

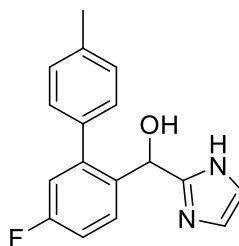
¹H NMR (400 MHz, DMSO) δ 11.95 (s, 1H), 7.58 (dd, $J = 8.7, 6.1$ Hz, 1H), 7.37 – 7.25 (m, 3H), 7.25 – 7.15 (m, 2H), 7.02 (dd, $J = 10.0, 2.8$ Hz, 2H), 6.78 (s, 1H), 6.02 (s, 1H), 5.69 (s, 1H), 2.34 (s, 3H)

¹³C NMR (101 MHz, DMSO) δ 160.73 (d, $J = 243.7$ Hz), 150.15, 142.25 (d, $J = 7.5$ Hz), 139.03, 137.34, 137.03 (d, $J = 2.5$ Hz), 130.37 (d, $J = 8.4$ Hz), 130.07, 128.15, 127.98, 126.52, 125.75, 121.26, 115.43 (d, $J = 21.2$ Hz), 114.18 (d, $J = 20.8$ Hz), 65.50, 21.02

¹⁹F NMR (471 MHz, CDCl₃) δ -113.70 – -113.85 (m)

HRMS (ESI) m/z [M+H]⁺ calcd for C₁₇H₁₆FN₂O 283.1247, found 283.1248.

(5-Fluoro-4'-methyl-[1,1'-biphenyl]-2-yl)(1*H*-imidazol-2-yl)methanol (3.26)



Prepared according to **General Procedure E** using 1-((2-(trimethylsilyl)ethoxy)methyl)-1*H*-imidazole (111 mg, 0.56 mmol), THF (1 mL), ⁿBuLi (284 μL, 0.56 mmol) and 5-fluoro-4'-methyl-[1,1'-biphenyl]-2-carbaldehyde (107 mg, 0.50 mmol) as a solution in THF (1 mL). The deprotection was performed in a microwave vial with the crude, CH₂Cl₂ (2 mL) and TFA (2 mL), yielding (5-fluoro-4'-methyl-[1,1'-biphenyl]-2-yl)(1*H*-imidazol-2-yl)methanol (50 mg, 0.18 mmol, 36% yield) as a white solid.

IR (ν_{max}, cm⁻¹) 3188, 1681, 1211, 1029

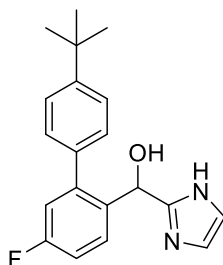
¹H NMR (500 MHz, DMSO) δ 11.98 (s, 1H), 7.57 (dd, *J* = 8.7, 6.2 Hz, 1H), 7.44 (d, *J* = 8.0 Hz, 2H), 7.26 (d, *J* = 7.8 Hz, 2H), 7.18 (td, *J* = 8.6, 2.7 Hz, 1H), 7.01 (dd, *J* = 10.0, 2.7 Hz, 2H), 6.78 (s, 1H), 6.04 (s, 1H), 5.70 (s, 1H), 2.36 (s, 3H)

¹³C NMR (126 MHz, DMSO) δ 161.22 (d, *J* = 243.8 Hz), 150.68, 142.62 (d, *J* = 7.7 Hz), 137.58 (d, *J* = 3.0 Hz), 137.33, 136.70, 130.87 (d, *J* = 8.6 Hz), 129.83, 129.23, 127.76, 116.22, 115.93 (d, *J* = 21.0 Hz), 114.57 (d, *J* = 21.0 Hz), 65.97, 21.20

¹⁹F NMR (471 MHz, DMSO) δ -115.62 (td, *J* = 9.0, 6.8 Hz)

HRMS (ESI) *m/z* [M+H]⁺ calcd for C₁₇H₁₆FN₂O 283.1247, found 283.1248

(4'-(tert-Butyl)-5-fluoro-[1,1'-biphenyl]-2-yl)(1*H*-imidazol-2-yl)methanol (3.28)



Prepared according to **General Procedure E** using 1-((2-(trimethylsilyl)ethoxy)methyl)-1*H*-imidazole (79 mg, 0.40 mmol), THF (1 mL), ⁿBuLi (203 μL, 0.40 mmol) and 4'-(tert-butyl)-5-fluoro-[1,1'-biphenyl]-2-carbaldehyde (113 mg, 0.44 mmol) as a solution in THF (1 mL). The deprotection was performed in a microwave vial using the crude, CH₂Cl₂ (2 mL) and TFA (2 mL), yielding (4'-(tert-butyl)-5-fluoro-[1,1'-biphenyl]-2-yl)(1*H*-imidazol-2-yl)methanol (87 mg, 0.27 mmol, 67% yield) as a white solid.

IR (ν_{max} , cm⁻¹) 1612, 1585, 1267, 1031

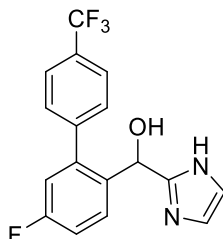
¹H NMR (500 MHz, DMSO) δ 12.00 (s, 1H), 7.59 – 7.45 (m, 5H), 7.18 (td, J = 8.6, 2.6 Hz, 1H), 7.05 (dd, J = 10.0, 2.7 Hz, 1H), 7.00 (s, 1H), 6.78 (s, 1H), 6.04 (s, 1H), 5.72 (s, 1H), 1.33 (s, 9H).

¹³C NMR (126 MHz, DMSO) δ 161.24 (d, J = 243.7 Hz), 150.75, 150.43, 142.54 (d, J = 7.7 Hz), 137.63 (d, J = 3.1 Hz), 136.69, 130.92 (d, J = 8.1 Hz), 129.71, 125.45, 116.23, 115.93 (d, J = 20.7 Hz), 114.63 (d, J = 21.5 Hz), 65.95, 34.80, 31.61

¹⁹F NMR (471 MHz, DMSO) δ -115.51 (td, J = 8.9, 6.3 Hz)

HRMS (ESI) m/z [M+H]⁺ calcd for C₂₀H₂₂FN₂O 325.1716, found 325.1713

(5-Fluoro-4'-(trifluoromethyl)-[1,1'-biphenyl]-2-yl)(1*H*-imidazol-2-yl)methanol
(3.27)



Prepared according to **General Procedure E** using 1-((2-(trimethylsilyl)ethoxy)methyl)-1*H*-imidazole (99 mg, 0.50 mmol), THF (1 mL), ⁿBuLi (254 μL, 0.50 mmol) and 5-fluoro-4'-(trifluoromethyl)-[1,1'-biphenyl]-2-carbaldehyde (148 mg, 0.55 mmol) as a solution in THF (1 mL). The deprotection was performed in a microwave vial with the crude, CH₂Cl₂ (2 mL) and TFA (2 mL), yielding (5-fluoro-4'-(trifluoromethyl)-[1,1'-biphenyl]-2-yl)(1*H*-imidazol-2-yl)methanol (41 mg, 0.12 mmol, 25% yield) as a white solid.

IR (ν_{\max} , cm⁻¹) 3201, 1321, 1282, 1163, 1022

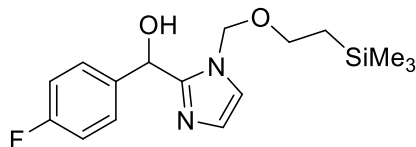
¹H NMR (500 MHz, DMSO) δ 11.98 (s, 1H), 7.82 (d, J = 8.2 Hz, 2H), 7.76 (d, J = 8.1 Hz, 2H), 7.63 (dd, J = 8.8, 6.0 Hz, 1H), 7.28 (td, J = 8.6, 2.7 Hz, 1H), 7.12 (dd, J = 9.7, 2.7 Hz, 1H), 7.00 (s, 1H), 6.78 (s, 1H), 6.11 (d, J = 4.4 Hz, 1H), 5.63 (d, J = 4.3 Hz, 1H).

¹³C NMR (126 MHz, DMSO) δ 161.26 (d, J = 244.2 Hz), 150.30, 143.74, 141.07 (d, J = 7.8 Hz), 137.67 (d, J = 3.2 Hz), 130.94 (d, J = 8.6 Hz), 130.76, 128.62 (q, J = 32.0 Hz), 125.49 (q, J = 3.4 Hz), 124.78 (q, J = 271.9 Hz), 116.28, 116.12 (d, J = 21.8 Hz), 115.55 (d, J = 21.0 Hz), 66.03

¹⁹F NMR (471 MHz, DMSO) δ -60.92 (s), -115.19 (td, J = 8.9, 6.3 Hz)

HRMS (ESI) m/z [M+H]⁺ calcd for C₁₇H₁₃F₄N₂O 337.0959, found 337.0959

Synthesis of (4-fluorophenyl)(1-((2-(trimethylsilyl)ethoxy)methyl)-1*H*-imidazol-2-yl)methanol (3.15')



Prepared according to **General Procedure C** using 1-((2-(trimethylsilyl)ethoxy)methyl)-1*H*-imidazole (198 mg, 1.0 mmol), THF (2 mL), ⁿBuLi (560 μL, 1.1 mmol) and 4-fluorobenzaldehyde (149 mg, 1.2 mmol) as a solution in THF (2 mL). The crude residue was purified by flash chromatography, eluting in 0-50% EtOAc in petroleum ether to afford (4-fluorophenyl)(1-((2-(trimethylsilyl)ethoxy)methyl)-1*H*-imidazol-2-yl)methanol (320 mg, quant.) as a clear oil.

IR (ν_{\max} , cm^{-1}) 2953, 1602, 1247, 1099

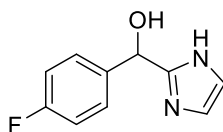
¹H NMR (500 MHz, CDCl₃) δ 7.34 (dd, $J = 8.5, 5.4$ Hz, 2H), 7.05 – 6.95 (m, 4H), 5.96 (s, 1H), 5.08 (d, $J = 10.7$ Hz, 1H), 5.03 (d, $J = 10.7$ Hz, 1H), 3.27 (t, $J = 8.3$ Hz, 2H), 0.80 – 0.76 (m, 2H), -0.05 (s, 9H)

¹³C NMR (126 MHz, CDCl₃) δ 162.61 (d, $J = 246.6$ Hz), 149.24, 136.70 (d, $J = 3.0$ Hz), 128.52 (d, $J = 8.2$ Hz), 126.85, 121.05, 115.59 (d, $J = 21.6$ Hz), 75.33, 68.86, 66.57, 17.88, -1.39

¹⁹F NMR (471 MHz, CDCl₃) δ -114.34 (tt, $J = 8.7, 5.4$ Hz)

HRMS (ESI) m/z [M+H]⁺ calcd for C₁₆H₂₄FN₂O₂Si 323.1586, found 323.1587

(4-Fluorophenyl)(1*H*-imidazol-2-yl)methanol (3.15)



Prepared according to **General Procedure D** using (4-fluorophenyl)(1-((2-(trimethylsilyl)ethoxy)methyl)-1*H*-imidazol-2-yl)methanol (160 mg, 0.50 mmol), CH₂Cl₂ (2 mL) and TFA (2 mL). The crude was then diluted in CH₂Cl₂ (2 mL) and hexane (2 mL) and concentrated under a constant flow of air until a solid crashed out. The solid was filtered off and washed with hexane to yield (4-fluorophenyl)(1*H*-imidazol-2-yl)methanol (25 mg, 0.13 mmol, 26% yield) as a white solid.

IR (ν_{\max} , cm⁻¹) 3167, 1604, 1552, 1224, 1055

¹H NMR (500 MHz, DMSO) δ 11.88 (s, 1H), 7.41 (dd, $J = 8.3, 5.8$ Hz, 2H), 7.13 (t, $J = 8.9$ Hz, 2H), 7.01 – 6.73 (m, 2H), 6.17 (d, $J = 4.3$ Hz, 1H), 5.72 (d, $J = 4.1$ Hz, 1H)

¹³C NMR (126 MHz, DMSO) δ 161.74 (d, $J = 242.4$ Hz), 150.40, 139.95 (d, $J = 3.0$ Hz), 128.76 (d, $J = 8.2$ Hz), 115.11 (d, $J = 21.2$ Hz), 69.34. C₄ and C₅ of imidazole not observed due to peak broadening.

¹⁹F NMR (471 MHz, DMSO) δ -115.97 (tt, $J = 9.1, 5.6$ Hz)

HRMS (ESI) m/z [M+H]⁺ calcd for C₁₀H₁₀FN₂O 193.0777, found 193.0772

6.3.5 Biological Methods

- All synthesised compounds submitted for biological testing were analysed by HPLC to confirm purity of >95%
- The skin keratinocyte cell line NCTC2544, stably expressing both a human PAR2 and NF- κ B construct, were previously generated in-house

6.3.5.1 PAR2 Signal Transduction Assays (Performed by Dr K. A. McIntosh)

NF- κ B reporter cells were cultured in a Corning Black 96-well Assay Plate with Clear, Flat Bottom in cell culture media to near confluence. Cell culture media was then removed and serum-free media (100 μ L) added to quiesce cell growth. After incubation overnight, cells were pre-treated with drugs (10 μ L in DMSO) for 60 minutes, prior to addition of agonist (trypsin, 100 nM) for 4 hours. Serum-free media was then removed, and the cells washed twice with 100 μ L of cold PBS. The luciferase substrate was then added to the cells as a solution in lysis buffer (100 μ L, 0.15 mg/mL) and incubated for 5 minutes. Luminescence (RLU) of each well was then measured at 450 nm using a Wallac Microbeta luminometer (Perkin Elmer)

Lysis buffer consists of Tris Base (pH 7.8, 25 mM), MgCl₂ (8 mM), Triton X 100 (1% v/v), Glycerol (15% v/v), ATP (1 mM), BSA (1% w/v) and DTT (1 mM) in distilled water and pH modified to 7.8.

Chapter 7 References

- (1) Chackalamannil, S.; Wang, Y.; Greenlee, W. J.; Hu, Z.; Xia, Y.; Ahn, H. S.; Boykow, G.; Hsieh, Y.; Palamanda, J.; Gans-Fantuzzi, J.; et al. Discovery of a Novel, Orally Active Himbacine-Based Thrombin Receptor Antagonist (SCH 530348) with Potent Antiplatelet Activity. *J Med Chem.* **2008**, *51* (11), 3061–3064.
- (2) Covic, L.; Gresser, A. L.; Talavera, J.; Swift, S.; Kuliopulos, A. Activation and Inhibition of G Protein-Coupled Receptors by Cell-Penetrating Membrane-Tethered Peptides. *Proc. Natl. Acad. Sci. U. S. A.* **2002**, *99* (2), 643–648.
- (3) Shearer, A. M.; Rana, R.; Austin, K.; Baleja, J. D.; Nguyen, N.; Bohm, A.; Covic, L.; Kuliopulos, A. Targeting Liver Fibrosis with a Cell-Penetrating Protease-Activated Receptor-2 (PAR2) Peptide. *J. Biol. Chem.* **2016**, *291* (44), 23188–23198.
- (4) Cheng, R. K. Y.; Fiez-vandal, C.; Schlenker, O.; Edman, K.; Aggeler, B.; Brown, D. G.; Brown, G. A.; Cooke, R. M.; Dumelin, C. E.; Doré, A. S.; et al. Structural Insight into Allosteric Modulation of Protease-Activated Receptor 2. *Nat. Publ. Gr.* **2017**, *545* (7652), 112–115.
- (5) Cooper, G. M. Functions of Cell Surface Receptors. In *The Cell: A Molecular Approach*; 2000.
- (6) Munk, C.; Isberg, V.; Mordalski, S.; Harpsøe, K.; Rataj, K.; Hauser, A. S.; Kolb, P.; Bojarski, A. J.; Vriend, G.; Gloriam, D. E. GPCRdb: The G Protein-Coupled Receptor Database – an Introduction. *Br. J. Pharmacol.* **2016**, *173* (14), 2195–2207.
- (7) Hauser, A. S.; Attwood, M. M.; Rask-andersen, M.; Schiöth, H. B.; Gloriam, D. E. Trends in GPCR Drug Discovery : New Agents , Targets and Indications. *Nat. Publ. Gr.* **2017**, *16* (12), 829–842.
- (8) Kobilka, B. K. G Protein Coupled Receptor Structure and Activation. *Biochim. Biophys. Acta (BBA)-Biomembranes* **2007**, *1768* (4), 794–807.
- (9) Fisyunov, A. I. Molecular Mechanisms of G Protein-Independent Signaling Mediated by 7-Transmembrane Receptors. *Neurophysiology* **2012**, *44* (3), 255–264.
- (10) Davies, M. N.; Secker, A.; Freitas, A. A.; Mendao, M.; Timmis, J.; Flower, D. R. On the Hierarchical Classification of G Protein-Coupled Receptors. *Bioinformatics* **2007**, *23* (23), 3113–3118.
- (11) Bjarnadóttir, T. K.; Gloriam, D. E.; Hellstrand, S. H.; Kristiansson, H.; Fredriksson, R.; Schiöth, H. B. Comprehensive Repertoire and Phylogenetic Analysis of the G Protein-Coupled Receptors in Human and Mouse. *Genomics* **2006**, *88*, 263–273.
- (12) Bräuner-osborne, H.; Wellendorph, P.; Jensen, A. A. Structure , Pharmacology and Therapeutic Prospects of Family C G-Protein Coupled Receptors. *Curr. Drug Targets* **2007**, *8* (1), 169–184.
- (13) Pándy-Szeker, G.; Munk, C.; Tsonkov, T. M.; Mordalski, S.; Harpsøe, K.; Hauser, A. S.; Bojarski, A. J.; Gloriam, D. E.; Pándy-Szeker, G.; Munk, C.; et al. GPCRdb in 2018 :

- Adding GPCR Structure Models and Ligands. *Nucleic Acids Res.* **2018**, *46*, 440–446.
- (14) Katritch, V.; Cherezov, V.; Stevens, R. C. Structure-Function of the G-Protein-Coupled Receptor Superfamily. *Annu. Rev. Pharmacol. Toxicol.* **2013**, *53*, 531–556.
- (15) Purcell, R. H.; Hall, R. A. Adhesion G Protein – Coupled Receptors as Drug Targets. *Annu. Rev. Pharmacol. Toxicol.* **2018**, *58*, 429–452.
- (16) Malbon, C. C. Frizzleds: New Members of the Superfamily of G-Protein-Coupled Receptors. *Front. Biosci.* **2004**, *9*, 1048–1058.
- (17) Poyner, D. R.; Hay, D. L. Secretin Family (Class B) G Protein-Coupled Receptors – from Molecular to Clinical. *Br. J. Pharmacol.* **2012**, *166*, 1–3.
- (18) Weis, W. I.; Kobilka, B. K. The Molecular Basis of G Protein – Coupled Receptor Activation. *Annu. Rev. Biochem.* **2018**, *87*, 897–919.
- (19) Woulfe, D. S. Platelet G Protein-Coupled Receptors in Hemostasis and Thrombosis. *J Thromb Haemost* **2005**, No. 3, 2193–2200.
- (20) Lohse, M. J.; Hein, P.; Hoffmann, C.; Nikolaev, V. O.; Vilardaga, J.-P.; Bünemann, M. Kinetics of G-Protein-Coupled Receptor Signals in Intact Cells. *Br. J. Pharmacol.* **2008**, *153* (December 2007), S125-32.
- (21) Koppen, C. J. Van; Jakobs, K. H. Arrestin-Independent Internalization of G Protein-Coupled Receptors. *Mol. Pharmacol.* **2004**, *66* (3), 365–367.
- (22) Duc, N. M.; Kim, H. R.; Young, K. Structural Mechanism of G Protein Activation by G Protein-Coupled Receptor. *Eur. J. Pharmacol.* **2015**, *763*, 214–222.
- (23) Lambright, D. G.; Sondek, J.; Bohm, A.; Skiba, N. P.; Hamm, H. E.; Sigler, P. B. The 2.0 Å Crystal Structure of a Heterotrimeric G Protein. *Nature* **1996**, *379*, 311–319.
- (24) Cabrera-Vera, T. M.; Vanhauwe, J.; Thomas, T. O.; Medkova, M.; Preininger, A.; Mazzoni, M. R.; Hamm, H. E. Insights into G Protein Structure, Function, and Regulation. *Endocr. Rev.* **2003**, *24* (6), 765–781.
- (25) Dessauer, C. W.; Chen-Goodspeed, M.; Chen, J. Mechanism of Galpha I-Mediated Inhibition of Type V Adenylyl Cyclase. *J. Biol. Chem.* **2002**, *277* (32), 28823–28829.
- (26) Ma, Y. C.; Huang, J.; Ali, S.; Lowry, W.; Huang, X. Y. Src Tyrosine Kinase Is a Novel Direct Effector of G Proteins. *Cell* **2000**, *102* (5), 635–646.
- (27) Neubig, R. R.; Siderovski, D. P. Regulators of G-Protein Signalling as New Central Nervous System Drug Targets. *Nat. Rev. Drug Discov.* **2002**, *1* (3), 187–197.
- (28) Soundararajan, M.; Willard, F. S.; Kimple, A. J.; Turnbull, A. P.; Ball, L. J.; Schoch, G. A.; Gileadi, C.; Fedorov, O. Y.; Dowler, E. F.; Higman, V. A.; et al. Structural Diversity in the RGS Domain and Its Interaction with Heterotrimeric G Protein Alpha-Subunits. *Proc. Natl. Acad. Sci. U. S. A.* **2008**, *105* (17), 6457–6462.
- (29) Chen-Goodspeed, M.; Lukan, A. N.; Dessauer, C. W. Modeling of Galpha s and Galpha i

- Regulation of Human Type V and VI Adenylyl Cyclase. *J. Biol. Chem.* **2005**, *280* (3), 1808–1816.
- (30) Joshi-Tope, G.; Gillespie, M.; Vastrik, I.; D'Eustachio, P. D.; Schmidt, E.; de Bono, B.; Jassal, B.; Gopinath, G. R.; Wu, G. R.; Matthews, L.; et al. Reactome - a Knowledgebase of Human Biological Pathways. *Nucleic Acids Res.* **2005**, *33*, 428–432.
- (31) Lian, L.; Wang, Y.; Draznin, J.; Eslin, D.; Bennett, J. S.; Poncz, M.; Wu, D.; Abrams, C. S. The Relative Role of PLCbeta and PI3Kgamma in Platelet Activation. *Blood* **2005**, *106* (1), 110–117.
- (32) Berridge, M. J.; Lipp, P.; Bootman, M. D. The Versatility and Universality of Calcium Signalling. *Nat. Rev. Mol. Cell Biol.* **2000**, *1* (1), 11–21.
- (33) Ballou, L. M.; Chattopadhyay, M.; Li, Y.; Scarlata, S.; Lin, R. Z. Galphaq Binds to P110alpha/P85alpha Phosphoinositide 3-Kinase and Displaces Ras. *Biochem. J.* **2006**, *394* (Pt 3), 557–562.
- (34) Bence, K.; Ma, W.; Kozasa, T.; Huang, X. Y. Direct Stimulation of Bruton's Tyrosine Kinase by G(q)-Protein Alpha-Subunit. *Nature* **1997**, *389* (6648), 296–299.
- (35) Tiruppathi, C.; Yan, W.; Sandoval, R.; Naqvi, T.; Pronin, A. N.; Benovic, J. L.; Malik, A. B. G Protein-Coupled Receptor Kinase-5 Regulates Thrombin-Activated Signaling in Endothelial Cells. *Proc. Natl. Acad. Sci.* **2000**, *97* (13), 7440–7445.
- (36) Jiang, Y.; Ma, W.; Wan, Y.; Kozasa, T.; Hattori, S.; Huang, X. Y. The G Protein G Alpha12 Stimulates Bruton's Tyrosine Kinase and a RasGAP through a Conserved PH/BM Domain. *Nature* **1998**, *395* (6704), 808–813.
- (37) Chen, Z.; Guo, L.; Hadas, J.; Gutowski, S.; Sprang, S. R.; Sternweis, P. C. Activation of P115-RhoGEF Requires Direct Association of Galpha13 and the Dbl Homology Domain. *J. Biol. Chem.* **2012**, *287* (30), 25490–25500.
- (38) Shankaranarayanan, A.; Thal, D. M.; Tesmer, V. M.; Roman, D. L.; Neubig, R. R.; Kozasa, T.; Tesmer, J. J. G. Assembly of High Order G Alpha Q-Effector Complexes with RGS Proteins. *J. Biol. Chem.* **2008**, *283* (50), 34923–34934.
- (39) Dupré, D. J.; Robitaille, M.; Rebois, R. V.; Hébert, T. E. The Role of Gβγ Subunits in the Organization, Assembly, and Function of GPCR Signaling Complexes. *Annu. Rev. Pharmacol. Toxicol.* **2009**, *49*, 31–56.
- (40) Suire, S.; Condliffe, A. M.; Ferguson, G. J.; Ellson, C. D.; Guillou, H.; Davidson, K.; Welch, H.; Coadwell, J.; Turner, M.; Chilvers, E. R.; et al. Gbetagammmas and the Ras Binding Domain of P110gamma Are Both Important Regulators of PI(3)Kgamma Signalling in Neutrophils. *Nat. Cell Biol.* **2006**, *8* (11), 1303–1309.
- (41) Li, Z.; Hannigan, M.; Mo, Z.; Liu, B.; Lu, W.; Wu, Y.; Smrcka, A. V.; Wu, G.; Li, L.; Liu, M.; et al. Directional Sensing Requires G Beta Gamma-Mediated PAK1 and PIX Alpha-Dependent Activation of Cdc42. *Cell* **2003**, *114* (2), 215–227.
- (42) Lowry, W. E.; Huang, X.-Y. G Protein Beta Gamma Subunits Act on the Catalytic Domain

- to Stimulate Bruton's Agammaglobulinemia Tyrosine Kinase. *J. Biol. Chem.* **2002**, 277 (2), 1488–1492.
- (43) Park, D.; Jhon, D. Y.; Lee, C. W.; Lee, K. H.; Rhee, S. G. Activation of Phospholipase C Isozymes by G Protein Beta Gamma Subunits. *J. Biol. Chem.* **1993**, 268 (7), 4573–4576.
- (44) Rang, H. P.; Dale, M. M.; Ritter, J. M.; Flower, R. J.; Henderson, G. *Pharmacology*, Seventh Ed.; Elsevier, Churchill Livingstone: Edinburgh, 2012.
- (45) Felder, C. C. *GPCR Drug Discovery-Moving beyond the Orthosteric to the Allosteric Domain*, 1st ed.; Elsevier Inc., 2019; Vol. 86.
- (46) Johnson, M. Beta 2 -Adrenoceptors : Mechanisms of Action of Beta 2 -Agonists. *Paediatr. Respir. Rev.* **2001**, 1, 57–62.
- (47) Bartow, R. A.; Brogden, R. N. Formoterol. An Update of Its Pharmacological Properties and Therapeutic Efficacy in the Management of Asthma. *Drugs* **1998**, 55 (2), 303–322.
- (48) Steiropoulos, P.; Tzouveleakis, A.; Bouros, D. Formoterol in the Management of Chronic Obstructive Pulmonary Disease. *Int. J. Chron. Obstruct. Pulmon. Dis.* **2008**, 3 (2), 205–215.
- (49) Merlos, M.; Giral, M.; Balsa, D.; Ferrando, R.; Queralt, M.; Puigdemont, A.; Garcí, N.; Uriach, J. Rupatadine , a New Potent , Orally Active Dual Antagonist of Histamine and Platelet-Activating Factor (PAF). *J. Pharmacol. Exp. Ther.* **1997**, 280 (1), 114–121.
- (50) Jordan, S.; Koprivica, V.; Chen, R.; Tottori, K.; Kikuchi, T.; Altar, C. A. The Antipsychotic Aripiprazole Is a Potent, Partial Agonist at the Human 5-HT1A Receptor. *Eur. J. Pharmacol.* **2002**, 441 (3), 137–140.
- (51) Swainston Harrison, T.; Perry, C. M. Aripiprazole: A Review of Its Use in Schizophrenia and Schizoaffective Disorder. *Drugs* **2004**, 64 (15), 1715–1736.
- (52) Friedman, J. H. Pimavanserin for the Treatment of Parkinson's Disease Psychosis. *Expert Opin. Pharmacother.* **2013**, 14 (14), 1969–1975.
- (53) de Francisco, A. L. M. Cinacalcet HCl: A Novel Therapeutic for Hyperparathyroidism. *Expert Opin. Pharmacother.* **2005**, 6 (3), 441–452.
- (54) Moe, S. M.; Cunningham, J.; Bommer, J.; Adler, S.; Rosansky, S. J.; Urena-Torres, P.; Albizem, M. B.; Guo, M. D.; Zani, V. J.; Goodman, W. G.; et al. Long-Term Treatment of Secondary Hyperparathyroidism with the Calcimimetic Cinacalcet HCl. *Nephrol. Dial. Transplant* **2005**, 20 (10), 2186–2193.
- (55) Husted, S.; Giezen, J. J. J. Van. Ticagrelor : The First Reversibly Binding Oral P2Y 12 Receptor Antagonist. **2009**, 27, 259–274.
- (56) Vu, T. K.; Hung, D. T.; Wheaton, V. I.; Coughlin, S. R. Molecular Cloning of a Functional Thrombin Receptor Reveals a Novel Proteolytic Mechanism of Receptor Activation. *Cell* **1991**, 64 (6), 1057–1068.
- (57) Nystedt, S.; Emilsson, K.; Larsson, A. K.; Strombeck, B.; Sundelin, J. Molecular Cloning

and Functional Expression of the Gene Encoding the Human Proteinase-Activated Receptor 2. *Eur. J. Biochem.* **1995**, *232* (1), 84–89.

- (58) Ishihara, H.; Connolly, A. J.; Zeng, D. W.; Kahn, M. L.; Zheng, Y. W.; Timmons, C.; Tram, T.; Coughlin, S. R. Protease-Activated Receptor 3 Is a Second Thrombin Receptor in Humans. *Nature* **1997**, *386* (6624), 502–506.
- (59) Xu, W. F.; Andersen, H.; Whitmore, T. E.; Presnell, S. R.; Yee, D. P.; Ching, A.; Gilbert, T.; Davie, E. W.; Foster, D. C. Cloning and Characterization of Human Protease-Activated Receptor 4. *Proc. Natl. Acad. Sci. U. S. A.* **1998**, *95*, 6642–6646.
- (60) Adams, M. N.; Ramachandran, R.; Yau, M.-K.; Suen, J. Y.; Fairlie, D. P.; Hollenberg, M. D.; Hooper, J. D. Structure, Function and Pathophysiology of Protease Activated Receptors. *Pharmacol. Ther.* **2011**, *130* (3), 248–282.
- (61) Liu, L. W.; Vu, T. K.; Esmon, C. T.; Coughlin, S. R. The Region of the Thrombin Receptor Resembling Hirudin Binds to Thrombin and Alters Enzyme Specificity. *J. Biol. Chem.* **1991**, *266* (26), 16977–16980.
- (62) Coughlin, S. R. Thrombin Signalling and Protease-Activated Receptors. *Nature* **2000**, *407* (6801), 258–264.
- (63) Leger, A. J.; Jaques, S. L.; Badar, J.; Kaneider, N. C.; Derian, C. K.; Andrade-Gordon, P.; Covic, L.; Kuliopulos, A. Blocking the Protease-Activated Receptor 1-4 Heterodimer in Platelet-Mediated Thrombosis. *Circulation* **2006**, *113* (9), 1244–1254.
- (64) Nakanishi-Matsui, M.; Zheng, Y. W.; Sulciner, D. J.; Weiss, E. J.; Ludeman, M. J.; Coughlin, S. R. PAR3 Is a Cofactor for PAR4 Activation by Thrombin. *Nature* **2000**, *404* (6778), 609–613.
- (65) Ossovskaya, V. S.; Bunnett, N. W. Protease-Activated Receptors: Contribution to Physiology and Disease. *Physiol. Rev.* **2004**, *84* (2), 579–621.
- (66) Baltoumas, F. A.; Theodoropoulou, M. C.; Hamodrakas, S. J. Interactions of the Alpha-Subunits of Heterotrimeric G-Proteins with GPCRs, Effectors and RGS Proteins: A Critical Review and Analysis of Interacting Surfaces, Conformational Shifts, Structural Diversity and Electrostatic Potentials. *J. Struct. Biol.* **2013**, *182* (3), 209–218.
- (67) Ricks, T. K.; Trejo, J. Phosphorylation of Protease-Activated Receptor-2 Differentially Regulates Desensitization and Internalization. *J. Biol. Chem.* **2009**, *284* (49), 34444–34457.
- (68) Hammes, S. R.; Shapiro, M. J.; Coughlin, S. R. Shutoff and Agonist-Triggered Internalization of Protease-Activated Receptor 1 Can Be Separated by Mutation of Putative Phosphorylation Sites in the Cytoplasmic Tail. *Biochemistry* **1999**, *38* (29), 9308–9316.
- (69) Grimsey, N.; Soto, A. G.; Trejo, J. Regulation of Protease-Activated Receptor Signaling by Posttranslational Modifications. *IUBMB Life* **2011**, *63* (6), 403–411.
- (70) Ramachandran, R.; Noorbakhsh, F.; DeFea, K.; Hollenberg, M. D. Targeting Proteinase-

- Activated Receptors: Therapeutic Potential and Challenges. *Nat. Rev. Drug Discov.* **2012**, *11* (1), 69–86.
- (71) Dery, O.; Corvera, C. U.; Steinhoff, M.; Bunnett, N. W. Proteinase-Activated Receptors: Novel Mechanisms of Signaling by Serine Proteases. *Am. J. Physiol.* **1998**, *274* (6), C1429–52.
- (72) French, S. L.; Hamilton, J. R. Protease-Activated Receptor 4 : From Structure to Function and Back Again. *Br. J. Pharmacol.* **2016**, *16*, 2952–2965.
- (73) McCoy, K. L.; Traynelis, S. F.; Hepler, J. R. PAR1 and PAR2 Couple to Overlapping and Distinct Sets of G Proteins and Linked Signaling Pathways to Differentially Regulate Cell Physiology. *Mol. Pharmacol.* **2010**, *77* (6), 1005–1015.
- (74) Voss, B.; Mclaughlin, J. N.; Holinstat, M.; Zent, R.; Hamm, H. E. PAR1 , but Not PAR4 , Activates Human Platelets through a G i / o / Phosphoinositide-3 Kinase Signaling Axis. *Mol. Pharmacol.* **2007**, *71* (5), 1399–1406.
- (75) Mclaughlin, J. N.; Patterson, M. M.; Malik, A. B. Protease-Activated Receptor-3 (PAR3) Regulates PAR1 Signaling by Receptor Dimerization. *Proc. Natl. Acad. Sci. U. S. A.* **2007**, *104* (13), 1–6.
- (76) Cunningham, M.; McIntosh, K.; Bushell, T.; Sloan, G.; Plevin, R. Proteinase-Activated Receptors (PARs) as Targets for Antiplatelet Therapy. *Biochem. Soc. Trans.* **2016**, *44* (2), 606–612.
- (77) Macfarlane, S. R.; Seatter, M. J.; Kanke, T.; Hunter, G. D.; Plevin, R. Proteinase-Activated Receptors. *Pharmacol. Rev.* **2001**, *53* (2), 245–282.
- (78) Owen, W. G. PAR-3 Is a Low-Affinity Substrate, High-Affinity Effector of Thrombin. *Biochem. Biophys. Res. Commun.* **2003**, *305* (1), 166–168.
- (79) Gieseler, F.; Ungefroren, H.; Settmacher, U.; Hollenberg, M. D.; Kaufmann, R. Proteinase-Activated Receptors (PARs) - Focus on Receptor-Receptor-Interactions and Their Physiological and Pathophysiological Impact. *Cell Commun. Signal.* **2013**, *11* (1), 86.
- (80) Zhao, P.; Metcalf, M.; Bunnett, N. W. Biased Signaling of Protease-Activated Receptors. *Front. Endocrinol. (Lausanne).* **2014**, *5* (MAY), 1–16.
- (81) Duvernay, M.; Young, S.; Gailani, D.; Schoenecker, J.; Hamm, H. E.; Hamm, H. Protease-Activated Receptor (PAR) 1 and PAR4 Differentially Regulate Factor V Expression from Human Platelets. *Mol. Pharmacol.* **2013**, *83* (4), 781–792.
- (82) World Health Organization. Cardiovascular Disease Fact Sheet (May 2017) <http://www.who.int/mediacentre/factsheets/fs317/en/>.
- (83) Savage, B.; Saldívar, E.; Ruggeri, Z. M. Initiation of Platelet Adhesion by Arrest onto Fibrinogen or Translocation on von Willebrand Factor. *Cell* **1996**, *84* (2), 289–297.
- (84) Kuwahara, M.; Sugimoto, M.; Tsuji, S.; Matsui, H.; Mizuno, T.; Miyata, S.; Yoshioka, A.

- Platelet Shape Changes and Adhesion under High Shear Flow. *Arterioscler. Thromb. Vasc. Biol.* **2002**, *22* (2), 329–334.
- (85) Blair, P.; Flaumenhaft, R. Platelet Alpha-Granules: Basic Biology and Clinical Correlates. *Blood Rev.* **2009**, *23* (4), 177–189.
- (86) Furie, B. B. C.; Furie, B. B. C. Mechanisms of Thrombus Formation. *N. Engl. J. Med.* **2008**, *359* (9), 938–949.
- (87) Semple, J. W.; Italiano, J. E. J.; Freedman, J. Platelets and the Immune Continuum. *Nat. Rev. Immunol.* **2011**, *11* (4), 264–274.
- (88) Scheraga, H. A. The Thrombin-Fibrinogen Interaction. *Biophys. Chem.* **2004**, *112* (2-3 SPEC. ISS.), 117–130.
- (89) Ma, Y.-Q.; Qin, J.; Plow, E. F. Platelet Integrin Alpha(IIb)Beta(3): Activation Mechanisms. *J. Thromb. Haemost.* **2007**, *5* (7), 1345–1352.
- (90) Li, Z.; Zhang, G.; Liu, J.; Stojanovic, A.; Ruan, C.; Lowell, C. A.; Du, X. An Important Role of the Src Family Kinase Lyn in Stimulating Platelet Granule Secretion. *J. Biol. Chem.* **2010**, *285* (17), 12559–12570.
- (91) Faruqi, T. R.; Weiss, E. J.; Shapiro, M. J.; Huang, W.; Coughlin, S. R. Structure-Function Analysis of Protease-Activated Receptor 4 Thetered Ligand Peptides. Determinants of Specificity and Utility in Assays of Receptor Function. *J. Biol. Chem.* **2000**, *275* (26), 19728–19734.
- (92) McCoy, K. L.; Traynelis, S. F.; Hepler, J. R. PAR1 and PAR2 Couple to Overlapping and Distinct Sets of G Proteins and Linked Signaling Pathways to Differentially Regulate Cell Physiology. *Mol. Pharmacol.* **2010**, *77* (6), 1005–1015.
- (93) Kahn, M. L.; Nakanishi-Matsui, M.; Shapiro, M. J.; Ishihara, H.; Coughlin, S. R. Protease-Activated Receptors 1 and 4 Mediate Activation of Human Platelets by Thrombin. *J. Clin. Invest.* **1999**, *103* (6), 879–887.
- (94) Li, Z.; Delaney, M. K.; O'Brien, K. a.; Du, X. Signaling During Platelet Adhesion and Activation. *Arterioscler. Thromb. Vasc. Biol.* **2010**, *30* (12), 2341–2349.
- (95) Gale, A. Current Understanding of Hemostasis. *Toxicol Pathol.* **2011**, *39* (1), 273–280.
- (96) Chen, L.; Deng, H.; Cui, H.; Fang, J.; Zuo, Z. Inflammatory Responses and Inflammation-Associated Diseases in Organs. *Oncotarget* **2018**, *9* (6), 7204–7218.
- (97) Cláudia, A.; Castelo, C.; Seiti, F.; Yoshikawa, Y.; Pietrobon, A. J.; Sato, M. N. Role of Histamine in Modulating the Immune Response and Inflammation. *Mediators Inflamm.* **2018**, *2018*, 1–10.
- (98) Pober, J. S.; Sessa, W. C. Inflammation and the Blood Microvascular System. *Cold Spring Harb Perspect Biol* **2015**, *7*, 1–11.
- (99) Ashina, K.; Tsubosaka, Y.; Nakamura, T.; Omori, K. Hyperpermeability by Increasing Blood Flow and Endothelial Barrier Disruption In Vivo. *PLoS One* **2015**, *10* (7), 1–16.

- (100) Mantovani, A.; Allavena, P.; Sica, A.; Balkwill, F. Cancer-Related Inflammation. *Nature* **2008**, *454* (7203), 436–444.
- (101) Samad, F.; Ruf, W. Inflammation, Obesity, and Thrombosis. *Blood* **2019**, *122* (20), 3415–3423.
- (102) Rothmeier, A. S.; Ruf, W. Protease-Activated Receptor 2 Signaling in Inflammation. *Semin. Immunopathol.* **2012**, *34* (1), 133–149.
- (103) Levi, M.; van der Poll, T. Inflammation and Coagulation. *Crit. Care Med.* **2010**, *38* (2 Suppl), S26–34.
- (104) Butenas, S. Tissue Factor Structure and Function. *Scientifica (Cairo)*. **2012**, *2012*, 1–15.
- (105) Riewald, M.; Ruf, W. Mechanistic Coupling of Protease Signaling and Initiation of Coagulation by Tissue Factor. *Proc. Natl. Acad. Sci.* **2001**, *2001*, 7742–7747.
- (106) Ferrell, W. R.; Lockhart, J. C.; Kelso, E. B.; Dunning, L.; Plevin, R.; Meek, S. E.; Smith, A. J. H.; Hunter, G. D.; Mclean, J. S.; Mccgarry, F.; et al. Essential Role for Proteinase- Activated Receptor-2 in Arthritis. *J. Clin. Invest.* **2003**, *111* (1), 35–41.
- (107) Yang, Y. H.; Hall, P.; Milenkovski, G.; Sharma, L.; Hutchinson, P.; Melis, E.; Carmeliet, P.; Tipping, P.; Morand, E. Reduction in Arthritis Severity and Modulation of Immune Function in Tissue Factor Cytoplasmic Domain Mutant Mice. *Am. J. Pathol.* **2004**, *164* (1), 109–117.
- (108) Noorbakhsh, F.; Tsutsui, S.; Vergnolle, N.; Boven, L. A.; Shariat, N.; Vodjgani, M.; Warren, K. G.; Andrade-gordon, P.; Hollenberg, M. D.; Power, C. Proteinase-Activated Receptor 2 Modulates Neuroinflammation in Experimental Autoimmune Encephalomyelitis and Multiple Sclerosis. *J. Exp. Med.* **2006**, *203* (2), 425–435.
- (109) Steinhoff, M.; Vergnolle, N.; Young, S. H.; Tognetto, M.; Amadesi, S.; Ennes, H. S.; Trevisani, M.; Hollenberg, M. D.; Wallace, J. L.; Caughey, G. H.; et al. Agonists of Proteinase-Activated Receptor 2 Induce Inflammation by a Neurogenic Mechanism. *Nat. Med.* **2000**, *6* (2), 151–158.
- (110) Dai, Y.; Moriyama, T.; Higashi, T.; Togashi, K.; Kobayashi, K.; Yamanaka, H.; Tominaga, M.; Noguchi, K. Proteinase-Activated Receptor 2-Mediated Potentiation of Transient Receptor Potential Vanilloid Subfamily 1 Activity Reveals a Mechanism for Proteinase-Induced Inflammatory Pain. **2004**, *24* (18), 4293–4299.
- (111) Amadesi, S.; Nie, J.; Vergnolle, N.; Cottrell, G. S.; Grady, E. F.; Trevisani, M.; Manni, C.; Geppetti, P.; Mcroberts, J. A.; Ennes, H.; et al. Protease-Activated Receptor 2 Sensitizes the Capsaicin Receptor Transient Receptor Potential Vanilloid Receptor 1 to Induce Hyperalgesia. *J. Neurosci.* **2004**, *24* (18), 4300–4312.
- (112) Amadesi, S.; Cottrell, G. S.; Divino, L.; Chapman, K.; Grady, E. F.; Bautista, F.; Karanjia, R.; Barajas-lopez, C.; Vanner, S.; Vergnolle, N.; et al. Protease-Activated Receptor 2 Sensitizes TRPV1 by Protein Kinase C ϵ - and A-Dependent Mechanisms in Rats and Mice. *J. Physiol.* **2006**, *2*, 555–571.

- (113) Vergnolle, N.; Bunnett, N. W.; Sharkey, K. A.; Brussee, V.; Compton, S. J.; Grady, E. F.; Cirino, G.; Gerard, N.; Basbaum, A. I.; Andrade-Gordon, P.; et al. Proteinase-Activated Receptor-2 and Hyperalgesia: A Novel Pain Pathway. *Nat. Med.* **2001**, *7* (7), 821–826.
- (114) Ruf, W.; Mueller, B. M. Thrombin Generation and the Pathogenesis of Cancer. *Semin. Thromb. Hemost.* **2006**, *32 Suppl 1*, 61–68.
- (115) Shi, X.; Gangadharan, B.; Brass, L. F.; Ruf, W.; Mueller, B. M. Protease-Activated Receptors (PAR1 and PAR2) Contribute to Tumor Cell Motility and Metastasis. *Mol. Cancer Res.* **2004**, *2* (7), 395–402.
- (116) Albreksten, T.; Sørensen, B. B.; Hjortø, G. M.; Fleckner, J.; Rao, L. V. M.; Petersen, L. C. Transcriptional Program Induced by Factor VIIa-Tissue Factor, PAR1 and PAR2 in MDA-MD-231 Cells. *J Thromb Haemost* **2007**, *5* (8), 1588–1597.
- (117) Versteeg, H. H.; Spek, C. A.; Richel, D. J.; Peppelenbosch, M. P. Coagulation Factors VIIa and Xa Inhibit Apoptosis and Anoikis. *Oncogene* **2004**, *23* (2), 410–417.
- (118) Sorensen, B. B.; Rao, L. V. M.; Tornehave, D.; Gammeltoft, S.; Petersen, L. C. Antiapoptotic Effect of Coagulation Factor VIIa. *Blood* **2003**, *102* (5), 1708–1715.
- (119) Zhang, C.; Srinivasan, Y.; Arlow, D. H.; Fung, J. J.; Palmer, D.; Zheng, Y.; Green, H. F.; Pandey, A.; Dror, R. O.; Shaw, D. E.; et al. High-Resolution Crystal Structure of Human Protease-Activated Receptor 1 Bound to the Antagonist Vorapaxar. *Nature* **2013**, *492* (7429), 387–392.
- (120) Wu, C. C.; Huang, S. W.; Hwang, T. L.; Kuo, S. C.; Lee, F. Y.; Teng, C. M. YD-3, a Novel Inhibitor of Protease-Induced Platelet Activation. *Br. J. Pharmacol.* **2000**, *130* (6), 1289–1296.
- (121) Ahn, H.-S.; Foster, C.; Boykow, G.; Stamford, A.; Manna, M.; Graziano, M. Inhibition of Cellular Action of Thrombin by N3-Cyclopropyl-7-[[4-(1-Methylethyl)Phenyl]Methyl]-7H-Pyrrolo[3,2-f]Quinazoline-1,3-Diamine (SCH79797), a Nonpeptide Thrombin Receptor Antagonist. *Biochem. Pharmacol.* **2000**, *60*, 1425–1434.
- (122) Leonardi, S.; Tricoci, P.; White, H. D.; Armstrong, P. W.; Huang, Z.; Wallentin, L.; Aylward, P. E.; Moliterno, D. J.; Van De Werf, F.; Chen, E.; et al. Effect of Vorapaxar on Myocardial Infarction in the Thrombin Receptor Antagonist for Clinical Event Reduction in Acute Coronary Syndrome (TRA-CER) Trial. *Eur. Heart J.* **2013**, *34* (23), 1723–1731.
- (123) O'Brien, P. J.; Prevost, N.; Molino, M.; Hollinger, M. K.; Woolkalis, M. J.; Woulfe, D. S.; Brass, L. F.; Brien, P. J. O.; Prevost, N.; Molino, M.; et al. Thrombin Responses in Human Endothelial Cells. *Biochemistry* **2000**, *275* (18), 13502–13509.
- (124) O'Callaghan, K.; Kuliopulos, A.; Covic, L. Turning Receptors On and Off with Intracellular Peptidic: New Insights into G-Protein-Coupled Receptor Drug Development. *J. Biol. Chem.* **2012**, *287* (16), 12787–12796.
- (125) Remsberg, J. R.; Lou, H.; Tarasov, S. G.; Dean, M.; Tarasova, N. I. Structural Analogues of Smoothed Intracellular Loops as Potent Inhibitors of Hedgehog Pathway and Cancer Cell Growth. *J. Med. Chem.* **2007**, *50* (18), 4534–4538.

- (126) Kaneider, N. C.; Agarwal, A.; Leger, A. J.; Kuliopulos, A. Reversing Systemic Inflammatory Response Syndrome with Chemokine Receptor Pepducins. *Nat. Med.* **2005**, *11* (6), 661–665.
- (127) Covic, L.; Misra, M.; Badar, J.; Singh, C.; Kuliopulos, A. Pepducin-Based Intervention of Thrombin-Receptor Signaling and Systemic Platelet Activation. *Nat. Med.* **2002**, *8* (10), 1161–1165.
- (128) Kubo, S.; Ishiki, T.; Doe, I.; Sekiguchi, F.; Nishikawa, H.; Kawai, K.; Matsui, H.; Kawabata, A. Distinct Activity of Peptide Mimetic Intracellular Ligands (Pepducins) for Proteinase-Activated Receptor-1 in Multiple Cells/Tissues. *Ann. N. Y. Acad. Sci.* **2006**, *1091*, 445–459.
- (129) Zhang, P.; Gruber, A.; Kasuda, S.; Kimmelstiel, C.; O’Callaghan, K.; Cox, D. H.; Bohm, A.; Baleja, J. D.; Covic, L.; Kuliopulos, A. Suppression of Arterial Thrombosis without Affecting Hemostatic Parameters with A Cell-Penetrating PAR1 Pepducin. *Circulation* **2012**, *126* (1), 83–91.
- (130) Carlson, K. E.; Mccurry, T. J.; Iii, S. W. H. Pepducins: Lipopeptide Allosteric Modulators of GPCR Signaling. *Drug Discov. Today. Technol.* **2012**, *9* (1), e33–e39.
- (131) Kuliopulos, A.; Covic, L. Blocking Receptors on the inside: Pepducin-Based Intervention of PAR Signaling and Thrombosis. *Life Sci.* **2003**, *74* (2–3), 255–262.
- (132) Zhang, P.; Leger, A. J.; Baleja, J. D.; Rana, R.; Corlin, T.; Nguyen, N.; Koukos, G.; Bohm, A.; Covic, L.; Kuliopulos, A. Allosteric Activation of a G Protein-Coupled Receptor with Cell-Penetrating Receptor Mimetics. *J. Biol. Chem.* **2015**, *290* (25), 15785–15798.
- (133) Swift, S.; Leger, A. J.; Talavera, J.; Zhang, L.; Bohm, A.; Kuliopulos, A. Role of the PAR1 Receptor 8th Helix in Signaling: The 7-8-1 Receptor Activation Mechanism. *J. Biol. Chem.* **2006**, *281* (7), 4109–4116.
- (134) Gurbel, P. A.; Bliden, K. P.; Turner, S. E.; Tantry, U. S.; Gesheff, M. G.; Barr, T. P.; Covic, L.; Kuliopulos, A. Cell-Penetrating Pepducin Therapy Targeting PAR1 in Subjects With Coronary Artery Disease. *Arterioscler. Thromb. Vasc. Biol.* **2016**, *36* (1), 189–197.
- (135) Boire, A.; Covic, L.; Agarwal, A.; Jacques, S.; Sherifi, S.; Kuliopulos, A. PAR1 Is a Matrix Metalloprotease-1 Receptor That Promotes Invasion and Tumorigenesis of Breast Cancer Cells. *Cell* **2005**, *120* (3), 303–313.
- (136) Agarwal, A.; Covic, L.; Sevigny, L. M.; Kaneider, N. C.; Azabdaftari, G.; Sharifi, S.; Kuliopulos, A. Targeting a Metalloprotease-PAR1 Signaling System with Cell-Penetrating Pepducins Inhibits Angiogenesis, Ascites, and Progression of Ovarian Cancer. *Mol Cancer Ther.* **2008**, *7* (9), 2746–2757.
- (137) Cisowski, J.; O’Callaghan, K.; Kuliopulos, A.; Yang, J.; Nguyen, N.; Deng, Q.; Yang, E.; Fogel, M.; Tressel, S.; Foley, C.; et al. Targeting Protease-Activated Receptor-1 with Cell-Penetrating Pepducins in Lung Cancer. *Am. J. Pathol.* **2011**, *179* (1), 513–523.
- (138) Kuliopulos, A. Safety of PZ-128 in Subjects Undergoing Non-Emergent Percutaneous Coronary Intervention

<https://clinicaltrials.gov/ct2/show/record/NCT02561000?view=record>.

- (139) De Ceunynck, K.; Peters, C. G.; Jain, A.; Higgins, S. J.; Aisiku, O.; Fitch-Tewfik, J. L.; Chaudhry, S. A.; Dockendorff, C.; Parikh, S. M.; Ingber, D. E.; et al. PAR1 Agonists Stimulate APC-like Endothelial Cytoprotection and Confer Resistance to Thromboinflammatory Injury. *Proc. Natl. Acad. Sci. U. S. A.* **2018**, *115* (5), E982–E991.
- (140) Hamilton, J. R.; Trejo, J. Challenges and Opportunities in Protease-Activated Receptor Drug Development. *Annu. Rev. Pharmacol. Toxicol.* **2017**, *57* (1), 349–373.
- (141) Kelso, E. B.; Lockhart, J. C.; Hembrough, T.; Dunning, L.; Plevin, R.; Hollenberg, M. D.; Sommerhoff, C. P.; Mclean, J. S.; Ferrell, W. R. Therapeutic Promise of Proteinase-Activated Receptor-2 Antagonism in Joint Inflammation. *J. Pharmacol. Exp. Ther.* **2006**, *316* (3), 1017–1024.
- (142) Suen, J. Y.; Barry, G. D.; Lohman, R. J.; Halili, M. A.; Cotterell, A. J.; Le, G. T.; Fairlie, D. P. Modulating Human Proteinase Activated Receptor 2 with a Novel Antagonist (GB88) and Agonist (GB110). *Br. J. Pharmacol.* **2012**, *165*, 1413–1423.
- (143) Suen, J. Y.; Cotterell, A.; Lohman, R. J.; Lim, J.; Han, A.; Yau, M. K.; Liu, L.; Cooper, M. A.; Vesey, D. A.; Fairlie, D. P. Pathway-Selective Antagonism of Proteinase Activated Receptor 2. *Br. J. Pharmacol.* **2014**, *171* (17), 4112–4124.
- (144) Yau, M. K.; Liu, L.; Suen, J. Y.; Lim, J.; Lohman, R. J.; Jiang, Y.; Cotterell, A. J.; Barry, G. D.; Mak, Y. W.; Vesey, D. A.; et al. PAR2 Modulators Derived from GB88. *ACS Med. Chem. Lett.* **2016**, *7* (12), 6–11.
- (145) Hopkins, A. L.; Groom, C. R.; Alex, A. Ligand Efficiency : A Useful Metric for Lead Selection. *Drug Discov. Today* **2004**, *9* (10), 430–431.
- (146) Palomo, J. M. Solid-Phase Peptide Synthesis : An Overview Focused on the Preparation of Biologically Relevant Peptides. *RSC Adv.* **2014**, *4*, 32658–32672.
- (147) Atwood, B. K.; Lopez, J.; Wager-Miller, J.; Mackie, K.; Straiker, A. Expression of G Protein-Coupled Receptors and Related Proteins in HEK293, AtT20, BV2, and N18 Cell Lines as Revealed by Microarray Analysis. *BMC Genomics* **2011**, *12* (14), 1–14.
- (148) Leger, A. J.; Covic, L.; Kuliopulos, A. Protease-Activated Receptors in Cardiovascular Diseases. *Circulation* **2006**, *114* (10), 1070–1077.
- (149) Sonin, D. L.; Wakatsuki, T.; Routhu, K. V; Harmann, L. M.; Petersen, M.; Meyer, J.; Strande, J. L. Protease-Activated Receptor 1 Inhibition by SCH79797 Attenuates Left Ventricular Remodeling and Profibrotic Activities of Cardiac Fibroblasts. *J Cardiovasc Pharmacol Ther.* **2013**, *18* (5), 460–475.
- (150) Arunlakshana, O.; Schild, H. O. Some Quantitative Uses of Drug Antagonists. *Br. J. Pharmacol. Chemother.* **1959**, *14* (1), 48–58.
- (151) Hulme, E. C.; Trevethick, M. a. Ligand Binding Assays at Equilibrium: Validation and Interpretation. *Br. J. Pharmacol.* **2010**, *161* (October 2009), 1219–1237.

- (152) Christopoulos, A.; Kenakin, T. G Protein-Coupled Receptor Allostereism and Complexing. *Pharmacol. Rev.* **2002**, *54* (2), 323–374.
- (153) Roskoski, R. J. ERK1/2 MAP Kinases: Structure, Function, and Regulation. *Pharmacol. Res.* **2012**, *66* (2), 105–143.
- (154) Tinning, P. W.; Franssen, A. J. P. M.; Hridi, S. U.; Bushell, T. J.; McConnell, G. A 340 / 380 Nm Light-Emitting Diode Illuminator for Fura-2 AM Ratiometric Ca²⁺ Imaging of Live Cells with Better than 5 NM. *J. Microsc.* **2018**, *269* (3), 212–220.
- (155) Daily, N. J.; Santos, R.; Vecchi, J.; Kemanli, P.; Wakatsuki, T. Calcium Transient Assays for Compound Screening with Human iPSC-Derived Cardiomyocytes: Evaluating New Tools. *J. Evol. stem cell Res.* **2017**, *1* (2), 1–11.
- (156) Bleasdale, J. E.; Thakur, N. R.; Gremban, R. S.; Bundy, G. L.; Fitzpatrick, F. A.; Smith, R. J.; Bunting, S. Selective Inhibition of Receptor-Coupled Phospholipase C-Dependent Processes in Human Platelets and Polymorphonuclear Neutrophils. *J. Pharmacol. Exp. Ther.* **1990**, *255* (2), 756–768.
- (157) Mizuno, N.; Itoh, H. Functions and Regulatory Mechanisms of Gq-Signaling Pathways. *Neurosignals* **2009**, *17*, 42–54.
- (158) Uemura, T.; Kawasaki, T.; Taniguchi, M.; Moritani, Y.; Hayashi, K.; Saito, T.; Takasaki, J.; Uchida, W.; Miyata, K. Biological Properties of a Specific G_q / 11 Inhibitor, YM-254890, on Platelet Functions and Thrombus Formation under High-Shear Stress. *Br. J. Pharmacol.* **2006**, *148*, 61–69.
- (159) Stockert, J. C.; Horobin, R. W.; Colombo, L. L.; Blazquez-Castro, A. Tetrazolium Salts and Formazan Products in Cell Biology: Viability Assessment, Fluorescence Imaging, and Labeling Perspectives. *Acta Histochem.* **2018**, *120* (3), 159–167.
- (160) Findlay, D. M.; Raggatt, L. J.; Bouralexis, S.; Hay, S.; Atkins, G. J.; Evdokiou, A. Calcitonin Decreases the Adherence and Survival of HEK-293 Cells by a Caspase-Independent Mechanism. *J. Endocrinol.* **2002**, *175* (3), 715–725.
- (161) Andersen, H.; Greenberg, D. L.; Fujikawa, K.; Xu, W.; Chung, D. W.; Davie, E. W. Protease-Activated Receptor 1 Is the Primary Mediator of Thrombin-Stimulated Platelet Procoagulant Activity. *Proc. Natl. Acad. Sci. U. S. A.* **1999**, *96* (20), 11189–11193.
- (162) Fadok, V. A.; Bratton, D. L.; Frasch, S. C.; Warner, M. L.; Henson, P. M. The Role of Phosphatidylserine in Recognition of Apoptotic Cells by Phagocytes. *Cell Death Differ.* **1998**, *5* (7), 551–562.
- (163) van de Langemheen, H.; Korotkovs, V.; Bijl, J.; Wilson, C. Polar Hinges as Functionalized Conformational Constraints in (Bi)Cyclic Peptides. **2017**, 387–395.
- (164) Bijl, J. Method Development for the Synthesis of Cyclic Peptides. Bachelor Thesis, University of Glasgow, 2016.
- (165) van de Langemheen, H.; van Hoeke, M.; Quarles van Ufford, H. C.; Kruijtzter, J. A. W.; Liskamp, R. M. J. Scaffolded Multiple Cyclic Peptide Libraries for Protein Mimics by

Native Chemical Ligation. *Org. Biomol. Chem.* **2014**, *12* (25), 4471–4478.

- (166) Kolb, H. C.; Finn, M. G.; Sharpless, K. B. Click Chemistry : Diverse Chemical Function from a Few Good Reactions. *Angew. Chem. Int. Ed.* **2001**, *40*, 2004–2021.
- (167) Shultz, M. D. Improving the Plausibility of Success with Inefficient Metrics. *ACS Med. Chem. Lett.* **2014**, *5* (1), 2–5.
- (168) Schultes, S.; De Graaf, C.; Haaksma, E. E. J.; De Esch, I. J. P.; Leurs, R.; Krämer, O. Ligand Efficiency as a Guide in Fragment Hit Selection and Optimization. *Drug Discov. Today Technol.* **2010**, *7* (3), 157–162.
- (169) Abad-zapatero, C. Ligand Efficiency Indices for Effective Drug Discovery. *Expert Opin. Drug Discov.* **2007**, *2* (4), 469–488.
- (170) Johnson, J. J.; Miller, D. L.; Jiang, R.; Liu, Y.; Shi, Z.; Williams, R.; Balsara, R.; Sauter, E. R.; Stack, M. S. Protease Activated Receptor-2 (PAR-2)-Mediated Nf-KB Activation Suppresses Inflammation-Associated Tumor Suppressor MicroRNAs in Oral Squamous Cell Carcinoma. *J. Biol. Chem.* **2016**, *291*, 6936–6945.
- (171) Trott, O.; Olson, A. J. AutoDock Vina : Improving the Speed and Accuracy of Docking with a New Scoring Function , Efficient Optimization , and Multithreading. *J. Comput. Chem.* **2010**, *31*, 455–461.
- (172) Jones, G.; Willett, P.; Glen, R. C.; Leach, A. R.; Taylor, R. Development and Validation of a Genetic Algorithm for Flexible Docking. *J. Mol. Biol.* **1997**, *267* (3), 727–748.
- (173) Hartshorn, M. J.; Verdonk, M. L.; Chessari, G.; Brewerton, S. C.; Mooij, W. T. M.; Mortenson, P. N.; Murray, C. W. Diverse, High-Quality Test Set for the Validation of Protein–Ligand Docking Performance. *J. Med. Chem.* **2007**, *50* (4), 726–741.
- (174) Mooij, W. T. M.; Verdonk, M. L. General and Targeted Statistical Potentials for Protein-Ligand Interactions. *Proteins* **2005**, *61* (2), 272–287.
- (175) Eldridge, M. D.; Murray, C. W.; Auton, T. R.; Paolini, G. V; Mee, R. P. Empirical Scoring Functions: I. The Development of a Fast Empirical Scoring Function to Estimate the Binding Affinity of Ligands in Receptor Complexes. *J. Comput. Aided. Mol. Des.* **1997**, *11* (5), 425–445.
- (176) Murray, C. W.; Auton, T. R.; Eldridge, M. D. Empirical Scoring Functions. II. The Testing of an Empirical Scoring Function for the Prediction of Ligand-Receptor Binding Affinities and the Use of Bayesian Regression to Improve the Quality of the Model. *J. Comput. Aided. Mol. Des.* **1998**, *12* (5), 503–519.
- (177) Korb, O.; Stu, T.; Exner, T. E. Empirical Scoring Functions for Advanced Protein - Ligand Docking with PLANTS. **2009**, 84–96.
- (178) Wilson, K. L. Evaluating the Application and Limitations of Bio-Based Solvents within Organic Synthesis. PhD Thesis, University of Strathclyde, 2018.
- (179) Wu, H.; Handoko; Raj, M.; Arora, P. S. Iterative Design of a Biomimetic Catalyst for

Amino Acid Thioester Condensation. *Org. Lett.* **2017**, *19* (19), 5122–5125.

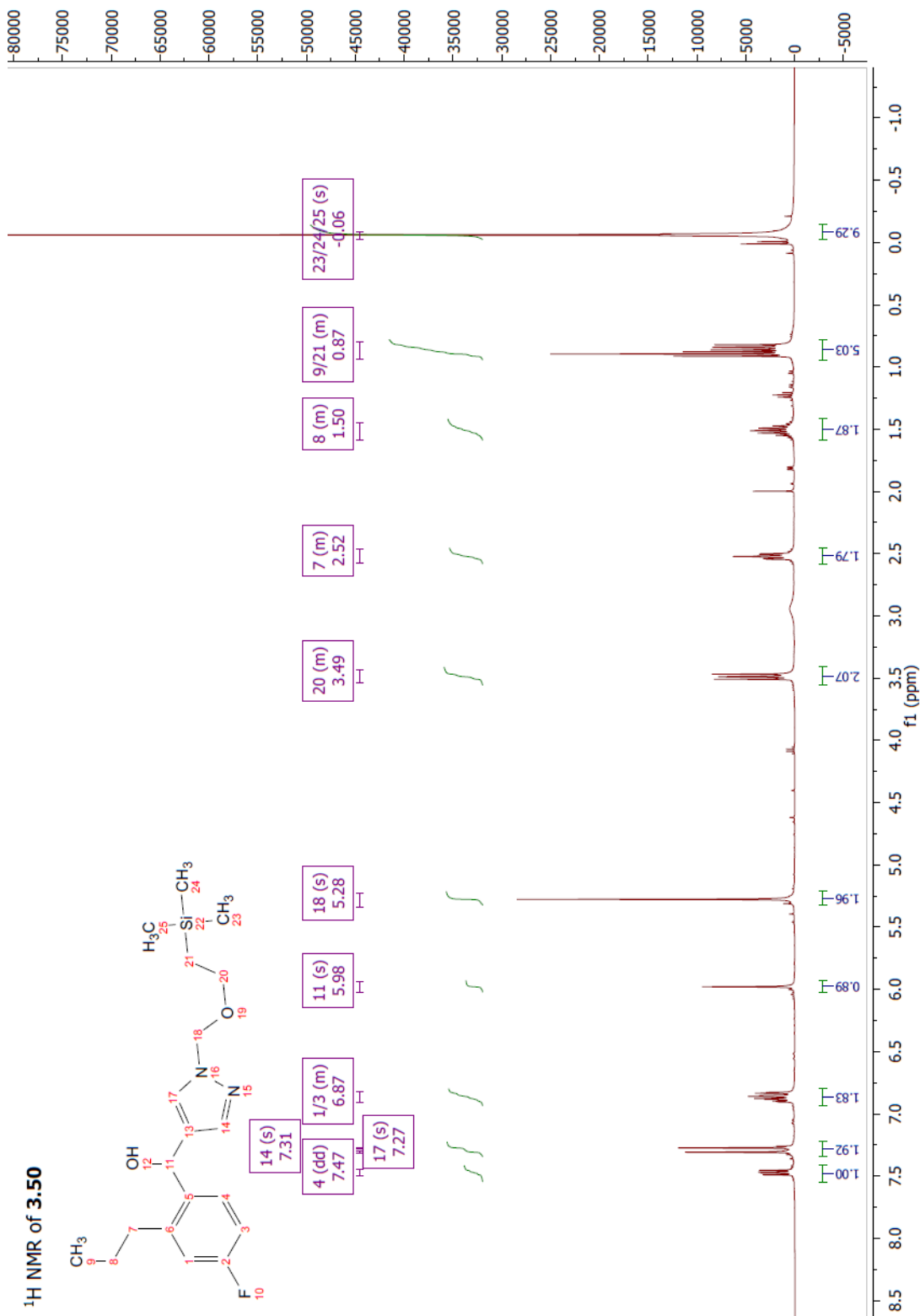
- (180) Bueno, A. B.; Agejas, J.; Broughton, H.; Dally, R.; Durham, T. B.; Fe, J.; Gonza, R.; Hahn, P. J.; Marcos, A.; Sanz, G.; et al. Optimization of Hydroxyethylamine Transition State Isoesters as Aspartic Protease Inhibitors by Exploiting Conformational Preferences. *J. Med. Chem.* **2017**, *60*, 9807–9820.
- (181) Choi, Y. L.; Lee, H.; Kim, B. T.; Choi, K.; Heo, J.-N. Direct Synthesis of Pyrazolo[5,1-a] Isoindoles via Intramolecular Palladium-Catalyzed C-H Bond Activation. *Adv. Synth. Catal.* **2010**, *352*, 2041–2049.
- (182) Liu, Y.; Shen, L.; Prashad, M.; Tibbatts, J.; Repic, O.; Blacklock, T. J. A Green N - Detosylation of Indoles and Related Heterocycles Using Phase Transfer Catalysis. **2008**, No. 5, 778–780.
- (183) Nair, R. N.; Bannister, T. D. Tale of Two Protecting Groups - Boc vs SEM - for Directed Lithiation. *Org. Process Res. Dev.* **2016**, *20*, 1370–1376.
- (184) Vuluga, D.; Legros, J.; Crousse, B.; Bonnet-Delpon, D. Synthesis of Pyrazoles through Catalyst-Free Cycloaddition of Diazo Compounds to Alkynes. *Green Chem.* **2009**, *11*, 156–159.
- (185) Sharma, V. G.; Jain, S. L.; Sain, B. Metallophthalocyanines Catalyzed Cyclopropanation of Olefins with Trimethylsilyldiazomethane: A Facile and Stereoselective Synthesis of Silylcyclopropanes. *Catal. Commun.* **2006**, *7* (7), 454–456.
- (186) Fors, B. P.; Hawker, C. J. Control of a Living Radical Polymerization of Methacrylates by Light. *Angew. Chem. Int. Ed.* **2012**, *51*, 8850–8853.
- (187) Bregman, H.; Simard, R.; Andrews, K. L.; Ayube, S.; Chen, H.; Gunaydin, H.; Guzman-perez, A.; Hu, J.; Huang, L.; Huang, X.; et al. The Discovery and Hit-to-Lead Optimization of Tricyclic Sulfonamides as Potent and Efficacious Potentiators of Glycine Receptors. *J. Med. Chem.* **2017**, *60*, 1105–1125.
- (188) Martin, C.; Mailliet, P.; Maddaluno, J. Synthesis of Oxa-Bridged Analogues of Farnesyltransferase Inhibitor RPR 115135. *J. Org. Chem.* **2001**, *66*, 3797–3805.
- (189) Belyk, K. M.; Beguin, C. D.; Palucki, M.; Grinberg, N.; Dasilva, J.; Yasuda, N. A Rapid Catalytic Asymmetric Synthesis of 1, 3, 4-Trisubstituted Pyrrolidines. *Tetrahedron Lett.* **2004**, *45*, 3265–3268.
- (190) Pflum, D. A.; Krishnamurthy, D.; Han, Z.; Wald, S. A.; Senanayake, C. H. Asymmetric Synthesis of Cetirizine Dihydrochloride. *Tetrahedron Lett.* **2002**, *43* (6), 923–926.
- (191) Fyfe, J. W. B.; Watson, A. J. B. Recent Developments in Organoboron Chemistry : Old Dogs , New Tricks. *Chem* **2017**, *3* (1), 31–55.
- (192) Roush, W. R.; Walts, A. E.; Hoong, L. K. Diastereo- and Enantioselective Aldehyde Addition Reactions Class of Tartrate Ester Modified Allylboronates. *J. Am. Chem. Soc.* **1985**, *107* (11), 8186–8190.

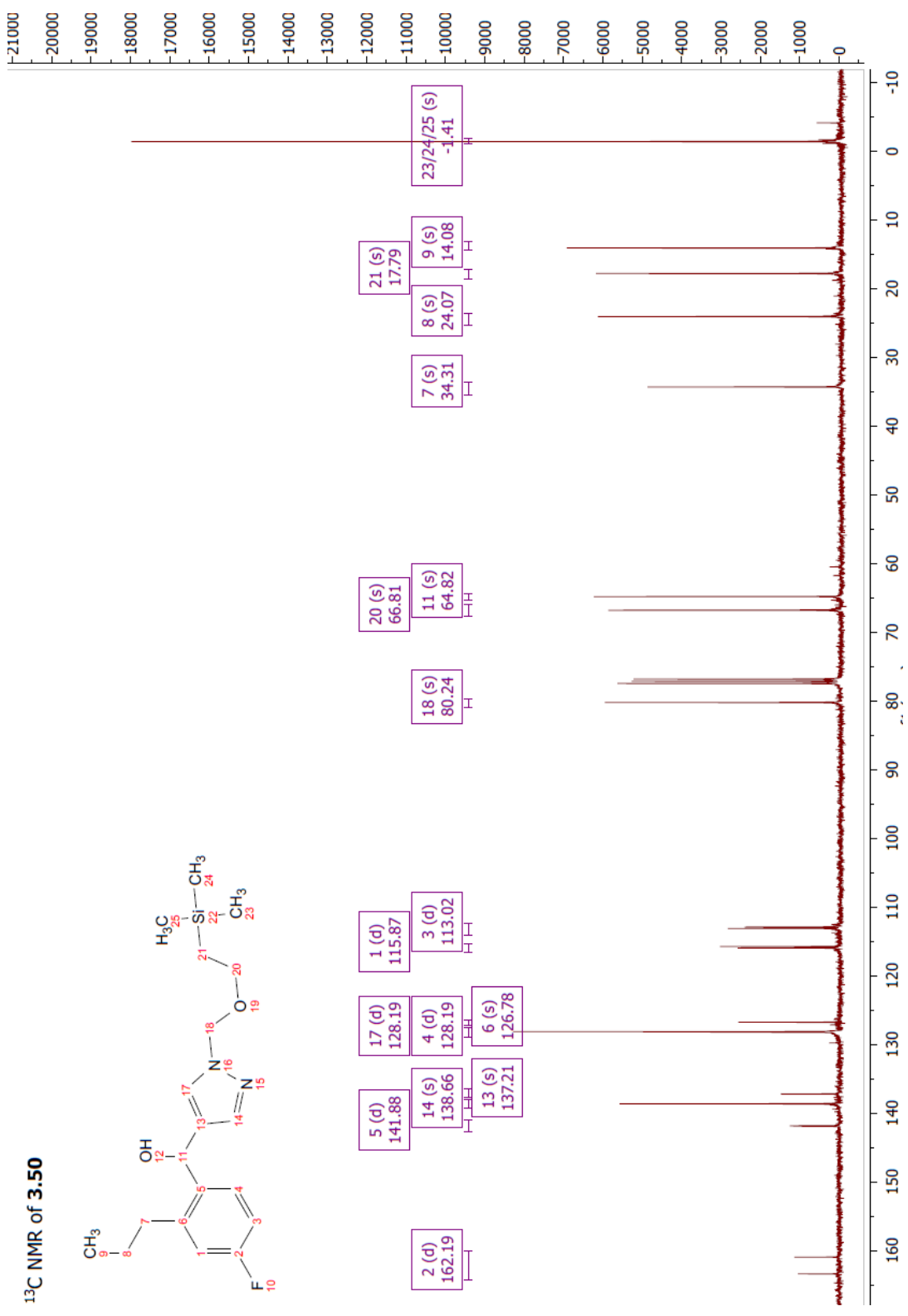
- (193) Yoo, K. S.; Yoon, C. H.; Jung, K. W. Oxidative Palladium (II) Catalysis : A Highly Efficient and Chemoselective Cross-Coupling Method for Carbon - Carbon Bond Formation under Base-Free and Nitrogenous-Ligand Conditions. *J. Am. Chem. Soc.* **2006**, *128*, 16384–16393.
- (194) Yoon, C. H.; Yoo, K. S.; Yi, S. W.; Mishra, R. K. Oxygen-Promoted Palladium (II) Catalysis : Facile C (Sp 2) – C (Sp 2) Bond Formation via Cross-Coupling of Alkenylboronic Compounds and Olefins. *Org. Lett.* **2004**, *6* (22), 4037–4039.
- (195) Luqman, S.; Pezzuto, J. M. NFκB: A Promising Target for Natural Products in Cancer Chemoprevention. *Phyther. Res.* **2010**, *24* (7), 949–963.
- (196) Hart, L. A.; Krishnan, V. L.; Adcock, I. M.; Barnes, P. J.; Chung, K. F. Activation and Localization of Transcription Factor, Nuclear Factor-KappaB, in Asthma. *Am. J. Respir. Crit. Care Med.* **1998**, *158* (5 Pt 1), 1585–1592.
- (197) Pamukcu, B.; Lip, G. Y. H.; Shantsila, E. The Nuclear Factor--Kappa B Pathway in Atherosclerosis: A Potential Therapeutic Target for Atherothrombotic Vascular Disease. *Thromb. Res.* **2011**, *128* (2), 117–123.
- (198) Mattson, M. P.; Camandola, S. NF-KappaB in Neuronal Plasticity and Neurodegenerative Disorders. *J. Clin. Invest.* **2001**, *107* (3), 247–254.
- (199) Goh, F. G.; Ng, P. Y.; Nilsson, M.; Kanke, T.; Plevin, R. Dual Effect of the Novel Peptide Antagonist K-14585 on Proteinase-Activated Receptor-2-Mediated Signaling. *Br. J. Pharmacol.* **2009**, *158* (7), 1695–1704.
- (200) Goh, F. G.; Sloss, C. M.; Cunningham, M. R.; Nilsson, M.; Cadalbert, L.; Plevin, R. G-Protein-Dependent and -Independent Pathways Regulate Proteinase-Activated Receptor-2 Mediated P65 NFκB Serine 536 Phosphorylation in Human Keratinocytes. *Cell. Signal.* **2008**, *20* (7), 1267–1274.
- (201) de Meijere, A. Bonding Properties of Cyclopropane and Their Chemical Consequences. *Angew. Chemie Int. Ed. English* **1979**, *18* (11), 809–826.
- (202) Barnes-Seeman, D.; Jain, M.; Bell, L.; Ferreira, S.; Cohen, S.; Chen, X. H.; Amin, J.; Snodgrass, B.; Hatsis, P. Metabolically Stable Tert-Butyl Replacement. *ACS Med. Chem. Lett.* **2013**, *4* (6), 514–516.
- (203) Noyori, R.; Hashiguchi, S. Asymmetric Transfer Hydrogenation Catalyzed by Chiral Ruthenium Complexes Asymmetric Transfer Hydrogenation of Ketones. *Acc. Chem. Res.* **1997**, *30* (2), 97–102.
- (204) Kirchner, G.; Scollar, M. P.; Klibanov, A. M. Resolution of Racemic Mixtures via Lipase Catalysis in Organic Solvents. *J. Am. Chem. Soc.* **1985**, *107*, 7072–7076.
- (205) Lee, S. Y.; Murphy, J. M.; Ukai, A.; Fu, G. C. Nonenzymatic Dynamic Kinetic Resolution of Secondary Alcohols via Enantioselective Acylation: Synthetic and Mechanistic Studies. *J. Am. Chem. Soc.* **2012**, *134*, 15149–15153.
- (206) Armarego, W. L. F.; Chai, C. L. L. *Purification of Laboratory Chemicals*, 7th ed.; Elsevier

Inc.: Oxford, 2012.

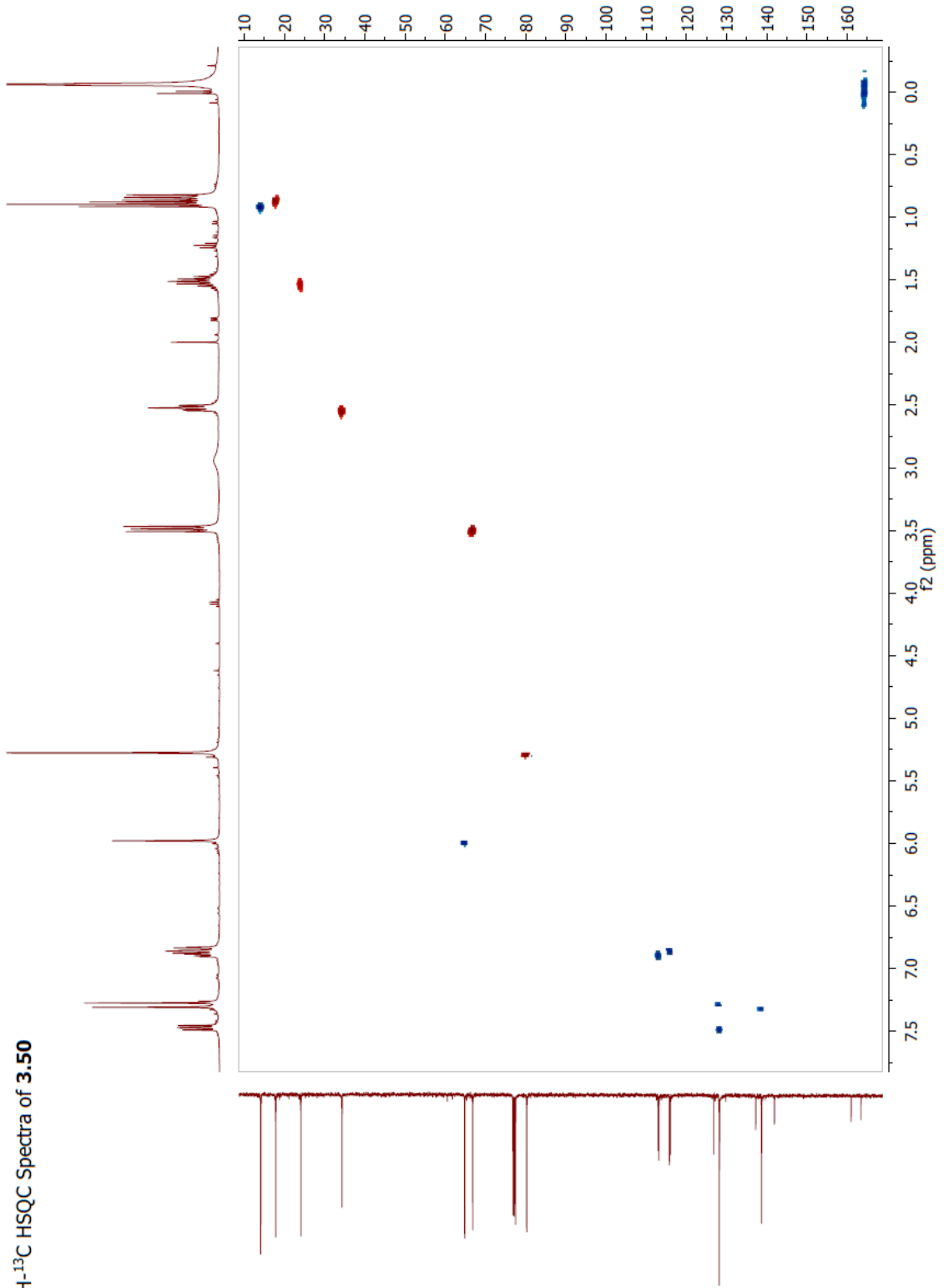
- (207) Whitten, J. P.; Matthews, D. P.; McCarthy, J. R. [2-(Trimethylsilyl)Ethoxy]Methyl (SEM) as a Novel and Effective Imidazole and Fused Aromatic Imidazole Protecting Group. *J. Org. Chem.* **1986**, *51*, 1891–1894.
- (208) Guy, R. K.; Slavish, P. J.; Shadrick, W. R.; Young, B. M.; Boyd, V. A.; Bharatham, N.; Price, J. E.; Shelat, A. Tetrahydroquinoline-Based Bromodomain Inhibitors. WO 2018111805, 2018.
- (209) Allin, S. M.; Barton, W. R. S.; Bowman, W. R.; Bridge, E.; Elsegood, M. R. J.; Mcinally, T.; Mckee, V. Bu₃SnH-Mediated Radical Cyclisation onto Azoles. *Tetrahedron* **2008**, *64*, 7745–7758.
- (210) Fugina, N.; Holzer, W.; Wasicky, M. The [2-(Trimethylsilyl)Ethoxy]Methyl Function as a Suitable N-1 Protecting Group in Lithiation Reactions with Pyrazoles and 1,2,4-Triazoles. *Heterocycles* **1992**, *34* (2), 303–314.
- (211) Holzer, W.; Jäger, C.; Slatin, C. N-Substituted Bromopyrazoles: Synthesis and ¹³C Nmr Study. *Heterocycles* **1994**, *38* (11), 2433–2448.
- (212) Keeley, A.; Ábrányi-Balogh, P.; Keserű, G. M. Design and Characterization of a Heterocyclic Electrophilic Fragment Library for the Discovery of Cysteine-Targeted Covalent Inhibitors†. *Med. Chem. Comm.* **2019**, *10* (2), 263–267.
- (213) Qiu, Z.; Lin, X.; Zhang, W.; Zhou, M.; Guo, L.; Kocer, B.; Wu, G.; Zhang, Z.; Liu, H.; Shi, H.; et al. Discovery and Pre-Clinical Characterization of Third-Generation 4 - H Heteroaryldihydropyrimidine (HAP) Analogues as Hepatitis B Virus (HBV) Capsid Inhibitors. *J. Med. Chem.* **2017**, *60*, 3352–3371.
- (214) Sun, A. D.; Love, J. A. Nickel-Catalyzed Selective Defluorination to Generate Partially Fluorinated Biaryls. *Org. Lett.* **2011**, *13*, 2750–2753.
- (215) Lu, F.; Sun, H.; Du, A.; Feng, L.; Li, X. Selective Alkylation and Arylation of C – F Bond with Grignard Reagents. *Org. Lett.* **2014**, *16*, 772–775.
- (216) Yingjun, Z.; Qingyun, R.; Xinchang, L.; Goldmann, S. Dihydropyrimidine Compounds and Their Application in Pharmaceuticals. WO2014/29193, 2014.
- (217) Melzig, L.; Rauhut, C. B.; Naredi-rainer, N.; Knochel, P. Difunctionalisation of Arenes and Heteroarenes by Directed Metallation and Sulfoxide – Magnesium Exchange. *Chem. – A Eur. J.* **2011**, *6* (Scheme 1), 5362–5372.
- (218) Gloanec, P.; Schaffner, A.-P.; Sansilvestri-morel, P.; Rupin, A.; Mennecier, P.; Vallez, M.-O. Compounds of Phosphinanes and Azaphosphinanes, a Process for Their Preparation and Pharmaceutical Compositions Containing Them. US2018/16288, 2018.
- (219) Min, J. Y.; Chang, S. Y.; Lee, J. H.; Kang, S. H.; Kong, S. J.; Jo, S. Y.; Park, K.; Kim, Y. M.; Choi, J. Preparation of Heteroaryl Compounds as Antiviral Agents. WO 2018062978, 2018.

Appendix I – 2D NMR Spectra for 3.50

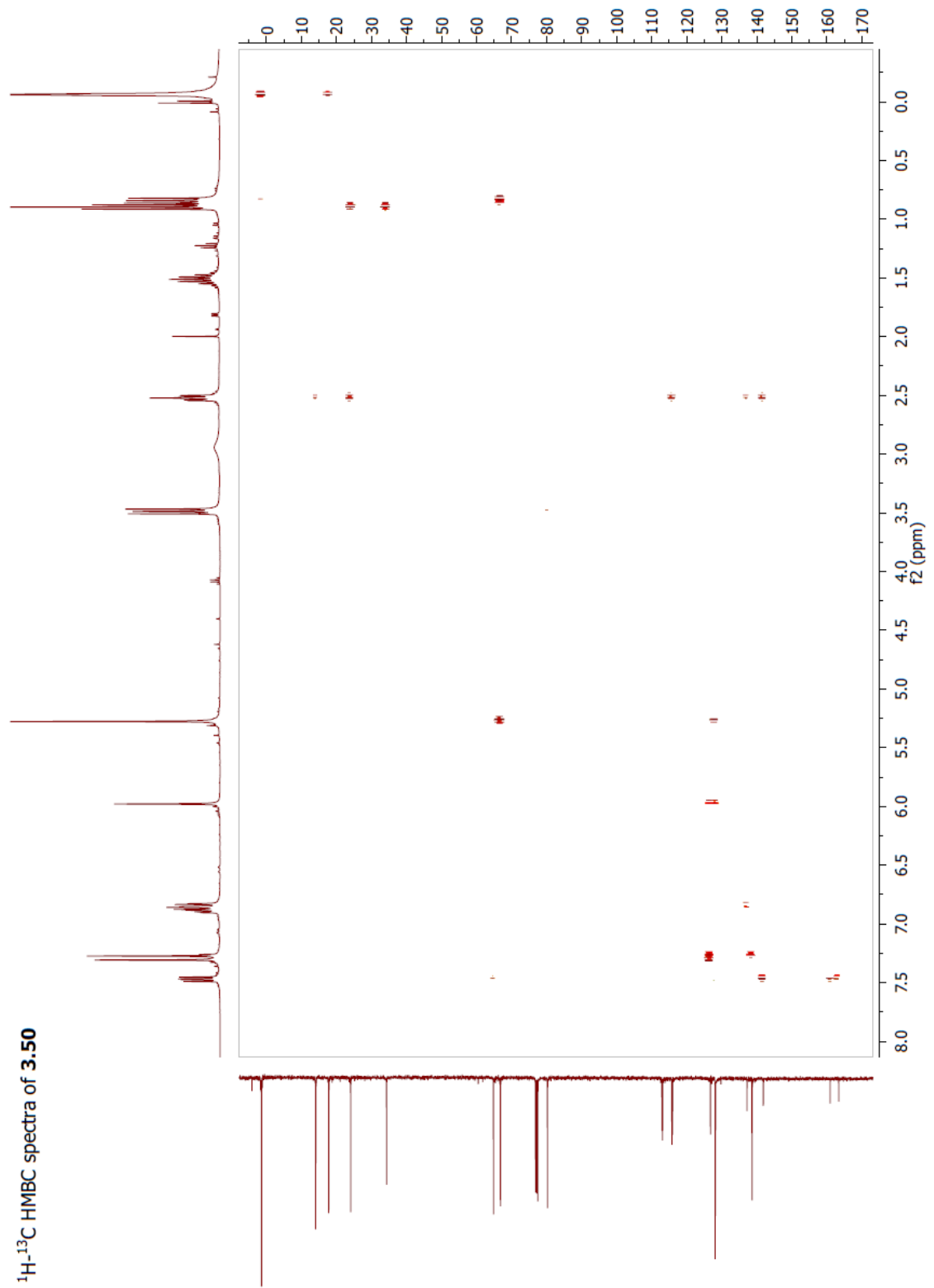




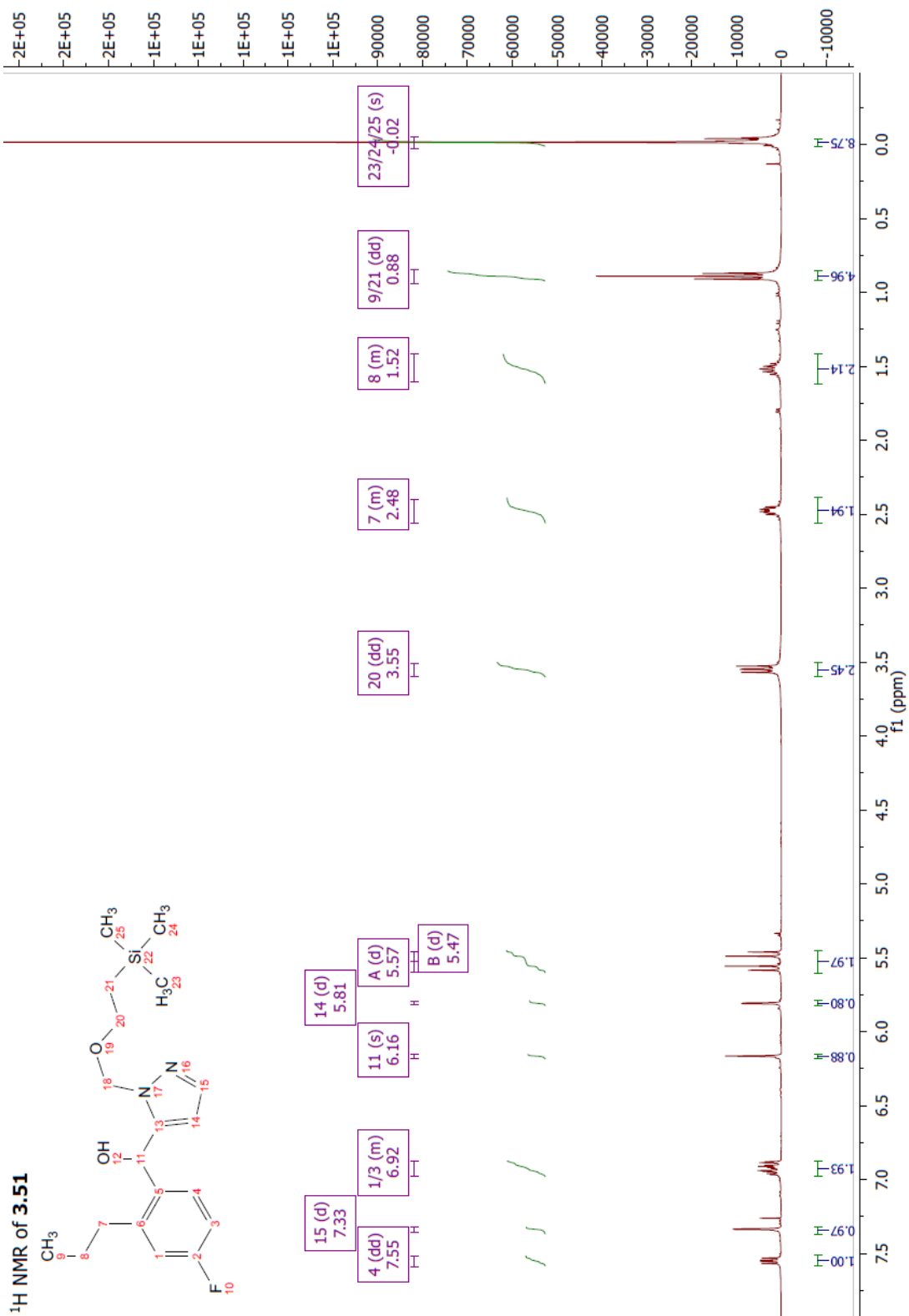
^1H - ^{13}C HSQC Spectra of **3.50**



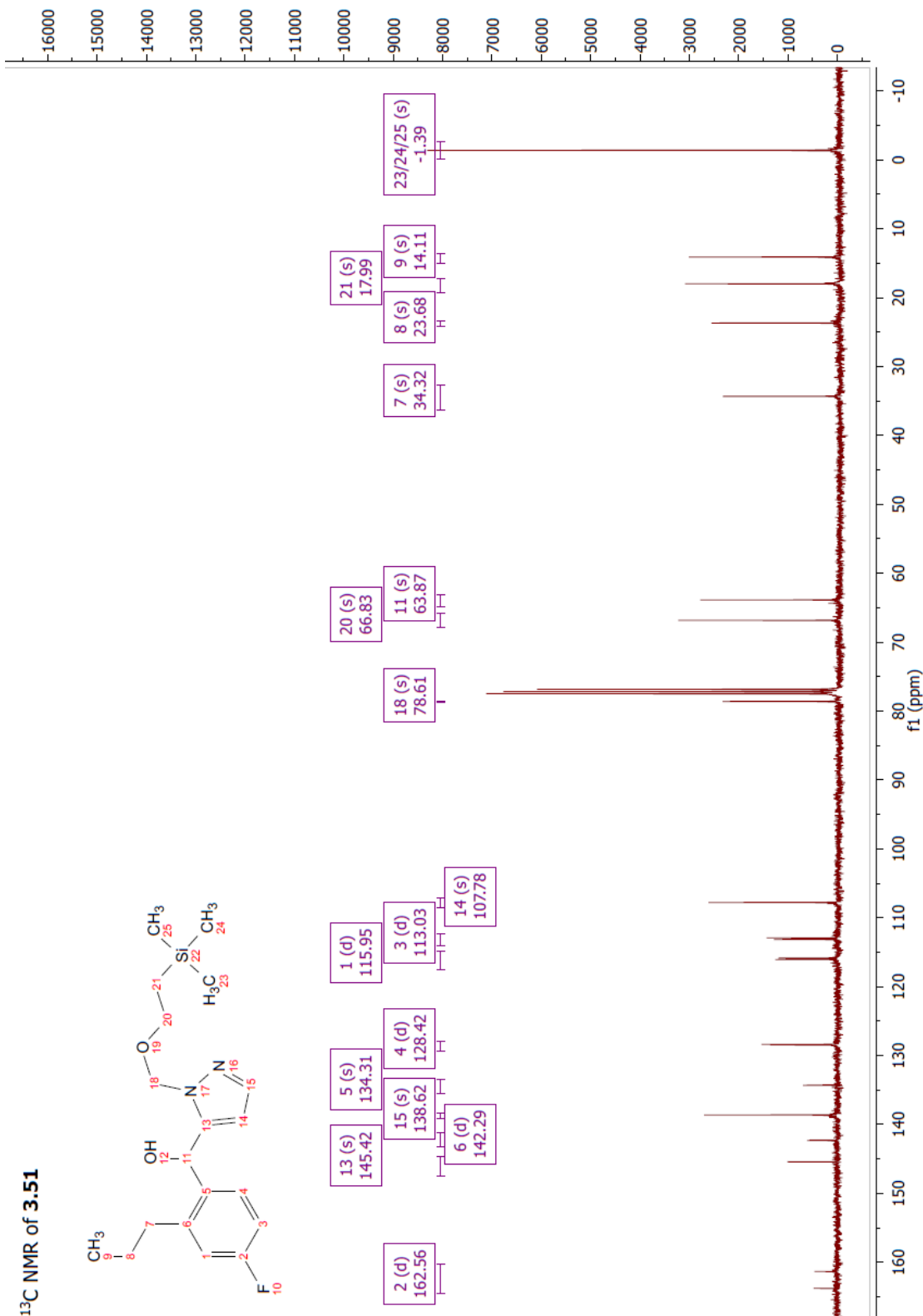
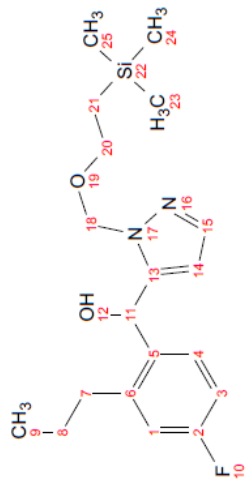
^1H - ^{13}C HMBC spectra of **3.50**



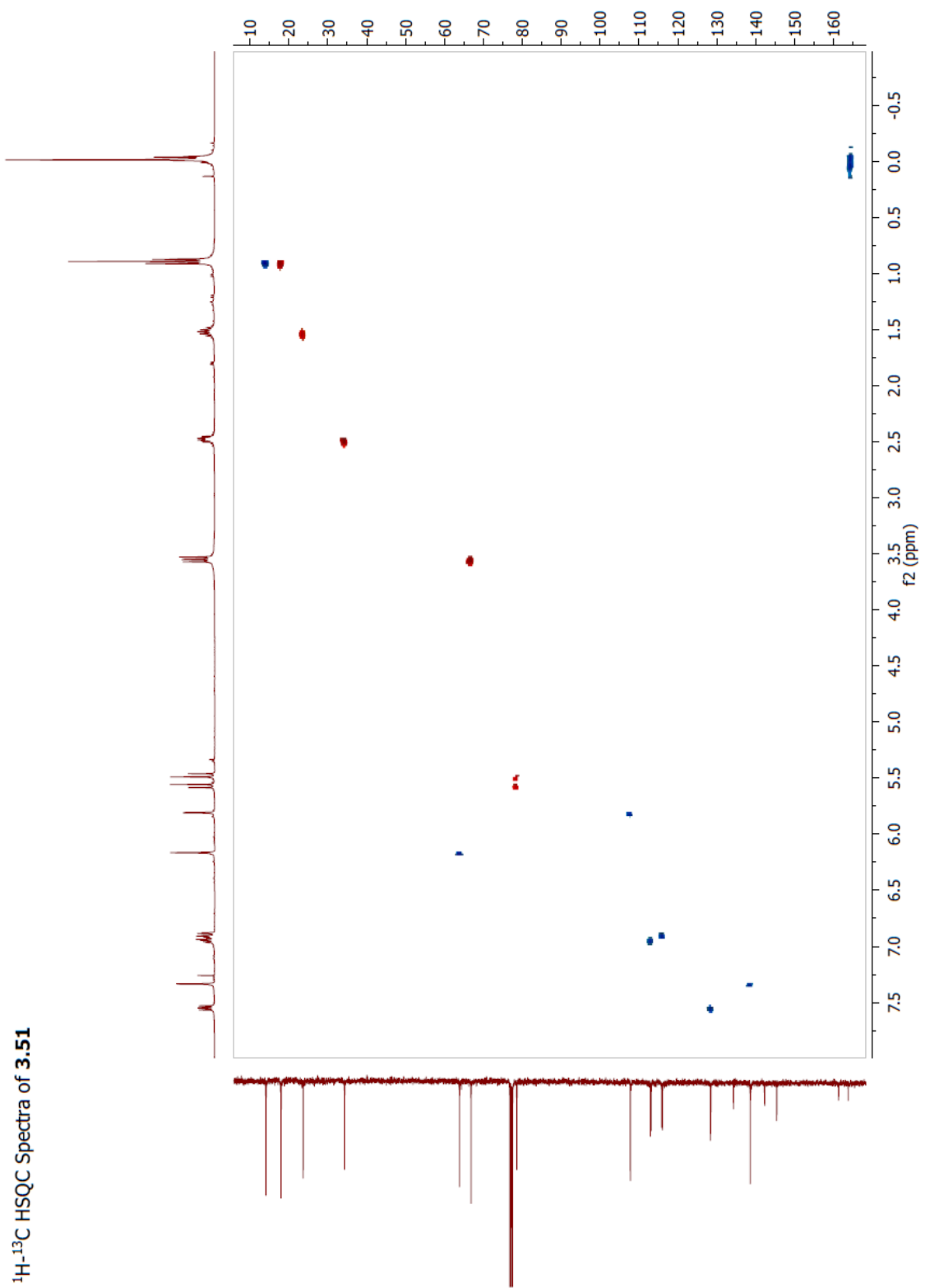
Appendix II – 2D NMR Spectra for 3.51



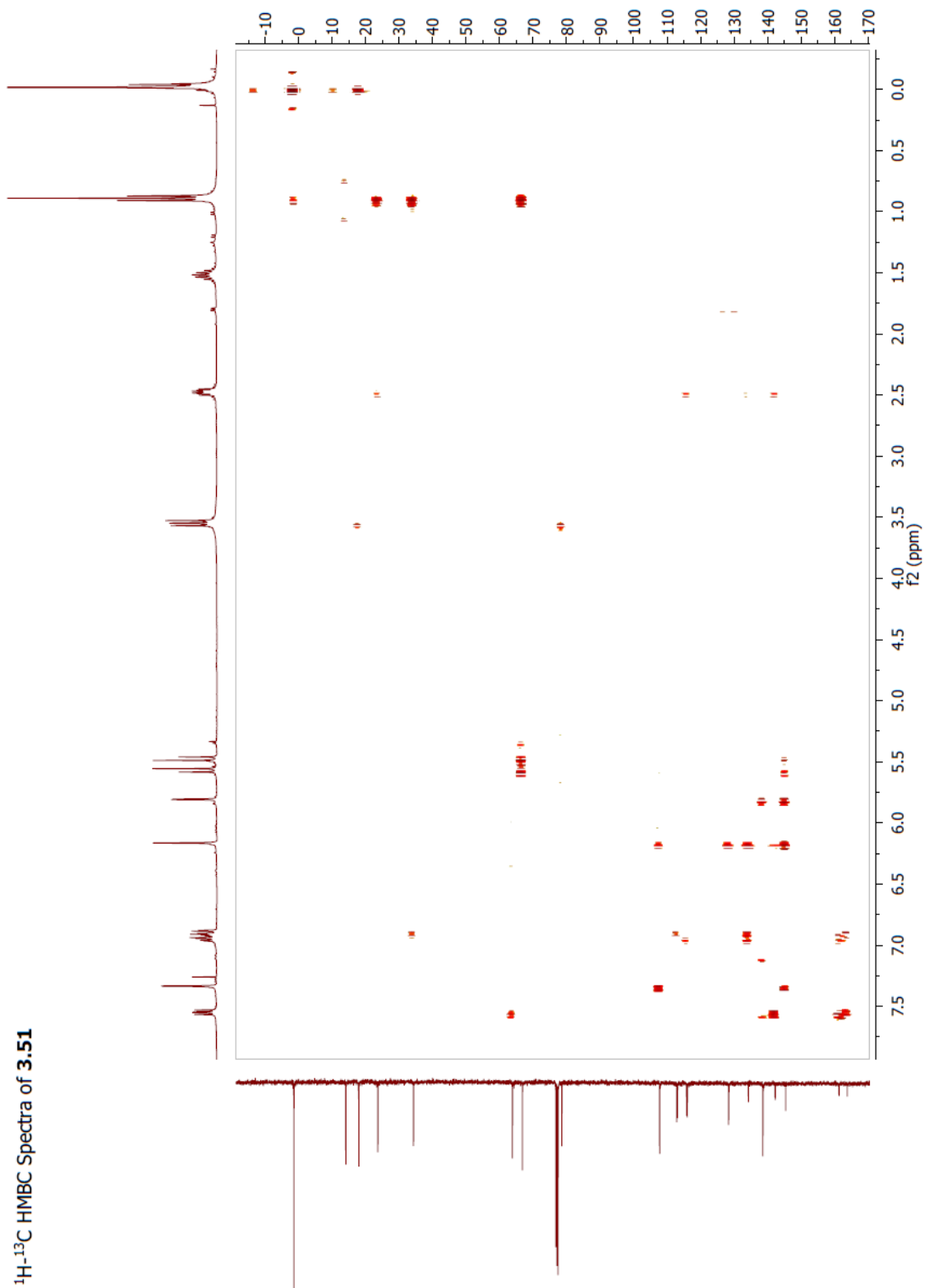
¹³C NMR of **3.51**



^1H - ^{13}C HSQC Spectra of **3.51**



^1H - ^{13}C HMBC Spectra of **3.51**



Appendix III – Variable Temperature Studies with 3.24

